Development of Fluorescent Polymeric Nano-Assemblies for Studying Organelle Interactions in Intracellular Drug Release and Accumulation

विद्या वाचस्पति की
उपाधि की अपेक्षाओं की आंशिक पूर्ति में प्रस्तुत शोध प्रबंध

A thesis submitted in partial fulfillment of the requirements of the degree of Doctor of Philosophy

द्वारा / By
मिशिका विरमानी / Mishika Virmani

२०१५२०२४ / 20152024

शोध प्रबंध पर्यवेक्षक / Thesis Supervisor:
मणिक्कम जयकन्नान / Prof. Manickam Jayakannan

भारतीय विज्ञान शिक्षा एवं अनुसंधान संस्थान पुणे
INDIAN INSTITUTE OF SCIENCE EDUCATION AND RESEARCH PUNE
April 2024

DEDICATION

This dissertation is dedicated to Dr. Kalpana Chawla (1962–2003), the first Indian woman to break barriers to travel to space, transcending the bounds of Earth's atmosphere and demonstrating that the sky is not the limit.

CERTIFICATE

Certified that the work incorporated in the thesis entitled '***Development of Fluorescent Polymeric Nano-Assemblies for Studying Organelle Interactions in Intracellular Drug Release and Accumulation'***, submitted by Mishika Virmani was carried out by the candidate, under my supervision. The work presented here or any part of it has not been included in any other thesis submitted previously for the award of any degree or diploma from any other University or institution.

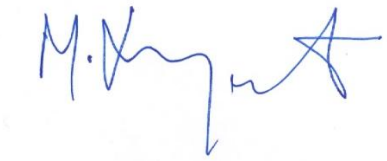

Manickam Jayakannan

April 1, 2024

DECLARATION

I declare that this written submission represents my ideas in my own words and I have adequately cited and provided the references from original source, where ever ideas of others are included. I also declare that I have adhered to all the principles of scientific honesty and integrity and have not misrepresented or fabricated or falsified any idea/data/fact/source in my submission. I understand that the violation of above will be cause for disciplinary action by institute and can also evoke penal action from the sources which have this not been properly cited or from whom proper permission has not been taken when needed.

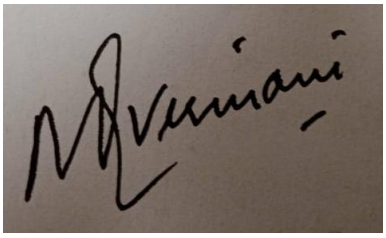

Date: 29th March 2024 Mishika Virmani

Pune (MH) India Reg ID: 20152024

ACKNOWLEDGEMENTS

This, to me, is the most cherished page of my thesis, where I took the privilege of expressing my profound gratitude towards people who helped shape both me and my work. At the outset of my thesis, I wrote this part first to remind myself of this terrific journey and to draw energy and inspiration from it throughout the otherwise hectic process of writing a thesis.

I took this opportunity to introduce all the characters in order of entry into my Ph.D. life and appreciate the invaluable support they offered me. Coming from a background where education was a far-fetched dream for my parents, they struggled hard to ensure I got a good education. I was fortunate to be born to my parents, ***Mrs. Sunita Virmani*** and ***Mr. Sushil Virmani,*** who I fondly call mummy and papa. No words can describe my feelings for them and how much I owe them. Both my parents supported my decision to come to IISER-P well. I can only recollect, but cannot write in words, the happiness and pride I saw in their eyes when they first came to see me off at IISER-P, where I began my MS-Ph.D. dual degree program in 2015. Ever since those eyes kept me going every time, I felt I was not enough. I recently became interested in learning Sanskrit, so I would appreciate their role by saying **।। मातृ देवौ भव, पितृ देवौ भव ।।**

The role of a guru in life is as long and profound as that of parents. I remember listening to a lecture by ***Prof. Manickam Jayakannan***, my thesis advisor at Sir C.V. Raman Auditorium. He perfectly appeared to me like one of the mad and crazy scientists, Prof. Frink, I once saw in an animated movie, The Simpsons. I had little idea about the science he did, but his energy and passion for science drew me to work in his lab. Over the years, I held varying perceptions of him, initially as someone tough but ultimately as the most consistently inspiring mentor. He has, without fail, appreciated the good points in me and never missed an opportunity to remind me to work on areas for improvement. He once told me, '*It is hard to be a critic. I become the bad guy in order to make you work right*'. We never resonated on a similar thought, but all those discussions made me return to him with a better literature search the next day. However, despite this, he gave me ample space to experiment without hesitation on different topics that I believed were worthy of exploration. He believes in me; that is all a student needs to know. He has always stood by my side and saved me from many difficult and awkward situations. I am working hard on all his advice and changes in me that he has asked for, and I hope to make him proud one day. **।। आचार्य देवौ भव**

I I I am genuinely thankful to ***Prof. Asha S.K.*** for being such a gracious scientist for letting me conduct various research activities in her lab at NCL-Pune during my PhD days. She has always been friendly and admiring in her approach towards me. I remember her attending my pre-synopsis examination, where her constructive remarks truly motivated me. Sir and Madam were extremely pleasant in hosting various joint lab lunch and dinner parties at their beautiful residence at NCL-Pune, serving us great food and playing board games. I will never forget my time at their home during the Pongal celebrations. I would like to extend my sincere thanks to both y RAC members, ***Prof. Raghavendra Kikkeri*** and ***Prof. Ashootosh Ambade*** for being so making time and giving constructive suggestions during my RAC meetings. This section would be incomplete without thanking my Ph.D. mentors, ***Dr. Madan Ambhore***, and ***Dr. Karnati Narsimha.*** I am so proud to be mentored by them and earn their friendship, which continued all these years even after they left the lab. There were times when I missed good food, and then there was Narismha, who fed me egg rice on many occasions. It will be correct to say that I missed his good food more than I missed him. They were just great, and I was just myself around them. No learning is complete without becoming a teacher yourself. Several BS-MS and project students over the years of my Ph.D. were a breath of fresh air, asking me plenty of questions about research and, in general, giving me a sense of responsibility. A special thanks to ***Jewel***, an exceptionally talented BS-MS student who showed faith in me and chose to work with me.

Life away from family at a hostel has its perks and challenges. Well, I count myself among those lucky people who always had good friends and lab mates around me. I guess the lab becomes your home, where you work round the clock. Productivity mandates a healthy lab atmosphere. My lab mates kept me working, never letting me feel a shortage of anything. Thanks to all of them. A special thanks my senior ***Dr. Sonashree Saxena*** for guiding me and teaching me Tissue Culture. Many thanks to all my friends at IISER-P and to ***Dr. Suman Manna***. He indeed kept me going and motivated me. He is a precious gem to have and safeguard, and I wish I had known him earlier. This next person, I am to mention, was the most difficult to accommodate in a specific section of acknowledgments as his contribution to my Ph.D. life extended beyond any specific role. A mentor, a teacher, a friend, my family, my Skype buddy, an all-in-one package, who recently bagged a title as my husband. I cannot thank my husband, ***Dr. Prathamesh Madhav Datar***, enough, who complements me in all aspects of my life. I could not have been luckier to have him in my life. A religious routine of coffee over Skype calls twice daily for nearly 2800 days kept the

7900-mile geographical distance between us relatively short. His unfathomable faith in me and treating me as no less than him makes him the best human being I have known.

Thank you so much for being there for me. I am equally honored and happy to be a part of his beautiful family, which now becomes mine. Thanks to my second set of parents, ***Mr. Madhav Datar***, my baba, and ***Mrs. Mohita Datar***, who I fondly call Aai. They ensured an incessant supply of homemade *laddoos* to my hostel. Not just laddoos, but tasty Alphonso mangoes stocked up my hostel room during mango season. Prathamesh's younger sister, ***Charuta,*** is fun to be around. Her witty remarks about her brother keep the atmosphere delightful and happy. I am highly fond of this mesmerizing young girl. I am incredibly fortunate to have them in my life. I know a very kind-hearted yet strong woman, ***Mrs. Ujwala Joshi***, Prathamesh's maternal grandmother, fondly known as Aaji. Life claimed her too early, and I truly miss her. Her esteemed wish was to see us both complete our PhDs and be together. How I wish she were here to celebrate this day. I always sensed a time-space difference whenever I returned home. It was like stepping back in time, a feeling my siblings, ***Chetna*** and ***Naman***, helped to recreate. Being with them revived our shared childhood memories and the joy that came with them. During the Covid pandemic, the extended stay at home with both of them is something I remember fondly every day. The best part about having siblings is that they keep you connected to that fearless, carefree child inside you. I consider myself incredibly fortunate to have both of them in my life. Thanks to all the technical staff at IISER-P, which helped reduce half our work. It was a wholesome experience here at IISER-P. I spent nine years of my young life here at this campus, but an enormous thanks to this campus for keeping me lively. Evening walks and morning jogs at this picturesque campus are everyone's dream. I will miss this verdant campus that kept me fit and energetic. Thank you all for helping me come this far in my life. It was not easy; It just got easy because of you all!

SYNOPSIS

Drug delivery via nano-carriers enabled the translation of promising therapeutics into successful therapies. Nanotechnology evolved over the years and led to the development of various nano-delivery scaffolds. Much research has been dedicated towards the design optimization of nano carriers to bring in the maximum drug efficacy. However, the current design paradigm is mainly focused from materials perspective and little attention is given to the biological aspects. Administered nanoparticles face plethora of biological obstacles which rather limit their ability to reach their desired targets. These obstacles are prevalent both at the macro and the micro level. Macro level obstacles comprise of organ level barriers to sub-organ level barriers, whereas micro level barriers are generally encountered at the intracellular level. The inability of the drug to reach and populate at the target site renders 1 out of 9 newly discovered drug delivery systems ineffective by authorities, leading to high attrition rates of such delivery systems in the later stage clinical trials. Most of the clinical trials of these drug delivery systems fails due to reduced efficacy which perhaps stems from a heterogenous patient response. The relatively low success rate of these drugs has prompted a need to better understand the underlying pharmacology mechanism at single cell level. This thesis aims to visualize the delivery aspects of nano carrier at cellular level to appreciate the barriers operational at micro level which then modulates the therapeutic efficacy of a drug delivery system. The thesis is divided into 4 chapters whose details are mentioned below:

- **Chapter 1:** The first chapter extensively discussed the materials and biological aspects of drug delivery. Material aspects such as type of therapeutic and type of delivery system have been discussed. Emphasis is also given on biological barriers which stands tall in hampering the efficacy of drug delivery system. Intracellular barrier of lysosome drug sequestration plays a significant role in the reducing the therapeutic effect of the small molecule drugs by sequestering the therapeutic away from target site.
- **Chapter 2:** The success of nano-carrier-mediated drug delivery following endocytosis hinges on the efficacious drug delivery to the target site. The second chapter of this thesis focuses on understanding the real-time visualization of delivery aspects of a fluorescent nano-carrier to deliver a fluorescent drug or dye molecule by employing FRET as a versatile imaging tool. Following the nano-carrier's endocytosis and localization to endosomes, inter-organelle interaction with lysosomes mediates its cellular fate, which

generally terminates at lysosomes where the encapsulated drug is released. Fluorescence-abled visualization of nano-carrier can help track their organelle residence, determining its drug efficacy.

- **Chapter 3:** Cellular organelles such as Lysosomes and endosomes are known to sequester weakly basic therapeutics such as doxorubicin from target nuclear site. Alterations or defects in lysosome-endosome fusion can abate the therapeutic efficacy of weakly basic drugs. Although comprehending this intricate process can help understand drug sequestration leading to poor drug efficacy and concomitant poor prognosis, visualizing it remains challenging due to the difficulties with probe designs. Towards this, the third chapter of the thesis is focused on structural engineering of pH-responsive ESIPT nano-emitter that would be proficient in understanding the inter-organelle interaction in sequestration of the drug molecules at the single cell level. This requires the labelling of the endosomes and lysosomes in two fluorescent different colors that would able its differential visualization while live monitoring cells with a confocal microscope. Therefore, the engineered probe should be two color emitting in repose to the pH conditions in endosomes and lysosomes. In this chapter efforts were taken to develop and structurally engineer a nano-emitter fluorescent probe that was single-wavelength excitable and two-color emitting, which could possibly label organelles of different acidity.
- **Chapter 4:** After optimizing the pH responsive nano-emitter, in-depth analysis was done to study their ability to annotate the endocytic vesicles *i.e.* endosomes and lysosomes in two different fluorescent colors. The lysosomes were labeled with green fluorescence and endosomes were labelled with green fluorescence that abled the monitoring of their dynamic interaction under single wavelength excitation. This probe was leveraged to understand the dynamic interactions between endosomes and lysosomes that were instrumental in sequestering of weakly basic doxorubicin drug.

In ***chapter 2***, fluorescent vesicles were engineered to monitor their localization in cells by imaging them under a confocal microscope. The blue luminescent polymersomes were constructed via stitching a blue luminescent Aggregation Induced Emission fluorophore, Tetraphenylethylene; TPE. This AIE chromophore was chosen because these class of fluorophores shows emission upon aggregation or self-assembly. Dextran was conjugated with TPE and a vesicle director unit, Penta decyl phenol via enzyme sensitive ester linkage. The produced DEX-TPE-PDP self-assembled in

water to form blue emissive polymersomes; P_{TPE} of size, 200 nm as confirmed via various soft techniques. The P_{TPE} polymersomes were highly compatible with cells and showed high degree of localization in lysosomes of the cells as confirmed via a colocalization assay employing Lysotracker dye. The blue luminescence emanating from the polymersomes make them highly trackable inside the cells. After been able to successfully track the polymersomes, we subsequently checked them for their cargo loading abilities and subsequently unloading abilities in presence of enzyme. To monitor the process of unloading of cargo in presence of enzymes, we employed a fluorescent cargo, Rose Bengal. Rose Bengal loaded polymersomes, P_{TPE+RB} interestingly, showed energy transfer between TPE and Rose Bengal via FRET. Upon exciting donor, TPE molecule at 405 nm wavelength, energy go transferred from TPE to Rose Bengal and are emission was seen from Rose Bengal instead of self-emission from TPE. Subsequently, to monitor the unloading ability of P_{TPE+RB} it was treated with esterase. Enzyme effectively cleaved the esterase bond as confirmed via NMR experiments with a model compound and resulted in the unloading of the cargo as confirmed via the release profiles of Rose Bengal. The treatment of P_{TPE+RB} with esterase led to the disassembly of the polymersomes and further led to disintegration of the FRET pair leading to vanishing of FRET signal and concomitant appearance of self-emission of TPE. The decrease in FRET emission and increase in self- emission of TPE can be used as a simple yet powerful readout to comment on the integrity and unloading abilities of P_{TPE+RB}. Thrilled by a FRET tool set in hands to monitor the enzyme mediated unloading of fluorescent cargo, Rose Bengal, we immediately resorted our attention to cellular studies. The time dependent monitoring of P_{TPE+RB} intracellular journey showed a stable FRET signal until 2 hours. After 2 hours, FRET signal started to reduce in intensity and concomitantly the self-emissions corresponding to TPE instead illuminated the cells. The P_{TPE+RB} effectively reported its intracellular location and also reported on its structural integrity and concomitant cargo unloading in presence of enzymes. Having an enzyme responsive FRET based polymersomes in hands, we checked for their doxorubicin unloading abilities. Surprisingly, doxorubicin loaded polymersomes, $P_{TPE+DOX}$ formed a dark pair that interestingly showed fluorescence quenching via FRET. $P_{TPE+DOX}$ upon treatment with cellular esterase showed a retrieval in the fluorescence intensity of TPE and Doxorubicin in a time dependent manner. This shed light on the loss in integrity of doxorubicin loaded polymersomes upon treatment with esterase which subsequently release doxorubicin from its cavity. The disassembly of the dark pair stopped the FRET process and retrieved both their

emission intensities. Excited, we conducted cellular experiments. P_{TPE+RB} showed excellent drug efficacy as evident from reduced cellular viability. This simply point towards the good unloading abilities of polymersomes for doxorubicin. We next conducted live cell imaging experiment to visualize this process in real time. The sample showed no fluorescence for about 45 minutes of imaging under confocal microscope. A sudden red emission was seen in the nucleus of the cells. The disintegration of the P_{TPE+RB} released doxorubicin which showed a enhancement in fluorescence after binding to nuclear DNA. The nucleus became intense red with time and the lysosomes started to show more self-emission of TPE as compared to doxorubicin. This is because, doxorubicin generally has low quantum yield in water but shows great enhancement in the fluorescence intensity upon binding to nuclear DNA. This was truly thrilling as the cargo unloading process increased at the cellular lysosomes, they glowed blue and the cargo shuttled to the nuclear target which fluoresced red in a time dependent manner. Although simple, this FRET based tool is highly insightful in commenting upon the release kinetics of the drug delivery system which might explain heterogenous patient response due to different pharmacology mechanism operational for different patients at cellular level. This chapter provides suitable method for understanding the efficacy of a drug delivery system by simply monitoring its drug release abilities inside the cells.

However, drug efficacy can be altered or perturbed by their entrapment or sequestration by acidic endocytic vesicles such as endosomes and lysosomes. This appears counter intuitive as the last chapter celebrated the role of lysosomes in disintegrating and unloading of the cargo from polymersomes. However, all the drug in the cellular lysosome never finds way to the cellular nucleus. This is the property exhibited by weakly basic drugs which due to their lipophilic nature can conveniently diffuse via a hydrophobic membrane to inside of lysosome. However, the opposite becomes untrue for these weakly basic drugs. Upon reaching the acidic lumen of endocytic vesicles, they become reversibly protonated due to their low Pka values and high pH inside the acidic endocytic vesicles. An equilibrium is established between the protonated and the neutral form of the drug, which leads to persistent entrapment of the protonated form inside the lysosomes, whereas the neutral form shuttles to out the lysosome to irreversibly bind with the nuclear DNA. It however remains unclear of what endocytic vesicles, endosome or lysosomes can sequester drug molecules. Further the fate of sequestered drug molecules remains unclear. The sequestration of drugs reduces the cytosolic concentration of freed rug to bring about cytotoxicity,

leading to Multidrug resistance. We tried to answer the role of endosomes and lysosomes and their related interaction in sequestering drug molecules as they are implicated in reduced drug efficacy. ***Chapter 3*** of this thesis aims toward optimizing the structure of a single molecule-based pH responsive dye to distinctly label endosomes and lysosomes in two colors upon single wavelength excitation. Significant efforts have been taken in the past few decades for fluorescently mapping the acidity of endocytic vesicles. But these fluorophores are rather dual wavelength excitable and dual emitting in nature. Single wavelength excitable and dual-emitting fluorophores rathe remain scarce. Single wavelength excitable, dual-emitting molecular probes are highly desirable in bioimaging applications because they offer distinct advantage over conventional two wavelength excitable dyes. The dual wavelength excitable dyes are subject to spectral cross talk and are difficult to multiplex with other dyes. Further, single wavelength excitable dyes can enhance the maximum available imaging speed. Significant efforts have been dedicated to annotate these organelles by fluorescently mapping their acidity. Matile et al. employed mechanosensitive flipper probes conjugated with cell-penetrating peptides with pKa ~10.6 to unidirectionally penetrate the pH gradient along the endocytic pathway. Utilizing Fluorescence Lifetime Imaging Microscopy (FLIM), these mechanosensitive flipper probes were demonstrated to effectively annotate endocytic vesicles, notably endosomes, which are typically challenging to label. Recently, there has been a shift in focus towards designing probes capable of annotating endocytic organelles regardless of targeting features, particularly in cases of abnormal organelle status where many pH probes lose their efficacy. An example of such an approach involves anchoring an intensiometric pH probe to the plasma membrane, providing an opportunity to monitor vesicle dynamics as it inwardly invaginates, forming endocytic vesicles with the anchored pH probe still anchored to its inner leaflet. The intensiometric probe showed an enhancement in fluorescence intensity as it moved from the environment of low acidity in early endosomes to high acidity in lysosomes. Although several attempts have been made to label the endocytic organelles, probes proficient to monitor their dynamic interactions remains scarce. Contemporary technology employs double labeling using a two-fluorophore system to monitor these dynamic interactions as they engage in content exchange of two fluorescent dyes. For instance, double staining with traditional green fluorophore, Dextran-FITC (λ_{exc}= 488 nm, λ_{ems}= 500- 540 nm) and red fluorophore, Dextran-Rhodamine (λ_{exc}= 561, λ_{ems}= 580- 700 nm) is used to stain endosomes and lysosomes respectively. However, such a system utilizing two sources of excitation often causes spectral cross-talk or

excitation cross-talk due to overlap between their excitation wavelengths. While to a lesser extent, rhodamine can be co-excited when exciting fluorescein using a 488 nm laser. Further, emissions corresponding to fluorescein may be detected in photomultiplier or widefield channels typically reserved for rhodamine. Additionally, such systems are difficult to multiplex with other fluorescent drugs and dyes which have overlapping excitation and emission profiles. The design featured a donor-acceptor (D-A) core comprising of a green-fluorescent 4-amino-naphthalimide (A) and salicylaldehyde (D) connected via an imine-linkage. The resulting **SA-Imine** gave red emission around 600 nm via excited state intramolecular proton transfer. The hydrolysis of **SA-Imine** under reduced pH conditions would regenerate the acceptor, 4-aminonapthalmide molecule that shows green fluorescence with the emission maxima around 540 nm. However, the photophysics of **SA-Imine** was complicated by the presence of another emissive state at 520- 530 nm, that was assigned as anion emission which was generated upon deprotonation of the enol species. This process was confirmed via various experimental methods and NMR. ESIPT fluorophores are known to show deprotonation of the -OH group to solvents, leading to the generation and concomitant emission from the anionic form. Therefore, ESIPT molecules are highly sensitive to their immediate environment. AIE property arising due to formation of nano-aggregates prevents the interaction of the molecules from polar solvents such as water. This leads to the reduction of anion generation under such conditions. Likewise, for the current molecule under investigation, AIE was exploited in order for the **SA-Imine** molecule to show enhanced ESIPT reaction upon formation of nano-aggregates in water. The small molecule upon dispersing in water forms small aggregates which leads Aggregation induced emission that favored the ESIPT reaction that becomes functional in the nano-aggregates. AIE due to ESIPT is a common property of many salicylaldehyde based Schiff bases. The formation of aggregates that led to ESIPT was confirmed using DLS other electron microscopy techniques such as AFM, FESEM. Nevertheless, the presence of anion species in water happens to a small extent. This anion formed along with the enol species in the ground state leads to a heterogenous ground state. The anion and aggregates formed in the ground state can be photo selected leading two different emission. Upon excitation at 405 nm, the system shows equi-intensity green emission due to anion and red emission due to enol species undergoing ESIPT reaction in the excited state. The similar emitting anion species and 4-amino naphthalimide would make the interpretation of the pH dependent difficult. Hence, efforts were taken to modulate the Ex-De in **SA-Imine**. It has been reported by many investigators that under certain conditions

of solvation/vectorization as provided by micellar domains or by changing the electronic effects, the acidity of the phenolic group can be modulated. Such effects can affect the stability of the exited states and can indeed turn out as an effective strategy to control the dual emissions. It also can lead to simple deprotonation reaction leading to anionic species which fluoresces different in the excited state as compared to the excited state or the keto form. To this end, both the effect of electronic substitution and vectorization was studied to modulate the emission properties of the D-A scaffold. The formation of anion depends upon the pK_a of the -OH group. By changing the electronics, it is rather possible to change the pK_a of the molecule which can affect the anion formation in water. The AIE although facilitates the ESIPT reaction, but the aggregates formed often impedes the biological application of such ESIPT dyes. Vectorization involving encapsulation of ESIPT dyes in the polymeric nano-carriers or functionalization with hydrophilic groups can make them suitable for bioimaging applications. The hydrophobic environment can further prevent its interaction with the outside water which can reduce the formation of anion in the water medium. Thus, structural engineering was attempted to enhance primarily keto emission in water, which upon further hydrolysis leads to green emission in response to the pH of the environment. The structural optimization produced PEG-PDP-Imine, which self-assembled to form tiny micelles, called nano-emitter in water. This fluorophore buried inside its micellar environment avoided contacts with the outside water molecules and stabilized the ESIPT reaction leading to prominent red emission centered at 595 nm. This also avoided the formation of anion and led to annihilation of the green emission at 520- 530 nm which was seen in the case of **SA-Imine** molecule when dispersed in water. This structural optimization led to exclusively red emission which upon hydrolysis under acidic pH condition generated PEG-Naph molecule that showed green emission. Both nano-emitter and its hydrolyzed form could be monochromatically co-excited using 405 nm laser due to similar absorbance profile. This led to design of the singe wavelength excitable and dual emitting fluorophore which showed dual emission depending upon the pH conditions. The nano-emitter showed red emission under neutral pH conditions and under the pH conditions of the endosomes. The nano-emitter further showed green emission due to its hydrolysis under the acidic pH conditions of the lysosomes.

Chapter 4 of this thesis aims at employing pH responsive ESIPT active nano-emitter for live monitoring the interactions between endosomes and lysosomes of the cells. The nano-emitter marked vesicle organelles and separated them into two cohorts, one showing red and the other

showing green emission, when the system was excited using 405 nm laser. We anticipated this color annotation of vesicles by nano emitter was due to its ability to hydrolyze under hydrolytic conditions of lysosomes and stay stable in endosome's pH conditions. To check for the color annotation by lysosomes was correct, we carried out co-staining experiments with other cellular markers. We checked for colocalization of nano-emitter with lysotracker, Mito tracker and ER-tracker. The nano-emitter showed high degree of colocalization with lysotracker as evident from Pearson's coefficient. A point, however to be noted here is that the lysotracker showed colocalization with both the green fluorescent vesicles and red color vesicles, only the green fluorescent vesicle colocalized with the red fluorescent vesicles more. Lysotracker is a lysmotropic dye which marks acidic organelle on the basis of their pH, however it can't differentiate between acidic organelle. Being sure, that nano-emitter marks endocytic vesicles we did transient transfections to accurately label three endocytic organelles namely, early endosomes, late endosomes and lysosomes with a GFP protein. The green vesicles colocalized perfectly with GFP labelled lysosomes and red fluorescence was localized in both GFP labelled early and late endosomes. This experiment made clear the color annotation by nano-emitter wherein it annotated endosomes as red and lysosome as green fluorescent. We next conducted live imaging experiments to monitor the dynamic interactions between red fluorescent endosomes and green fluorescent lysosomes. Their dynamic interactions could be monitored as they engaged in exchange fluorescent contents amongst themselves. A movie was recorded where the green fluorescence was seen flowing from lysosomes to endosomes and red fluorescent contents flowed form endosomes to lysosomes as they engaged in transient fusions. Their complete fusions and subsequent fission were also captured where a red fluorescent endosome completely fused with green fluorescent lysosome forming yellow fluorescent endo-lysosome. Green fluorescent lysosome was seen budding out from yellow fluorescent yellow endo-lysosome. We leveraged nano-emitter to monitor to the sequestration of doxorubicin by endosomes and lysosomes. It became very evident form the data doxorubicin resided amongst both the acidic organelles. However, to persistently trap the doxorubicin within them, they interacted and transferred the drug amongst themselves. This transfer was captured happening by various processes such as transfer of drug between them by formation of tubules. The transfer happened via fission as the drug carrying lysosomes budded out from drug carrying parent endo-lysosome. The fate of sequestered drug was realized which were seen to be persistently trapped amongst acidic organelles, a finding which is yet to reported

in literature. In a nutshell this thesis attempted to understand the effect of inter organelle interactions between endosomes and lysosomes in monitoring drug release and drug accumulation. The polymersomes following intercellular trafficking was seen to unloading drug in a time dependent manner. This happens as polymersomes end up in lysosomes, where the enzyme ruptures the polymersomes to release the cargo. The journey of polymersomes to end terminal of endocytic journey i.e. lysosome is mediated via such interactions. Secondly, it was realized that such interactions are also at forefront in the persistent entrapment of drug molecules. These effects modulate the efficacy of therapeutics at cellular level, which can help rationalize the heterogeneity in patient response to therapeutics and subsequently can pave way for alternatives. Such dyes can be further tied to the polymeric drug delivery systems which can shed light on the precise location of the polymeric nano-carriers in either endosomes or lysosomes and can help to understand the drug sequestration abilities by these acidic organelles as they leach out of the nano-carrier system.

TABLE OF CONTENTS

LIST OF TABLES

LIST OF FIGURES

LIST OF APPENDICES

Chapter 1

Introduction

1.1 Nanotechnology – a brief overview

Advances in nanotechnology, catalyzed by seminal work of giants like Maeda, Langer, Mitragotri and many others in the field, helped evolve the landscape of nanoparticle-mediated delivery of therapeutics. This understanding has brought about a paradigm shift in converting therapeutics to successful therapies which facilitated patient compliance by enhancing the localization of therapeutics to the diseased site and concomitantly minimizing off-target effects[1]. Drug delivery by definition is defined as the ability of the carrier to bring the therapeutic from outside of the body to its cellular target inside the body[2, 3]. The choice of nano carrier ranges from being artificial such as liposomes or polymeric nanoparticles to bio-inspired or biomimetic delivery vehicles employing attenuated virus to systematically deliver payloads[3]. This arsenal of delivery vectors as a result of biological and chemical engineering made possible the delivery of different class of therapeutics ranging from small molecules to more sensitive nucleic acids and genetic cargo[1]. The advent of nanotherapeutics changed the landscape of many clinical mainstream human diseases with high mortality such as cancer, rheumatoid arthritis, cardiovascular diseases etc[4]. This is because nanoparticles, with their complex architecture and stability, significantly overcome the limitations of highly potent therapeutics, enabling the treatment of otherwise life-threatening diseases[5]. However, the rise in high-mortality diseases has placed a significant burden on the field of nano drug delivery, necessitating bridging of the gap between highly potent existing drugs and the considerable compromise in quality of life associated with traditional therapies. This demand has fueled the development of new drug delivery technologies, resulting in an explosion in the several billion-dollar market[5].

This chapter is aimed to discuss both the material and biological aspects that are essential in the design of nanoparticles. Significant attention is devoted to understanding of intracellular biological barriers, as they significantly impact the efficacy of nano-drug delivery systems. However, comprehending these barriers is often hindered due to the absence of appropriate techniques and imaging modalities capable of visualizing nano-system interactions within the cellular environment. The reader is subsequently introduced to the aim of this thesis, which highlights the importance of effective imaging systems in (i) visualizing the journey of drug-loaded nano-systems and (ii) revealing lysosome sequestration as an effective biological barrier that hampers the bioavailability of clinically important drug- doxorubicin.

1.2 Definition- The right size in nanobiotechnology

Ever since its advent in the early 1980s, the field of nanotechnology has undergone several changes in terms of design and application. It's important to note that its definition has also evolved with changing needs and applications. In its original form, nanotechnology sought to meet two essential requirements: the technology must have a manmade component, and its dimensions must be in the range of one to 100 nanometers. However, in the last decade, given the recent use of bacteria, viruses, and other pathogens as biomimetic or natural vectors for delivering payloads to diseased sites, the man-made requirement of nanotechnology is now less stringent. However, the question of the correct size in nanotechnology was unanimously addressed by leaders in the field who argued that the definition of 'small' depends on the operational function[6]. Small structures share a common interest for both physical and biological sciences, hence their size requirements are less strict and can range from 1 nm to 1 mm, depending on the application. Very recently, it has been recognized that the "legal definition" of nanomaterials isn't the same around the world. The differing regulatory frameworks among countries produce varying outcomes for the same material, creating ambiguity for stakeholders[7].

Harmonization and international convergence on the definition of nanomaterials are crucial to reduce confusion and enhance transparency in their assessment and regulation. Communities worldwide are now arriving at a unanimous definition of what constitutes a nanomaterial: one that has at least one dimension at the nanometer scale, i.e., between 1 and 100 nm[6, 7].

1.3 The central dogma of drug delivery

Intersection of nanoscience in biomedical science was realized for several different reasons as discussed ahead. The unparalleled examples of nanoscience in biology and biotechnology are realized in the fields of drug delivery, where nano-vector mediated delivery of therapeutics offer several different advantages over traditional drugs. This being enhancement in solubility, increase in bioavailability, increase in circulation, and reduction in side-affects due to reduction in non-specific distribution of drugs in the body.

Nanoscience extends to the field of nano-particle mediated delivery of imaging agents, wherein paramagnetic nanoparticles made of gadolinium and iron oxide are used for non-invasive MRI imaging of lymph node metastases in patients diagnosed with prostate cancer, which is otherwise a clinical occult[2]. Iron oxide nanoparticles having dextran coating outperform conventionally used

gadolinium MRI as it provided better contrast during intraoperative imaging and superior detectability at low magnetic strength. Furthermore, nanoparticles have been found to be profoundly useful in the MRI-based early detection of angiogenesis at very early stages in a variety of cancers[2, 8]. This is due to the nanoparticles' ability to sense picomolar concentrations of the epitopes they target. Apart from these abovementioned advantages, nanoscience bought a paradigm shift in our understanding of combined therapy. Combination therapy is a management model that is new approach towards drug repurposing which employs the cocktail of two or more approved drugs to manage many human diseases[4]. This approach of repurposing existing and approve drugs reduces the development cost involved in design of any therapeutics. However, such drug cocktails often times leads to antagonistic effects leading to toxic side effects. Another milestone of nanoscience is the revival and revolutionization of combination therapy, which involves the use of two or more drugs[4]. Often, such drug combinations suffer from issues like poor solubility and asynchronous distribution, leading to antagonistic effects. Multifunctional nanoparticles have been designed to load and enhance the solubility of two or more drugs and regulate their simultaneous or spatial release to bring about synergistic effects[4].

These advantages offered by nanotherapeutics over traditional drugs led to the ***central dogma of drug delivery:*** *to achieve maximum therapeutic efficacy with reduced side effects by rapidly steering therapeutics and imaging agents to specific tissues or cellular sites*[3].

1.4 Engineering nanoparticles for drug delivery

To facilitate the clinical translation of such nano technologies, US government sanctioned a 227-million-dollar budget in year 2000 outlining the grand challenges in the field. Nanotechnology could mitigate the limitations of traditional drugs[5]. However, an immense period of research and development didn't enhance the propensity of drugs to localize *en masse* at the target site. These systems offer only marginally augmented therapeutic efficacy compared to traditional ones, resulting in modest patient response to treatment. The inability of the drug to reach and populate at the target site renders 1 out of 9 newly discovered drug delivery systems ineffective by authorities, leading to high attrition rates of such delivery systems in the later stage clinical trials[2]. This is due to the interaction of the nanoparticles with the biological system including biomolecules, organs etc. when they are transported through the body. Nano-vehicle design and

resultant interactions with the biological system dictates the fate of nano-vehicle and associated drug inside the body.

The nano-vehicle design paradigm is currently approached primarily from a physical viewpoint, focusing on the chemical and material properties. However, there is a lack of understanding from a biological perspective[9]. The material aspects include selecting the appropriate delivery vector to overcome specific delivery challenges for a given class of therapeutics. Meanwhile, biological barriers such as the lack of site-specific delivery and poor circulation are ultimate impediments to nanoparticle-based drug delivery, often limiting its efficacy[9]. Both the material aspects and biological barriers associated with nano-vehicles are crucial factors that significantly influence the success of nano delivery systems[10]. They are briefly discussed in the coming sections.

1.5 Material aspects of Drug delivery

This section describes the material aspects of drug delivery. The drug and the delivery strategy are inherent to any drug delivery system. There are many classes of therapeutics and each one comes with their own delivery challenges. The understanding of the class of drug is important to choose a suitable a delivery vector. First the class of therapeutic agents and the challenges associated with their delivery are discussed[1, 10]. Next, delivery strategies are discussed and important paradigms are identified to mitigate drug delivery challenges associated with each class of therapeutic[1, 10]. These delivery strategies include modifying drugs, changing the environment around the drug, and development drug delivery systems such as transdermal patches, hydrogels, controlled release implants, microparticle depots, nanoparticles etc[1, 2, 10].

1.5.1 *Class of therapeutics and associated delivery challenges*

As the world continues to battle new infections and pandemics, the disease rate in the population has soared, placing tremendous pressure on the healthcare system. In response to this increase in disease rates, the therapeutic landscape has evolved beyond small molecule drugs[1, 10]. Broadly speaking, there are five classes of therapeutics: small molecules, nucleic acids, antibodies, protein or peptides, and live cells. Due to their small size (<900 daltons), ***small molecule*** drugs can easily navigate through the tight and complex vasculature of all types of tissues by diffusing across various biological barriers such as biological fluids, cell membranes, etc. However, 90% of drugs due to their poor solubility remain a challenge to be delivered[1]. Interestingly, ***small molecule*** drugs

were the first to arrive in the therapeutic landscape, laying a strong treatment foundation against many diseases. However, they only target 3-5% of the human genome (See Figure 1.1).

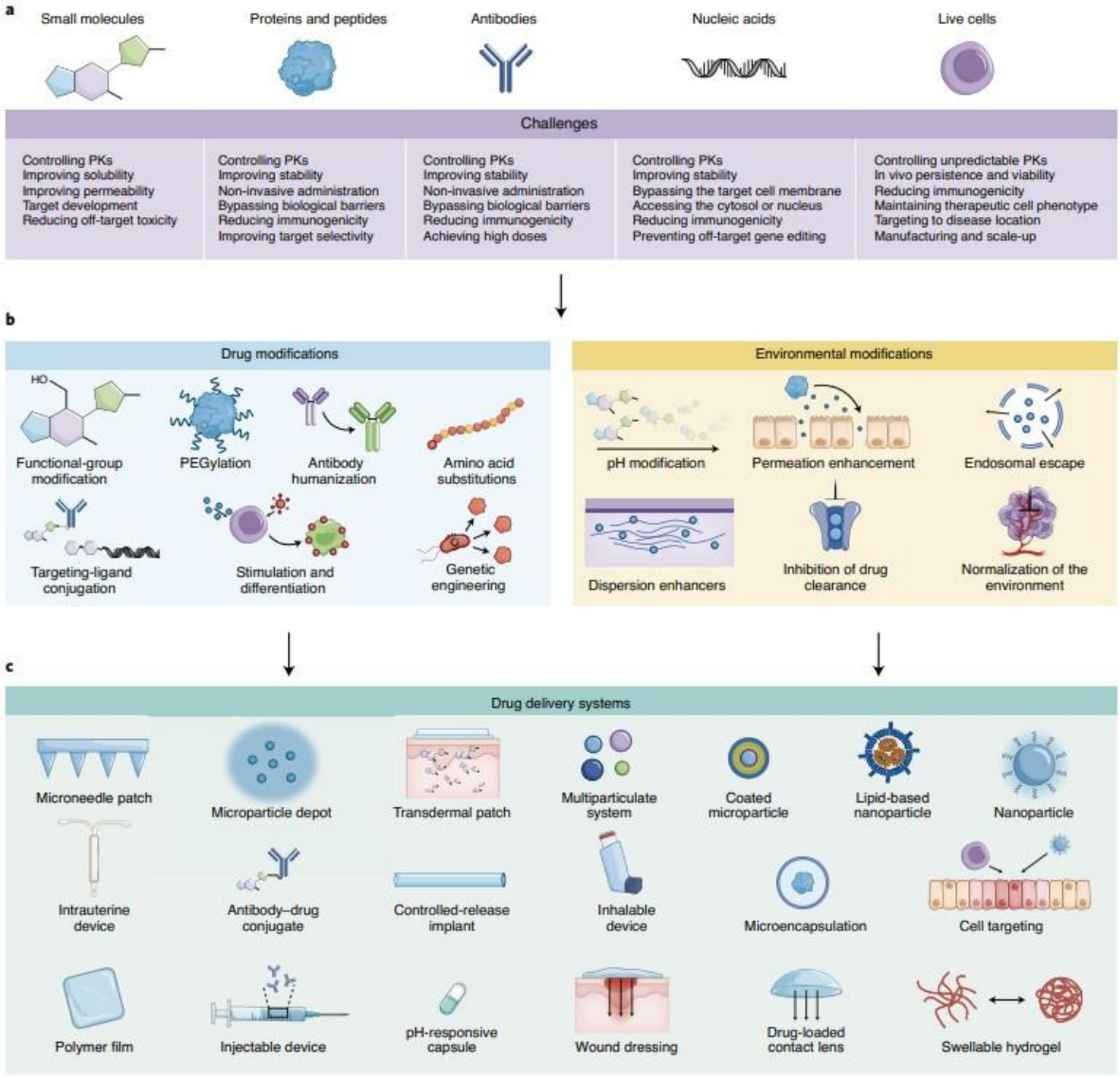

Figure 1.1: *Image showing different class of therapeutics and their associated delivery challenges. Adapted from Mitrogotri et al., Nat. Biomed. Eng* **2021**, *5* (9), 951-967.

To circumvent this problem, alternative classes of therapeutics such as ***proteins or peptides*** dominated the therapeutic landscape[1]. Due to their unique tertiary structures and appropriate size, they perfectly fit with many proteins of interest, leading to a reduction in toxicity and an increase in potency over small molecules (See Figure 1.1). Although their size and structure imbibe them with superior performance, it also leads to unwarranted problems of reduced stability under

ambient storage conditions. They are prone to degradation by enzymes and proteins like ubiquitous proteases. Proteins and peptides are also known to activate the immune response by recognizing antigens on their surface. More than 500 ongoing clinical trials and almost 70 approved in the U.S. alone, ***antibodies*** are hailed for being successful alternative to small molecule drugs[1-3] (See Figure 1.1). Antibodies, due to their specific binding to the target antigen, can nullify or neutralize them, subsequently preventing their interaction with other signaling molecules to halt undesirable disease-causing cellular processes. However, some antibodies used in treatment are known to produce anti-antibodies, leading to adverse effects and subsequent banning of such antibodies from the market.

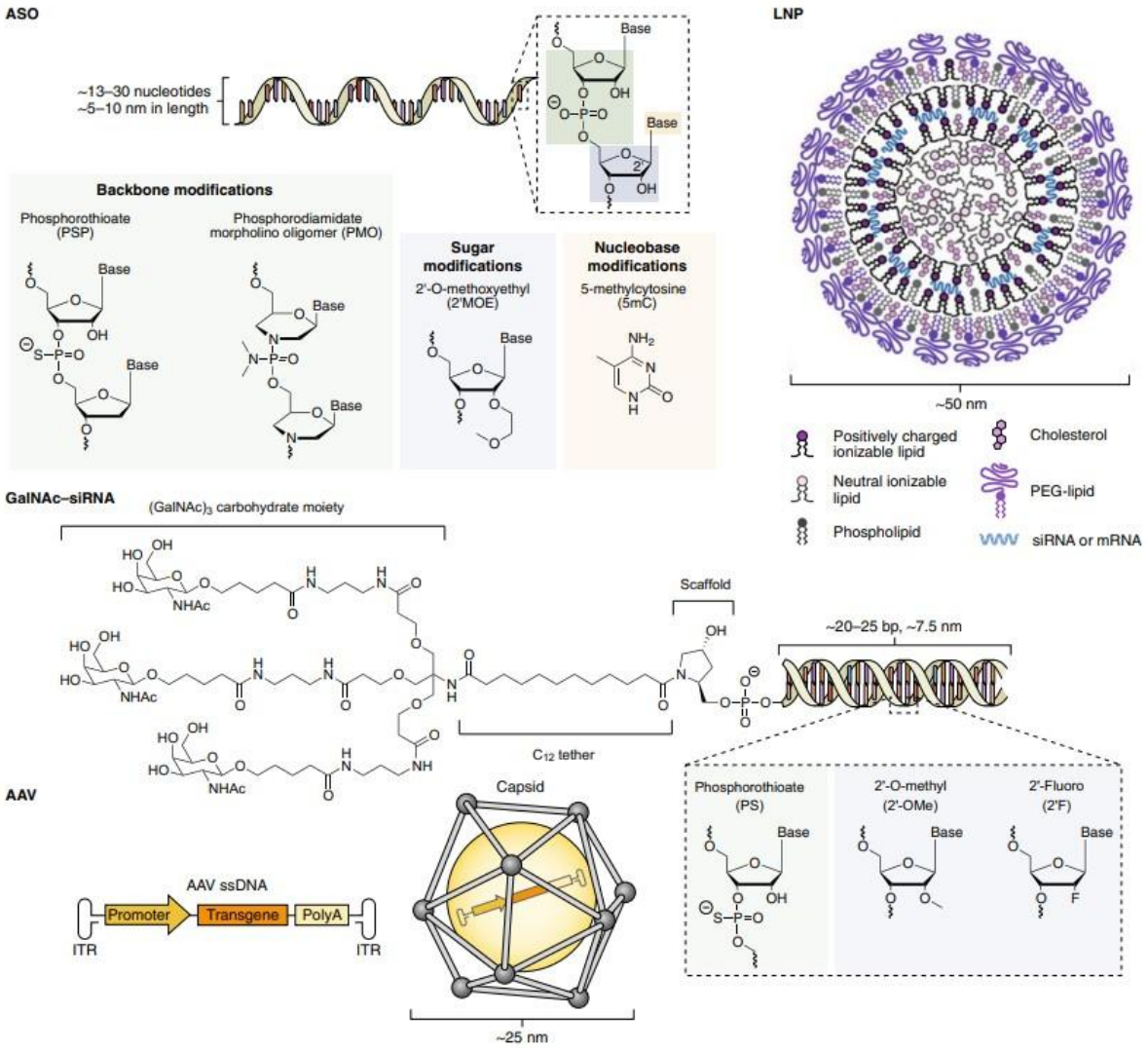

Figure 1.2: *Approved delivery stratergies for delivery of nucleic acids in the clinic. Adapted from Kulkarni et al., Nat. Nanotechnol.* **2021**, *16* (6), 630-643.

They generally require high doses and invasive methods of injection due to their mechanism of action, which involves their interaction with the dynamic immune system. These challenges call for appropriate delivery strategies, as discussed in the coming sections. Due to their unique ability to silence or repair genes by precisely controlling gene expression, ***nucleic acids*** can enhance the expression of genes that are easily druggable targets[2, 11]. Naked nucleic acid for the delivery to cytoplasm in the form of siRNA, mRNA or for delivery to nucleus in form of DNA are prone to degradation which limits their half -life. They are also easily detectable by immune system, which identifies them as foreign and eliminates the from the body. However, many number of nucleic acids have either been approved or in the late-stage clinical trials due to the high success rate of the nucleic acid therapies[11]. These therapeutics rely on four broadly classified platform technologies as shown in Figure 1.2. The use of lipid-based nanoparticles as shown in Figure 1.2 has sown promising outcomes in clinic trials. The recent use of lipid based nanoparticles in delivery of nucleic acids for covid 19 treatment is no short of realization of the power of nucleic acids therapeautics[12]. Recently, the use of ***live cells*** as treatments for various forms of cancer and tissue healing has added a new dimension to the multidimensional field of therapeutics as shown in Figure 1.1. These cells, often endowed with inherent therapeutic functions, have shown remarkable abilities to promote or regulate otherwise compromised biological processes. For instance, pluripotent stem cells are renowned for their potential to heal damaged tissues[13]. Furthermore, specialized cells can be genetically engineered to enhance their therapeutic capacities. A notable example is genetically engineered T cells, which are designed to express chimeric antigen-binding proteins on their surface, enabling them to recognize cancer cell antigens[14-16]. Known as CAR T cell therapy, this innovative approach allows these cells to identify specific antigens on cancer cells and, upon recognition, to naturally initiate the cancer cell's destruction[16]. However, this therapy faced several challenges in terms of delivery owing to its large size of the cells which re known to be trapped in lung capillaries and late eliminated. Although in 2017, the first CAR T cell therapy got approval, however its cost of treatment is the major trouble as a viable treatment option[15]. Furthermore, these cells, due to their size, often find it difficult to navigate through the complex and hostile tumor environment, resulting in low cancer tissue penetration during adoptive cell therapy. Pragmatic problems involving the viability, persistence, and large-scale production of these efficacious live cells remain challenging. They are also limited by storage, shipment, and the overall cost associated with the therapy. In order to alleviate these

delivery challenges associated with each class of therapeutics, three paradigms were identified by Mitragotri and his team[1].

1.5.2 *Paradigms of drug delivery- addressing delivery challenges*

Having realized all the potential challenges associated with each class of therapeutic, drug delivery strategies have had to adapt and accommodate these challenges. *Mitrogotri* et al. analyzed the challenges associated with each class and identified three important paradigms that could elevate the current drug delivery landscape to match the level of expectations. These paradigms include modifying the drug, altering the microenvironment around the drug, and creating an appropriate interface, such as a nano-vector, that can facilitate drug delivery by manipulating and subsequently controlling the drug's interaction with its environment[1]. Each paradigm is relevant to the problems discussed above with each class of therapeutic and is briefly discussed ahead.

1.5.2.1 *Modification of drug*

Problems such as solubility of drug, degradation of proteins/peptides/nucleic acid, instability of nucleic acids can all be simply mitigated by bringing about minor chemical changes to their structure, eventually leading to modification of drug. Many ***small molecule*** drugs are often converted to ester or are modified with thiazole to improve the solubility leading to concomitant increase in absorption and bioavailability of the drugs. For example, ionizable group of two drugs namely, benazepril[17] and enalapril[17] used for inhibition of enzyme responsible for converting angiotensin are protected with ethyl ester to increase their absorption and bioavailability. Also drug for HIV, ritonavir is modified with a thiazole group to increase water solubility, thereby enhancing its absorption and bioavailability[1, 18]. Similarly, modification or introduction of unnatural amino acids in proteins/peptides is seen to be effective in improving the stability and increasing the half-life of the peptide/protein. One notable example employing this strategy has been seen in the case of natural peptide therapy employing clinically approved desmopressin[19], an improved version of vasopressin but with better half-life and stability. Similarly, modification of antibodies with cytotoxic small molecules combines the strengths of small molecule drugs with those of antibodies. These chemically-linked antibody-drug conjugates (ADCs) offer several advantages by effectively targeting the cytotoxic small molecule drug using the antibody and synergistically augments the benefits of both the drug and antibody. One example of an ADC in

the clinical setting is Kadcyla[20], which is employed in the treatment of breast and stomach cancer. It chemically conjugates a human epidermal growth factor receptor 2-targeting antibody, trastuzumab, with a cytotoxic small molecule drug, *mertansine.* Other antibody drug conjugates employ trastuzumab conjugated with Maytansinoid[21] as shown in figure 1.3.

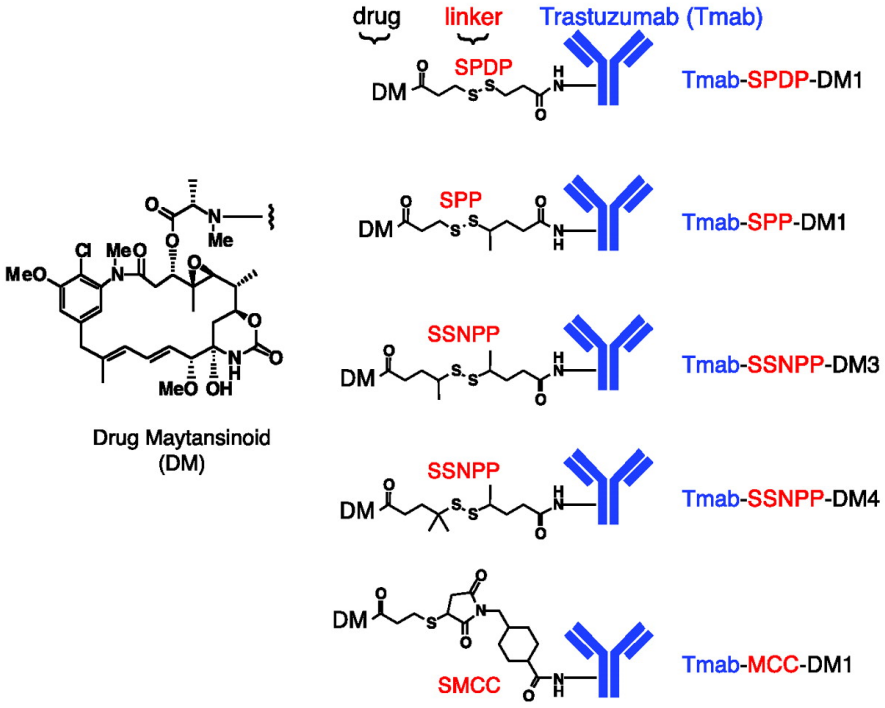

Figure 1.3: *Structure of trastuzumab- maytansinoid conjugates, which is drug antibody conjugate. Adapted from Phillips et al., Cancer Research* **2008**, *68* (22), 9280-9290

This combination was seen to be useful in bringing out the therapeutic efficacy of *mertansine and* maytansinoid by targeting it to the cancer site using antibody, which alone would otherwise be toxic instead of being efficacious in clinical use. ***Nucleic acids***, post chemical modifications share similar benefits with that of other class of therapeautics. A slight chemical modification in the nucleobases, the sugar rings, and the 3' or 5' ends of nucleic acids was seen to bring drastic stability to these otherwise unstable nucleic acids and also reduce immunogenicity. These subtle yet powerful changes led to the development of *Nusinersen*, the only clinically approved drug for the treatment of muscle atrophy, in 2016.

1.5.2.2 *Alteration of environment around the drug*

Another approach that seems to work in magically solubilizing or delivering otherwise difficult-to-deliver therapeutics is by changing the microenvironment around the drug. These microenvironmental changes can be highly targeted at the site of action or systematically by administering adjuvants to modify the host environment. Further changes in increasing the permeability of the cellular membranes can help navigate therapeutics through the plethora of biological hurdles. ***Small molecules*** benefit from changing the environment around them by bringing down the local pH leading to enhancement in their solubility. This enabled successful clinical translation of ciprofloxacin[22], which employed the use of lactic acid to increase its solubility by bringing down the local pH. Other microenvironmental changes includes, inhibition of clearance pathways and inhibition of drug metabolism to help small molecules easily navigate through biological barriers. For ***nucleic acids***, these modifications include modification in the endosomal pH, use of cell penetrating peptides to locally improve endosomal escape and increase intracellular uptake. These subtle yet thoughtful changes led to clinical translation of a *Onpattro*[23], which is siRNA by employing the use of ionizable cationic lipids that helps its endosome escape following its endocytosis by disturbing the endosome homeostasis. ***Proteins and peptides*** benefit quite from microenvironmental changes. This involves redirecting the use of citric acid to inhibit proteolysis, thereby improving the stability of proteins and peptides under physiological conditions. Systematic injection of steroids contributes in manipulating the local immune environment so as to reduce the side effects of proteins or peptides[24, 25]. To support ***T cell*** expansion in the hostile tumor environment CAR T cells were engineered to secret cytokines to restructure immunosuppressive tumor microenvironment[26, 27].

1.5.2.3 *Drug delivery system*

Drug delivery platforms integrate the above-mentioned strategies by creating an interface between the drug and its microenvironment in a single scaffold. The pharmacokinetic (PK) parameters of the drugs such as biodistribution of the drug, half-life etc. can be altered by the choice of nanocarrier as it modulates the rate of release of the drugs under physiological conditions. Drug delivery systems entail a wide variety of devices, ranging from macro devices such as microneedle patches[28], controlled-release depots[29], and transdermal patches[30], to micro devices such as microparticles[31], hydrogels[32] etc. to nanodevices such as nanobots, engineered viruses[33],

nanoparticles, biomimetic pathogens etc. see Figure 1.1. These devices can control the release profile of same drug which can result in alteration of its PK properties. Transdermal patches for insulin release based on closed loop mechanism was reported. In enhancement of glucose in the blood sugar, Gox converts glucose to gluconic acid leading to reduction in local pH and bio reduction of -NO_2 group to -NH_2 which leads to dissociation of nanoparticle and subsequent release of insulin[28]. Such transdermal patches based on close loop system gained popularity to their unique yet effective designs see Figure 1.4.

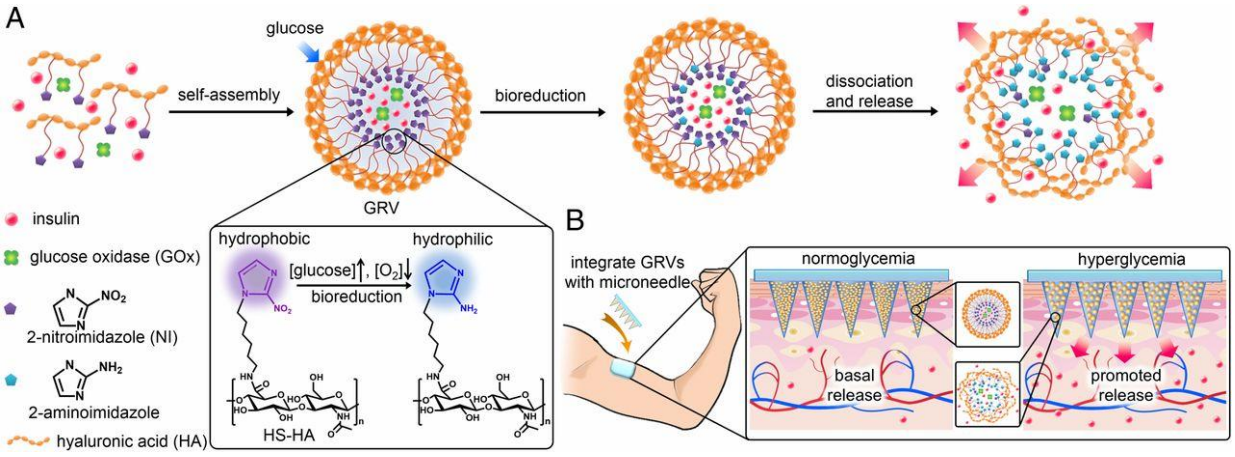

Figure 1.4: *Transdermal patches for the controlled release of insulin in response to increase in blood glucose level. Adapted from Zhang et al., Proc Natl Acad Sci USA* **2015**, *112* (27), 8260-8265.

Controlled release capsules for the release of small molecule drugs are being sold in the market under the brand names of Methylphenidate HCl[34], fexofenadine[2, 35] etc. Similarly controlled release implants for small drug molecule are being sold in the market such as etonogestrel implants[36] etc. Controlled release microparticle depots are currently being employed for the controlled release of proteins and peptides and are sold in the market under the brand names of Lupron depot[29]. Of all the delivery platform mentioned, nanodevices comprising of nanoparticles is the most sought after. It offers a varied variety of nanoarchitectures which have been found to highly efficient in the delivery of many potent classes of therapeutics. Next section briefly discusses about the principle of nanoparticle design and their types depending upon the drug payload.

1.5.3 *Nanoparticles in drug delivery: Design principle and Type*

Design Principle: This section discusses the material aspect in the design of nanoparticles for drug delivery applications. It is important to first understand the basic design principles of nanoparticle design to realize effective therapeutic efficiency. Langer and team briefly described the three important principles of nanoparticle design which are summarized below[35]. Firstly, the architecture of nanoparticle should be fine-tuned to carry either hydrophobic or hydrophilic drug or sometimes both in a single scaffold. This architecture should remain stable under circulation conditions in the physiological medium. Secondly, it should have the ability to target and later accumulate and distribute thoroughly at the sub-cellular or anatomic targets. In other words, it should be able to navigate its way through various biological barriers to the site the target cell and interact with cells to successfully enter the intracellular space by endocytosis or other uptake mechanism. It under the action of cellular stimuli like enzymes, pH, redox environment etc. should only release the payload. Lastly, it should be biocompatible, it should not activate any immune response following its administration.

Type of nanoparticles: Due to advancement in synthetic approaches and understanding of nanostructures, the design of nanoarchitecture can be engineered based upon the requirements and the payload. The nanoparticles currently used for delivery of therapeutics are both synthetic and biomimetic. Bio-inspired nanoparticles or biomimetic systems employs pathogens such as attenuated strains of small viruses and other pathogens such as bacteria to deliver various class of therapeutic across biological barriers. Recombinant bacteria for the delivery of RNA therapeutics are currently in the phase 1 trials whereas virus like particles employing viral capsids for the delivery of small molecules, DNA, and vaccine have already traversed to market. These vectors are FDA approved are currently being sold under various brand names of Gardasil[37, 38] and Cervarix[38]. The discussion ahead focuses on the synthetic nanoparticles with special emphasis is given on polymersomes, a class of polymer vesicles. Synthetic nanoparticles are broadly classified to three main classes comprising of lipid, polymeric and inorganic nanoparticles. Lipid based nanoparticles or liposomes are one of the first synthetic nanoparticles to arrive on nano-vector landscape. They generally are spherical in morphology and have at least one lipid bilayer that surrounds an aqueous interior core[2]. Depending on the morphology and soft internal features they are further known to be of three different types raging from liposome, lipid nanoparticles and emulsions as shown in the figure 1.5. Liposomes are discussed in greater detail in section ahead

and comparison is drawn with their polymer congeners; polymersomes. These lipid-based nanoparticles are generally simple to formulate and difference in the ratio of participating lipids offers them control over different soft features. There structure comprising of long chain fatty acids makes them highly compatible and interactive with the biological interface leading to their very high bioavailability.

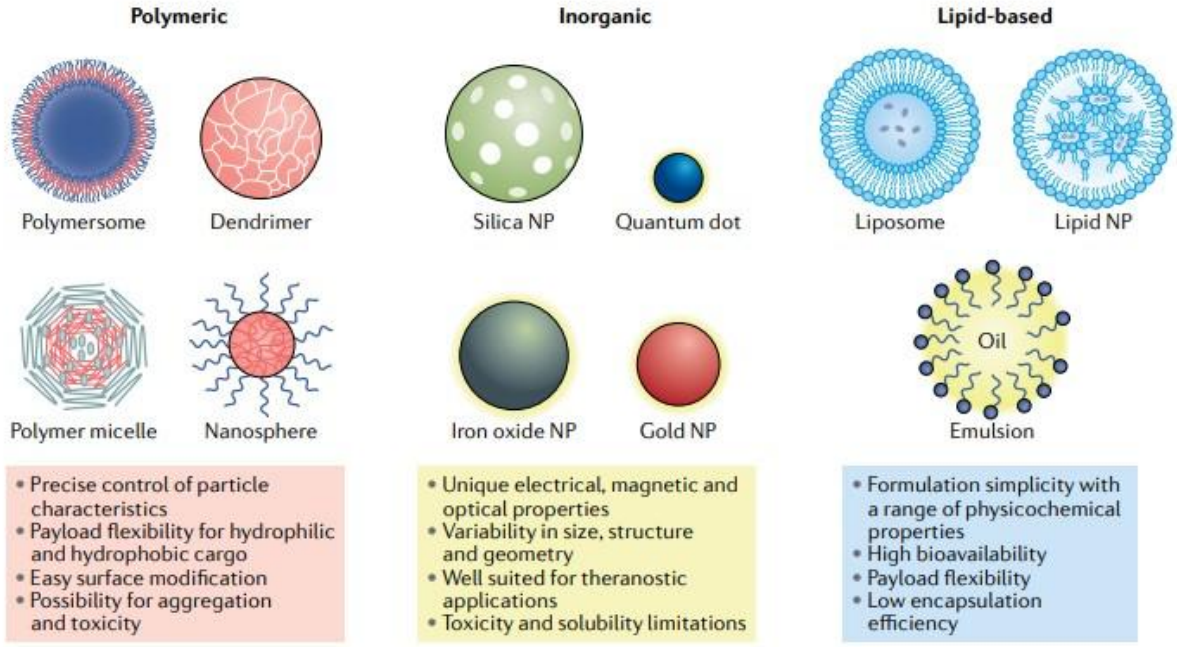

Fig. 2 | **Classes of NPs.** Each class of nanoparticle (NP) features multiple subclasses, with some of the most common highlighted here. Each class has numerous broad advantages and disadvantages regarding cargo, delivery and patient response.

Figure 1.5: *Different type of nanoparticles for drug delivery applications. Adapted from Mitchell et al., Nat. Rev. Drug Discov.* **2021**, *20* (2), 101-124.

One of the most common classes of lipids, comprising of phospholipids, is known to form uni- or multilamellar vesicular structures. It is due to this complex architecture that helps compartmentalize both hydrophilic and hydrophobic payloads in a single scaffold. These unique features and simple formulations have made lipid NPs as one of the most FDA-approved nano-vectors in the clinical landscape so far. Inorganic nanoparticles on the other hand find plethora of theragnostic applications due to their unique magnetic and optical properties. “Theragnostic” as the word suggests combines therapy and diagnostics in a single operational modality. The metal center comprising of silver, gold etc. imbibes them with various optical and electrical properties

making them most suitable candidates for theragnostic applications. Iron abased nanoparticles are the most used MRI contrast agents. They offer better contrast over the conventional MRI nuclei at a very low magnetic strength. Iron nanoparticles are most commonly used in the treatment of iron deficiency anemia under various circumstances. Many such formulations bagged FDA approval in early 2000s and are sold under the brand name of Venofer and Injectafer etc. However, these nanoparticles are seen to be little less soluble and therefor exerts toxicity at higher doses.

Polymeric nanoparticles are the area of active research and the most sought-after candidate for the delivery of various therapeutics towards the treatment of many diseases. They have various architectures such as polymersomes, dendrimer, micelles and nanospheres as shown in figure 1.5. Various synthetic approaches to prepare polymeric nanoparticles can lead to precise control over the particle characteristics. Their architecture can be designed to suit the needs for the type of payload delivery of both hydrophobic and hydrophilic drugs. Due to the synthetic control over the design of polymeric nanoparticles, there surface can be easily manipulated for charge, providing them with better opportunity to circulate better under physiological conditions. Nature offers many architectures that remain stable under physiological conditions. Vesicular structures have an edge over any other morphology in terms of applications in biology as nature itself chooses vesicular architectures for carrying out many biological functions. The choice of polymer can be a gamechanger in formulation of vesicles that interacts minimally with the physiological fluids and macromolecules. Next section briefly discusses the utility of vesicles, both liposomes and polymersomes in drug delivery and subsequently deals with polymer vesicles or polymersomes an emerging nano-vector on drug delivery landscape.

1.5.4 *Lipid Vesicles and Polymer Vesicles*

The prevalence of self-assembled architectures is ubiquitous to biology which employs vesicular architectures for carrying out various complex cellular functions[39]. The hierarchically self-assembled vesicular architecture has always fascinated the interests of scientists in the field of both biology and chemistry. Vesicles are analogous to cells having a bilayer membrane composed of phospholipids, whose interior is composed of long fatty acid providing it with highly dynamic and hydrophobic interior. The bilayer of cell is highly interactive with outside environment and has evolved to support the binding of various proteins, signaling sugars, receptors and ion channels through covalent or non-covalent interactions[39-41]. The bilayer protects within an aqueous lumen

and offers hydrophilic environment. It therefore an innate tendency of natural lipids or the synthetic lipid analogues to self-assemble to form liposomes (or lipid vesicles). Liposomes are unornamented version of cells as it lacks surface functionalization.

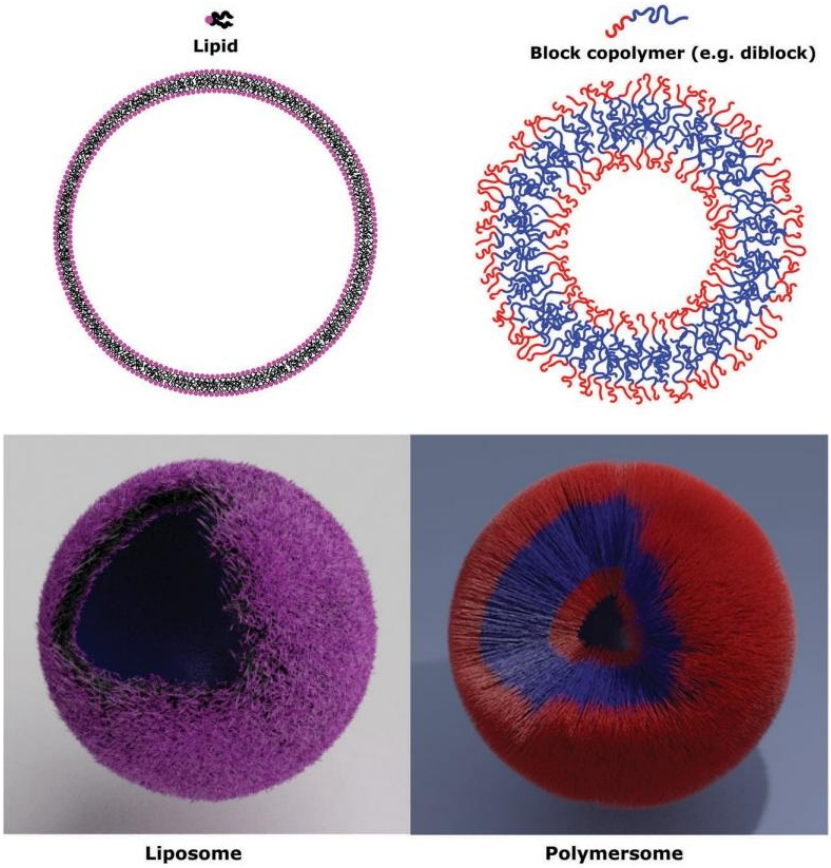

Figure 1.6: *Structure of Liposome and its comparison with Polymersomes. Adapted from Rideau et al., Chem. Soc. Rev.* **2018**, *47* (23), 8572-8610

Traditionally speaking, for liposomes, building blocks are designed in such a way that allows them to spontaneously arrange into higher order vesicular structure when they reach the state of equilibrium. Additionally, the process of self-assembly is guided by the intended functionality of the assembled structures. By carefully designing the building block it is possible to control the formation of desired vesicular structure with potential uses and functions. Lipids have been highly employable recently in the delivery of many therapeutics such as small molecules, nucleic acids etc. Doxil is a liposome formulation for the delivery of doxorubicin and has shown superior performance with a half-life of 50- 60 hours in blood plasma and reduced side effects, leading to its clinical usage in early 2000s[42-44]. The liposome comprises of cocktail of three

lipids which are: PEG-2000 modified DSPE (abbreviated as *N*-(carbonyl-methoxypolyethylene glycol 2000)-1,2-distearoyl-*sn*-glycero-3-phosphoethanolamine sodium salt), hydrogenated phosphatidylcholine and cholesterol[44].

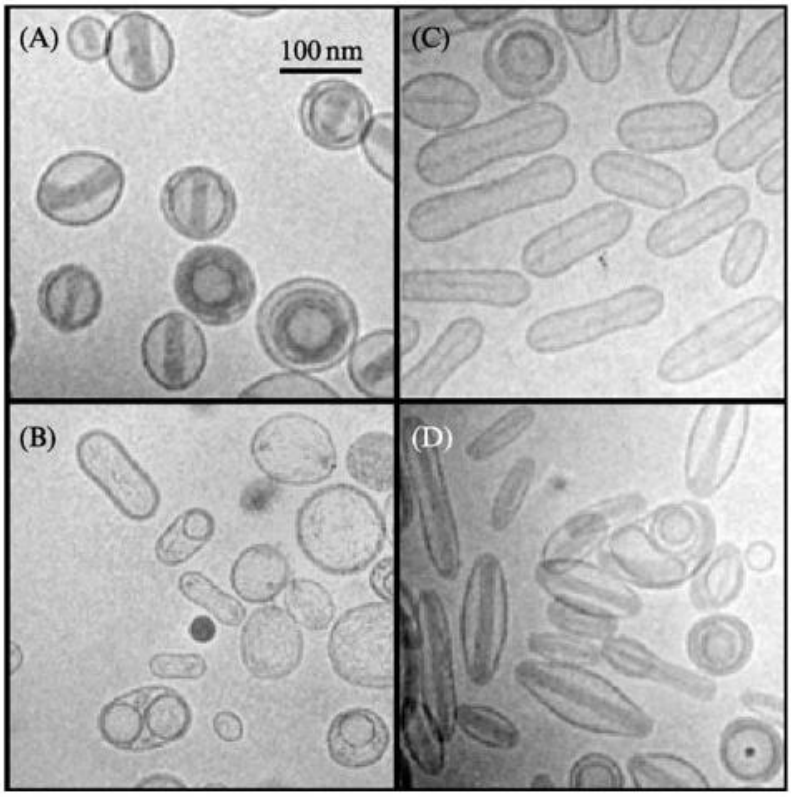

Figure 1.7: *Liposomal formulation of doxorubicin made by altering the ratios of (a) DMPC/Chol or (b) DSPC/Chol and prepared in two different buffer systems as shown in c and d. Adapted from Methods in Enzymology*, **2005**, *391*, 71-97.

The PEG provides stealth effect and shields the liposome against the absorption of many plasma components, leading to extended circulation in the blood and increased half time. Recently developed mRNA based covid vaccine employed lipid nanoparticles for the delivery of mRNA to immune cells. However, the lipid-based formulations required extremely low temperature for its storage and transportation. This underscores the need for the development of polymeric vesicles because they offer superior performance over lipid-based delivery platforms. Amphiphilic block copolymers and grafted polymers have shown to extensively self-assemble into many classical self-assemblies such as vesicles. Theoretically speaking three main factors such as molecular weight, interaction of the hydrophobic part of the polymer with water, and weight fraction of the hydrophilic part in the polymer mainly contributes to the formation of polymersomes. The

hydrophobic to hydrophilic fraction in the molecule required to form polymersomes can be figured out from this equation: $p = \frac{v}{al}$, where p represents the packing parameter, a represents the approximate area of the hydrophilic head group, v represents the volume occupied by the hydrophobic chains and l represents the length of the hydrophobic chain[39]. For $^1/_2 \leq p \leq 1$, vesicles morphology is mostly formed. The superior physical properties as discussed underneath accounts for the better performance of polymer vesicles or polymersomes over lipid-based vesicles or liposomes.

1.5.4.1 *Comparison of physical properties: Polymersomes vs. Liposomes*

Polymersomes are polymer congeners of liposomes and offers superior properties in comparison to liposomes[39]. These properties include size, permeability, mechanical and rheological properties and last being chemical versatility and the comparison is shown in Figure 1.8.

1.5.4.1.1 *Size*

Talking in terms of molecular weight, phospholipids, the building block of liposomes are typically in the range from 100- 1000gmol-1.

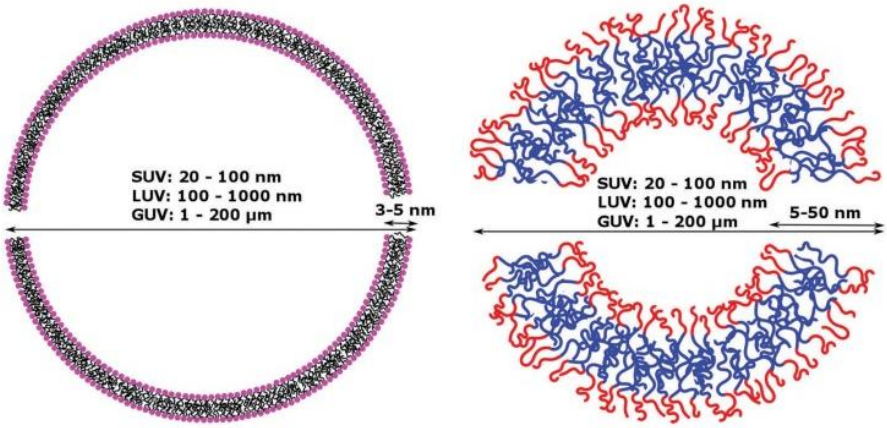

	Liposomes	Polymersomes	Eukaryotic cells
Molecular weight of building compounds	10^2–10^3 g mol^{-1}	10^3–10^4 g mol^{-1}	10^2–10^5 g mol^{-1}
Membrane thickness	3–5 nm	5–50 nm	8–10 nm (including membrane proteins)
Diameter	SUV: 20–100 nm LUV: 100–1000 nm GUV: 1–200 µm		Animal cells: 10–30 µm Plant cells: 10–100 µm
Encapsulating volume (calculated)	SUV: 10^{-15}–10^{-13} µL LUV: 10^{-13}–10^{-9} µL GUV: 10^{-9}–10^{-3} µL	SUV: 0–10^{-13} µL LUV: 0–10^{-9} µL GUV: 10^{-9}–10^{-3} µL	Animal cells: 10^{-6}–10^{-5} µL Plant cells: 10^{-6}–10^{-3} µL

Figure 1.8: *Comparision of physical properties of lipososmes and Polymersomes. Adapted from Rideau et al., Chem. Soc. Rev.* **2018**, *47* (23), 8572-8610

However, for polymersomes, this range is pushed to 1000- 10000 gmol-1as their building blocks are typically amphiphilic block copolymers. The molecular weight is also reflected on the membrane thickness of the self assembles vesicles. For liposomes, this thickness is often less and is in the range of 3- 5nm. Interestingly, the membrane thickness in the polymersomes ranges from 5- 50 nm, which is closer to that of natural cells having membrane thickness in the range of 8- 10 nm. In terms of size, both polymersomes and liposomes are known to form small and large vesicles. The small vesicles also called as small unilamellar vesicles or SUVs can range anywhere between 20- 100 nm and large or giant vesicles called LUVs and GUVs respectively. LUVs have size range in between 100 nm- 1μm, whereas GUVs are on the scale of several microns for both polymersomes and liposomes.

1.5.4.1.2 *Permeability and stability*

Alike in terms of size, differences between polymersomes and liposomes become enormous in terms of stability of the self-assembled architecture and ease of permeability of the bilayer membrane. Although their vesicle architecture is known for the ability to retain both the hydrophobic and hydrophilic cargo, liposomes are often described as problematically leaky and can't retain their cargo effectively.

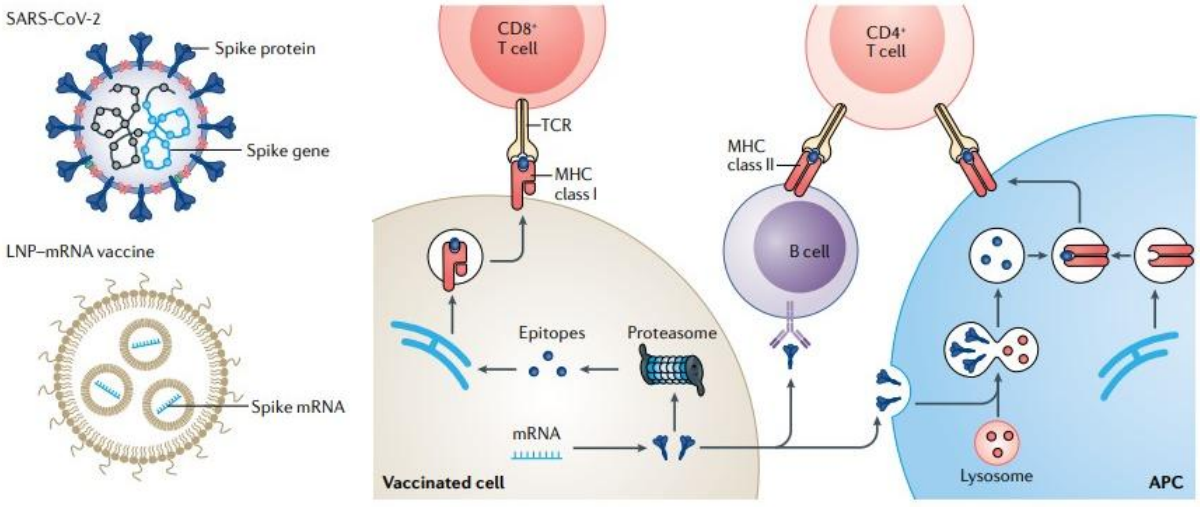

Figure 1.9: *Lipid based covid-19 vaccine. Schematic showing the internalization pathway of nanoparticles inside the somatic cells. Adapted from Hou et al., Nature Reviews Materials* ***2021****, 6 (12), 1078-1094.*

This happens because of the high permeability of the bilayer membrane in liposomes which is the result of high lateral fluidity arising due to the low molecular weight of the phospholipid monomers. Opposed to that, amphiphilic block copolymers due to their high molecular weight often ends with low lateral fluidity upon self-assembly leading to highly stable and less permeable bilayer membrane. This imparts polymersomes with high retention ability of the cargo and are therefore seldom leaky. The low lateral diffusivity imparts polymersomes thermodynamic stability[39]. Lateral diffusivity depends upon the packing of the bilayer membrane which further depends upon the molecular weight and glass transition temperature of the amphiphilic block polymer chain. It also depends upon the entanglement tendency of the hydrophobic section of the block copolymer chains. The lateral diffusivity and hence the permeability of the bilayer of the polymersomes can easily be tweaked by changing the chemical composition of the participating amphiphilic blocks. The chemical nature and lateral fluidity greatly affect the stability of both liposomes and polymersomes. Liposomes are short lived due to high membrane fluidity and less stable monomers. Liposomes are unstable due to chemical instability of the monomers and not due to the entropically favored disassembly of the monomers[45, 46]. The success of recent covid 19 vaccines employing liposomal formulation (as shown in Figure 1.9) suffered from the problems of shelf life and transport. The shelf life of the liposomes can be increased by changing their storage conditions. Both the temperatures, environments and presence of cryoprotectants such as sucrose, trehalose etc. are known to affect the stability of the liposome formulation. The fatty acid is prone to oxidation by reactive oxygen species whose extent be greatly reduce by storing at lower temperature conditions of less than -20^{o} C. This makes mRNA- lipid covid vaccine difficult to preserve and transport[45]. The polymersomes on the other hand are very sturdy and remain stable up to months at room temperature in both the solution and the powder form.

1.5.4.1.3 *Mechanical and Rheological Properties*

The nano-vectors are prone to suffer from the wear and tears under blood circulation and also experiences deformities as they pass through tight capillaries. The ability of nano-vector to withstand such mechanical damage during circulation is of prime importance to drug delivery. Biological membrane due to their fluid structure are prone to undergo two elastic deformations: bending and stretching. The bending of the membrane can be characterized by two important parameters namely, bending rigidity modulus "κ", and its spontaneous or preferred curvature

"m"[47]. The combination of these two parameters gives the measure for the spontaneous tension described by 2 κm^2. The physical significance of the bending rigidity is the resistance of the membrane against the bending deformation. Membrane stretching or compression elasticity refers to the ability of the member to deform in response to mechanical forces. Membrane stretching or membrane compression are determined by the mechanical tension which is present within the membrane of the vesicle bilayer[47]. Even in the absence of mechanical forces such as the pressure of the blood circulation etc. these two elastic deformations are coupled to each other in the vesicle volume. Therefore, it is true to say that that the *mechanical tension* in the membrane is dependent on its spontaneous curvature and bending rigidity, or simply on its *spontaneous tension*[47]. The value of mechanical tension can be smaller or comparable to the value of the spontaneous tension. Apart from these two, there is an additional third quantity called as the lysis tension, which is the tension at which the membrane breaks.

Bending rigidity modulus is a mathematical parameter to understand stiffness of any membrane. Polymersomes have thicker membranes and therefore are stiff, offering a high value of bending rigidity modulus and vice a versa[47]. In simple words, bending rigidity modulus parameters gives the value for stiffness of membrane and in turn would reflect on the thickness of the bilayer membrane. It comes as no surprise that the bending rigidity modulus of polymersomes are typically higher than liposomes in solution phase. The polymersomes are referred to as tough vesicles because it withstands forces leading to the rupture of its membrane and hence have high lysis tension values (20 mN m^{-1}) over liposomes (5- 10 mN m^{-1}).

1.5.4.1.4 *Chemical versatility*

The lipids are very specialized molecules but are limited by the fact that they lack space for chemical functionalization. This poses limitation on the available monomers for self-assembly and hence further puts repercussions on the self-assembly properties. The lipid groups can be easily be modified for their head groups but can only be modified for the hydrophilic groups. The hydrophobic long chains are hard to modify and often requires 9- 10 synthetic steps for modifications[39]. On the contrary the polymersomes enjoy the benefits of easy chemically tunable and versatile amphiphilic polymer blocks and offer various distinct properties upon self-assembly. They are easily functionalizable and their surface can be easily functionalized to accommodate variety of ligands, fluorophores and targeting groups. Due to this property of surface

functionalization, they find extensive use in targeting therapies. The easy chemical modification of blocks further offers an advantage of being tailored to respond to various stimuli. Upon being prompted by stimuli, the monomer disintegrates and disturbs the hydrophobic- hydrophilic balance. This disturbance in the balance brings down the self- assembly which in turn leads to release of cargo. The hydrophobic and hydrophilic parts can be connected to each other via various stimuli responsive units like ester, acid labile units like imine etc., which are discussed extensively in next sections.

1.5.5 *Stimuli responsive Polymersomes*

Polymersomes due to their easy synthesis, surface modification, enhanced stability and presence of a thick hydrophobic membrane and large aqueous lumen makes possible the loading of both hydrophobic drugs in its hydrophobic bilayer and hydrophilic drug in the aqueous lumen.

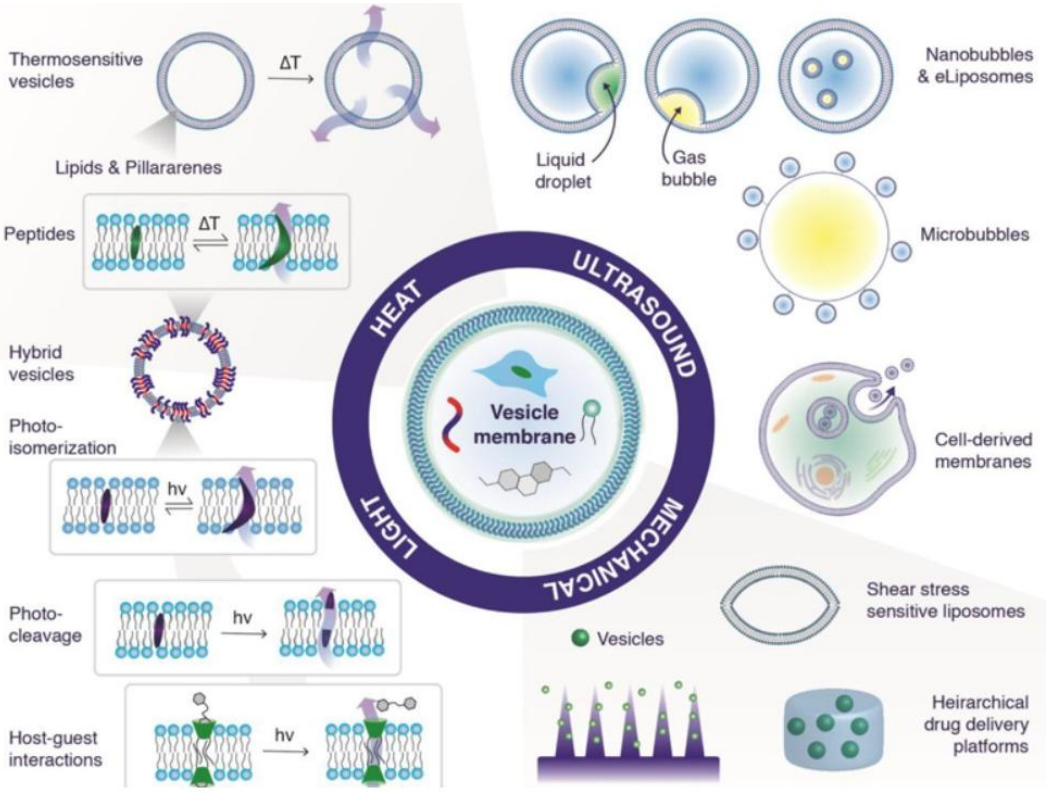

Figure 1.10: *Different Stimuli repsonisve units integrated to the bilayer of the polymersomes. Adapted from Kauscher et al., Adv Drug Deliv Rev* **2019**, *138,* 259-275

The thick hydrophobic membrane greatly reduces the leakiness of the vesicles but at the same time it also makes it difficult to small drug molecules to diffuse through its thick and hydrophobic bilayer membrane. For polymersomes to offer controlled release appropriate approaches must be used to make bilayer membrane with controlled permeability. The simplest yet smart approach seems to be use of smart polymers that tend to imbibe membrane with a responsive functional group. The bilayer membrane integrated with responsive group should be able to process external environmental inputs or cues such as pH, temperature, enzymes, mechanical forces, electrical impulses, light etc. as shown in Figure 1.10. This is done to bring about detectable functional outputs such as volume contraction or expansion, morphological transitions, or enhancement of the membrane permeability to allow the diffusion of small molecules across the bilayer membrane[48, 49]. The amphiphilic polymer can be therefore custom designed to incorporate various stimuli responsive handles as discussed below.

1.5.5.1 *Enzyme responsive polymersomes*

Enzyme-responsive polymers introduce unique capabilities into polymers, thanks to the specificity and efficiency of enzymes, facilitating the transition of supramolecular structures between assembly and disassembly. This concept has been primarily explored in micelles for drug delivery, with fewer studies on enzyme-responsive polymersomes. For example, Heise et al. developed biohybrid vesicles using block copolymers incorporating L-alanine with different ratios, finding that a higher L-alanine content led to increased degradation by enzymes like elastase and thermolysin[50]. Deming's group crafted amphiphilic copolypeptides that self-assembled into vesicles, which upon exposure to reductase enzymes, transitioned from spherical to sheet-like structures due to a change in the hydrophilicity of methionine sulfoxide segments, facilitating cargo release[51]. These enzyme-responsive polymersomes show promise as drug delivery systems, particularly for targeting regions with elevated enzyme expressions, such as tumors. Dextran-based vesicles were engineered to release drugs like Rhodamine-B and camptothecin upon esterase action, demonstrating enhanced cellular uptake and perinuclear localization, offering a novel approach for dual drug delivery. This advancement underscores the potential of enzyme-responsive polymersomes in biomedical applications, providing a platform for the targeted and controlled release of therapeutic agents.

1.5.5.2 *pH responsive polymersomes*

The exploration of pH-responsive polymersomes is notably driven by the biological significance of pH gradients, such as those in endosomes and lysosomes, for the degradation of biomolecules. This principle was harnessed in early research by Eisenberg's group with triblock copolymers, achieving pH-driven morphological changes between vesicles and aggregates[52]. Building on this, a novel polymersomes exhibiting a reversible "breathing" action under pH variations was developed, significantly enhancing its permeability and offering potential for controlled release mechanisms. Further advancements included the creation of polymersomes capable of forming pH-sensitive transmembrane channels by Chiu's team and the development of cross linkable polymersomes by Armes and co-workers, which maintained integrity through pH shifts[53].

The variation of pH amongst different endocytic organelles and microenvironment of some tumors makes it one of the widely used chemical stimuli in the design of stimuli responsive nanoarchitectures. Typically speaking there are two different ways to design a pH responsive polymersomes. In the first method the pH responsive bonds such as imine[54, 55], oxime[56], hydrazones[57, 58], and acetals[59] are incorporated either in the side chain or the main chain of the polymer scaffold. Zhao et al. synthesized crosslinked block co-polymers for the controlled release of doxorubicin and paclitaxel under dual stimuli of temperature and pH as shown in Figure 1.11[60]. These bonds facilitate the easy chemical conjugation of doxorubicin which has both a ketone and amine functional handle to be conjugated with polymer containing either amine or aldehyde functionality. Alexander et al elegantly showed the use of passerine reaction to make a functionalize polymer with relatively less steps and had a functional aldehyde handle[55].

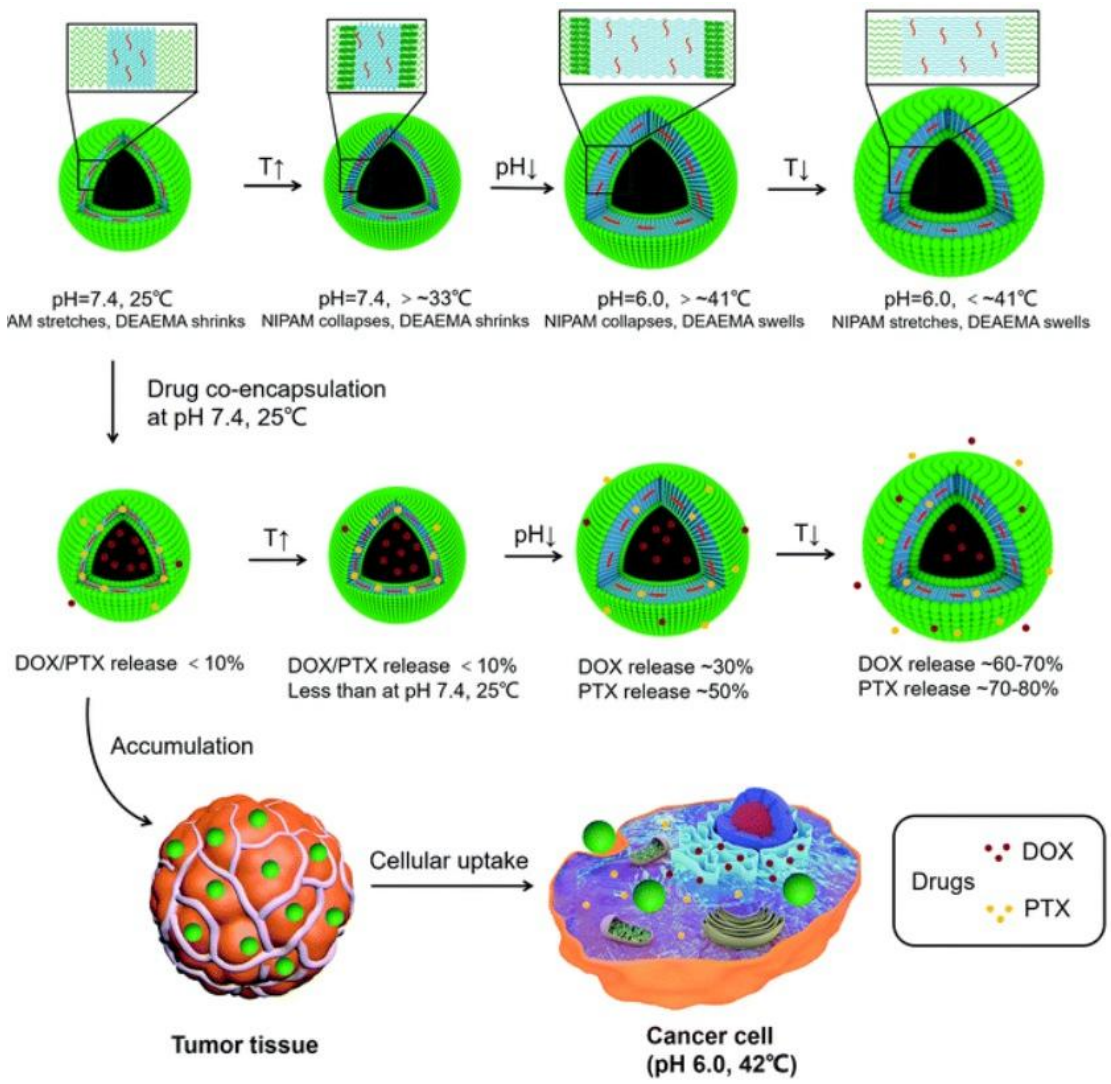

Figure 1.11: *pH and temperature dual responsive polymersomes were synthesized for the controlled release of doxorubicin and paclitaxel. Adapted from Zhao et al., J. Mater. Chem. B* **2021**, *9*(3), 801-808

The polymer self-assembled to form polymersomes and could successfully encapsulate doxorubicin drug. Further, the aldehyde handle was used to react with amine functional group of doxorubicin leading to 100% conjugation of the drug to the polymersomes. They later showed 90% release of the drug and good efficacy in 2D- monolayer forming triple negative breast cancer cells; MBA-MB-231 and also in their 3D spheroid model. In another interesting approach Qui et al, employed an amphiphilic polyphosphazine containing a 5 membered ortho ester group functionalized with a benzene ring that promoted non covalent attractive forces between the ester group and doxorubicin which were further facilitated by the benzene ring that promoted strong π-

π interactions between the benzene ring of Ortho ester and the aromatic core of doxorubicin. These enhanced interactions of doxorubicin with the polymer scaffold facilitated the formation of polymersomes that were loaded with doxorubicin. In an interesting approach they employed cholesterol succinate to stop the premature release of doxorubicin from the polymer scaffold.

1.5.5.3 *Temperature responsive polymersomes*

Temperature-sensitive polymersomes leverage the phase transition of polymers like PNIPAM across its lower critical solution temperature (LCST) around 32 °C to enable smart drug delivery. Below its LCST, PNIPAM transitions from hydrophobic to hydrophilic, facilitating the disassembly of polymersomes and the release of their cargo.

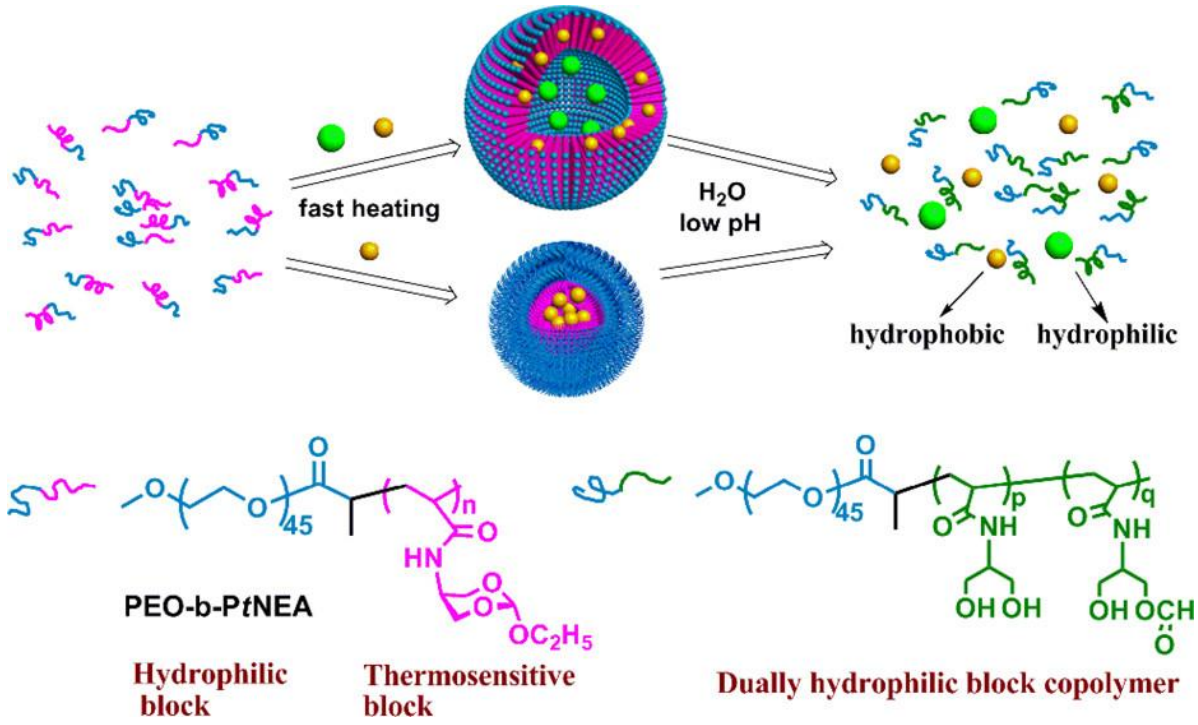

Figure 1.12: *Temperature and pH dual-repsonive polymersome synthezized of block copolymers for doxorubicin release. Adapted from Li et al., Biomacromolecules* **2013**, *14* (5), 1555-1563

This was exemplified by Yang et al. with their PEO-b-PNIPAM polymersomes, capable of encapsulating and temperature-controlled release of drugs[61]. McCormick's group introduced PAMPA-b-PNIPAM and PDMAEMA-b-PNIPAM polymers that formed temperature-responsive aggregates, with some forming hybrid structures incorporating gold nanoparticles for enhanced

stability and functionality[62]. Novel temperature-sensitive triblock copolymers, PVCLn-b-PDMS65-b-PVCLn, reported by another study, demonstrated the ability for transient pore formation at elevated temperatures, allowing for the controlled release of therapeutics like DOX within the physiologically relevant range of 37–42 °C. Furthermore, O'Reilly's group observed thermally induced transitions from micelles to vesicles in PNIPAM-based diblock copolymers, showcasing the potential for reversible and tunable drug delivery systems[63]. Beyond single-stimuli responses, dual-responsive systems have been developed, such as Li and co-workers' PEO-b-PtNEA diblock copolymers, which respond to both temperature and pH, altering their morphology and stability accordingly[64] as shown in Figure 1.12. Additionally, temperature and UV-responsive vesicles formed from pillar[7]arene and azobenzene-containing copolymers illustrate the ability to undergo reversible transformations between vesicles and nanospheres, offering advanced control over delivery mechanisms. These advancements highlight the potential of temperature-responsive polymersomes as versatile and efficient carriers for targeted and controlled drug delivery.

1.5.5.4 *Redox responsive polymersomes*

Leveraging the stark contrast in redox potentials between intracellular and extracellular environments, as well as between tumor and normal tissues, polymersome membranes are engineered to respond to specific redox conditions, granting them unique functionalities for targeted drug delivery. The high concentration of glutathione (GSH) within cells, particularly in cytosol and nuclei (10 mM) compared to the extracellular space (2–20 μM), is exploited to trigger the responsive behavior of these polymersome systems[65]. Disulfide linkages in polymers like the PEG-SS-PPS and the triblock copolymer pPEGMA-PCL-SS-PCL-pPEGMA are designed to break down in the presence of intracellular GSH, enabling rapid release of therapeutic agents directly into the cancerous cells, thus enhancing the effectiveness of cancer treatments. This reduction-sensitive approach not only facilitates the disassembly of nanocarriers but also allows for morphological transformations, such as the micelle-to-vesicle transition observed with block copolymers like PEG-SS-P(Asp) in the presence of reducing agents like DTT. Conversely, oxidation-responsive polymersomes utilize reactive oxygen species (ROS), such as hydrogen peroxide (H_2O_2), to transition from hydrophobic to hydrophilic states, causing structural changes from vesicles to micelles. This mechanism is harnessed for applications in drug delivery, biosensing, and biodetection, with notable examples including PPS-based vesicles for delivering

antigens and adjuvants to dendritic cells, significantly boosting the immune response when used as a vaccine delivery platform. Additionally, ferrocene-containing polymers provide a novel approach to oxidation-responsive systems, utilizing reversible electrochemical reactions to control the assembly and disassembly of polymersome structures.

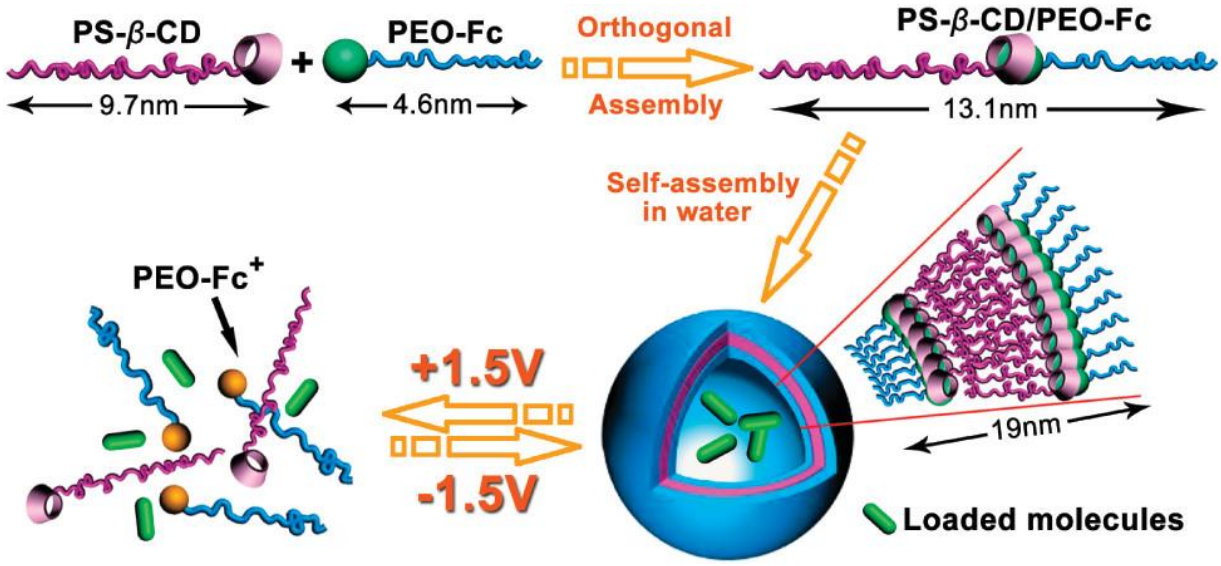

Figure 1.13: *Illustration of the Electrified Regulation of Assembly and Disassembly in PS-β-CD/PEO-Fc Supramolecular Vesicles. Adapted from Yuan et al., J. Am. Chem. Soc.* **2010**, *132*, 9268-9270.

This behavior is exemplified by Yuan's group, which developed a pseudo-block copolymer system that can cyclically transition between assembled and disassembled states under electrochemical stimuli, demonstrating the versatility of redox-responsive polymersomes in dynamic and controlled delivery applications[66]

1.5.6 *Polysaccharide Polymersomes*

Having discussed the various stimuli responsive handles to bring out detectable functional[67] outputs in the polymersomes bilayer permeability and polymersomes appearance, it is important to give weightage to the type of polymer forming the polymersomes. Most of the polymersomes discussed above are synthetically made from highly functionalized monomers. In fact, most of the polymersomes available in literature are intolerant to the cells given. The polymer choice in the design of polymersomes can be a game changer for it can avert the problems of cytotoxicity and

are easily recognized by the cells to be facilitate easy uptake. Sugas are ubiquitous to cells and enjoys an evolutionary advantage to be used by the cells as they participate in various cellular activities. As the cellular glycans present on the surface of the cells reach far out in the extracellular space, they directly participate in various intra and inter cellular activities such as cell signaling, cell migration, and cellular recognition. They are also involved in various host cell interactions involving bacteria and other pathogens which infect mammalian cells by binding to its protein with the surface sugars of the cells. The sugars due to this evolutionary advantage are easily taken up the cells and therefore the use of sugar in nanoparticle system can help alleviate the problem of compromised cellular uptake. Since vesicles are preferred by the cells and so are sugars, there combination that is vesicles made of sugar should be an obvious solution to enhance their uptake by the cells. Our group has pioneered the development of stimuli responsive polysaccharide polymersomes for the controlled release of various therapeutics and dye molecules.

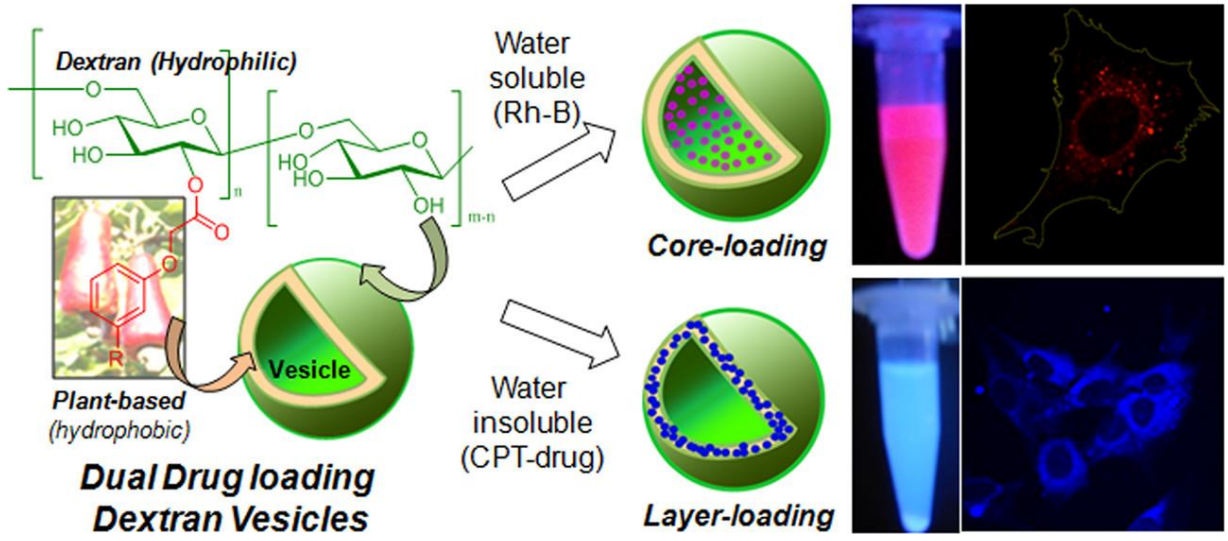

Figure 1.14: *Dextran based stimuli responsive polysaccharide polymersomes. Adapted from Jayakannan et al., Biomacromolecules* **2012**, *13* (11), 3627-3640.

Pramod et al. reported dextran vesicular nano scaffolds, comprising polysaccharide and renewable alkyl tail components that were engineered for simultaneous encapsulation and delivery of hydrophilic and hydrophobic drugs into cells[68]. The influence of hydrophobic segments on dextran self-organization into vesicles or nanoparticles was extensively investigated as shown in

Figure 1.14. These vesicles served as a unique dual carrier, selectively encapsulating water-soluble molecules like Rhodamine-B in the hydrophilic core and polyaromatic anticancer drug camptothecin (CPT) in the hydrophobic layer. Notably, they exhibited superior protection of the plasma-sensitive CPT lactone pharmacophore against hydrolysis compared to CPT alone in PBS. Furthermore, the esterase-cleavable aliphatic ester linkage facilitated rapid release of CPT or Rh-B under physiological conditions. Assessment of cytotoxicity on mouse embryonic fibroblast cells (MEFs) revealed the non-toxic nature of the dextran vesicular scaffold, with CPT-loaded vesicles demonstrating significantly higher efficacy in inducing fibroblast cell death compared to CPT alone in PBS. Confocal microscopy confirmed cellular uptake of both Rh-B and CPT loaded vesicles, indicating potential applications for dual loading and delivery of hydrophilic and hydrophobic drug molecules. Further this approach was extended for the design of pH responsive polymersomes for the controlled release of doxorubicin[69]. Later, targeted stimuli responsive drug delivery system was exploited for the biotin mediated targeting of polymersomes to cells as shown in Figure 1.15. Novel biotin-conjugated polysaccharide vesicular nanocarriers, featuring redox-degradable disulfide and enzyme-biodegradable aliphatic ester linkages, were custom-designed for receptor-mediated endocytosis in cancer cells and intracellular drug delivery[70].

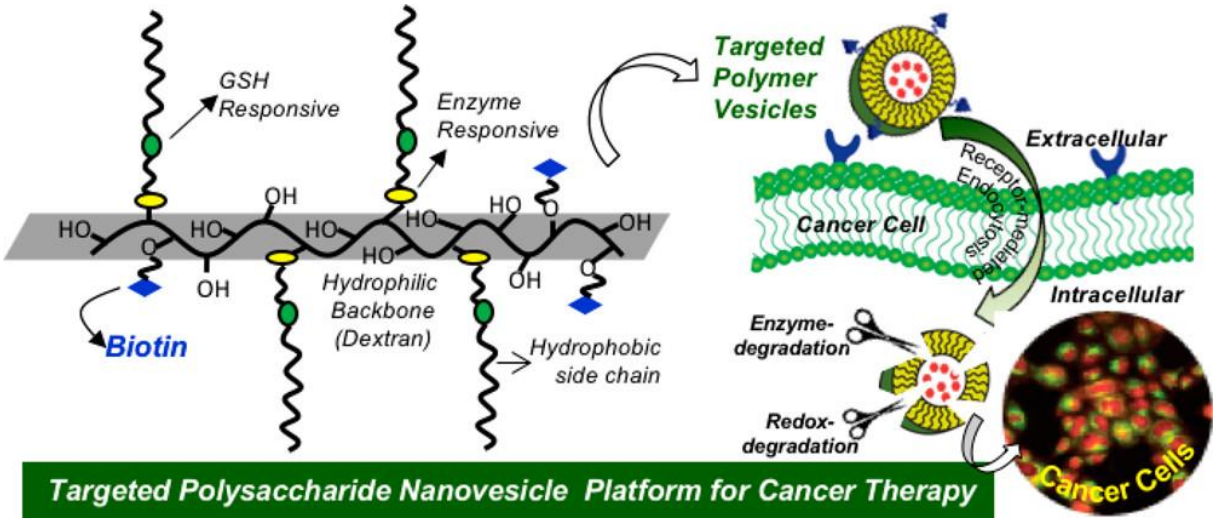

Figure 1.15: *Biotin tagged polymersomes for the targeted delivery to HeLa cells over expression biotin receptors. Adapted from Jayakannan et al., Biomacromolecules* **2018**, *19* (8), 3572-3585

These vesicles, <200 nm in size, exhibited high affinity towards membrane receptors, confirmed by avidin-HABA assay. Loaded with doxorubicin-hydrochloride (DOX.HCl), they

demonstrated stable formulation in PBS and FBS, with 60% drug release under redox conditions and >98% release via lysosomal esterase enzyme. Cellular uptake studies in cervical cancer cells (HeLa) showed enhanced drug accumulation and killing compared to normal cells, indicating successful receptor-mediated endocytosis. Control experiments supported the specificity of this targeted delivery approach, offering promising insights into the potential of biotin-tagged polysaccharide vesicles for cancer therapy.

1.6 Biological Barriers

The majority of nanoparticles tend to accumulate in unintended tissues, posing challenges for targeted delivery. Delivery efficiency is influenced by various factors such as size, shape, surface chemistry, stiffness, and chemical composition of the delivery vehicles, yet achieving optimal design for specific biological targets remains unclear. Current design approaches primarily focus on physical properties rather than biological considerations[9]. Nanoparticles encounter various biological barriers during their journey from administration site to target disease site, hindering effective delivery. Accumulation in off-target tissues leads to adverse effects and diminishes drug concentration at the disease site, thereby reducing formulation efficacy[9]. This section delves into the significance of biological barriers in nanoparticle design journey to the respective cellular targets. The barriers can be broadly divided into organ level barriers, sub-organ level barriers and subcellular level barriers as shown in Figure 1.16.

1.6.1 *Organ Level Barriers*

Nanoparticles face significant challenges at the organ level, particularly in their interaction with the liver and spleen, which are key components of the reticuloendothelial system (RES)[2, 9, 71]. These organs act as principal filters, responsible for removing biological debris and foreign particulates from circulation. However, while performing this vital function, they also pose substantial barriers to intravenously administered nanoparticles, including quantum dots, micelles, gold nanoparticles, and liposomes[2, 71]. The liver, in particular, plays a crucial role in nanoparticle sequestration, primarily through the action of Kupffer cells lining the liver sinusoids[72]. These cells actively capture nanoparticles as they circulate, leading to the prolonged retention of non-degradable nanoparticles within the liver parenchyma. This sequestration phenomenon can significantly impede the delivery of nanoparticles to their intended target sites[9, 71]. Although the

RES presents a promising route for nanomedicine delivery, circumventing this system is essential to enhance the therapeutic efficacy of nanoparticle-based treatments. Additionally, other organs, such as the kidneys, can eliminate nanoparticles based on their physicochemical properties, further complicating the delivery process and necessitating innovative strategies to overcome these barriers effectively[2].

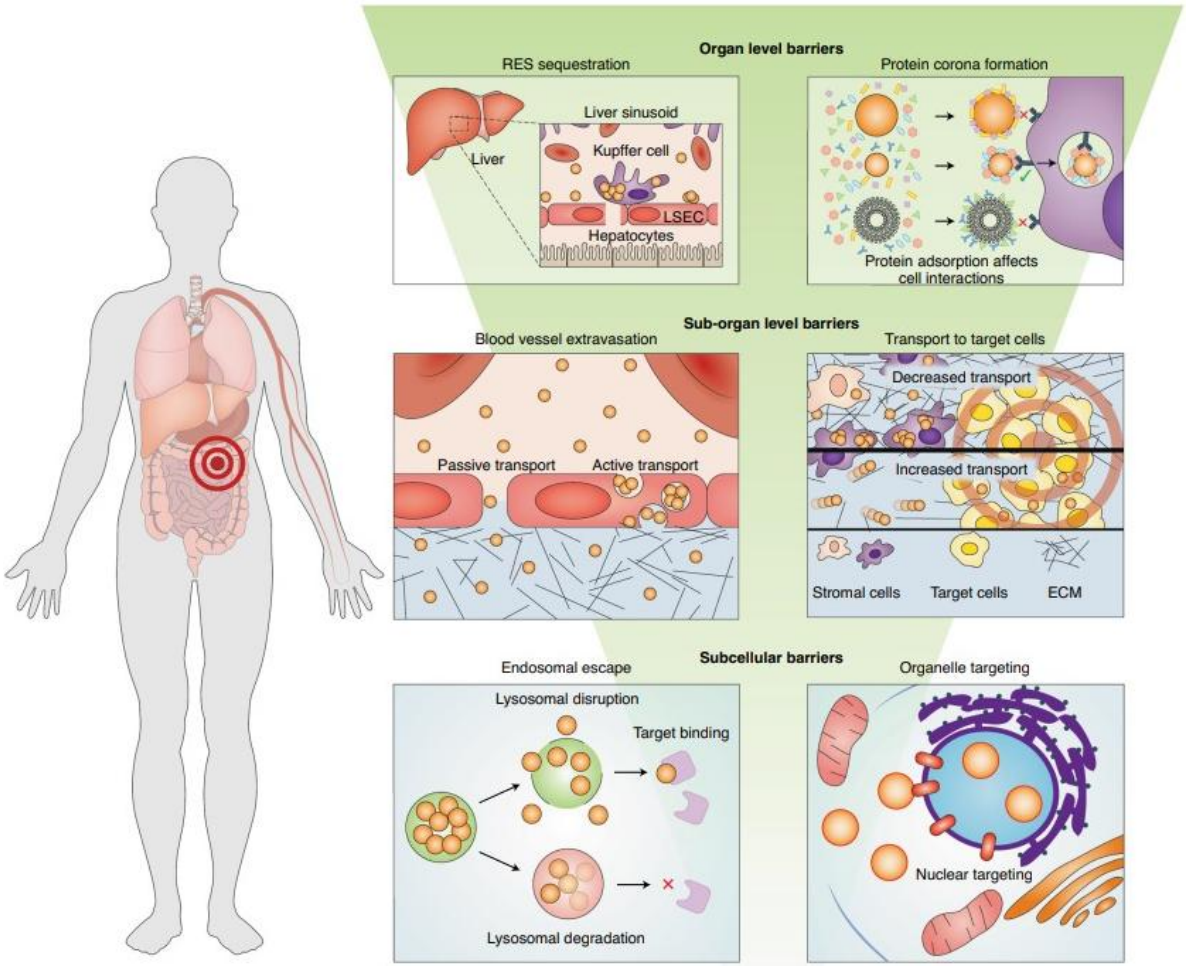

Figure 1.16: *Classification of Biological barriers functional for a nanoparticle. Adapted from Chan et al., Nat. Nanotechnol.* ***2020****, 15 (10), 819-829.*

1.6.2 *Sub-Organ Level Barriers*

At the sub-organ level, nanoparticles encounter a complex network of blood vessels, each characterized by unique physiological features that profoundly influence nanoparticle transport

and distribution within tissues. Factors such as vessel fenestration and permeability play a pivotal role in determining the passage of nanoparticles through the vasculature[9]. For instance, sinusoidal vessels in the liver exhibit fenestrations that enable nanoparticles smaller than these fenestrae (<100 nm) to diffuse into the space of Disse[73]. Similarly, the glomeruli of the kidneys possess fenestrated vessels, albeit with a smaller effective cut-off size (<6 nm) due to the structural composition of the glomerular basement membrane[71]. Moreover, specialized barriers like the blood-brain barrier pose significant challenges to nanoparticle-mediated drug delivery, limiting access to critical organs such as the brain[9, 74]. Overcoming these sub-organ level barriers necessitates precise engineering of nanoparticle properties to facilitate extravasation and tissue-specific targeting, thereby improving therapeutic outcomes.

1.6.3 *Subcellular Barriers*

Upon reaching the target tissue, nanoparticles must navigate intricate subcellular barriers to reach their intended cellular destinations. These barriers include the extracellular matrix (ECM) and off-target cells present within the tissue stroma, which can impede nanoparticle diffusion and sequester nanoparticles before they reach their intended target cells[9]. The composition of the ECM varies between tissues and can be significantly altered in pathological conditions, further complicating nanoparticle transport. Additionally, off-target cells, such as tumour-associated macrophages, can intercept nanoparticles within the stroma, hindering their delivery to specific cell types[75]. Successful nanoparticle-mediated drug delivery necessitates overcoming these barriers to ensure effective payload delivery to target cells. Furthermore, nanoparticles may need to enter target cells to exert their therapeutic effects, requiring them to navigate various cellular uptake mechanisms[9]. Strategies to facilitate endosomal escape and access specific organelles within cells are essential for enhancing the efficacy of nanoparticle-based therapies and minimizing off-target effects. Sometimes, the drug molecules are not able leave the endocytic organelles and reach their cellular target. This happens generally in the lysosomes of the cells and is called as lysosome mediated drug sequestration. Most nanoparticles are designed to intentionally land up in the lysosomes of the cells, so that the action of lysosomal conditions can lead to break opening of the deli every system and subsequently release the drug. However, drugs are sometimes not able to leave the lysosomes and are rather sequestered by them. This is called as drug sequestration by lysosomes. This topic is discussed in the next section. Understanding and overcoming these subcellular

barriers are critical for the development of next-generation nanocarriers optimized for precise and efficient drug delivery[9].

1.6.3.1 *Lysosome Drug Sequestration and Multi Drug Resistance (MDR)*

Lysosomes, cellular organelles characterized by their acidic environment and containing a plethora of digestive enzymes, serve a vital role beyond mere digestion within cells. They participate in various cellular functions such as autophagy, chaperone-mediated autophagy, and maintaining cholesterol homeostasis[76, 77]. Additionally, lysosomes are involved in the degradation of receptor tyrosine kinase receptors and growth factors. In the context of cancer, lysosomes exhibit a dual role.

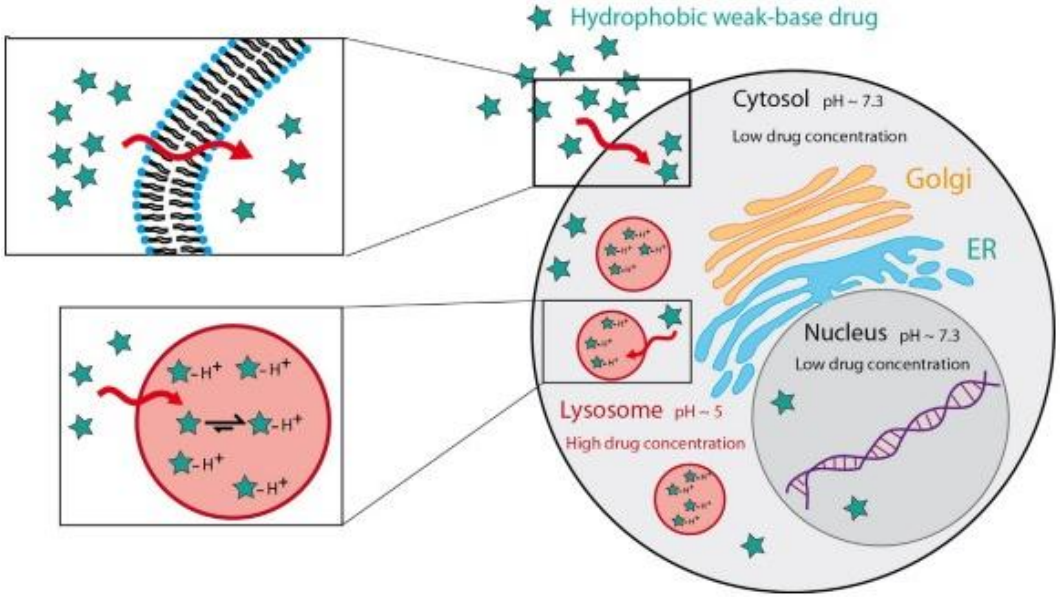

Figure 1.17: *Lysoosme mediated Drug sequestrion of hydrophobic weak bases. Adapted from Assaraf et al., Drug Resistance Updates* **2016**, *24*, 23-33

On one hand, lysosomal proteases like cathepsins are exploited by tumor cells to promote invasion, angiogenesis, and metastasis by degrading extracellular matrix components. Conversely, translocation of lysosomal proteases to the cytosol can induce apoptosis and cell death in neoplastic cells. A significant challenge in cancer treatment is multidrug resistance (MDR), where cancer cells develop resistance to multiple structurally and pharmacologically unrelated drugs. The

drug transporter permeability-glycoprotein (P-gp) is well-known for contributing to MDR[78-80]. Recent research by Al-Akra and colleagues has highlighted the role of lysosomal P-gp in conferring drug resistance, with observations of P-gp localization within lysosomes. Lysosomal sequestration of chemotherapeutic drugs, particularly weak bases, presents a notable mechanism contributing to MDR as shown in Figure 1.17. Certain chemotherapeutic agents, such as doxorubicin and mitoxantrone, preferentially accumulate in lysosomes due to their weak base properties and become trapped within the lysosomal lumen upon protonation. This sequestration reduces drug concentrations in the cytoplasm and nucleus, thereby diminishing their therapeutic effects on cancer cells. Although the term "drug trapping" in lysosomes may suggest a permanent sequestration, it's important to note that the process is reversible. The ionized form of the drug in equilibrium with the neutral form in the cytosol can rapidly diffuse back into the cytosol or plasma, indicating that lysosomes act more as a transient reservoir for cytotoxic drugs rather than permanently trapping them. Furthermore, lysosomal sequestration affects the distribution of chemotherapeutic drugs within cells, leading to decreased drug concentrations in the nucleus, where their intended targets reside. This altered distribution has been associated with decreased efficacy of drugs like daunorubicin and doxorubicin in cancer cells. Notably, cell lines with higher numbers of lysosomes have been found to exhibit greater resistance to certain chemotherapeutic agents. It is further not known with certainty of what happens to the fate of sequestered drugs. In conclusion, understanding the molecular mechanisms underlying lysosomal sequestration of chemotherapeutic drugs is crucial for overcoming MDR in cancer treatment. Targeting lysosomal pathways may offer new strategies to enhance the effectiveness of anticancer therapies.

1.7 Monitoring of intracellular drug delivery processes

This study introduces a novel approach to precise cancer therapy through the development of theranostic nanoprodrugs. These nanoprodrugs, surpassing traditional chemotherapy, effectively achieve self-tracking, targeted drug delivery, stimuli-triggered drug release, and reduced systemic toxicity[81]. A glutathione-responsive theranostic nanoprodrug with a high drug-loading content of 59.4 wt % and an average size of 46 nm was created. This nanoprodrug comprises paclitaxel, an anticancer drug, and a fluorescent imaging probe with high fluorescence quantum yield, linked by a glutathione-sensitive self-immolating linker. The emitted fluorescence allows for efficient self-tracking and sensitive "ON-OFF" glutathione sensing. When encountering high levels of

glutathione in cancer cells, the disulfide bond in the linker is cleaved, causing the linker halves to collapse into cyclic small molecules, leading to simultaneous release of the therapeutic drug and the imaging probe. This enables efficient monitoring of drug release through fluorescence changes.

The nanoparticles further demonstrated high cytotoxicity of these nano prodrugs against various cancer cells, particularly A549 and HEK-293 cells, outperforming free paclitaxel.

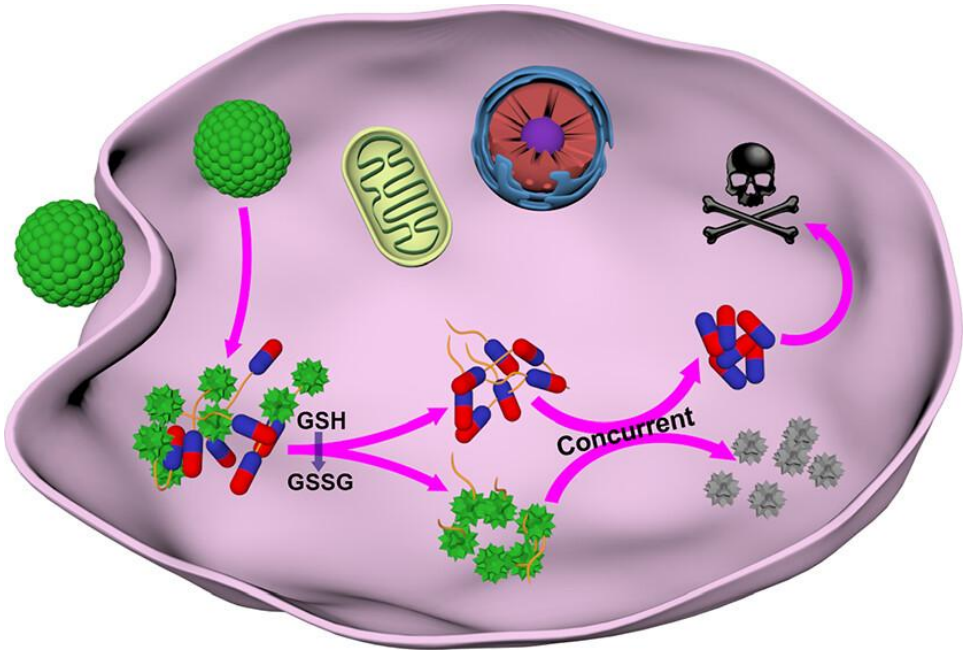

Figure 1.18: *Real time monitoring of intracellular drug release in GSH reponsive drug delivery sytem. Adapted from Sui et al., ACS Appl. Mater. Interfaces.* **2024**, *16* (6), 6859-6867.

Likewise, many small molecules drug conjugates have been utilized to monitor the intramolecular drug release under live conditions. The utilization of perylene-3-ylmethanol fluorescent organic nanoparticles as a drug delivery system was shown in this report[82]. A single-component photoresponsive nanocarrier based on fluorescent organic nanoparticles comprising perylene-3-ylmethanol has been developed. These nanoparticles serve both as drug nanocarriers and phototriggers for drug release. Within this system, the nanoparticles fulfill four crucial functions: serving as nanocarriers for drug delivery, acting as phototriggers for drug release, functioning as fluorescent chromophores for cell imaging, and operating as detectors for real-time monitoring of drug release. In vitro biological studies demonstrated the favorable biocompatibility and cellular uptake of the newly developed perylene-3-ylmethanol nanoparticles, along with their efficient

photoregulated release of anticancer drugs. This innovative application suggests the potential for designing a new class of promising photo responsive nanocarriers for drug delivery.

Notably, they exhibit good biocompatibility, efficient cellular uptake, and precise drug release upon irradiation, as indicated by changes in fluorescence color.

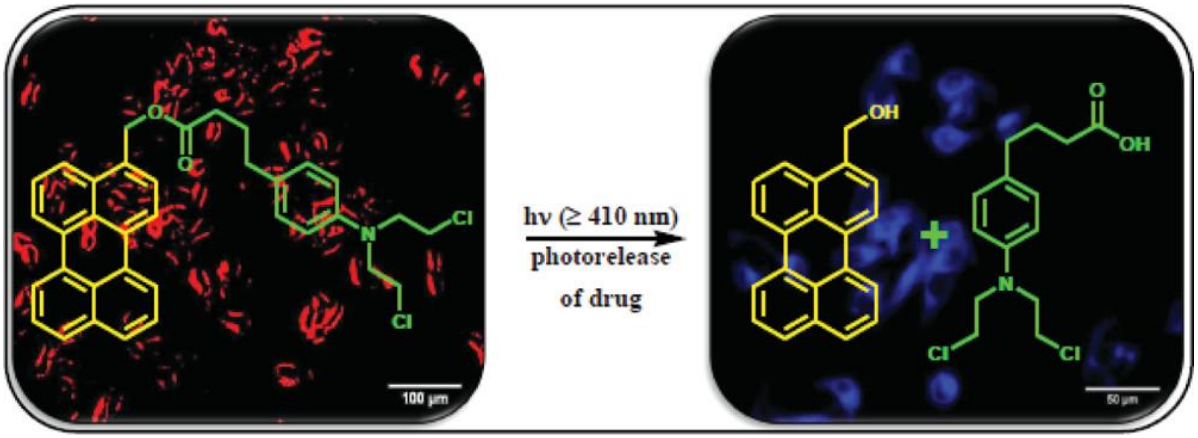

Figure 1.19*: Real-time monitoring of anticancer drug release from a photoresponsivity drug delivery system. Adapted from Singh et al., J. Am. Chem. Soc.* **2012**, *134* (18), 7656-7659

Future research aims to further explore the capabilities of fluorescent organic nanoparticles as photoresponsive nanocarriers for targeted drug delivery. In an unrelated system, a versatile real-time monitoring system based on fluorescence resonance energy transfer (FRET) was developed. This system utilizes coumarin-labeled-cysteine tethered mesoporous silica nanoparticles (MSNs) as drug carriers, fluorescein isothiocyanate-β-cyclodextrin (FITC-β-CD) as a redox-responsive molecular valve, and a FRET donor–acceptor pair of coumarin and FITC for monitoring drug release[83]. Under nonreducing conditions, the intact disulfide bond facilitates FRET from coumarin to FITC on the MSN surface. However, exposure to redox stimuli such as glutathione (GSH) cleaves the disulfide bond, triggering drug release and abolishing FRET. This system enables real-time monitoring of drug release by tracking changes in the FRET signal, offering potential applications in chemotherapy precision. Additionally, a self-tracking GSH-sensing theragnostic nano prodrug (BDP-PTX NPD) has been developed for real-time drug release monitoring in cancer

treatment. This nano prodrug consists of paclitaxel (PTX) and a fluorescent probe linked by a GSH-sensitive self-immolating linker, exhibiting fluorescence "ON-OFF" behavior in response to GSH.

Upon encountering GSH, the linker cleaves and releases PTX molecules, concurrently turning off fluorescence emission, reflecting drug release in real-time.

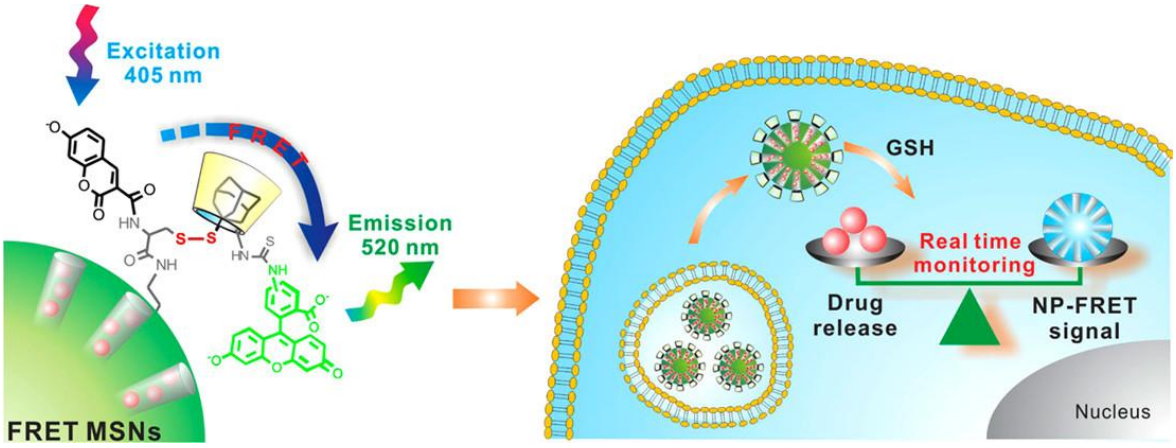

Figure 1.20: *FRET based mesoporous silica nanoparticles for Real-time monitoring of drug release. Adapted from Lee et al., ACS Nano* **2013**, *7* (3), 2741-2750.

Successful monitoring of BDP-PTX NPD's drug release in cancer cells has been demonstrated, showing promising therapeutic effects against cancer cell proliferation. The research summarized here accounts for the lack of trackable drug delivery system based on polymer scaffold, especially the one with polysaccharides.

1.8 Monitoring of intracellular organelle interaction

The involvement of intraorganellar interaction in mediating certain disease is becoming evident. Last few years saw an increase in interest regarding monitoring intracellular interactions. A study investigates the protective effect of 5 nm PtNPs on a human hepatic (HepG2) cell line exposed to dichlorodiphenylethylene (DDE) as a model of oxidative stress. Results indicate that PtNPs efficiently mitigate DDE-induced damage in HepG2 cells, in a dose-dependent manner[84]. PtNPs counteract mitochondrial dynamic imbalance induced by DDE and enhance expression of the

SOD2 mitochondrial enzyme, aiding in cellular recovery from oxidative stress. Notably, PtNPs, either alone or combined with DDE, prompt mitochondria to form contact sites with rough endoplasmic reticulum and endo-lysosomes containing nanoparticles, suggesting inter-organelle crosstalk mediates the protective capability of PtNPs. This study sheds light on the mechanisms underlying the protective action of PtNPs, revealing a novel nano-bio interaction mechanism at the intracellular level mediated by inter-organelle communication and signaling.

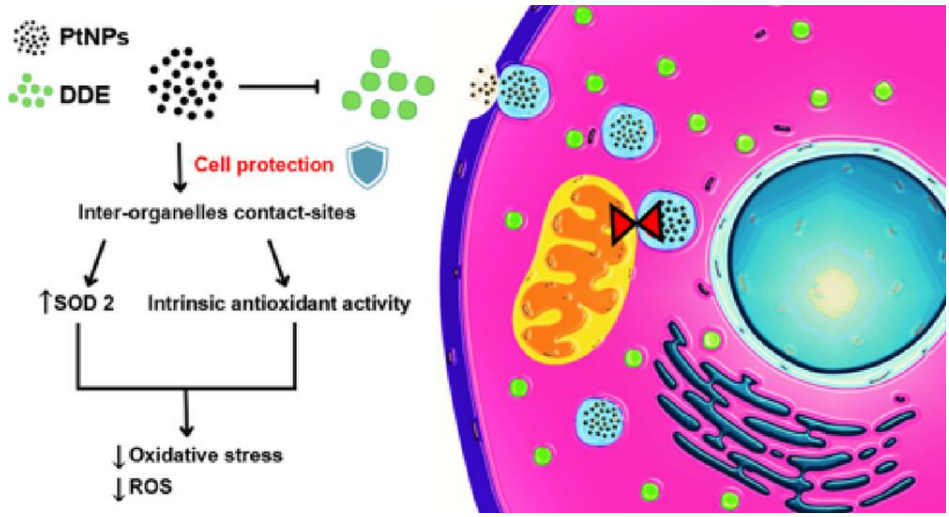

Figure 1.21: *Monitoring Cell nanoparticle interaction and resulting signaling. Adapted from Gaurneiri et al., ACS Appl. Mater. Interfaces.* **2023**, *15* (3), 3882-3893.

Another report devised a methodology to understand the organelle interaction amongst lysosomes. The exchange of contents between vesicles through membrane fusion processes such as kiss-and-run and full-collapse fusion has been extensively studied using artificial vesicles, providing insights into molecular mechanisms involved. However, direct observation of these fusion processes in real biological systems remains challenging due to technical obstacles[85]. A novel ratiometric two-photon probe was developed, enabling real-time tracking of lysosomal ATP with quantitative information for the first time. This probe has been applied to two-photon live-cell imaging, allowing direct observation of lysosomal membrane fusion processes and measurement of lysosomal ATP concentration. Results demonstrate that the kiss-and-run process involves repeated transient interactions between lysosomes with gradual content mixing, while full-fusion occurs instantaneously. Moreover, both fusion processes conserve the content of lysosomal ATP. The use of this small-molecule probe minimizes disturbance and holds potential for studying

various biological processes associated with lysosomal ATP. In another interesting example, inter-organelle interactions between lipid droplets and endoplasmic reticulum were understood. A single fluorescent probe (SF-probes) capable of simultaneous and two-color imaging of multiple targets was synthesized. It was based on excited-state intramolecular proton transfer (ESIPT)[86]. These SF-probes (PPC and EPC) were designed for simultaneous two-color fluorescence imaging of lipid droplets (LDs) and the endoplasmic reticulum (ER) under single-wavelength excitation.

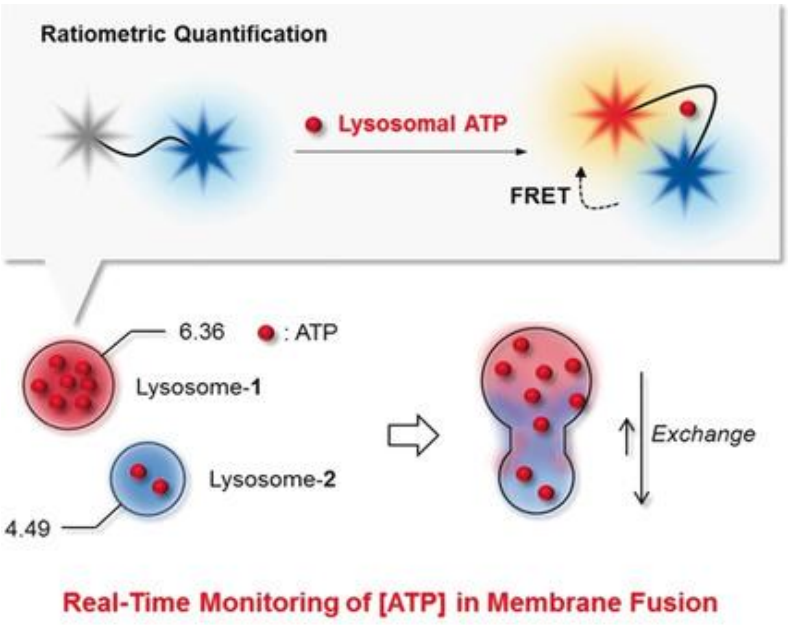

Figure 1.22: *Real time monitoring g of interactions between lysosomes via ATP dependent fluorescent probe. Adapted from Ahn et al., Angew. Chem. Int. Ed.* **2018**, *57*, 10142-10147

This was done to simultaneously and distinctly visualize different organelles and their interactions. These ESIPT probes, PPC and EPC, leverage their strong electron-donating side substituents to exhibit fluorescence spectra and colors highly sensitive to variations in water content between LDs and ER. As a result, LDs emit orange fluorescence while ER emits green fluorescence in the Lambda imaging mode. Employing PPC or EPC probes, we investigate the morphology, size, and distribution of LDs and ER in live cells and tissues. Through in situ and real-time fluorescence imaging in Lambda mode, they observed the generation of newborn LDs near ER regions, with both organelles displaying shared identical fluorescence colors. This observation supports the mainstream hypothesis suggesting LDs originate from the ER. The exceptional imaging

capabilities of these SF-probes position them as valuable tools for unravelling biological processes related to LD-ER interactions.

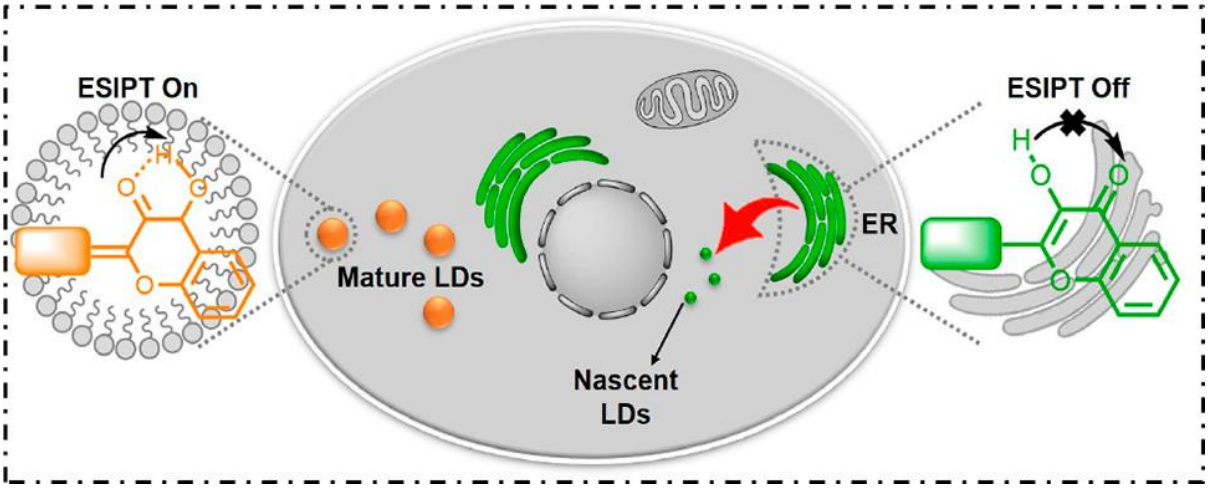

Figure 1.23: *ESIPT base fluorescent probes to simultaneously label; endoplasmic reticulum and lipid droplets to monitor their interaction. Adapted from Yu et al., J. Am. Chem. Soc.* **2021**, *143*, 3169-3179

1.9 Aim of this Thesis

The first objective of this thesis is to delve into the intricate journey undertaken by nanoparticles within cells, elucidating their pathway until they reach specific subcellular locations where cargo unloading occurs. This journey is of paramount importance because it dictates the eventual intracellular distribution of nanoparticles, which in turn profoundly influences the efficiency of cargo release. Understanding and visualizing this journey are imperative as they serve as pivotal indicators of the efficacy of drug-loaded nanoparticle systems. One critical aspect that warrants attention is the interactions occurring between different organelles within the cell. These interactions can significantly impact the fate of drug molecules encapsulated within nanoparticles. For instance, while lysosomes play a vital role in the degradation and release of cargo, they also possess the capability to sequester drug molecules. This dual role of lysosomes exemplifies the complexity of intracellular dynamics and underscores the importance of unravelling these processes for optimizing drug delivery strategies.

However, despite the significance of elucidating these processes, our progress is hindered by the limited availability of suitable fluorescent tools for visualization. The ability to accurately track

and visualize the movement of nanoparticles within cells is essential for gaining insights into their behavior and interactions with various cellular components. Overcoming this limitation is paramount for advancing our understanding of drug delivery mechanisms and enhancing the efficacy of nanoparticle-based therapies. In this thesis we intend to develop trackable system that could shed light on the drug delivery abilities of the polymeric drug delivery system based on polysaccharide. Since polysaccharide are easily recognized and taken up by the cells, they remain ultimate choice for the development of such trackable platform. Further polymersomes are unique for the physical characteristics, their stability and ability to load multiple drugs and dyes. We intended to design trackable polysaccharide based polymersomes for monitoring the drug release inside the cells. Due to recent evidence in inter-organelle interaction being operational and culprit of various cellular pathologies. We next aimed at understanding their effect on drug efficacy. Primarily we wished to understand the effect of lysosome- endosome interaction in sequestering drug molecules and to study that, a novel nano-emitter probe with dual fluorescent labelling was intended in the design, which would then be used to study such intricate interactions and their role in drug sequestration. With this brief introduction about the type and choice of delivery vectors, and associated barriers in biology, we aimed to track the delivery and sequestration effect of drug mediated via organelle interactions.

1.10 Bibliography

(1) Vargason, A. M.; Anselmo, A. C.; Mitragotri, S. The evolution of commercial drug delivery technologies. *Nat. Biomed. Eng* **2021**, *5* (9), 951-967.
(2) Mitchell, M. J.; Billingsley, M. M.; Haley, R. M.; Wechsler, M. E.; Peppas, N. A.; Langer, R. Engineering precision nanoparticles for drug delivery. *Nat. Rev. Drug Discov.* **2021**, *20* (2), 101-124.
(3) Yoo, J.-W.; Irvine, D. J.; Discher, D. E.; Mitragotri, S. Bio-inspired, bioengineered and biomimetic drug delivery carriers. *Nat. Rev. Drug Discov.* **2011**, *10* (7), 521-535.
(4) Li, X.; Peng, X.; Zoulikha, M.; Boafo, G. F.; Magar, K. T.; Ju, Y.; He, W. Multifunctional nanoparticle-mediated combining therapy for human diseases. *Signal Transduction and Targeted Therapy* **2024**, *9* (1), 1.
(5) Kakkar, A.; Traverso, G.; Farokhzad, O. C.; Weissleder, R.; Langer, R. Evolution of macromolecular complexity in drug delivery systems. *Nature Reviews Chemistry* **2017**, *1* (8), 0063.
(6) Whitesides, G. M. The 'right' size in nanobiotechnology. *Nature Biotechnology* **2003**, *21* (10), 1161-1165.
(7) Rasmussen, K.; Riego Sintes, J.; Rauscher, H. How nanoparticles are counted in global regulatory nanomaterial definitions. *Nat. Nanotechnol.* **2024**, *19* (2), 132-138.
(8) Torchilin, V. P. Multifunctional, stimuli-sensitive nanoparticulate systems for drug delivery. *Nat. Rev. Drug Discov.* **2014**, *13* (11), 813-827.
(9) Poon, W.; Kingston, B. R.; Ouyang, B.; Ngo, W.; Chan, W. C. W. A framework for designing delivery systems. *Nat. Nanotechnol.* **2020**, *15* (10), 819-829.
(10) Mitragotri, S.; Burke, P. A.; Langer, R. Overcoming the challenges in administering biopharmaceuticals: formulation and delivery strategies. *Nat. Rev. Drug Discov.* **2014**, *13* (9), 655-672.
(11) Kulkarni, J. A.; Witzigmann, D.; Thomson, S. B.; Chen, S.; Leavitt, B. R.; Cullis, P. R.; van der Meel, R. The current landscape of nucleic acid therapeutics. *Nat. Nanotechnol.* **2021**, *16* (6), 630-643.
(12) Polack Fernando, P.; Thomas Stephen, J.; Kitchin, N.; Absalon, J.; Gurtman, A.; Lockhart, S.; Perez John, L.; Pérez Marc, G.; Moreira Edson, D.; Zerbini, C.; et al. Safety and Efficacy of the BNT162b2 mRNA Covid-19 Vaccine. *New England Journal of Medicine* **2020**, *383* (27), 2603-2615.
(13) Romito, A.; Cobellis, G. Pluripotent Stem Cells: Current Understanding and Future Directions. *Stem Cells International* **2016**, *2016*, 9451492.
(14) June, C. H.; O'Connor, R. S.; Kawalekar, O. U.; Ghassemi, S.; Milone, M. C. CAR T cell immunotherapy for human cancer. *Science* **2018**, *359* (6382), 1361-1365.
(15) Prasad, V. Tisagenlecleucel — the first approved CAR-T-cell therapy: implications for payers and policy makers. *Nature Reviews Clinical Oncology* **2018**, *15* (1), 11-12.
(16) Jackson, H. J.; Rafiq, S.; Brentjens, R. J. Driving CAR T-cells forward. *Nature Reviews Clinical Oncology* **2016**, *13* (6), 370-383.
(17) Beaumont, K.; Webster, R.; Gardner, I.; Dack, K. Design of Ester Prodrugs to Enhance Oral Absorption of Poorly Permeable Compounds: Challenges to the Discovery Scientist. *Current Drug Metabolism* **2003**, *4* (6), 461-485.
(18) Kempf, D. J.; Sham, H. L.; Marsh, K. C.; Flentge, C. A.; Betebenner, D.; Green, B. E.; McDonald, E.; Vasavanonda, S.; Saldivar, A.; Wideburg, N. E.; et al. Discovery of Ritonavir, a

Potent Inhibitor of HIV Protease with High Oral Bioavailability and Clinical Efficacy. *Journal of Medicinal Chemistry* **1998**, *41* (4), 602-617.
(19) Agersø, H.; Seiding Larsen, L.; Riis, A.; Lövgren, U.; Karlsson, M. O.; Senderovitz, T. Pharmacokinetics and renal excretion of desmopressin after intravenous administration to healthy subjects and renally impaired patients. *British Journal of Clinical Pharmacology* **2004**, *58* (4), 352-358.
(20) Verma, S.; Miles, D.; Gianni, L.; Krop Ian, E.; Welslau, M.; Baselga, J.; Pegram, M.; Oh, D.-Y.; Diéras, V.; Guardino, E.; et al. Trastuzumab Emtansine for HER2-Positive Advanced Breast Cancer. *New England Journal of Medicine 367* (19), 1783-1791.
(21) Lewis Phillips, G. D.; Li, G.; Dugger, D. L.; Crocker, L. M.; Parsons, K. L.; Mai, E.; Blättler, W. A.; Lambert, J. M.; Chari, R. V. J.; Lutz, R. J.; et al. Targeting HER2-Positive Breast Cancer with Trastuzumab-DM1, an Antibody–Cytotoxic Drug Conjugate. *Cancer Research* **2008**, *68* (22), 9280-9290.
(22) Sharma, P. C.; Jain, A.; Jain, S.; Pahwa, R.; Yar, M. S. Ciprofloxacin: review on developments in synthetic, analytical, and medicinal aspects. *Journal of Enzyme Inhibition and Medicinal Chemistry* **2010**, *25* (4), 577-589.
(23) Akinc, A.; Maier, M. A.; Manoharan, M.; Fitzgerald, K.; Jayaraman, M.; Barros, S.; Ansell, S.; Du, X.; Hope, M. J.; Madden, T. D.; et al. The Onpattro story and the clinical translation of nanomedicines containing nucleic acid-based drugs. *Nat. Nanotechnol.* **2019**, *14* (12), 1084-1087.
(24) Garber, K. Alnylam launches era of RNAi drugs. *Nature Biotechnology* **2018**, *36* (9), 777-778.
(25) Chen, S.; Zaifman, J.; Kulkarni, J. A.; Zhigaltsev, I. V.; Tam, Y. K.; Ciufolini, M. A.; Tam, Y. Y. C.; Cullis, P. R. Dexamethasone prodrugs as potent suppressors of the immunostimulatory effects of lipid nanoparticle formulations of nucleic acids. *J. Control. Release* **2018**, *286*, 46-54.
(26) Yeku, Oladapo O.; Brentjens, Renier J. Armored CAR T-cells: utilizing cytokines and pro-inflammatory ligands to enhance CAR T-cell anti-tumour efficacy. *Biochemical Society Transactions* **2016**, *44* (2), 412-418.
(27) Lee, S.; Margolin, K. Cytokines in Cancer Immunotherapy. In *Cancers*, 2011; Vol. 3, pp 3856-3893.
(28) Yu, J.; Zhang, Y.; Ye, Y.; DiSanto, R.; Sun, W.; Ranson, D.; Ligler, F. S.; Buse, J. B.; Gu, Z. Microneedle-array patches loaded with hypoxia-sensitive vesicles provide fast glucose-responsive insulin delivery. *Proc Natl Acad Sci USA* **2015**, *112* (27), 8260-8265.
(29) Schwendeman, S. P.; Shah, R. B.; Bailey, B. A.; Schwendeman, A. S. Injectable controlled release depots for large molecules. *J. Control. Release* **2014**, *190*, 240-253.
(30) Prausnitz, M. R.; Langer, R. Transdermal drug delivery. *Nature Biotechnology* **2008**, *26* (11), 1261-1268.
(31) Anselmo, A. C.; Mitragotri, S. Nanoparticles in the clinic: An update. *Bioengineering & Translational Medicine* **2019**, *4* (3), e10143.
(32) Kamaly, N.; Yameen, B.; Wu, J.; Farokhzad, O. C. Degradable Controlled-Release Polymers and Polymeric Nanoparticles: Mechanisms of Controlling Drug Release. *Chem. Rev.* **2016**, *116* (4), 2602-2663.
(33) Poo, H.; Pyo, H.-M.; Lee, T.-Y.; Yoon, S.-W.; Lee, J.-S.; Kim, C.-J.; Sung, M.-H.; Lee, S.-H. Oral administration of human papillomavirus type 16 E7 displayed on Lactobacillus casei induces E7-specific antitumor effects in C57/BL6 mice. *International Journal of Cancer* **2006**, *119* (7), 1702-1709.

(34) Adler, L. A.; Zimmerman, B.; Starr, H. L.; Silber, S.; Palumbo, J.; Orman, C.; Spencer, T. Efficacy and Safety of OROS Methylphenidate in Adults With Attention-Deficit/Hyperactivity Disorder: A Randomized, Placebo-Controlled, Double-Blind, Parallel Group, Dose-Escalation Study. *Journal of Clinical Psychopharmacology* **2009**, *29* (3).
(35) Zhou, S.; Huang, G. Synthesis of anti-allergic drugs. *RSC Advances* **2020**, *10* (10), 5874-5885, 10.1039/C9RA10659F.
(36) Moazzam, A.; Luis, B.; Sihem Bent, L. Extended Effectiveness of the Etonogestrel-Releasing Contraceptive Implant and the 20 μg Levonorgestrel-Releasing Intrauterine System for 2 Years Beyond U.S. Food and Drug Administration Product Labeling. *Global Health: Science and Practice* **2017**, *5* (4), 534.
(37) Garland Suzanne, M.; Hernandez-Avila, M.; Wheeler Cosette, M.; Perez, G.; Harper Diane, M.; Leodolter, S.; Tang Grace, W. K.; Ferris Daron, G.; Steben, M.; Bryan, J.; et al. Quadrivalent Vaccine against Human Papillomavirus to Prevent Anogenital Diseases. *New England Journal of Medicine 356* (19), 1928-1943.
(38) Wu, W.; Hsiao, S. C.; Carrico, Z. M.; Francis, M. B. Genome-Free Viral Capsids as Multivalent Carriers for Taxol Delivery. *Angew. Chem. Int. Ed.* **2009**, *48* (50), 9493-9497.
(39) Rideau, E.; Dimova, R.; Schwille, P.; Wurm, F. R.; Landfester, K. Liposomes and polymersomes: a comparative review towards cell mimicking. *Chem. Soc. Rev.* **2018**, *47* (23), 8572-8610, 10.1039/C8CS00162F.
(40) Amos, R. C.; Nazemi, A.; Bonduelle, C. V.; Gillies, E. R. Tuning polymersome surfaces: functionalization with dendritic groups. *Soft Matter* **2012**, *8* (21), 5947-5958, 10.1039/C2SM25172H.
(41) Zhu, Y.; Cao, S.; Huo, M.; van Hest, J. C. M.; Che, H. Recent advances in permeable polymersomes: fabrication, responsiveness, and applications. *Chem. Sci.* **2023**, *14* (27), 7411-7437, 10.1039/D3SC01707A.
(42) Matoori, S.; Leroux, J.-C. Twenty-five years of polymersomes: lost in translation? *Materials Horizons* **2020**, *7* (5), 1297-1309, 10.1039/C9MH01669D.
(43) Ishida, T.; Ichihara, M.; Wang, X.; Yamamoto, K.; Kimura, J.; Majima, E.; Kiwada, H. Injection of PEGylated liposomes in rats elicits PEG-specific IgM, which is responsible for rapid elimination of a second dose of PEGylated liposomes. *J. Control. Release* **2006**, *112* (1), 15-25.
(44) Abraham, S. A.; Waterhouse, D. N.; Mayer, L. D.; Cullis, P. R.; Madden, T. D.; Bally, M. B. The Liposomal Formulation of Doxorubicin. In *Methods in Enzymology*, Vol. 391; Academic Press, 2005; pp 71-97.
(45) Zhao, P.; Hou, X.; Yan, J.; Du, S.; Xue, Y.; Li, W.; Xiang, G.; Dong, Y. Long-term storage of lipid-like nanoparticles for mRNA delivery. *Bioactive Materials* **2020**, *5* (2), 358-363.
(46) Hou, X.; Zaks, T.; Langer, R.; Dong, Y. Lipid nanoparticles for mRNA delivery. *Nature Reviews Materials* **2021**, *6* (12), 1078-1094.
(47) Lipowsky, R. Coupling of bending and stretching deformations in vesicle membranes. *Advances in Colloid and Interface Science* **2014**, *208*, 14-24.
(48) Kauscher, U.; Holme, M. N.; Björnmalm, M.; Stevens, M. M. Physical stimuli-responsive vesicles in drug delivery: Beyond liposomes and polymersomes. *Adv Drug Deliv Rev* **2019**, *138*, 259-275.
(49) Palivan, C. G.; Goers, R.; Najer, A.; Zhang, X.; Car, A.; Meier, W. Bioinspired polymer vesicles and membranes for biological and medical applications. *Chem. Soc. Rev.* **2016**, *45* (2), 377-411, 10.1039/C5CS00569H.

(50) Habraken, G. J. M.; Peeters, M.; Thornton, P. D.; Koning, C. E.; Heise, A. Selective Enzymatic Degradation of Self-Assembled Particles from Amphiphilic Block Copolymers Obtained by the Combination of N-Carboxyanhydride and Nitroxide-Mediated Polymerization. *Biomacromolecules* **2011**, *12* (10), 3761-3769.
(51) Rodriguez, A. R.; Kramer, J. R.; Deming, T. J. Enzyme-Triggered Cargo Release from Methionine Sulfoxide Containing Copolypeptide Vesicles. *Biomacromolecules* **2013**, *14* (10), 3610-3614.
(52) Liu, F.; Eisenberg, A. Preparation and pH Triggered Inversion of Vesicles from Poly(acrylic Acid)-block-Polystyrene-block-Poly(4-vinyl Pyridine). *J. Am. Chem. Soc.* **2003**, *125* (49), 15059-15064.
(53) Chiu, H.-C.; Lin, Y.-W.; Huang, Y.-F.; Chuang, C.-K.; Chern, C.-S. Polymer Vesicles Containing Small Vesicles within Interior Aqueous Compartments and pH-Responsive Transmembrane Channels. *Angew. Chem. Int. Ed.* **2008**, *47* (10), 1875-1878.
(54) Puglisi, A.; Bayir, E.; Timur, S.; Yagci, Y. pH-Responsive Polymersome Microparticles as Smart Cyclodextrin-Releasing Agents. *Biomacromolecules* **2019**, *20* (10), 4001-4007.
(55) Travanut, A.; Monteiro, P. F.; Smith, S.; Howdle, S. M.; Grabowska, A. M.; Kellam, B.; Meier, M. A. R.; Alexander, C. Passerini chemistries for synthesis of polymer pro-drug and polymersome drug delivery nanoparticles. *J. Mater. Chem. B* **2022**, *10* (20), 3895-3905, 10.1039/D2TB00045H.
(56) Rijpkema, S. J.; Langens, S. G. H. A.; van der Kolk, M. R.; Gavriel, K.; Toebes, B. J.; Wilson, D. A. Modular Approach to the Functionalization of Polymersomes. *Biomacromolecules* **2020**, *21* (5), 1853-1864.
(57) Brinkhuis, R. P.; de Graaf, F.; Hansen, M. B.; Visser, T. R.; Rutjes, F. P. J. T.; van Hest, J. C. M. Dynamically functionalized polymersomes via hydrazone exchange. *Polym. Chem.* **2013**, *4* (5), 1345-1350, 10.1039/C2PY20789C.
(58) Wang, V.; Kim, J.; Kim, J.; Lee, S. W.; Kim, K. T. On-demand shape transformation of polymer vesicles via site-specific isomerization of hydrazone photoswitches in monodisperse hydrophobic oligomers. *Polym. Chem.* **2021**, *12* (35), 5027-5036, 10.1039/D1PY00981H.
(59) Chen, W.; Meng, F.; Cheng, R.; Zhong, Z. pH-Sensitive degradable polymersomes for triggered release of anticancer drugs: A comparative study with micelles. *J. Control. Release* **2010**, *142* (1), 40-46.
(60) Zhou, D.; Fei, Z.; Jin, L.; Zhou, P.; Li, C.; Liu, X.; Zhao, C. Dual-responsive polymersomes as anticancer drug carriers for the co-delivery of doxorubicin and paclitaxel. *J. Mater. Chem. B* **2021**, *9* (3), 801-808, 10.1039/D0TB02462G.
(61) Qin, S.; Geng, Y.; Discher, D. E.; Yang, S. Temperature-Controlled Assembly and Release from Polymer Vesicles of Poly(ethylene oxide)-block- poly(N-isopropylacrylamide). *Advanced Materials* **2006**, *18* (21), 2905-2909.
(62) Li, Y.; Lokitz, B. S.; McCormick, C. L. Thermally Responsive Vesicles and Their Structural "Locking" through Polyelectrolyte Complex Formation. *Angew. Chem. Int. Ed.* **2006**, *45* (35), 5792-5795.
(63) Moughton, A. O.; Patterson, J. P.; O'Reilly, R. K. Reversible morphological switching of nanostructures in solution. *Chemical Communications* **2011**, *47* (1), 355-357, 10.1039/C0CC02160A.
(64) Qiao, Z.-Y.; Ji, R.; Huang, X.-N.; Du, F.-S.; Zhang, R.; Liang, D.-H.; Li, Z.-C. Polymersomes from Dual Responsive Block Copolymers: Drug Encapsulation by Heating and Acid-Triggered Release. *Biomacromolecules* **2013**, *14* (5), 1555-1563.

(65) Che, H.; van Hest, J. C. M. Stimuli-responsive polymersomes and nanoreactors. *J. Mater. Chem. B* **2016**, *4* (27), 4632-4647, 10.1039/C6TB01163B.
(66) Yan, Q.; Yuan, J.; Cai, Z.; Xin, Y.; Kang, Y.; Yin, Y. Voltage-Responsive Vesicles Based on Orthogonal Assembly of Two Homopolymers. *J. Am. Chem. Soc.* **2010**, *132* (27), 9268-9270.
(67) Golam, T. S.; Botelho, R. J. Lysosome Fission: Planning for an Exit. *Trends Cell Biol.* **2019**, *29* (8), 635-646.
(68) Pramod, P. S.; Takamura, K.; Chaphekar, S.; Balasubramanian, N.; Jayakannan, M. Dextran Vesicular Carriers for Dual Encapsulation of Hydrophilic and Hydrophobic Molecules and Delivery into Cells. *Biomacromolecules* **2012**, *13* (11), 3627-3640.
(69) Pramod, P. S.; Shah, R.; Jayakannan, M. Dual stimuli polysaccharide nanovesicles for conjugated and physically loaded doxorubicin delivery in breast cancer cells. *Nanoscale* **2015**, *7* (15), 6636-6652, 10.1039/C5NR00799B.
(70) Deshpande, N. U.; Jayakannan, M. Biotin-Tagged Polysaccharide Vesicular Nanocarriers for Receptor-Mediated Anticancer Drug Delivery in Cancer Cells. *Biomacromolecules* **2018**, *19* (8), 3572-3585.
(71) Ferrari, M. Cancer nanotechnology: opportunities and challenges. *Nat. Rev. Cancer.* **2005**, *5* (3), 161-171.
(72) Sadauskas, E.; Danscher, G.; Stoltenberg, M.; Vogel, U.; Larsen, A.; Wallin, H. Protracted elimination of gold nanoparticles from mouse liver. *Nanomedicine: Nanotechnology, Biology and Medicine* **2009**, *5* (2), 162-169.
(73) Poon, W.; Zhang, Y.-N.; Ouyang, B.; Kingston, B. R.; Wu, J. L. Y.; Wilhelm, S.; Chan, W. C. W. Elimination Pathways of Nanoparticles. *ACS Nano* **2019**, *13* (5), 5785-5798.
(74) Saraiva, C.; Praça, C.; Ferreira, R.; Santos, T.; Ferreira, L.; Bernardino, L. Nanoparticle-mediated brain drug delivery: Overcoming blood–brain barrier to treat neurodegenerative diseases. *J. Control. Release* **2016**, *235*, 34-47.
(75) Dai, Q.; Wilhelm, S.; Ding, D.; Syed, A. M.; Sindhwani, S.; Zhang, Y.; Chen, Y. Y.; MacMillan, P.; Chan, W. C. W. Quantifying the Ligand-Coated Nanoparticle Delivery to Cancer Cells in Solid Tumors. *ACS Nano* **2018**, *12* (8), 8423-8435.
(76) Halaby, R. Influence of lysosomal sequestration on multidrug resistance in cancer cells. *Cancer Drug Resistance* **2019**, *2* (1), 31-42.
(77) Zhitomirsky, B.; Assaraf, Y. G. Lysosomes as mediators of drug resistance in cancer. *Drug Resistance Updates* **2016**, *24*, 23-33.
(78) Yamagishi, T.; Sahni, S.; Sharp, D. M.; Arvind, A.; Jansson, P. J.; Richardson, D. R. P-glycoprotein Mediates Drug Resistance via a Novel Mechanism Involving Lysosomal Sequestration*. *J. Biol. Chem.* **2013**, *288* (44), 31761-31771.
(79) Chapuy, B.; Koch, R.; Radunski, U.; Corsham, S.; Cheong, N.; Inagaki, N.; Ban, N.; Wenzel, D.; Reinhardt, D.; Zapf, A.; et al. Intracellular ABC transporter A3 confers multidrug resistance in leukemia cells by lysosomal drug sequestration. *Leukemia* **2008**, *22* (8), 1576-1586.
(80) Mutvei, A. P.; Nagiec, M. J.; Blenis, J. Balancing lysosome abundance in health and disease. *Nat. Cell Biol.* **2023**, *25* (9), 1254-1264.
(81) Nisar, S.; Starosta, E.; Elayyan, M.; Regmi, A.; Sui, B. Photoinduced Electron Transfer-Based Glutathione-Sensing Theranostic Nanoprodrug with Self-Tracking and Real-Time Drug Release Monitoring for Cancer Treatment. *ACS Appl. Mater. Interfaces.* **2024**, *16* (6), 6859-6867.
(82) Jana, A.; Devi, K. S. P.; Maiti, T. K.; Singh, N. D. P. Perylene-3-ylmethanol: Fluorescent Organic Nanoparticles as a Single-Component Photoresponsive Nanocarrier with Real-Time Monitoring of Anticancer Drug Release. *J. Am. Chem. Soc.* **2012**, *134* (18), 7656-7659.

(83) Lai, J.; Shah, B. P.; Garfunkel, E.; Lee, K.-B. Versatile Fluorescence Resonance Energy Transfer-Based Mesoporous Silica Nanoparticles for Real-Time Monitoring of Drug Release. *ACS Nano* **2013**, *7* (3), 2741-2750.
(84) Migliaccio, V.; Blal, N.; De Girolamo, M.; Mastronardi, V.; Catalano, F.; Di Gregorio, I.; Lionetti, L.; Pompa, P. P.; Guarnieri, D. Inter-Organelle Contact Sites Mediate the Intracellular Antioxidant Activity of Platinum Nanozymes: A New Perspective on Cell–Nanoparticle Interaction and Signaling. *ACS Appl. Mater. Interfaces.* **2023**, *15* (3), 3882-3893.
(85) Jun, Y. W.; Wang, T.; Hwang, S.; Kim, D.; Ma, D.; Kim, K. H.; Kim, S.; Jung, J.; Ahn, K. H. A Ratiometric Two-Photon Fluorescent Probe for Tracking Lysosomal ATP: Direct In Cellulo Observation of Lysosomal Membrane Fusion Processes. *Angew. Chem. Int. Ed.* **2018**, *57* (32), 10142-10147.
(86) Guo, L.; Tian, M.; Zhang, Z.; Lu, Q.; Liu, Z.; Niu, G.; Yu, X. Simultaneous Two-Color Visualization of Lipid Droplets and Endoplasmic Reticulum and Their Interplay by Single Fluorescent Probes in Lambda Mode. *J. Am. Chem. Soc.* **2021**, *143* (8), 3169-3179.

Chapter 2

Unveiling Real-Time Cargo Delivery Dynamics of Polysaccharide Polymersomes via FRET signaling in Live Cells[1]

[1] The work presented in Chapter 2 is partially adapted from (i) Virmani, M.; Deshpande, N. U.; Jayakannan, M. Self-Reporting Polysaccharide Polymersome for Doxorubicin and Cisplatin Delivery to Live Cancer Cells. *ACS Polym. Au* **2022**, *2*, 181–193. (ii) Deshpande, N. U.; Virmani, M.; Jayakannan, M. An AIE-driven Fluorescent Polysaccharide Polymersome as an Enzyme-Responsive FRET Nanoprobe to Study the Real-Time Delivery Aspects in Live Cells. *Polym. Chem.* **2021**, *12*, 1549– 156.

2.1 Abstract

This chapter explores the realm of drug delivery systems by utilizing fluorescent vesicles and polymersomes to monitor drug localization and release within cellular environments. At the heart of this work lies the innovative use of Tetraphenylethylene (TPE), a blue luminescent Aggregation Induced Emission (AIE) fluorophore, known for its ability to emit light upon aggregation, which was integrated into the design of the vesicles. By conjugating dextran with TPE and a vesicle-directing unit, Pentadecyl phenol, through enzyme-sensitive ester linkages, this study successfully created self-assembling, blue emissive polymersomes of approximately 200 nm in diameter. These polymersomes, referred to as P_{TPE}, localized specifically within lysosomes, as confirmed through colocalization assays using Lysotracker dye. A significant aspect of this research was the ability to track these P_{TPE} polymersomes inside cells, thanks to their blue luminescence. Further, their potential for drug delivery was evaluated by loading them with the fluorescent cargo Rose Bengal (RB) and observing the energy transfer between TPE and RB through Fluorescence Resonance Energy Transfer (FRET). This process was monitored under the influence of esterases, enzymes known to cleave ester bonds, which triggered the disassembly of the polymersomes and the release of the encapsulated cargo, showcasing the polymersomes' efficient unloading capabilities in a controlled manner. Expanding on this mechanism, the study also delved into the release kinetics of doxorubicin, a widely used chemotherapeutic agent, loaded within the PTPE polymersomes. The interaction between doxorubicin and the polymersomes formed a "dark pair," exhibiting fluorescence quenching through FRET, which upon esterase treatment, reversed, indicating the release of doxorubicin. This release mechanism was visually tracked in cellular environments, highlighting a significant increase in fluorescence within the nucleus over time as the released doxorubicin interacted with nuclear DNA, illustrating the effective delivery and unloading of the drug within targeted cellular compartments.

This work not only demonstrates the practical application of FRET-based tools in monitoring the enzymatic unloading of fluorescent cargos but also emphasizes the potential of these engineered polymersomes in understanding and enhancing the efficacy of drug delivery systems. By providing a novel method to visually track unloading of therapeutic agents from nano vectors within cells, this research offers valuable insights and can be extended to study the variability of patient responses to treatment, paving the way for more personalized and effective therapeutic strategies.

2.2 Introduction

Enlarging therapeutic effects of anticancer drugs has become the holy grail of oncotherapy, thereby paving the way for the development of drug-delivery systems (DDSs) in cancer treatment[1-4]. Multitudes of delivery scaffolds ranging from liposomes[5], microspheres[6], dendrimers[7], polymeric drug conjugates[8], polymeric micelles[9], and polymersomes[10-12] have been a subject of extensive clinical research. The rationale of loading therapeutics in delivery vehicles is to reduce systemic toxicity by shielding the drug against a plethora of plasma components during its transport via the bloodstream and later accumulating inside the target site leading to enhanced efficacy[13]. These biological barriers pose multiple threats to the stability and efficacy of the nanocarrier system. After having crossed such organ and sub-organ level barriers, the nanocarriers are finally tested for their ability to enter the cells and unload the cargo upon reaching its subcellular destination. The performance and efficacy of a drug delivery system is subject to not just biological barriers as discussed above, both material design parameters are equally crucial in determining its efficacy. Material aspects such as the choice of the delivery scaffold, and its concomitant effects on drug efficacy is worth paying attention to improve the cancer treatment[14]. For instance, liposomal encapsulation of the chemotherapy drug doxorubicin (DOX) has shown considerable reduction in cardiotoxicity, simultaneously maintaining a high level of efficacy[15, 16]. Surprisingly, liposomal formulation of cisplatin-conjugated drug (SPI-77 or stealth cisplatin) showed rather poor efficacy owing to slow release inside the tumor[17, 18]. The problem of reduced efficacy due to poor uptake can be mitigated by a thoughtful choice of engineering the structural aspects of the nano scaffold. Sugars are ubiquitous to cell membranes, and hence, polysaccharide-based scaffolds such as dextran become candidates of choice as they are easily taken up by the cells owing to like–like interactions[8, 19-21]. The second problem of slower release kinetics inside the cells can be fine-tuned by the choice of the chemical linkages in DDSs. Employing pH-sensitive linkages such as oxime[22], imines[23], and acetals[24] and enzyme-sensitive linkages such as aliphatic esters[25, 26] offers release in a more controlled manner. Material aspects such as integrating the delivery scaffold with stimuli responsive units helps avoid unloading or premature release of cargo at undesired cellular locations. For this, drug delivery systems are equipped stimuli responsive handles such as enzyme, pH or light responsive materials to mention a few. The response of the nanocarriers under such

stimuli conditions is decisive in regulating its cargo release which is manifested in its efficacy. However, real time drug release from nanocarrier under the cellular stimuli is rather scarce. To understand the efficacy of a drug delivery system within cells, it is apparent that real-time monitoring of nanoparticle transport to subcellular compartments is necessary. Furthermore, simultaneous real-time monitoring of its stimuli-mediated cargo release abilities is essential. We intended to answer these two questions by designating an esterase responsive polysaccharide based polymersomes. Polymersomes are important classes of DDSs due to their unique capability to load both water-soluble and -insoluble drug molecules[1, 27, 28]. These polymersomes were tagged with a fluorophore that can further help shed light on its intracellular journey following cellular uptake[29, 30]. Therefore, next-generation polymer nanocarriers are required to create a smart self-reporting system, while they administrate the drug molecules. DDSs employing aggregation-induced emission (AIE)gen such as tetraphenylethylene (TPE) have recently gained considerable attention in bioimaging applications[31-34]. Conventional fluorophores or dyes typically undergo aggregation-caused quenching (ACQ) owing to strong π–π stacking in water, thereby limiting their usage in bioimaging applications[35]. AIEgens display fluorescence in highly aggregated states due to restriction of intramolecular rotation (RIM), thereby augmenting their usage in biological imaging[36]. From our research group, we have reported a renewable resource[37] approach to develop polysaccharide polymersomes for targeted and combination therapy of wide ranges of anticancer drugs[27, 38-43]. AIE-based polymersomes were reported in the past for material application in CO_2 capture; [44, 45] however, they are very rarely explored in biomedical research[46]. Self-reporting enzyme-responsive and AIEgen polysaccharide DDSs capable of loading a multitude of drugs with unperturbed efficacies are rather scarce in the literature. We therefore designed an esterase responsive polysaccharide based polymersomes system which was decorated with tetraphenylethylene TPE, an AIE active luminogenic. Herein, we report a polysaccharide (dextran)-based scaffold tagged with an AIE chromophore, TPE, which behaves as an excellent self-reporting nano assembly for drug delivery as shown in Figure 1. Dextran was conjugated with renewable 3-pentadecylphenol (PDP) and TPE via ester linkages and the resultant amphiphile was self-assembled into fluorescent polymersomes in water of size less than 200 nm. Uptake of polymersomes via endocytosis was very well-monitored due to its intrinsic blue luminescence via confocal microscopy. It is crucial for nanocarrier to indeed land up in the lysosomes to realize the stimuli responsive Behaviour of polymersomes, by the action of lysosomal esterase. Evidently, the

endocytosed polymersomes ended up in the lysosome compartment of the cells which was confirmed by study colocalization with lysosome staining dye, Lysotracker. We exploited the vesicular nature of the polysaccharide nanocarrier by loading it with rhodamine, which formed a FRET pair with TPE. We monitored the enzyme responsiveness of the nanocarrier and subsequently its ability to release dye through changes in FRET readout.

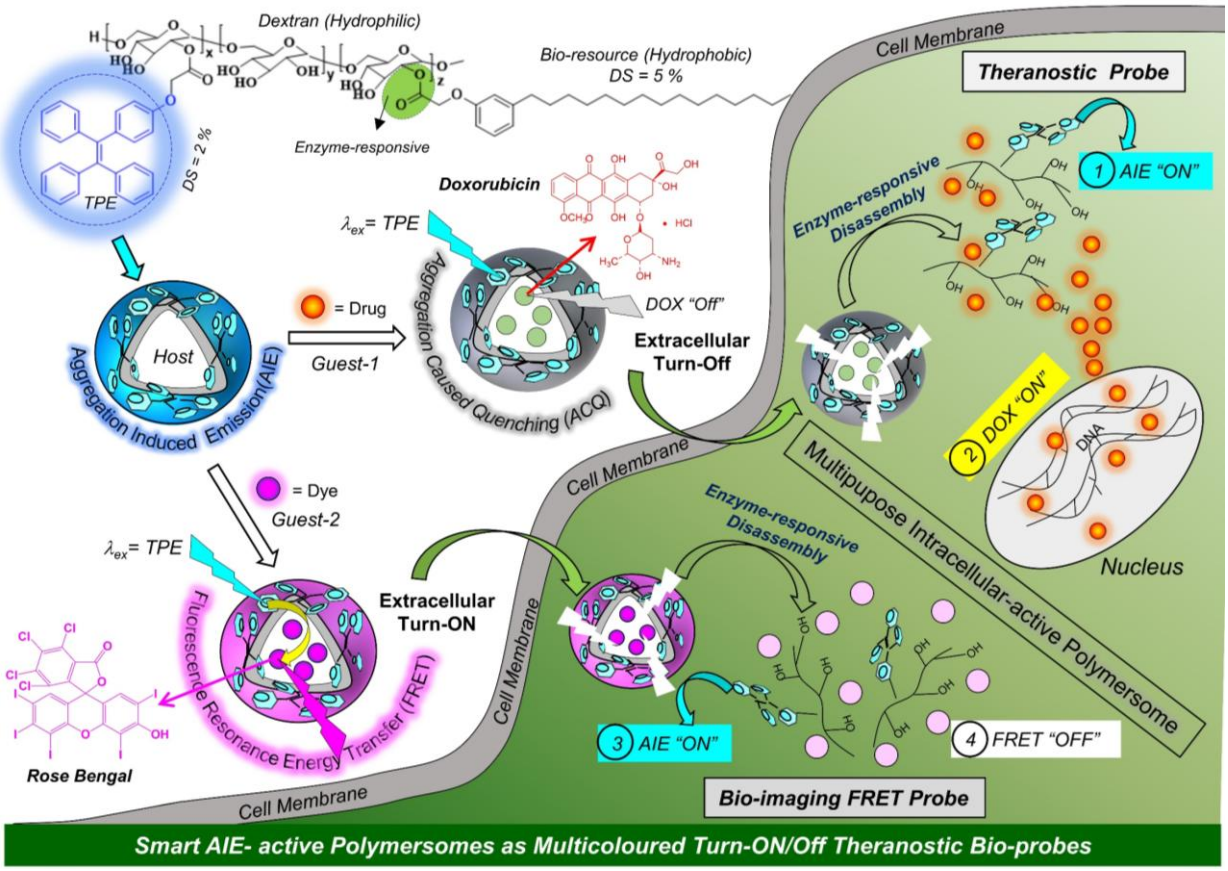

Figure 2.1: *Schematic showing the enzyme responsiveness of* P_{TPE+RB} *and* $P_{TPE+DOX}$ *inside the cells.*

After having established the enzyme responsive Behaviour of polymersomes by real time monitoring of its cellular journey, we next employed these polymersomes to load a commercially relevant anti-cancer drug, doxorubicin and understand its programmed release from nanocarrier in real time. Interestingly, TPE and Dox formed a FRET pair and led to a dark state in which the fluorescence of both the TPE donor and Doxorubicin was quenched.

2.3 Experimental Section

2.3.1 *Materials*

Benzophenone, 4-hydroxy benzophenone, Zinc powder, titanium tetrachloride, 3-Pentadecylphenol (PDP), Ethyl chloro acetate, triethylamine (TEA), dextran (mol. Wt 6000), dicyclohexyl carbodiimide (DCC), 4-dimethylamino pyridine (DMAP), doxorubicin hydrochloride (DOX), dextran (molecular weight = 6000 g/mol), nile red, rosebengal, dimethyl sulfoxide (DMSO) and horse liver esterase enzyme, O-methyl-D-glucose were purchased from Aldrich chemicals. Dialysis tubing (MWCO 3500 Da) was purchased from spectrum chemicals. NaOH and all other necessary reagents and solvents were purchased locally and purified following the standard procedures. PDP acid (compound **4**) was made by following the procedure reported in our earlier reports[27, 38]

2.3.2 *Instruments*

NMR spectra were recorded using a 400 MHz Jeol and 100-MHz Bruker NMR spectrometer using $CDCl_3$ or DMSO-d6 containing a small amount of TMS as an internal standard. The electronic spectra were recorded using Perkin-Elmer Lambda 45 UV−visible, and a Fluorolog HORIBA JOBIN VYON fluorescence spectrophotometer. Confocal microscopic images were recorded using LSM10 Confocal Microscope. The mass analysis of the compounds was carried out using high-resolution mass spectrometry (HRMS-ESI-Q-TOF LC-MS) and Applied Bio system 4800 PLUS matrix-assisted laser desorption/ionization (MALDI) TOF/TOF analyzer.

2.3.3 *Methods*

2.3.3.1 *Synthesis of 4-(1,2,2-triphenylvinyl) phenol (TPE-OH)*

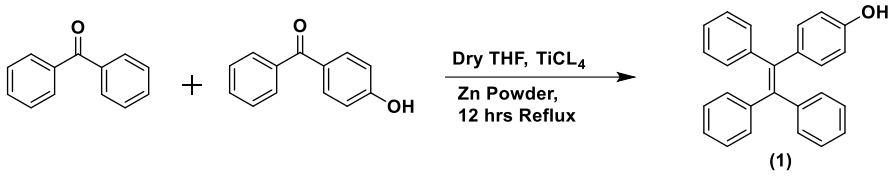

(1)

In a 250 mL round bottom flask, benzophenone (10.00 g, 55 mmol), 4-hydroxy benzophenone (10.50 g, 53 mmol), and Zinc powder (9.25 g, 142 mmol) were dissolved in 100 mL of dry THF while maintaining a temperature of 0 ºC under nitrogen purging. The reaction mixture was stirred for 0.5 hours, following which titanium tetrachloride (12.50 g, 66 mmol) was added dropwise at a temperature below 10 ºC. Subsequently, the reaction mixture was allowed to reach ambient temperature and then heated to reflux for 12 hours. After completion of the reflux, the mixture was cooled to room temperature, and THF was evaporated under reduced pressure. To the resulting residue, 100 mL of dilute hydrochloric acid (0.1 N) was added. The product was then extracted using ethyl acetate, dried over sodium sulfate, and subjected to purification by passing it through a silica gel column (100-200 mesh) using a solvent mixture of 5-15% ethyl acetate in petroleum ether. Yield =5.6 g (32 %). ^{1}H NMR (400 MHz, $CDCl_3$) δ ppm: 4.76 (s, 1 H, Ar-OH) 6.54 - 6.60 (m, 2 H) 6.88 - 6.94 (m, 2 H) 7.01 - 7.08 (m, 6 H) 7.08 - 7.15 (m, 9 H).^{13}C NMR (100 MHz, $CDCl_3$)δ ppm: 76.69 (s, 1 C) 77.32 (s, 1 C) 114.56 (s, 1 C) 126.24 (s, 1 C) 126.35 (s, 1 C) 127.58 (s, 1 C) 127.69 (s, 1 C) 131.31 (s, 1 C) 131.34 (s, 1 C) 132.71 (s, 1 C) 136.33 (s, 1 C) 140.14 (s, 1 C) 140.39 (s, 1 C) 143.86 (s, 1 C) 143.96 (s, 1 C) 153.95 (s, 1 C). MALDI-TOF: (MW: 348.15) m/z: 371.09 ($M+Na^+$). HR-MS (ESI+): m/z [M + H+] Calculated for $C_{26}H_{20}O$ [M+] = 348.1600; Found =348.1516.

2.3.3.2 *Synthesis of Ethyl 2-(4-(1,2,2-triphenylvinyl) phenoxy) acetate (TPE- Ester)*

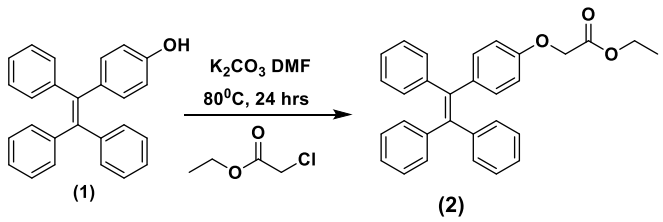

Compound 1 (5.00 g, 15 mmol) and K_2CO_3 (2.97 g, 22 mmol) were dissolved in 80.0 mL of acetonitrile and stirred at 80 ºC for 0.5 hours. Following this, the reaction mixture was cooled to room temperature, and ethyl chloro acetate (2.39 g, 15 mmol) was added dropwise. Subsequently, the mixture was heated at 90 ºC for 12 hours. Upon completion of the reaction time, the mixture was allowed to cool to room temperature, and K_2CO_3 was removed by filtration. The acetonitrile solvent was then concentrated under reduced pressure. The resulting product was extracted using ethyl acetate and dried over sodium sulfate. The crude product underwent purification by passing

it through a silica gel column (100-200 mesh) using a solvent mixture of 3-5% ethyl acetate in petroleum ether. Yield= 4.0 g (65 %).^{1}H NMR (400 MHz, $CDCl_3$) δ ppm:1.30 (t, 3 H) 4.28 (q, 2 H) 4.56 (s, 2 H) 6.67 (m, 2 H) 6.97 (m, 2 H) 7.01 - 7.08 (m, 6 H) 7.08 - 7.18 (m, 9 H).^{13}C NMR (100 MHz, $CDCl_3$)δ ppm:14.12 (s, 1 C) 61.27 (s, 1 C) 65.29 (s, 1 C) 76.69 (s, 1 C) 77.32 (s, 1 C) 113.74 (s, 1 C) 126.26 (s, 1 C) 126.36 (s, 1 C) 127.56 (s, 1 C) 127.68 (s, 1 C) 131.26 (s, 1 C) 131.32 (s, 1 C) 132.52 (s, 1 C) 137.11 (s, 1 C) 140.20 (s, 1 C) 140.36 (s, 1 C) 143.72 (s, 1 C) 143.78 (s, 1 C) 143.82 (s, 1 C) 156.25 (s, 1 C) 168.84 (s, 1 C).MALDI-TOF: (MW: 434.19) m/z : 473.09 ($M + K^+$). HR-MS (ESI+): m/z [M + H+] Calculated for $C_{30}H_{26}O_3$ [M+] = 435.1978; found =435.199.

2.3.3.3 *Synthesis of 2-(4-(1,2,2-triphenylvinyl) phenoxy) acetic acid (TPE-Acid)*

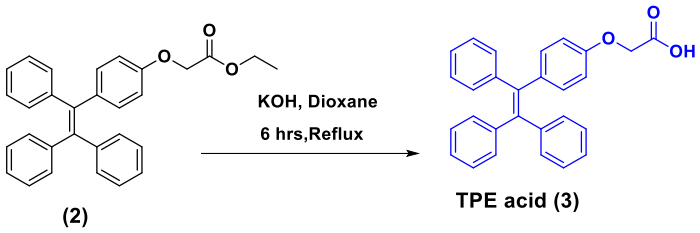

In a revised sequence, Compound 2 (4.00 g, 9.2 mmol) and KOH (1.55 g, 28.0 mmol) were dissolved in 50 mL of dioxane. The resulting mixture was refluxed for 6 hours. After completion of the reflux, the reaction mixture was allowed to cool to room temperature, and the dioxane solvent was removed under reduced pressure. The solid compound obtained was then dissolved in water, and the pH was adjusted to 6.0 using dilute hydrochloric acid (0.1 N). The product was subsequently extracted using ethyl acetate. The crude product was subjected to purification by passing it through a silica gel column (100-200 mesh) using a solvent mixture of 20-40% ethyl acetate and petroleum ether. Yield = 3.6 g (98 %). ^{1}H NMR (400 MHz, $CDCl_3$) δ ppm:4.63 (s, 2 H) 6.64 - 6.70 (m, 2 H) 6.95 - 7.00 (m, 2 H) 7.01 - 7.07 (m, 6 H) 7.08 - 7.17 (m, 9 H).^{13}C NMR (100 MHz, $CDCl_3$)δ ppm: 64.35 (s, 1 C) 76.36 (s, 1 C) 76.68 (s, 1 C) 113.42 (s, 1 C) 125.99 (s, 1 C) 126.03 (s, 1 C) 126.09 (s, 1 C) 127.27 (s, 1 C) 127.30 (s, 1 C) 127.40 (s, 1 C) 130.95 (s, 1 C) 130.99 (s, 1 C) 132.34 (s, 1 C) 137.25 (s, 1 C) 139.74 (s, 1 C) 140.24 (s, 1 C) 143.34 (s, 1 C) 143.40 (s, 1 C) 143.43 (s, 1 C) 155.46 (s, 1 C) 173.79 (s, 1 C).MALDI-TOF: (MW: 406.16) m/z :

445.06 ($M + K^+$).HR-MS (ESI+): m/z [M + H+] Calculated for $C_{28}H_{22}O_3$ [M+] = 406.1600; found = 406.1572.

2.3.3.4 *Synthesis of PDP and TPE substituted dextran derivative*

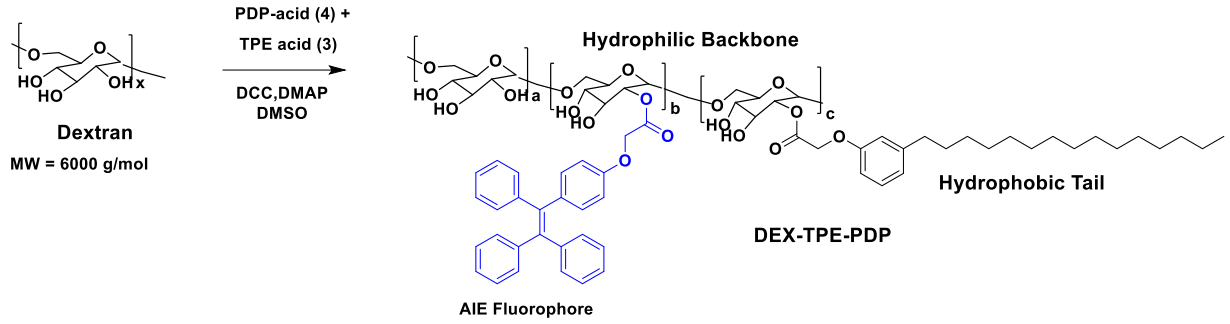

The procedure involved dissolving 1.00 g of dextran (6.10 mmol), 0.56 g of PDP Acid (1.55 mmol), and 0.15 g of TPE-Acid (0.37 mmol) in 25.0 mL of dry DMSO within a 100.0 mL round bottom flask. Subsequently, the reaction mixture underwent nitrogen purging for 0.5 hours. In parallel, 0.19 g of dimethyl amino pyridine (DMAP) (1.55 mmol) and 1.33 g of dicyclohexyl carbodiimide (DCC) (6.45 mmol) were individually dissolved in dry DMSO. These solutions were then added to the reaction mixture, which was allowed to proceed for 24 hours at 37°C. Following this, dicyclohexyl urea was removed via filtration, and vacuum distillation was employed to eliminate the DMSO. The resultant mixture was precipitated in methanol and underwent purification through a series of methanol precipitations after dissolving in a small volume of DMSO.Yield = 0.70 g (48 %). ^{1}H NMR (400 MHz, DMSOd6) δ ppm:δ 7.14-6.99 ppm (m, 10H, Ar−H), 6.98-6.95 ppm (m, 6H, Ar−H),6.88-6.86 ppm (t, 2H, Ar−H), 6.71-6.68 ppm (m, 5H, Ar−H) 4.63 ppm (s, dextran anomeric proton), 4.47, 4.82, 4.88 ppm(s, hydroxyl of dextran),3.14−3.69 ppm (dextran glucosidic protons), 2.49 ppm (2H, Ar−CH_2), 1.48 ppm (2H,Ar−CH_2−CH_2), 1.18−0.80 ppm(aliphatic protons).

2.3.3.5 *Synthesis of Methyl 4,6-O-Benzylidene-α-D-Glucopyranoside (Sugar derivative- 1)*

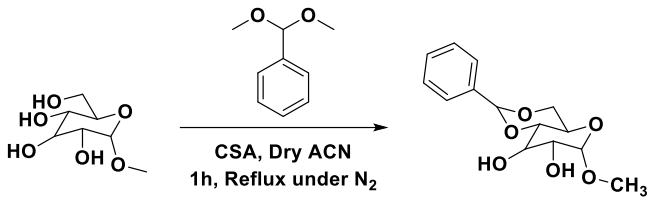

This experiment was carried out via following a reported procedure for unrelated compound[47]. Methyl α-D-glucopyranoside (3 g, 15.46 mmol) was taken in a 100 mL round bottom flask, followed by the addition of 30 mL of acetonitrile. To above suspension was added, benzaldehyde dimethyl acetal (4.44 mL, 29.43 mmol) and 90 mg of CSA (10-camphorsulfonic acid). The system was then refluxed for 1 h under nitrogen. The reaction was allowed to cool at room temperature followed by the addition of 0.5 mL of triethylamine. The solvent was removed under vacuum followed by Ethyl acetate and water workup. The solid compound was dissolved into 30 mL of ethyl acetate and washed several times with water. The organic layer was then dried over anhydrous Na_2SO_4. The solution was then concentrated under vacuum to give thick syrup which was precipitated in DCM and Hexane (1:8). The solid was then filtered and dried under vacuum to afford product 2 in 89% yield. (^{1}H NMR (400 MHz, $CDCl_3$) δ ppm: 7.50 (m, 2 H, aromatic) 7.37 (m, 3H, aromatic) 5.54 (s, 1 H) 4.81 (d, 1 H) 4.32 (dd, 1H) 3.94 (t, 1 H) 3.82-3.79 (m, 1H) 3.78- 3.73 (m, 1 H) 3.65 (m, 1 H) 3.53 (t, 1H) 3.47 (s, 3 H, OMe) 2.78 (bs, 1H, -OH) 2.78 (bs, 1H, -OH). ^{13}C NMR (100 MHz, $CDCl_3$) δ ppm: 129.24 (aromatic, 1 C) 128.31 (aromatic, 1 C) 126.28 (aromatic, 1 C) 101.92 (1 C, CHPh) 99.75 (1 C, C1) 80.91 (1 C, C4) 72.85 (1 C, C2) 71.71(1 C, C3) 68.90 (1 C, C6) 62.34 (1 C, C1) 55.54(1C, C5). MALDI-TOF: (MW: 282.29), m/z $(M + H)^+$: 283.18

2.3.3.6 *Synthesis of (4aR,6S,7R,8R,8aR)-7-hydroxy-6-methoxy-2-phenylhexahydropyrano[3,2-d][1,3]dioxin-8-yl 2-(3-pentadecylphenoxy)acetate (Sugar derivative-2, 3)*

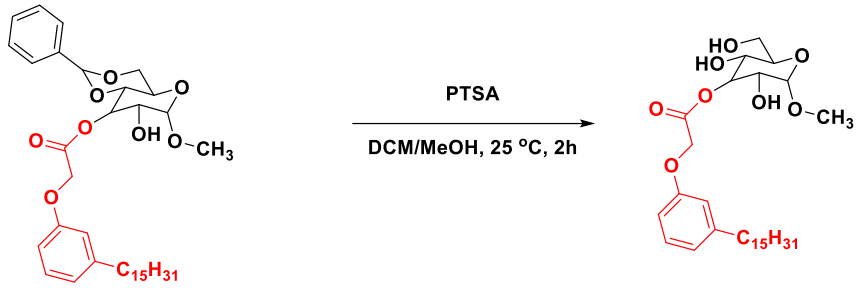

To a 100 mL 2 neck round bottom flask, compound **1** (0.5g, 1.77mmol), PDP- COOH (compound-4) (0.64g, 1.77mmol), EDC.HCl (0.35g, 3.5mmol), DMAP (44mg, 0.35 mmol) were taken and kept at high vacuum prior to reaction for 30 minutes. The system was removed off the vacuum and freshly dried DCM was added at 0°C under nitrogen atmosphere. The stirring was continued for 30 minutes at 0°C and then the reaction was continued for 12 hours at room temperature under nitrogen atmosphere. After 12 hours the reaction was stopped and works up was done with 10% $NaHCO_3$ solution (1X 100 mL). The organic layer was extracted and then washed with water (2X 100mL). The organic layer was the dried over anhydrous Na_2SO_4. The solution was evaporated under reduced pressure to give the crude product. Column Chromatography in 230-400 mesh silica was done to extract Sugar derivative- 3 as a crystalline white solid (0.26g). (^{1}H NMR (400 MHz, $CDCl_3$) δ ppm: 7.45-7.43 (m, 2 H, aromatic) 7.38-7.35 (m, 3H, aromatic) 7.03 (t, 1 H) 6.78- 6.76 (m, 2 H) 6.67- 6.64 (dd, 1H) 5.48- 5.43 (s +t, 2 H) 4.83 (d, 1H) 4.68- 4.69 (s, 2 H) 4.33- 4.30 (dd, 1 H) 3.92- 3.88 (m, 1H) 3.79- 3.73 (t, 1 H,) 3.68 (m, 1H,) 3.64 (t, 1H), 3.49 (s, 3H, -OMe), 2.54 (t, 2H), 1.26 (broad multiplet, 24 H), 0.89 (t, 3H). ^{13}C NMR (100 MHz, $CDCl_3$)δ ppm: 169.46 (1 C), 158.10 (1 C), 145.06 (1 C), 137.16 (1 C), 129.43 (1 C), 128.57 (1 C), 126.49 (1 C), 122.19 (1 C), 115.66 (1 C), 111.44 (1 C), 101.85 (1 C), 100.32 (1 C), 73.46 (1 C), 78.73 (1 C), 71.85 (1 C), 69.16 (1 C), 65.59 (1 C), 63.01 (1 C), 55.92 (1 C), 36.19 (1 C), 32.22 (1 C), 31.57 (1 C), 21.99 (1 C), 23.00 (1 C), 14.43 (1 C), MALDI-TOF: (MW: 626.83) ,m/z $(M + K)^+$: 665.4315, m/z $(M + K)^+$: 649.5124.

Small amount of 2,3-substituted ester (Sugar derivative- 2) was also successfully isolated and its NMR spectrum is given in the latter pages.

2.3.3.7 *Synthesis of (2R,3R,4S,5R,6S)-3,5-dihydroxy-2-(hydroxymethyl)-6-methoxytetrahydro-2H-pyran-4-yl 2-(3-pentadecylphenoxy) acetate (Sugar derivative-4, model compound)*

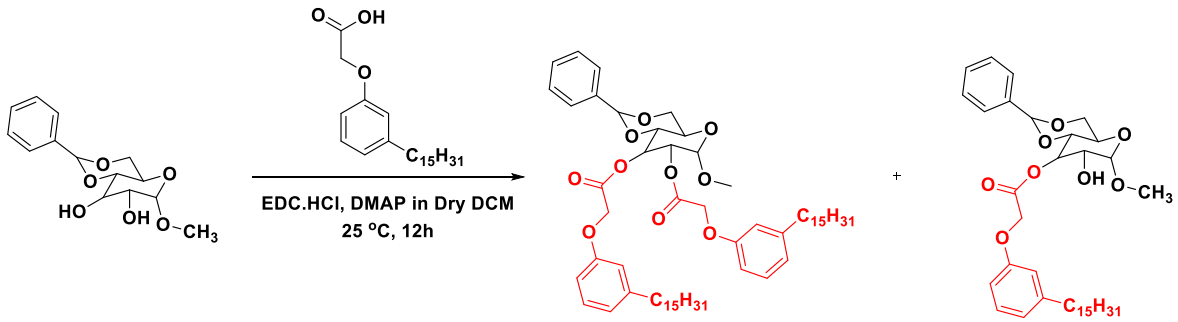

To a 25 mL RB, compound 6 (100 mg, 0.159mmol) and Para-toluene sulphonic acid (PTSA, 10mg, 0.3, 0.004 mmol) were taken. To it was added 10 mL of (1:1) DCM/MeOH. The system was stirred at room temperature for 2 hours. After 2 hours, triethylamine was added to quench PTSA. The solvent was distilled under reduced pressure to afford yellowish white solid. The impure compound was then subjected for column chromatography in 100- 200 mesh silica using 1% MeOH in DCM as eluent. The product was isolated as crystalline white solid (47mg, 56%).(^{1}H NMR (400 MHz, $CDCl_3$) δ ppm: 7.13-7.09 (t, 1 H, aromatic) 6.76-6.74(d, 1H, aromatic) 6.7- 6.69 (m, 1 H) 6.66- 6.63 (m, 1 H) 5.13- 5.09 (t, 1 H) 4.71 (d, 1H) 4.66 (s, 2 H) 3.78-3.75 (m,2 H) 3.58-3.57 (m, 2H) 3.53- 3.51 (m, 1 H,) 3.38 (s, 3H,) 2.51-2.47 (bs+t, 1H+2H), 2.10 (d,1H), 1.18 (24 H, b-multiplet), 0.83- 0.79 (t, 3H). ^{13}C NMR (100 MHz, $CDCl_3$)δ ppm: 170.51 (1 C), 157.71 (1 C), 145.05 (1 C), 129.33 (1 C), 122.15 (1 C), 115.09 (1 C), 111.32 (1 C), 99.38 (1 C), 71.28 (1 C), 70.78 (1 C), 68.80 (1 C), 65.39 (1 C), 62.01 (1 C), 55.51 (1 C), 35.97 (1 C), 31.95 (1 C), 29.72 (1 C), 22.71 (1 C), 14.14 (1 C) MALDI-TOF: (MW: 538.6) ,m/z $(M + K)^+$: 577.6

2.3.3.8 *In Vitro Drug Release Studies by dialysis method*

In vitro doxorubicin released from the fluorescent dextran vesicles was monitored using dialysis method described in our earlier report[40]. Typically, 3.0 mg of DOX loaded dextran vesicles were taken in dialysis bag (MWCO 3500) in immersed in 10.0 mL of PBS at 37°C. To determine the dox concentration in the dialysate, 3.0 mL of dialysate was withdrawn periodically and absorbance

was measured to calculated the amount of dox released. The percent cumulative release was calculated following the equation. A similar protocol was followed to monitor the esterase enzyme action on the dox release.

Cumulative Release = amount of drug release at time t/ total amount of drug taken in dialysis tube *100

2.3.3.9 *Cell Viability Assay and Cellular imaging*

A cell viability assay was performed in MCF 7, WTMEF cells using the tetrazolium salt, 3-4,5 dimethylthiazol-2,5-diphenyl tetrazolium bromide (MTT) to compare the cytotoxicities of free drug and drug loaded vesicles.1000 cells per well were seeded in 96 well plate in 100 µL of complete DMEM and allowed to adhere for 16 h. Different concentrations of the free drug and drug encapsulated vesicles were then added to the cells and incubated for another 72 h. Thereafter the media was aspirated and 100 µL of freshly prepared MTT solution (0.5 mg/ mL in complete media) was added and incubated for another 4h at 37 °C. The formed formazan crystals were dissolved in 100 µL of DMSO and the absorbance was immediately measured using varioscan micro plate reader at 570 nm. The data represents the mean value from at least three independent measurements. The relative percentage values, with respect to control, were calculated and plotted against the concentration. To envision the intracellular fate of free drug and drug loaded vesicles, cells were seeded at a density of 10^5 cells per well on 6 well-plates containing 2.0 mL of complete DMEM medium and incubated at 37 °C for 16 h. After 16 h, media was aspirated and cells were fed with 2.0 mL media having required concentration of the compounds. After incubating for 9 h, the media was removed and cells were washed using 1X PBS two times following the permeabilization using 4.0 % paraformaldehyde solution. After staining cells with necessary dyes, the cover slips were mounted on the surface of clean and flamed dried slides using 10% glycerol as mounting and were left to dry overnight at room temperature, away from light. The slides were then imaged using a confocal microscope employing 405 nm and 568 nm lasers as excitation sources. Image J software was used for processing the images. All the confocal images are recorded keeping all the parameters same for every measurement. DOX fluorescence intensity from the confocal images was calculated in Image J analysis software using the following equation:

Corrected Total Cell Florescence (CTCF) = Integrated Density – [Area of selected cell x Mean fluorescence of background reading]

2.3.3.10 *Tissue Culture Conditions*

Breast cancer cells (MCF 7) and wild type MEF (WTMEF) were cultured in complete DMEM media (with 5% fetal bovine serum (FBS) and 1% penicillin-streptomycin) at 37°C under 5% CO_2 humidified atmosphere. Cells were detached using trypsin and seeded in 60mm dishes or flasks as per requirement.

2.3.3.11 *Phalloidin Staining of the Polymersomes*

About 10^5 cells were seeded on 70% alcohol rinsed and flame dried coverslips and were placed carefully in a 6 well plate supplemented with DMEM media and 10 % FBS. The setup was incubated at 37 ºC for 16h in a 5% CO2 atmosphere. A lyophilized powder of P_{TPE} containing 1μM of the fluorophore and P_{RB} containing 5μM of fluorophore was added independently in two different wells of the 6 well chambers and were further incubated for 4h at ambient conditions. The media was aspirated followed by the washing of cells with cold PBS solution (3 X 1mL). The coverslips having cells were chemically fixed using 4% paraformaldehyde solution in PBS for 10 minutes at 4ºC. Next, the cells were gently washed twice with 1mL cold PBS solution. Cells were then stained with Alexa Flouro-488 Phalloidin and kept at a dark place for 5 minutes at room temperature. The unbound dye was washed off of the coverslips by treating it twice with 1 mL cold PBS solution. The coverslips were gently mounted in an inverted position onto a clean and flame dried glass slide using a drop of 10% glycerol solution as contact media. The coverslip was then sealed onto glass slide using transparent nail paint. CLSM imaging was carried using a confocal assisted microscope engaging 405 nm, 488nm and 568nm lasers respectively. A smart setup was created to avoid the spectral spill over. Images acquired were then processed using ImageJ software.

2.3.3.12 *Live cell imaging Protocols*

For a time dependent live cell experiment, 25000 cells per well were seeded in a 4 well chamber for 16 hours in a CO2 incubator maintained at 37^0C. The chamber was then placed on a Stage top incubator of a Zeiss Multiphoton instrument (Verdi/Mira 900; Coherent), maintaining a CO_2 humidified atmosphere at 37^0C. The image focus (using DIC) at 40X oil immersion and other

acquisition parameters were adjusted prior to compound addition. After the compound addition ($P_{TPE+DOX}$) to the first well, images were immediately acquired after 1 min, 5 min, 20 min, 45 min, and 60 min (lower time points) in the same ROI, focusing at the same cells (in one well only). Subsequently second, third and fourth wells were added with the compound and imaged at 2h, 3h and 4h (higher time points) respectively using a 405 nm and 488 nm laser respectively. For P_{TPE+RB} the compound was pre incubated for 24h, 12, 6h, 3h, 2h, 1h prior to imaging. For lower time point, compound addition was done on the stage top incubator and images were subsequently acquired using 405 and 561 nm laser respectively.

2.3.3.13 *Enzyme Degradation Studies of Model Compound-8*

Compound degradation in presence of esterase enzyme was studied following a reported protocol for unrelated ester compound[48]. K_2HPO_4 (0.88 mg) was dissolved in 900 µL of D_2O (solution-1). Horse liver esterase enzyme (0.1 mg) of was then dissolved and warmed to 37 ^oC for 2 minutes. Compound-8 (10 mg) was dissolved in 100 µL of acetone- d^6 and was then added to 900 µL of enzyme containing solution-1. The system was allowed to equilibrate for 5 minutes at 37^oC and then NMR was recorded. The same sample was then incubated at 37^oC for 12 hours and was then subjected for NMR analysis. (Note: Water suppression was not carried out as it would suppress the peaks of interest in its vicinity).

2.4 Result and Discussions

2.4.1 *Synthesis and characterization of DEX-TPE-PDP*

For the synthesis of AIE functionalized dextran derivative, monomers were first synthesized following literature procedures. Tetraphenylethylene (TPE) was synthesized with a carboxylic acid handle which could later be used to couple with the dextran polymeric background as shown in Figure 2.2. For this, benzophenone and 4-hydroxy benzophenone (1 : 1 mole ratio) were coupled using $TiCl_4$ and zinc powder to obtain 4-hydroxyl tetraphenylethylene (**1**). Compound (**1**) was then further alkylated using ethyl chloroacetate to get the TPE carboxylic ester (**2**) which was hydrolyzed to yield the TPE-carboxylic acid (**3**). 3-Pentadecylphenol from the cashew nut shell liquid was substituted using ethyl chloroacetate followed by hydrolysis to get the PDP carboxylic acid (**4**) following a reported procedure. PDP is known as a vesicle director. The anchorage of hydrophobic PDP group to the hydrophilic dextran backbone by ester[27] or imine[38] linkage was

shown previously by our group to yield perfect amphiphilic system that self-assembles to form vesicles[27, 38].

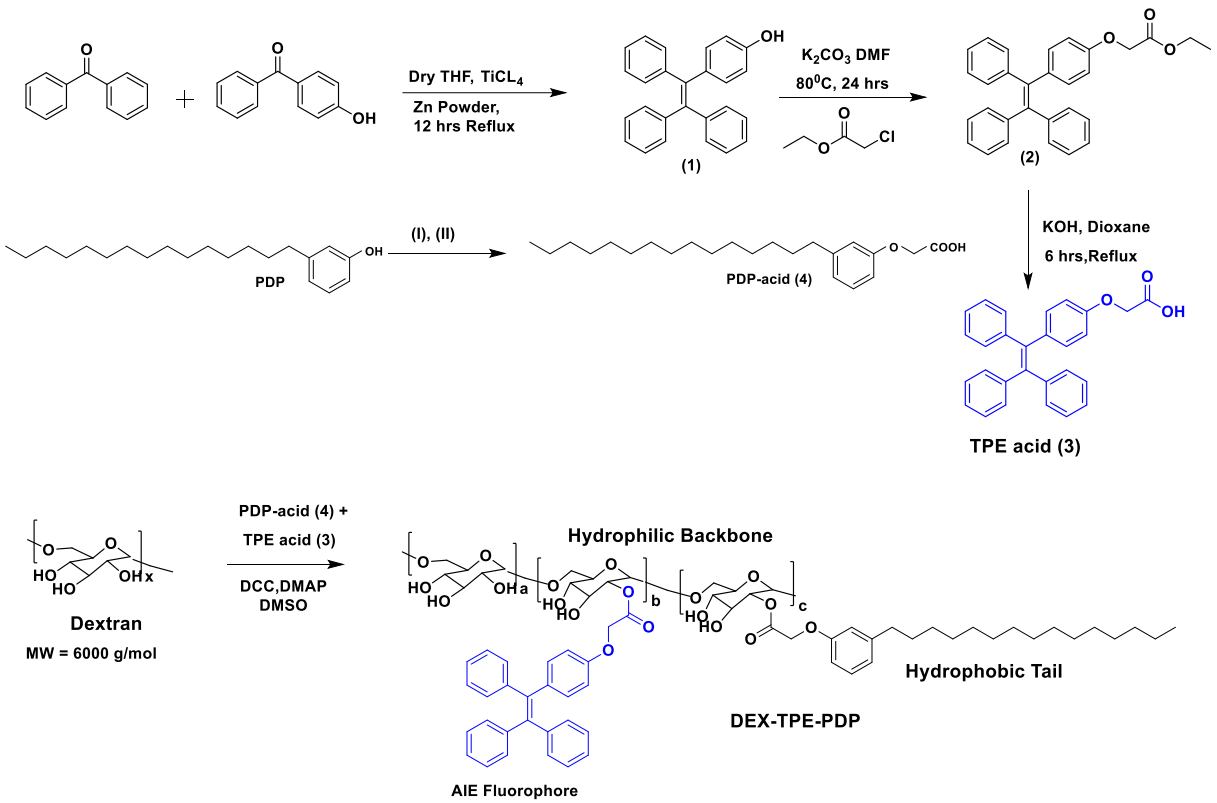

Figure 2.2*: Synthesis of small molecules and Dex-TPE-PDP.*

The synthesized TPE acid (**3**) and PDP acid (**4**) were anchored simultaneously on the dextran (polysaccharide, MW = 6000 g mol^{-1}) backbone in a one pot esterification reaction to yield TPE-conjugated amphiphilic dextran; DEX-TPE-PDP. The structure of the polymer was characterized by ^{1}H-NMR and the details are given in Figure 2.3 The substitution of the TPE unit on the dextran backbone was evident from the presence of peaks from 6.6 to 7.2 ppm with respect to the aryl-protons. The PDP aromatic protons merged with TPE units in the polymer spectrum, whereas the peaks with respect to the alkyl tail were distinctly visible in the region 0.8 to 1.5 ppm. The degree of substitution of PDP and TPE units on the dextran backbone was determined by comparing the integration values of the anomeric proton with PDP or TPE protons. Degrees of substitutions were obtained as ~2% and ~5% for TPE and PDP units in the dextran backbone, respectively. Substitution of a higher amount of aryl units (>10%) produced the water insoluble dextran sample; thus, the total amount of TPE + PDP was maintained <10% in order to make modified dextran useful for biomedical application.

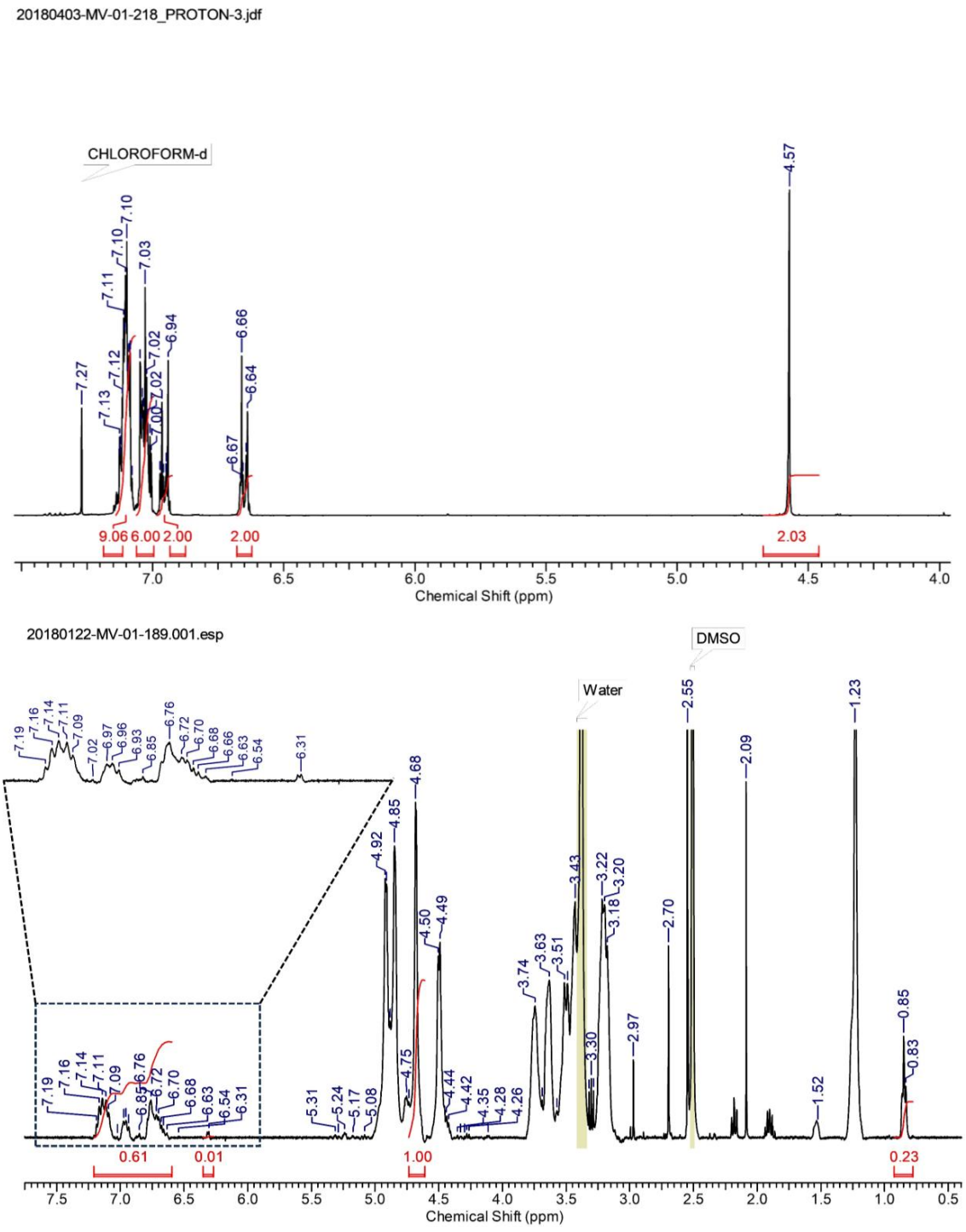

Figure 2.3: *1H NMR of TPE-COOH and DEX-TPE-PDP*

The increase in the hydrophobic content disturbs the self-assembly parameters, which leads to precipitation instead of forming vesicles in water.

2.4.2 *Self-Assembly of P_{TPE}*

Dialysis was employed to self-assembled the DEX-TPE-PDP derivative to form P_{TPE}. DEX-TPE-PDP shows monomeric emission when dissolved in organic solvent such as DSMO, but its monomeric emission starts to decrease and blue AIE emission originates as the result of formation of self-assembly in water as seen in Figure 2.4b.

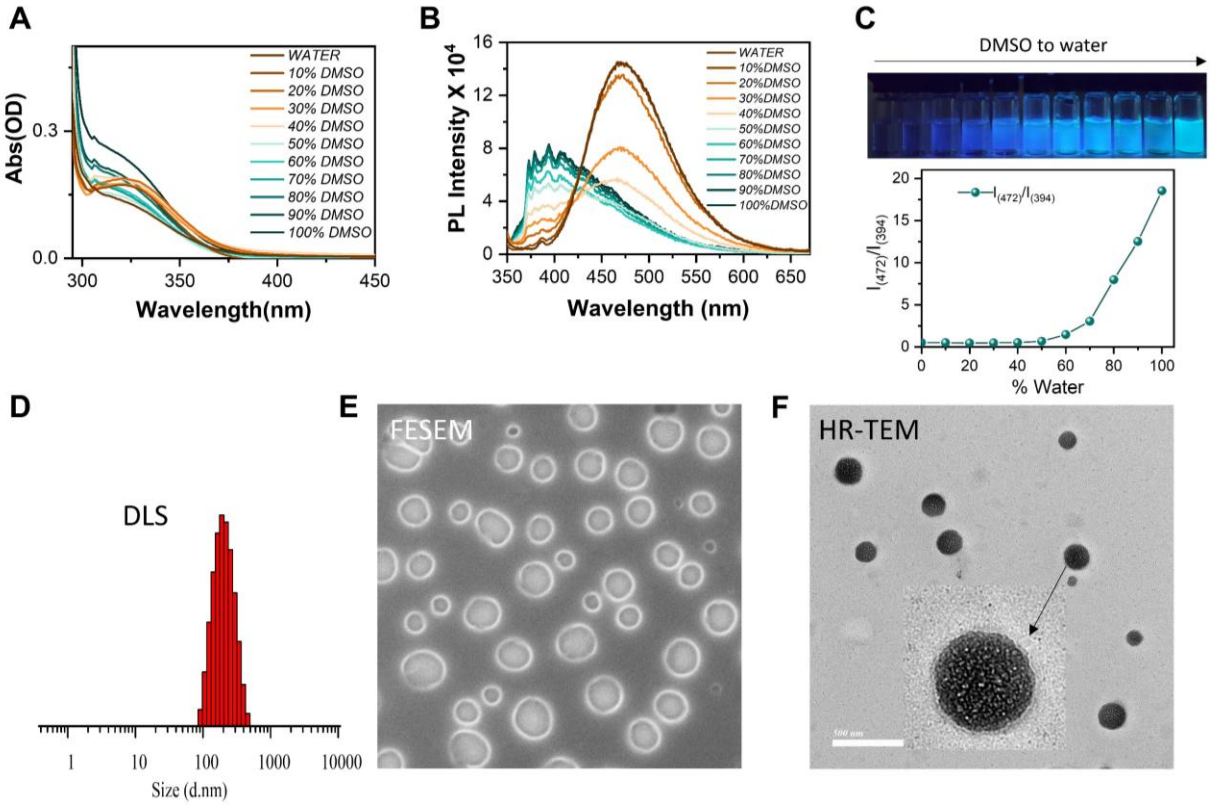

Figure 2.4: *Self-assembly of P_{TPE} in water.* ***A:*** *Absorbance and* ***B:*** *fluorescence profile of P_{TPE} in various compositions of DMSO and water.* ***C:*** *Ratio of AIE intensity to monomer intensity vs. composition shows a clear break point at around 60 percent of water.* ***D:*** *DLS,* ***E:*** *FESEM, and* ***F:*** *HR-TEM of P_{TPE} in water.*

This is evident from red shift in the absorption spectra which shifts towards red side and broadens as water is added to it as shown in Figure 2.4a. The break point is observed upon plotting the intensity ratio of two emissions vs. concentration as seen in Figure 2.4c. A clear increase in the blue emission is observed in the vials when the fraction of water increases beyond 40 percent

(Figure 2.4c). The formation of nanoparticles is confirmed by DLS which shows sizes of around 200 nm as seen in figure 2.4d. The formation of 200 nm vesicles is confirmed by FE-SEM which shows small vesicular hollow structures which is characteristic of these morphologies. HR-TEM corroborates with the FE-SEM data and confirms the vesicular morphology (Figure 2.4 e-f).

2.4.3 *Loading of Drug and Dyes in Polymersomes*

The next section briefly discusses the photophysical properties of the two systems which has been adapted from previous thesis from lab with DOI: http://hdl.handle.net/10603/448878.

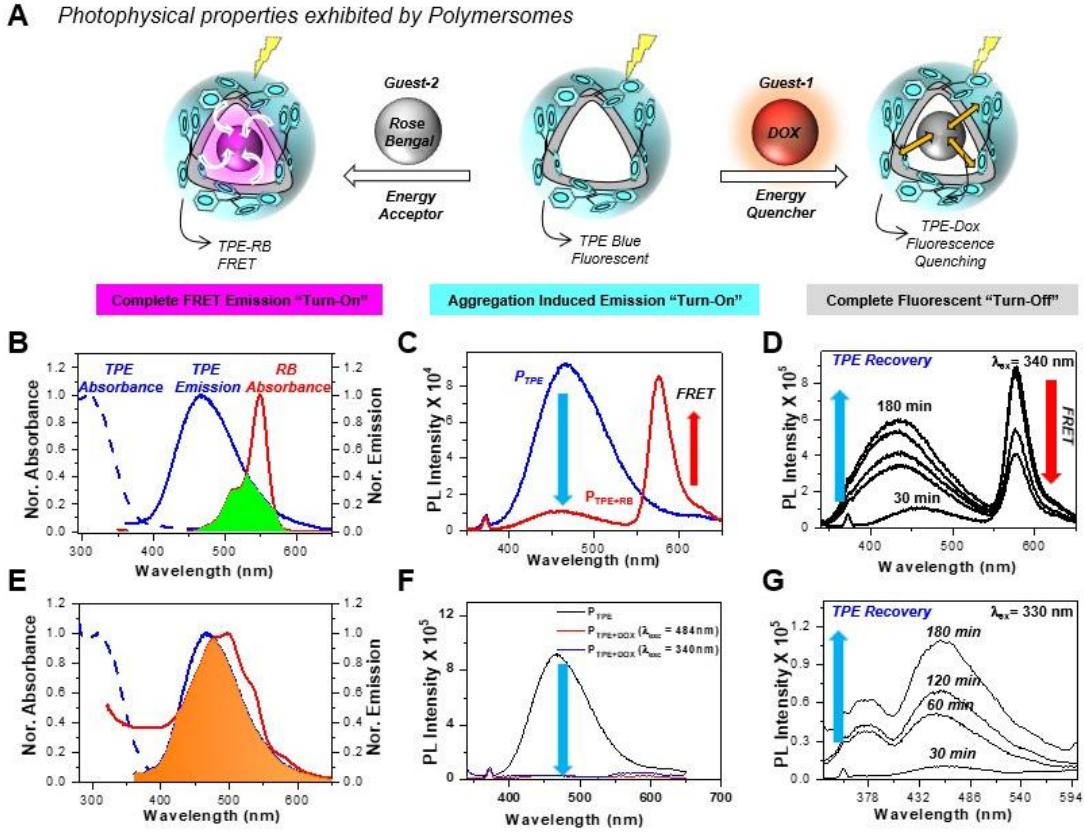

Figure 2.5: *The image is adapted from online repository (http://hdl.handle.net/10603/448878).* Photophysical properties of the P_{TPE+RB} and $P_{TPE+DOX}$. ***A:*** *Schematic showing the FRET of PTPE polymersomes with Rose Bengal and FRET mediated quenching of TPE with doxorubicin.* ***B:*** *Plot showing the absorbance of TPE and overlap of emission of TPE with absorbance of Rose Bengal.* ***C:*** *Plot showing FRET between TPE and Rose Bengal.* ***D:*** *Plot showing time dependent recovery of TPE emission and disappearance of FRET signal in presence of esterase enzymes.* ***E:*** *Plot showing the absorbance of TPE and overlap of emission of TPE with absorbance of Doxorubicin.* ***F:*** *Plot showing FRET between TPE and Doxorubicin resulting in dark pair and quenching of fluorescence.* ***G:*** *Plot showing time dependent recovery of TPE emission signal in presence of esterase enzymes for* $P_{TPE+DOX}$.

These structures were then loaded with a doxorubicin and Rose Bengal molecule which showed distinct photophysical properties as shown in Figure 2.5 a. The emission of TPE overlaps considerably with the absorbance spectra of both Rose Bengal and doxorubicin which are permissive to facilitate Forster resonance-based energy transfer; FRET as shown in figure 2.5b, e. Due to this overlap, both pairs showed FRET, however their emission properties were highly different. TPE shows FRET with Rose Bengal to give emission from rose Bengal. TPE shows FRET with Rose Bengal and showed red emission emanating from FRET acceptor Rose-Bengal due to energy transfer between TPE and Rose Bengal as shown in Figure 2.5c. Similarly, RB showed FRET with Doxorubicin, however no emission was seen from FRET acceptor doxorubicin, they both seem to form dark pair. Doxorubicin is known to form dark pairs with other fluorophore and with itself due to enhanced π-π interactions and leads to quenching of fluorescence emission[49, 50] as shown in Figure 2.5f. The intact assembly of polymersomes with Rose Bengal showed FRET, which can be modulated by disturbing the self-assembly. The changes in FRET emission such as decrease in the FRET emission and increase in the self-emission of TPE can serve as a readout for understanding the disassembly of polymersomes loaded with rose Bengal in presence of esterase enzyme as shown in figure 2.5d. Likewise, the disintegration of dark pair due to disassembly of polymersomes loaded with doxorubicin in presence of enzymes leads to recovery of both TPE and Doxorubicin emission as shown in figure 2.5g when excited using 330 nm. Hence, the time dependent recovery of both TPE and doxorubicin emission in presence of esterase enzyme serves as an excellent strategy to understand the drug release of polymersomes. Polymersomes retained their vesicular geometry even after encapsulation with drug and dye[46, 51].

2.4.4 *Confocal assisted monitoring of Self-assembly of P_{TPE+RB}*

Dialysis is a slow process which yields thermodynamically stable self-assembled structures which has been routinely used by our group to form highly reproducible vesicular assemblies of dextran. The vesicle morphology comprises of hydrophobic layer and a hydrophilic lumen. The vesicle formation is controlled by competitions between kinetics and thermodynamic parameters and overall free energy of the system then dictates this process[52]. We intended to capture the process of self-assembly and incorporation of dye molecules during this process of dialysis. A simple yet intuitive technique was followed to capture these highly dynamic structures. DEX-TPE-PDP was subjected to self-assembly in presence of Rose Bengal. Various aliquots were withdrawn and drop

casted on the glass surface to be observed under a confocal microscope. Owing to the dynamic nature of this process, they are rather difficult to capture and needs optimization in terms of concentration and time points of drop casting and time gap between sample drop casting and imaging.

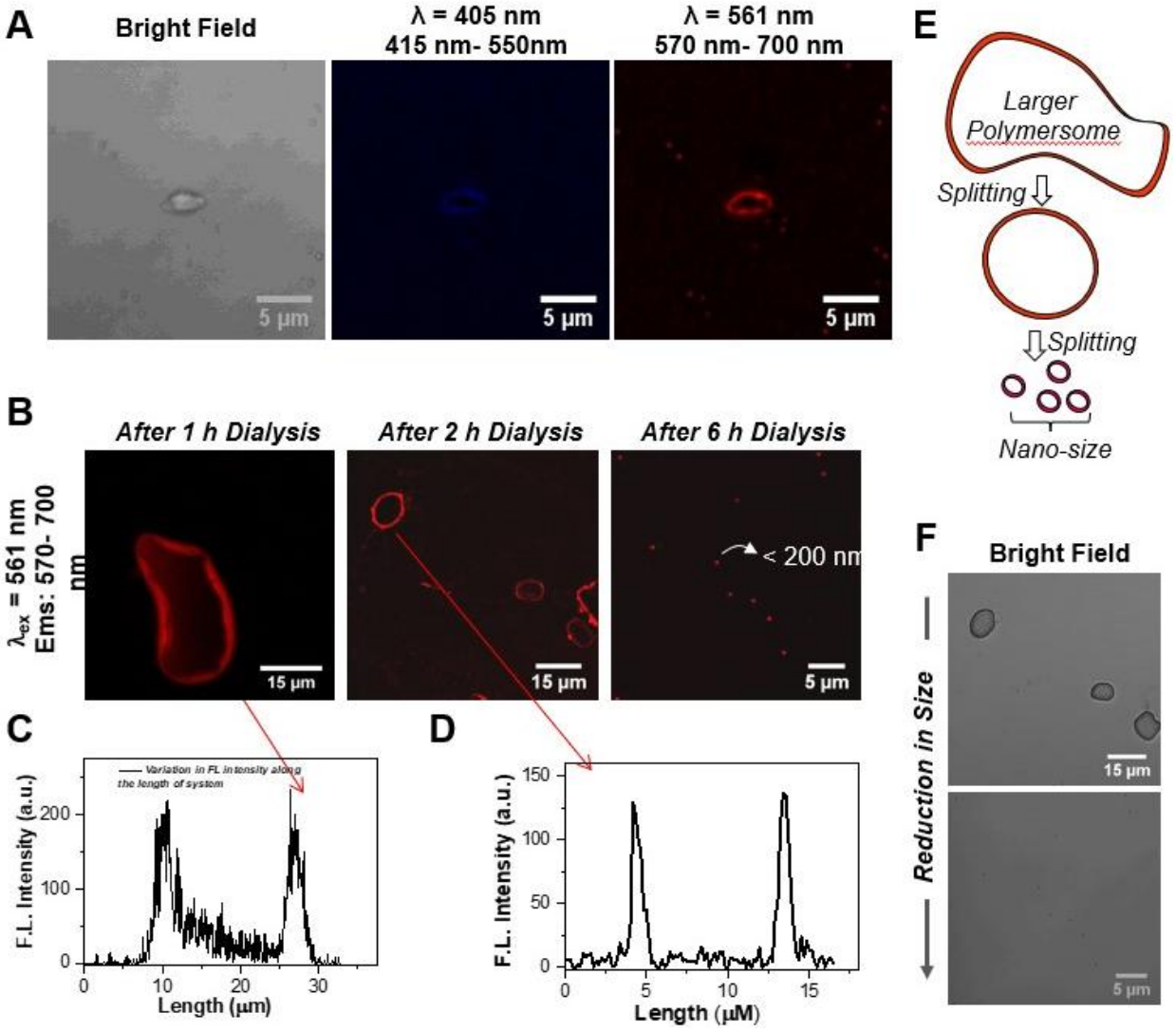

Figure 2.6: *Monitoring of Self Assembly of P_{TPE+RB} via confocal microscope imaging.* ***A:*** *P_{TPE+RB} forming a giant vesicle showing blue emission coming from TPE following excitation using 405 nm laser and red emission following excitation of Rose Bengal chromophore using 564 nm laser.* ***B:*** *Time dependent evolution of Self-assembly as monitored via exciting Rose Bengal.* ***C, D:*** *Intensity plots with distance.* ***E:*** *Cartoon representation showing the evolution of self-assembly.* ***F:*** *Bright field images showing reduction in size of self-assembled structures with time.*

Concentration of 5mg/mL was realized as optimal concentration wherein self-assembly happened and the sample concentration was sufficient to be observed under the microscope. Sample

preparation for confocal imaging was realized as the bottle neck to capture this dynamic structure, which were optimized after some trial and error. Empirically speaking, the process of self-assembly appears very alive which actively thrives in on aqueous milieu. The covering of sample with cover slips immediately after drop casting on glass slide and sealing the interface via transparent nail-paint, prevented drying of the sample and kept these dynamic equilibria functional which didn't halt the self-assembly process. First aliquot was withdrawn and drop-casted at roughly 1 hour. Large polymersomes were captured as seen in the bright field at the onset of self-assembly as seen in Figure 2.6a. Upon excitation using 405 nm laser, the blue emission of TPE came from the membrane of the giant vesicle as seen in Figure 2.6a. This indicates the presence of TPE in the membrane of vesicle, which appears intuitive as the self-assembly would have pushed the hydrophobic TPE fluorophore in the hydrophobic membrane. This confined location of TPE in the membrane would have restricted the intramolecular rotation of the TPE chromophores, resulting in AIE. Interestingly, upon exciting the Rose Bengal using 564 nm laser, the red emission came from the membrane as shown in Figure 2.6a. At first, this appears counter-intuitive for rose-Bengal is a water-soluble dye and hence should reside in the hydrophilic cavity. However, log P values suggests otherwise. Log P values of compounds are decisive in their localization of hydrophobic and hydrophilic rule where P= [Organic]/[Aqueous]. As per Lipinski's rule of 5, negative log P value is suggestive of affinity for hydrophilic phase, whereas positive log P value is indicative for affinity for hydrophobic phase. Log P value of near to zero is suggestive of amphiphilic nature of the molecule which partitions equally between organic and aqueous phase. Rose Bengal has log P value of 0.59 and has an equal propensity to reside in hydrophobic membrane or hydrophilic aqueous layer[53, 54]. With time a reduction in size of vesicular morphology was seen as seen in Figure 2.6b. A line drawn across the giant vesicle shows areas of high fluorescence intensity and depression in fluorescence intensity. The fluorescence intensity was seen highly concentrated in the membrane and absent in the polymersomes core as seen in Figure 2.6c, d. However, with increase in time, the structure became small to be resolved due to diffraction limit of light. The red fluorescence seems to be scattered all over the structure and exact location of emergence couldn't be identified. They appeared as tiny dots of size less than or close to 0.3 microns. Even in the bright field, the size was seen to be diminishing with increase in time as seen in Figure 2.6f. The self-assembly process was captured and is sown in the schematic, wherein large polymersomes vesicles converted to small vesicles as shown in Figure 2.6e. This presence of TPE

and rose Bengal in close vicinity of each other, possibly in the membrane would have facilitated the FRET between the two fluorophores as discussed in the next section.

2.4.5 *Release of cargo from Polymersomes*

This thesis chapter aimed at understanding the real time monitoring of polymersomes loaded with rose Bengal and doxorubicin inside cells.

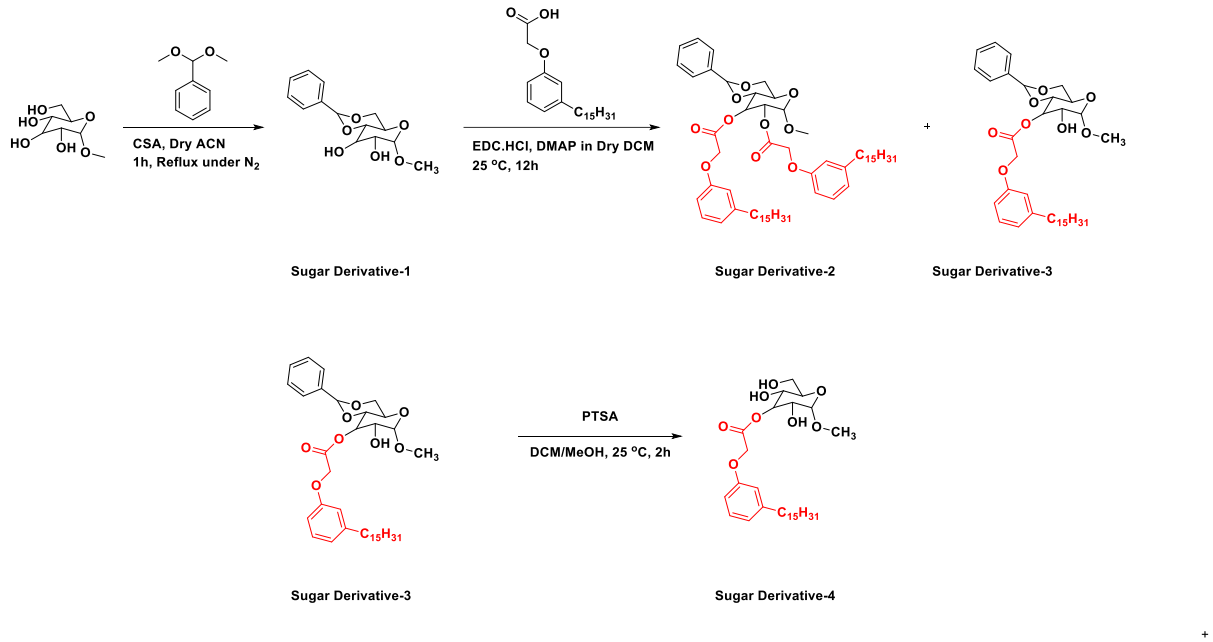

Figure 2.7: *Synthetic scheme for Model compound.*

In order for polymersomes show enzyme mediated drug or dye release, it becomes crucial for the polymersomes to reside into lysosomes. The action of lysosomal enzyme, esterase leads to break opening of the polymersomes and the subsequent release of the drug and dye molecule which can be understood from the changes in the quenching and FRET readout respectively. This would perhaps happen due to action of esterase which would cleave the ester bond and break open the polymersomes to release the drug or dye molecule. We checked this hypothesis by monitoring the hydrolysis of ester bond by recording 1H NMR at two time points. For this, a model compound as shown in Figure 2.7 was synthesized. Glucose conjugated with PDP was synthesized as model compound to check for the enzyme mediated hydrolysis of ester bond. Methyl α-D-glucopyranoside was converted to acetal protected sugar derivative-1 in presence of CSA and

benzaldehyde diacetyl. Next, esterification with PDP was carried on the remaining two -OH positions yielding a disubstituted and monosubstituted derivative sugar derivative 3.

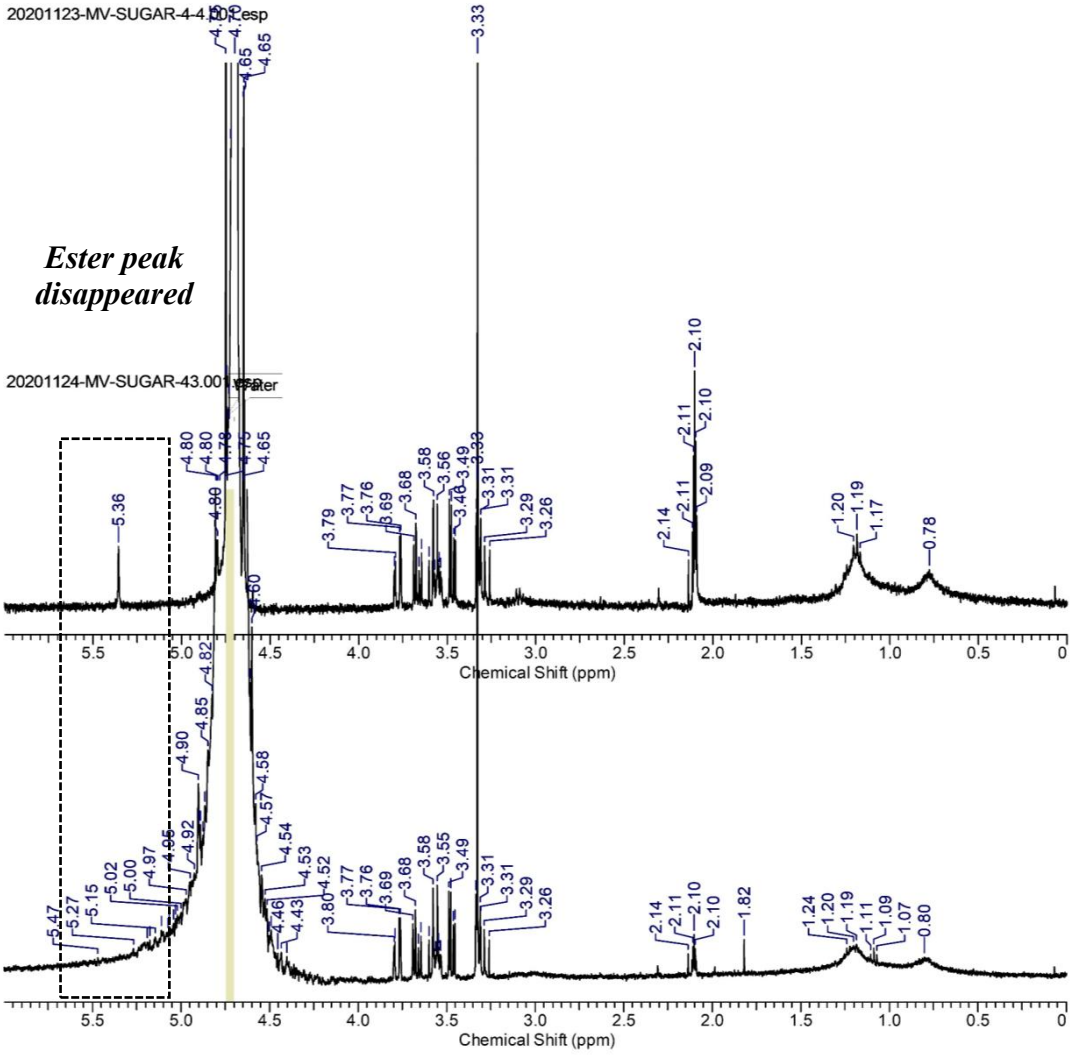

Figure 2.8: *1H NMR showing the response of model compound towards esterase*

The subsequent hydrolysis of sugar derivative 3 yielded sugar derivative- 4 which had similar ester linkage as that of DEX-TPE-PDP and hence was employed as a model compound to study the action of enzyme to cleave the ester bond. The model compound sugar-4 was subsequently treated with esterase in deuterated buffer and was NMR was recorded at t=0 and t= 4 hours as shown in Figure 2.8. A clear vanishing of ester peak was seen in the NMR, which concluded onto the enzyme

activity on the polymersomes to break them open and subsequently release the cargo. We also confirmed this process happening by monitoring the release of cargo by absorbance spectroscopy.

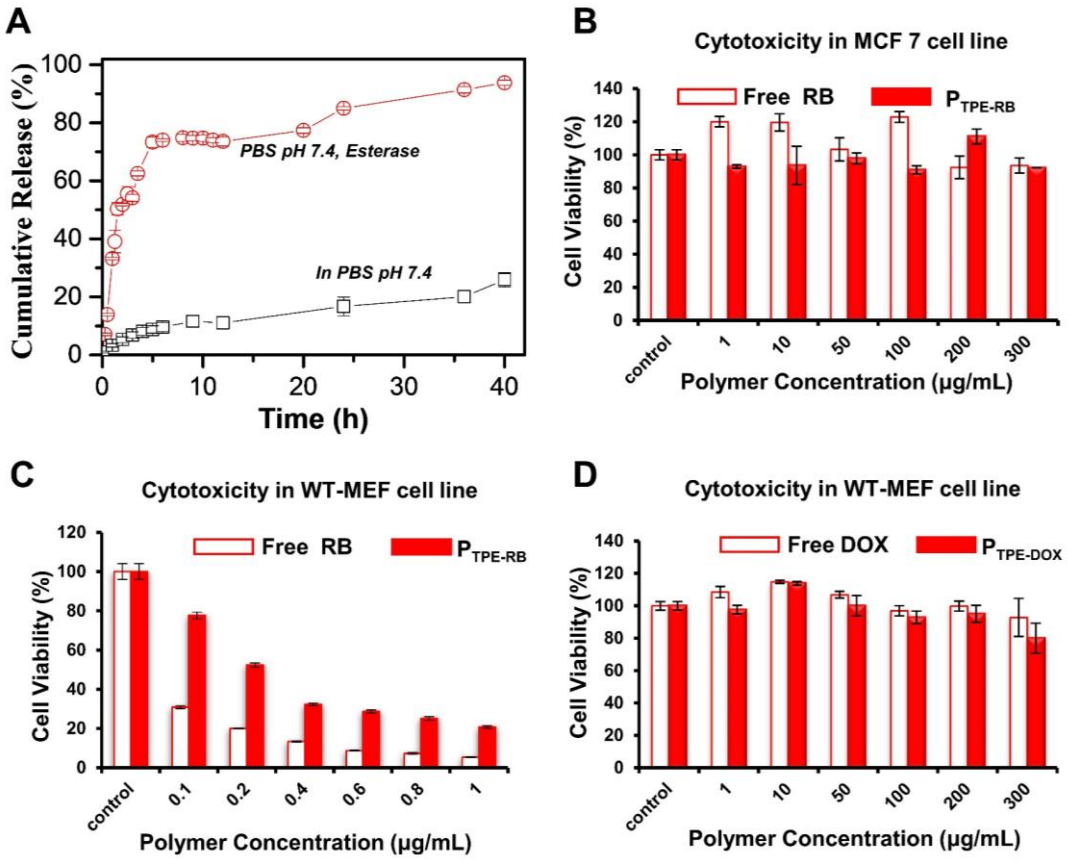

Figure 2.9: *Release and cytotoxicity data for polymersomes.* ***A:*** *Release data shown for* P_{TPE+RB}. ***B:*** *MTT data shown for* P_{TPE+RB} *in MCF 7 cells and* ***C:*** *WT-MEF.* ***D:*** *MTT data shown for* $P_{TPE+DOX}$ *in WT-MEF cells.*

We took P_{TPE+RB} as a representative to monitor the release of rose Bengal by monitoring changes in the absorbance spectra. Rhodamine was released from the polymersomes much faster as compared to PBS alone as shown in the Figure 2.9a. Having tested this, we conducted biological experiments. We stared the experiments by first checking for the cytotoxicity of both polymersomes system. P_{TPE+RB} was found to be extremely compatible with the cells as evident form its MTT data recorded both in MEF and MCF 7 cell lines as shown in figure 2.9b, c. The MTT data showed the efficacy of $P_{TPE+DOX}$ in decreasing the cellular viability, which was comparable to that of free drug as shown in Figure 2.9d.

2.4.6 *Lysotracker co-staining with Polymersomes*

The polymersomes were found to be highly compatible and showed excellent response to esterase.

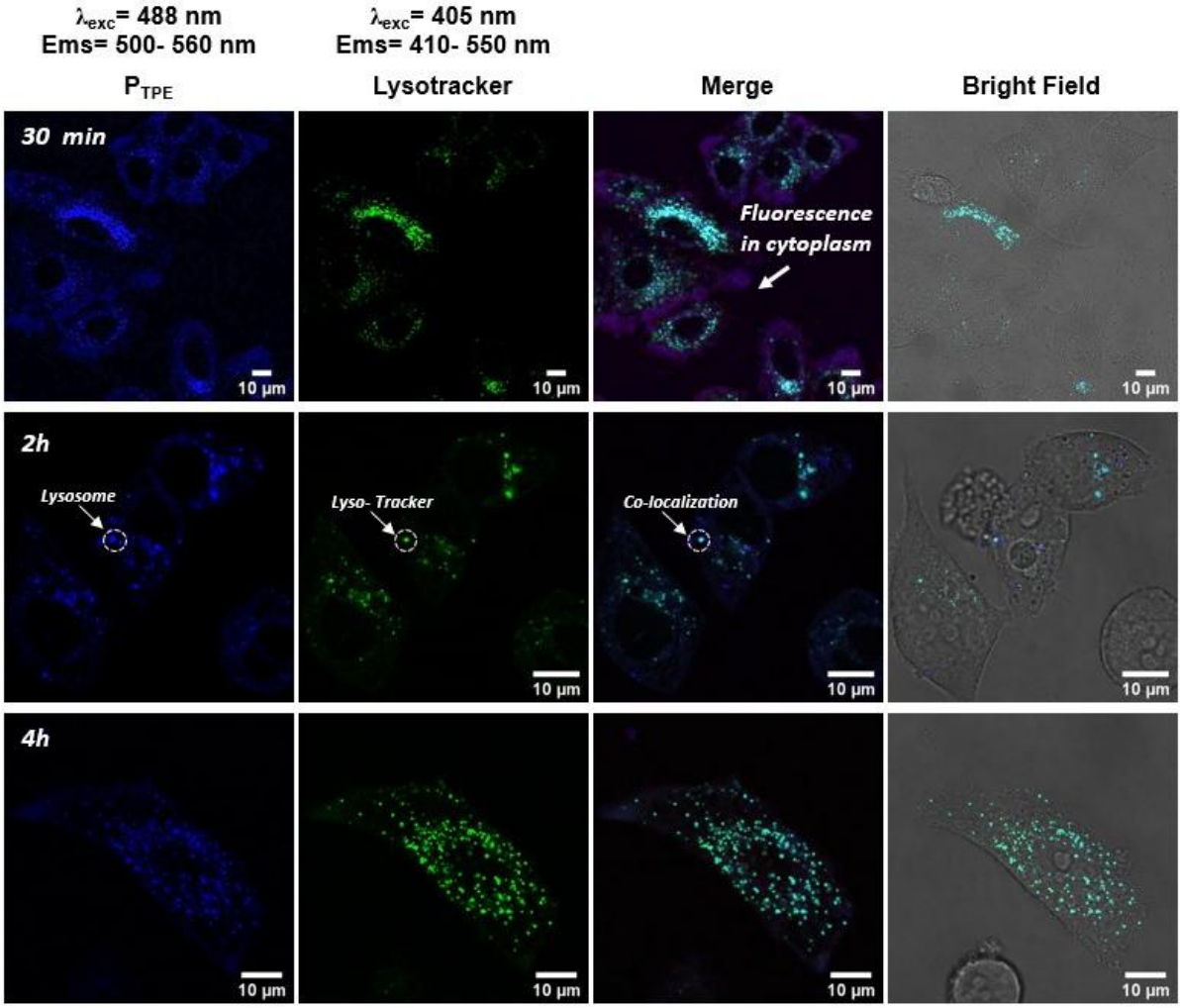

Figure 2.10: *Lysotracker colocalization with P_{TPE} at various time points.*

However, in order to show enzyme responsive action, it should first accumulate in lysosomes which are the store house of lysosomal esterase. Hence, it become important to understand first the localization of polymersomes inside the subcellular compartments. For this, we understood the subcellular localization of P_{TPE} alone since it is same delivery platform for both doxorubicin and Rose Bengal. At 30 minutes, the emission intensity of TPE was seen emanating from both discrete cellular organelles and the cytoplasm. The blue fluorescence intensity emanating from the discrete cellular organelles colocalized well with the fluorescence intensity emanating from lysotracker.

The co-residence of lysotracker green emission and blue emission of TPE from discrete cellular organelles implies that P_{TPE} localized in the lysosomes of the cells as shown in figure 2.10, first row 30 minutes data. However, the scattered fluorescence intensity in the cytoplasm disappeared in a time dependent manner. This is may be due to fact that during initial uptake, the P_{TPE} might be present in other cytosolic organelles like endosomes.

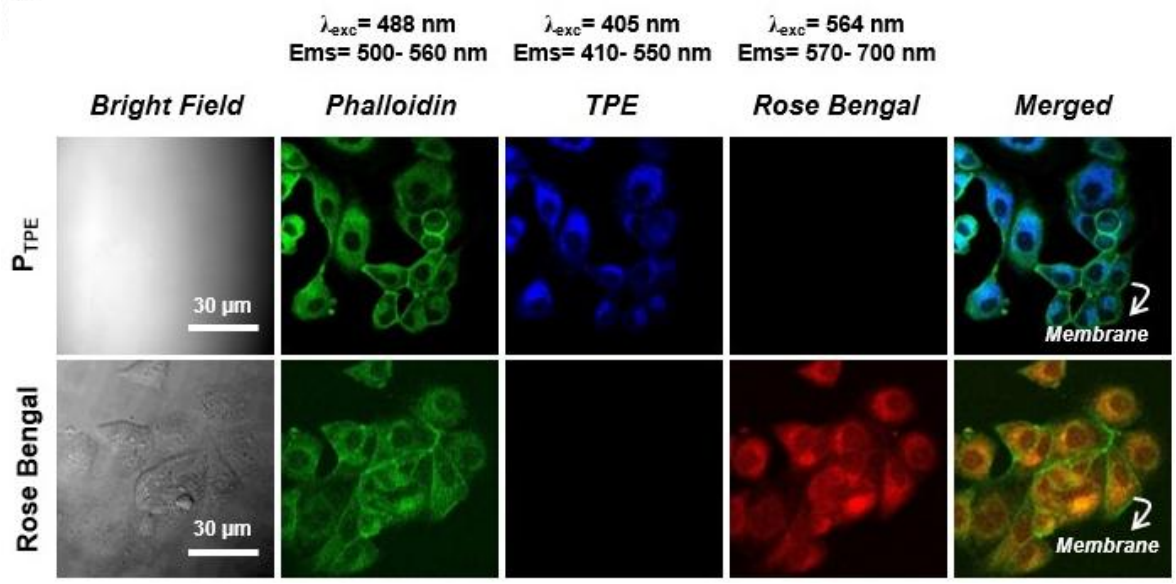

Figure 2.11: *Cellular imaging data for $P_{TPE+RB.}$* ***A:*** *MTT of $PTPE_{+RB}$ in MCF 7 and* ***B:*** *WT- MEF cell lines.* ***C:*** *Cellular imaging of P_{TPE} and Rose Bengal and its colocalization with Phalloidin Green.*

The lysosomes are the terminal stations of endocytosed cargo and therefore all the cargo moves from endosomes to lysosomes and it is due to this reason that the localization of P_{TPE} in discrete round shaped organelles increased with time as evident form enhanced colocalization of P_{TPE} blue emission with the green emission emanating from the lysotracker dye. There was a subsequent reduction in the localization of P_{TPE} in other cytosolic organelles as the time progressed from 30 minutes to 4 hours as P_{TPE} must have traversed in its endocytic trip form endosomes to their terminal station, lysosomes as the time progressed as shown in Figure 2.10. This experiment validated the fact that P_{TPE} indeed localized into lysosomes of the cells following its cellular uptake. This is very crucial for the polymersomes to transit to lysosomes of the cells. This is crucial and decisive in realizing the full potential of polymersomes to unload cargo at the cellular lysosomes. Before checking for their FRET emission in cells, we first checked and compared the emission behavior of P_{TPE+RB} and Rose Bengal at excitation using 405 nm and 565 nm. We also

wanted to see if nanoparticles entered the cell and populated the cytosolic organelles or instead stayed onto the cell periphery. It was seen that both PTPE and Rose Bengal didn't colocalize with phalloidin, simply assuring that both the nanoparticle and the dye smoothly entered the cells. It was seen that P_{TPE} upon excitation using 405 nm laser, shows emission only in TPE channel (410-550 nm) and showed no emission in the Rose Bengal channel (560- 700 nm) as shown in Figure 2.11. It is obvious for P_{TPE} to show no emission in the Rose Bengal channel, as there is no Rose Bengal in $P_{TPE.}$

Next, Rose Bengal upon excitation using 564 nm laser, shown only emission in the Rose Bengal channel and no emission was seen in the TPE channel. This experiment is important because it confirms that there is no spectral spillover of TPE into Rose Bengal channel upon excitation of TPE at 405 nm. Likewise, there is no spectral spillover of Rose Bengal emission into TPE channel upon excitation using 564 nm laser see Figure 2.11. This makes understand and interpret the FRET data better and points for presence for artifacts in the data, if any. For example, it might happen that because of spectral spillover of TPE emission in Rose Bengal channel, an emission in Rose Bengal channel can be misinterpreted for FRET. Hence, it is important to check for such spill overs. Now being sure of the emission range of TPE and Rose Bengal and the fact that are excited using their respective excitation wavelengths, now any emission in the Rose Bengal channel upon exciting TPE using 405 nm laser in P_{TPE+RB}, will indeed be due to FRET. A FRET channel is simply excitation of TPE fluorophore using 405 nm laser and looking for fluorescence emission form RB in red range. This excitation at 405 nm laser and collection of emission in red range (560- 700 nm) is therefore called as FRET channel. Although the collection range of both the FRET and red channel is same, the excitation wavelength is different, 405 nm for FRET channel and 564 nm for red channel. After having understood the annotation of FRET channel, we next conducted experiments to understand the FRET emission in P_{TPE+RB} by comparing it with $P_{TPE.}$

2.4.7 *FRET response of polymersomes in fixed cells*

P_{TPE} upon excitation using 405 nm laser showed emission only in the TPE channel as shown in Figure 2.12a. To our delight, the excitation of TPE chromophore in P_{TPE+RB} using 405 nm laser showed some emission in TPE channel and considerable emission in the FRET channel was also seen (see Figure 2.12a).

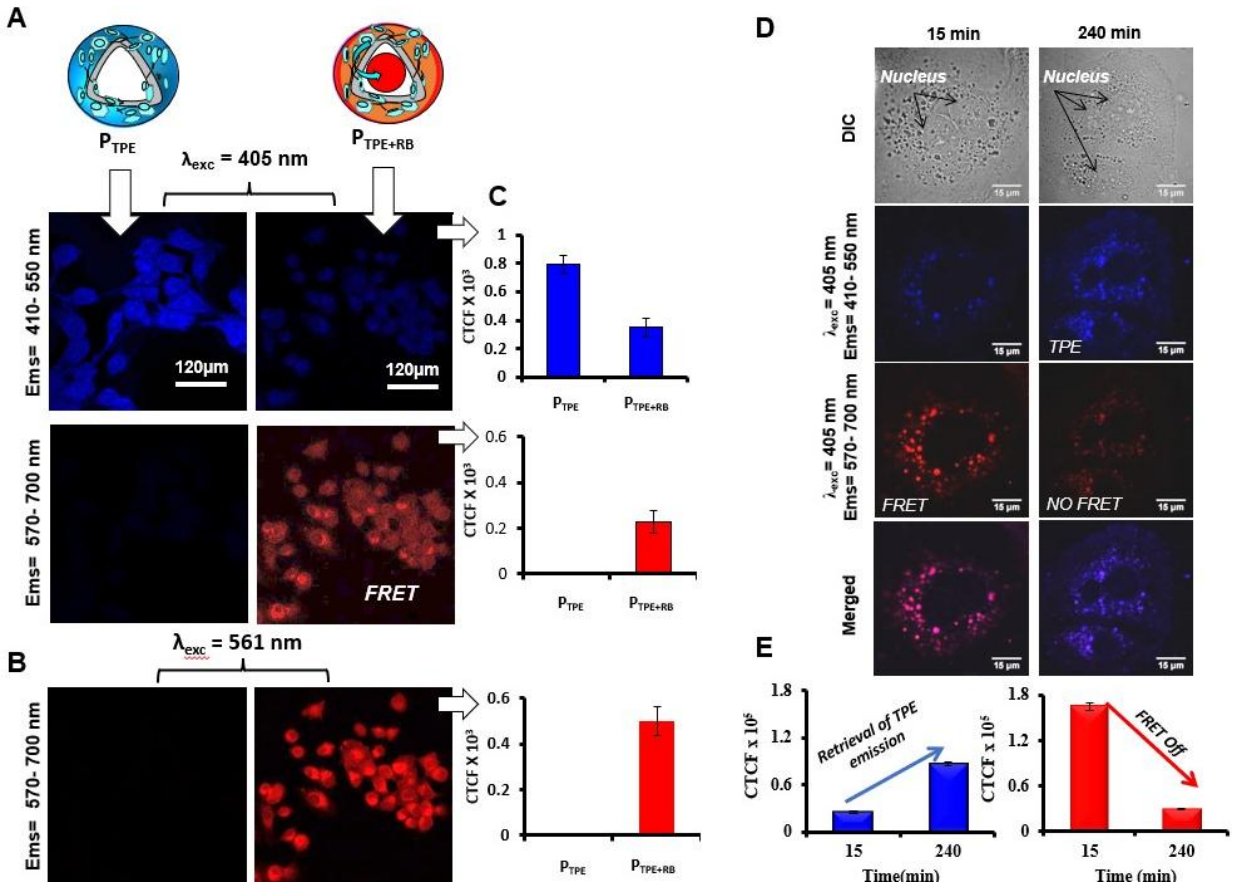

Figure 2.12: *Imaging of P_{TPE+RB} in MCF 7 cell lines.* ***A:*** *Confocal microscopy images for P_{TPE} and P_{TPE+RB} showing self and FRET emission when excited at 405 nm in the MCF 7 cell line.* ***B:*** *Images for P_{TPE+RB} showing self-emission when excited at 561 nm.* ***C:*** *CTCF intensities for self and FRET emission of P_{TPE} and P_{TPE+RB}.* ***D:*** *Time-dependent confocal microscopy images of P_{TPE+RB} polymersomes at various incubation times in the MCF 7 breast cancer cell line.* ***E:*** *Bar diagram showing the CTCF for the emission recovery of TPE and RB at various incubation times.*

The visual inspection parallelled with the quantified data upon comparing the CTCF of TPE channel in both P_{TPE+RB} and P_{TPE}. A lesser intense TPE emission was seen in P_{TPE+RB} as compared to P_{TPE} (see Figure 2.12c). This is obvious since, most of emission intensity of TPE in P_{TPE+RB} goes in energy transfer to excite Rose Bengal Chromophore. Likewise, no emission intensity was seen in the FRET channel of P_{TPE}, however substantial emission was seen in the FRET channel of P_{TPE+RB} (see Figure 2.12a). We also excited P_{TPE+RB} using 564 nm laser to specifically excite Rose Bengal to realize its full emission intensity. Interestingly, FRET intensities were found to be less than the fluorescence intensity in the red channel (see Figure 2.12b).

This is obvious for FRET emission to be less than self-emission of fluorophore upon exciting its absorbance maxima, since FRET is not 100 percent efficient. This means all the

molecules of Rose Bengal can't be excited following FRET which results in less emission in the FRET channel as compared to self-emission in the red channel (see Figure 2.12c). Next, we analyzed the time dependent esterase action on the FRET signal to validate the enzyme responsiveness of the enzyme. The fixed cell experiment was done before conducting the live cell experiments for two reasons: (i) to optimize and understand the time window in which the esterase mediated degradation of P_{TPE+RB} (ii) To understand the changes in the fluorescence signal, both FRET signal and self- emission of TPE with time and corelating with the process of disassembly and release of Rose Bengal. At 15 minutes, some intensity was seen in the TPE channel with considerable intensity seen in the FRET channel (see Figure 2.12d).

At 4 hours considerable enhancement of intensity in the TPE channel was seen and a concomitant reduction in the fluorescence intensity in the FRET channel was seen (see Figure 2.12d). A decrease in FRET signal with time and enhancement of intensity in the TPE channel points towards the breakage of FRET pair bought by the disassembly of P_{TPE+RB} which would decrease FRET emission and retrieval of self-emission of TPE. This also corroborated with quantification data which clearly showed decrease in FRET signal with concomitant enhancement in the TPE emission with time, which confirmed the enzyme mediated disassembly of P_{TPE+RB} as seen in Figure 2.12e. It also provided us a time window in which the process happened. Benefiting from this, we conducted live cell experiments to understand the enzyme responsive behaviors of P_{TPE+RB}.

2.4.8 *FRET response of Polymersomes in Live Cells*

Live cell experiments are more efficient and can give exact time points for a process which is otherwise difficult to rationalize or deduce under fixed cell conditions. Based on this we recorded the images at smaller time intervals. The time series generated showed a clear enhancement in the fluorescence intensity in the TPE channel and a concomitant reduction of intensity in the FRET channel (see Figure 2.13a). This trend points towards the steady action of enzyme on P_{TPE+RB} which lead to disassembly of the P_{TPE+RB} and release of Rose Bengal from its confined space. The CTCF quantification revealed the onset of this process at 2 hours, which peaked around 6 hours' time point and eventually became stagnant (see Figure 2.13b). We realized 2 to 3-hour time was crucial to populate P_{TPE+RB} in lysosomes and the realize the enzyme action to unload the cargo from

delivery scaffold. This information is crucial from a clinical perspective which makes it understanding of the efficacy of delivery scaffold easy.

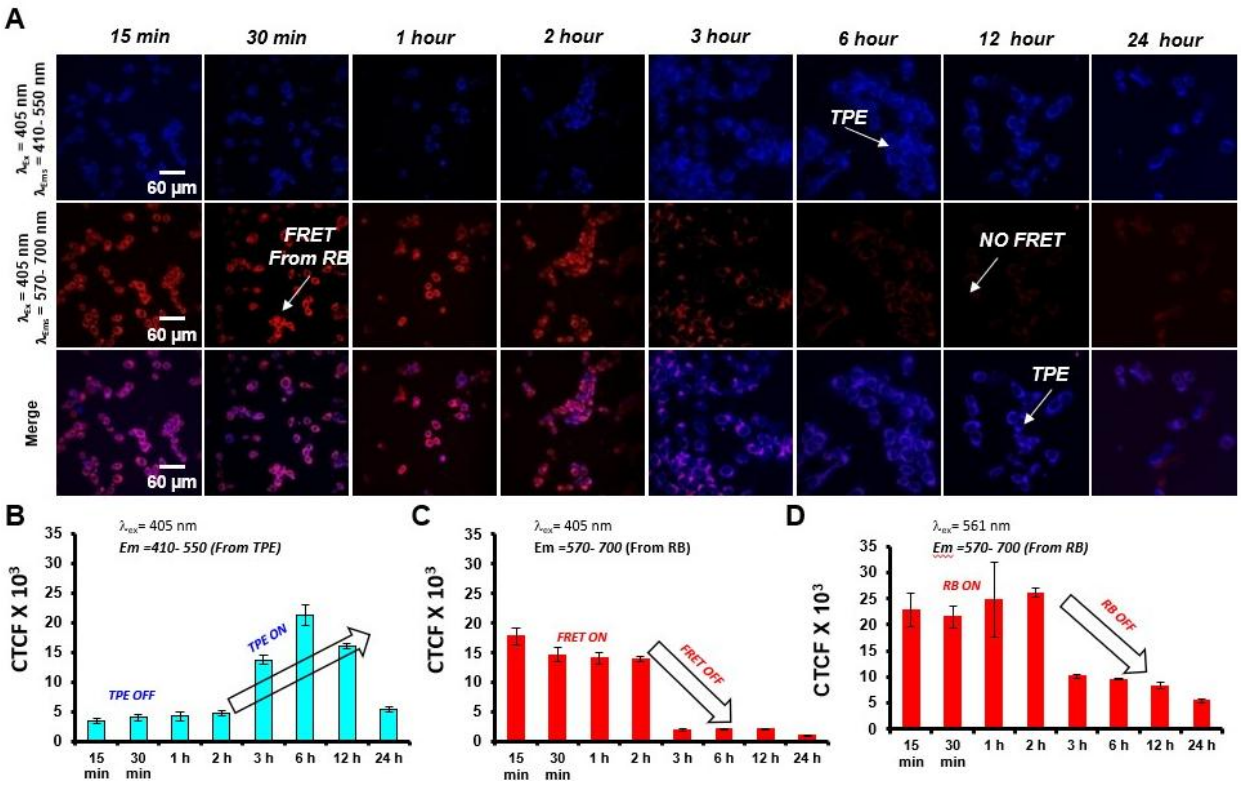

Figure 2.13: *Live Cell imaging employing P_{TPE+RB}.* ***A:*** *Live-cell confocal microscopy images for P_{TPE+RB} polymersomes at various incubation times in the WT-MEF cell line.* ***B:*** *Bar diagram showing the CTCF for the emission recovery of TPE at various incubation times followed by the selective photo-excitation of TPE using a 405 nm laser.* ***C:*** *Bar diagram showing the CTCF for the RB FRET emission at various incubation times followed by the selective photo-excitation of TPE using a 405 nm laser.* ***D:*** *Bar diagram showing the CTCF for the emission of RB at various incubation times followed by the selective photo-excitation of RB using a 561 nm laser. The images were recorded using the RB concentration at 5.0 µM in P_{TPE+RB} in 25 000 cells.*

A decrease or increase in the efficacy of a drug delivery system can be easily rationalized after carrying such simple yet insightful experiments. This also reflects on the kinetics of drug release, which can further be correlated with the pharmacokinetics and pharmacodynamics to optimize dosage for a successful clinical translation. After having established the enzyme responsiveness of the P_{TPE+RB} we ultimately understood such kinetics with a drug instead. This study was important and preceded before understanding the behavior of $P_{TPE+DOX}$ in release of doxorubicin. This is because the release of Rose Bengal was easy to follow due to red emission of FRET signal.

However, it's not the case with $P_{TPE+DOX}$ which instead shows quenching of fluorescence. Experiment with P_{TPE+RB} helped us understand the time window on enzyme action of polymersomes which becomes a good starting point to work with $P_{TPE+DOX.}$ We immediately carried out the live cell imaging experiments to understand the release of doxorubicin from $P_{TPE+DOX.}$ Doxorubicin is a DNA intercalator which binds the nuclear DNA and therefor illuminating the cellular DNA with intense fluorescence in the red region. Single cells were selected to better monitor the process of release of doxorubicin as shown in Figure xxx. There was initially no fluorescence in the TPE channel and red channel pointing towards the intact self-assembly (see Figure 2.14a). After 45 minutes, a faint emission was seen coming from nuclear DNA, however the cytoplasm still appeared dark (see Figure 2.14a). A point worth noticing is that there was a very little release of drug at this time.

2.4.9 *AIE Turn-ON Polymersomes*

A small release of the drug at around 45 minutes, bought about no detectable changes in the retrieval of TPE intensity. The system remained dark. However, nucleus showed some red emission. This is due to the fact that small amount of Doxorubicin upon binding with nuclear DNA leads to manifolds enhancement in the fluorescence. Hence, 45 minutes can be regarded as the onset of release from $P_{TPE+DOX}$ delivery system. This was followed by continuous enhancement in the fluorescence intensity in both the TPE and red channel in a time dependent manner. This also parallel with the quantification data (see Figure 2.14b-d).

The TPE fluorescence emission signals intensified in the cytoplasm and doxorubicin red emission signal intensified in the nucleus. The TPE emission came from the punctate lysosome inside the cells. This clearly suggests that the disassembly happened in the lysosomes and the release drug escaped the lysosome to find its way to nuclear DNA. Such methods are simple but provide powerful insights on the delivery behavior of delivery scaffold at intracellular level. It is also interesting to note that these processes are also affected due to inter-organelle interactions at cellular level. For instance, it is yet to be understood that why drug remains still trapped in the cellular lysosomes of the cells as also can be seen at 180 and 240 minutes in the current study. This phenomenon is called as lysosome drug sequestration, which disturbs the efficacy of drugs. Although, this effect is less in MCF 7 cell lines, because these cell lines are drug sensitive.

However, this phenomenon is highly functional in resistant cell lines and reduces not just the efficacy of small drugs but is reflected on decreased efficacy of nano delivery systems. This subject has been researched upon in chapter-4 of this thesis.

2.5 Conclusions

The successful clinical translation of a drug delivery system is subject to various organ and cellular level barriers. The inefficiency of many drug delivery systems at cellular levels often leads to poor drug efficacy. This study aimed to understand cellular barriers in administration of drug loaded nano delivery stem and monitor its drug release inside the cells. A good and controlled drug release is decisive to its efficacy, which can be rationalized by real0time monitoring of release dynamic of drug delivery system. Here we designed a polysaccharide based polymersomes integrate with AIE fluorophore TPE to monitor the subcellular location and concomitant delivery aspects of polymersomes inside the cells. The TPE tagged polymersomes hewed blue fluorescence and reflected on the intact self-assembly of these polymersomes. Furthest the encapsulation of these enzyme responsive polymersomes loaded commercially relevant drug doxorubicin and dye Rose Bengal. Due to physical interaction of doxorubicin with TPE and Rose Bengal with TPE led to FRET amongst these pairs. FRET between TPE and Rose Bengal led to red emission emanating from Rose Bengal when excited at TPE excitation wavelength of 405 nm. This makes them as efficient self-reporting system to reflect on their intactness inside the cells. An intact FRET between TPE and Rose Bengal would simply mean that the two chromophores are nearby and hence the self-assembly of the polymersomes must be intact to keep them close by in space which would retain their physical interactions. However, under the influence of lysosomal esterase, the self-assembly is broken due to hydrolysis of ester bonds. This leads to release of Rose Bengal form the close confined space of polymersomes, leading to disappearance if FRET signal and enhancement in the self-emission of TPE. This sheds light on the enzyme repulsive controlled release behavior of TPE conjugated polymersomes. This was then employed to study the cellular localization of polymersomes and its release of drug upon action of lysosomal enzymes in a time dependent manner. The assembly showed no fluorescence owing to dark state between the closely interacting TPE and Doxorubicin. However, following the action of cellular enzymes at around 1 hour, showed a gradual enhancement in the fluorescence intensity of the doxorubicin coming from the nuclear DNA. Such smart systems are important for that can self-report their location and

delivery aspects in repose to stimuli inside the cells. Such understanding of sub cellular dynamics is very important which is instrumental in determining the efficacy of the drugs following their cellular administration via delivery scaffolds. This paves way understanding of better scaffolds for clinical translation of therapeutic to therapies.

2.6 Bibliography

(1) Iqbal, S.; Blenner, M.; Alexander-Bryant, A.; Larsen, J. Polymersomes for Therapeutic Delivery of Protein and Nucleic Acid Macromolecules: From Design to Therapeutic Applications. *Biomacromolecules* **2020**, *21* (4), 1327-1350.
(2) Yin, Q.; Shen, J.; Zhang, Z.; Yu, H.; Chen, L.; Gu, W.; Li, Y. Multifunctional Nanoparticles Improve Therapeutic Effect for Breast Cancer by Simultaneously Antagonizing Multiple Mechanisms of Multidrug Resistance. *Biomacromolecules* **2013**, *14* (7), 2242-2252.
(3) Bobrin, V. A.; Lin, Y.; He, J.; Qi, Y.; Gu, W.; Monteiro, M. J. Therapeutic Delivery of Polymeric Tadpole Nanostructures with High Selectivity to Triple Negative Breast Cancer Cells. *Biomacromolecules* **2020**, *21* (11), 4457-4468.
(4) Pattni, B. S.; Chupin, V. V.; Torchilin, V. P. New Developments in Liposomal Drug Delivery. *Chem. Rev.* **2015**, *115* (19), 10938-10966.
(5) Jin, Q.; Deng, Y.; Chen, X.; Ji, J. Rational Design of Cancer Nanomedicine for Simultaneous Stealth Surface and Enhanced Cellular Uptake. *ACS Nano* **2019**, *13* (2), 954-977.
(6) Arcos, D.; López-Noriega, A.; Ruiz-Hernández, E.; Terasaki, O.; Vallet-Regí, M. Ordered Mesoporous Microspheres for Bone Grafting and Drug Delivery. *Chem. Mater.* **2009**, *21* (6), 1000-1009.
(7) Gupta, U.; Agashe, H. B.; Asthana, A.; Jain, N. K. Dendrimers: Novel Polymeric Nanoarchitectures for Solubility Enhancement. *Biomacromolecules* **2006**, *7* (3), 649-658.
(8) Rial-Hermida, M. I.; Rey-Rico, A.; Blanco-Fernandez, B.; Carballo-Pedrares, N.; Byrne, E. M.; Mano, J. F. Recent Progress on Polysaccharide-Based Hydrogels for Controlled Delivery of Therapeutic Biomolecules. *ACS Biomater. Sci. Eng.* **2021**, *7* (9), 4102-4127.
(9) Katterman, C.; Pierce, C.; Larsen, J. Combining Nanoparticle Shape Modulation and Polymersome Technology in Drug Delivery. *ACS Appl. Bio Mater.* **2021**, *4* (4), 2853-2862.
(10) Meng, F.; Zhong, Z.; Feijen, J. Stimuli-Responsive Polymersomes for Programmed Drug Delivery. *Biomacromolecules* **2009**, *10* (2), 197-209.
(11) Lale, S. V.; R. G, A.; Aravind, A.; Kumar, D. S.; Koul, V. AS1411 Aptamer and Folic Acid Functionalized pH-Responsive ATRP Fabricated pPEGMA–PCL–pPEGMA Polymeric Nanoparticles for Targeted Drug Delivery in Cancer Therapy. *Biomacromolecules* **2014**, *15* (5), 1737-1752.
(12) Moulahoum, H.; Ghorbanizamani, F.; Zihnioglu, F.; Timur, S. Surface Biomodification of Liposomes and Polymersomes for Efficient Targeted Drug Delivery. *Bioconjug. Chem.* **2021**, *32* (8), 1491-1502.
(13) Vargason, A. M.; Anselmo, A. C.; Mitragotri, S. The evolution of commercial drug delivery technologies. *Nat. Biomed. Eng* **2021**, *5* (9), 951-967.
(14) Mitchell, M. J.; Billingsley, M. M.; Haley, R. M.; Wechsler, M. E.; Peppas, N. A.; Langer, R. Engineering precision nanoparticles for drug delivery. *Nat. Rev. Drug Discov.* **2021**, *20* (2), 101-124.
(15) Browning, R. J.; Reardon, P. J. T.; Parhizkar, M.; Pedley, R. B.; Edirisinghe, M.; Knowles, J. C.; Stride, E. Drug Delivery Strategies for Platinum-Based Chemotherapy. *ACS Nano* **2017**, *11* (9), 8560-8578.
(16) Frenkel, V.; Etherington, A.; Greene, M.; Quijano, J.; Xie, J.; Hunter, F.; Dromi, S.; Li, K. C. P. Delivery of Liposomal Doxorubicin (Doxil) in a Breast Cancer Tumor Model: Investigation of Potential Enhancement by Pulsed-High Intensity Focused Ultrasound Exposure. *Acad. Radiol.* **2006**, *13* (4), 469-479.

(17) Kim, E. S.; Lu, C.; Khuri, F. R.; Tonda, M.; Glisson, B. S.; Liu, D.; Jung, M.; Hong, W. K.; Herbst, R. S. A phase II study of STEALTH cisplatin (SPI-77) in patients with advanced non-small cell lung cancer. *Lung Cancer* **2001**, *34* (3), 427-432.
(18) Veal, G. J.; Griffin, M. J.; Price, E.; Parry, A.; Dick, G. S.; Little, M. A.; Yule, S. M.; Morland, B.; Estlin, E. J.; Hale, J. P.; et al. A phase I study in paediatric patients to evaluate the safety and pharmacokinetics of SPI-77, a liposome encapsulated formulation of cisplatin. *Br. J. Cancer* **2001**, *84* (8), 1029-1035.
(19) Mammen, M.; Choi, S.-K.; Whitesides, G. M. Polyvalent Interactions in Biological Systems: Implications for Design and Use of Multivalent Ligands and Inhibitors. *Angew. Chem. Int. Ed.* **1998**, *37* (20), 2754-2794.
(20) Davis, A. P. Sticking to sugars. *Nature* **2010**, *464* (7286), 169-170.
(21) Salatin, S.; Yari Khosroushahi, A. Overviews on the cellular uptake mechanism of polysaccharide colloidal nanoparticles. *J Cell. Mol. Med.* **2017**, *21* (9), 1668-1686.
(22) Jin, Y.; Song, L.; Su, Y.; Zhu, L.; Pang, Y.; Qiu, F.; Tong, G.; Yan, D.; Zhu, B.; Zhu, X. Oxime Linkage: A Robust Tool for the Design of pH-Sensitive Polymeric Drug Carriers. *Biomacromolecules* **2011**, *12* (10), 3460-3468.
(23) Han, S.; Lee, J.; Jung, E.; Park, S.; Sagawa, A.; Shibasaki, Y.; Lee, D.; Kim, B.-S. Mechanochemical Drug Conjugation via pH-Responsive Imine Linkage for Polyether Prodrug Micelles. *ACS Appl. Bio Mater.* **2021**, *4* (3), 2465-2474.
(24) Gu, Y.; Zhong, Y.; Meng, F.; Cheng, R.; Deng, C.; Zhong, Z. Acetal-Linked Paclitaxel Prodrug Micellar Nanoparticles as a Versatile and Potent Platform for Cancer Therapy. *Biomacromolecules* **2013**, *14* (8), 2772-2780.
(25) Hershberger, K. K.; Gauger, A. J.; Bronstein, L. M. Utilizing Stimuli Responsive Linkages to Engineer and Enhance Polymer Nanoparticle-Based Drug Delivery Platforms. *ACS Appl. Bio Mater.* **2021**, *4* (6), 4720-4736.
(26) Arun, Y.; Ghosh, R.; Domb, A. J. Biodegradable Hydrophobic Injectable Polymers for Drug Delivery and Regenerative Medicine. *Adv. Funct. Mater.* **2021**, *31* (44), 2010284.
(27) Pramod, P. S.; Takamura, K.; Chaphekar, S.; Balasubramanian, N.; Jayakannan, M. Dextran Vesicular Carriers for Dual Encapsulation of Hydrophilic and Hydrophobic Molecules and Delivery into Cells. *Biomacromolecules* **2012**, *13* (11), 3627-3640.
(28) Anas, M.; Jana, S.; Mandal, T. K. Vesicular assemblies of thermoresponsive amphiphilic polypeptide copolymers for guest encapsulation and release. *Polym. Chem.* **2020**, *11* (16), 2889-2903, 10.1039/D0PY00135J.
(29) Bhattacharya, K.; Banerjee, S. L.; Das, S.; Samanta, S.; Mandal, M.; Singha, N. K. REDOX Responsive Fluorescence Active Glycopolymer Based Nanogel: A Potential Material for Targeted Anticancer Drug Delivery. *ACS Appl. Bio Mater.* **2019**, *2* (6), 2587-2599.
(30) Feiner-Gracia, N.; Glinkowska Mares, A.; Buzhor, M.; Rodriguez-Trujillo, R.; Samitier Marti, J.; Amir, R. J.; Pujals, S.; Albertazzi, L. Real-Time Ratiometric Imaging of Micelles Assembly State in a Microfluidic Cancer-on-a-Chip. *ACS Appl. Bio Mater.* **2021**, *4* (1), 669-681.
(31) Parthiban, C.; M, P.; Vinod Kumar Reddy, L.; Sen, D.; Singh, N. D. P. Single-Component Fluorescent Organic Nanoparticles with Four-Armed Phototriggers for Chemo-Photodynamic Therapy and Cellular Imaging. *ACS Appl. Nano Mater.* **2019**, *2* (6), 3728-3734.
(32) Yu, T.; Zhuang, W.; Su, X.; Ma, B.; Hu, J.; He, H.; Li, G.; Wang, Y. Dual-Responsive Micelles with Aggregation-Induced Emission Feature and Two-Photon Aborsption for Accurate Drug Delivery and Bioimaging. *Bioconjug. Chem.* **2019**, *30* (7), 2075-2087.

(33) Dong, Z.; Bi, Y.; Cui, H.; Wang, Y.; Wang, C.; Li, Y.; Jin, H.; Wang, C. AIE Supramolecular Assembly with FRET Effect for Visualizing Drug Delivery. *ACS Appl. Mater. Interfaces.* **2019**, *11* (27), 23840-23847.
(34) Jiang, Y.; Hadjichristidis, N. Tetraphenylethene-Functionalized Polyethylene-Based Polymers with Aggregation-Induced Emission. *Macromolecules* **2019**, *52* (5), 1955-1964.
(35) Birks, J. B. *Photophysics of aromatic molecules*; Wiley-Interscience, 1970.
(36) Leung, N. L. C.; Xie, N.; Yuan, W.; Liu, Y.; Wu, Q.; Peng, Q.; Miao, Q.; Lam, J. W. Y.; Tang, B. Z. Restriction of Intramolecular Motions: The General Mechanism behind Aggregation-Induced Emission. *Chem. Eur. J.* **2014**, *20* (47), 15349-15353.
(37) Balachandran, V. S.; Jadhav, S. R.; Vemula, P. K.; John, G. Recent advances in cardanol chemistry in a nutshell: from a nut to nanomaterials. *Chem. Soc. Rev.* **2013**, *42* (2), 427-438, 10.1039/C2CS35344J.
(38) Pramod, P. S.; Shah, R.; Jayakannan, M. Dual stimuli polysaccharide nanovesicles for conjugated and physically loaded doxorubicin delivery in breast cancer cells. *Nanoscale* **2015**, *7* (15), 6636-6652, 10.1039/C5NR00799B.
(39) Inchanalkar, S.; Deshpande, N. U.; Kasherwal, V.; Jayakannan, M.; Balasubramanian, N. Polymer Nanovesicle-Mediated Delivery of MLN8237 Preferentially Inhibits Aurora Kinase A To Target RalA and Anchorage-Independent Growth in Breast Cancer Cells. *Mol. Pharmaceutics* **2018**, *15* (8), 3046-3059.
(40) Deshpande, N. U.; Jayakannan, M. Biotin-Tagged Polysaccharide Vesicular Nanocarriers for Receptor-Mediated Anticancer Drug Delivery in Cancer Cells. *Biomacromolecules* **2018**, *19* (8), 3572-3585.
(41) Deshpande, N. U.; Jayakannan, M. Cisplatin-Stitched Polysaccharide Vesicles for Synergistic Cancer Therapy of Triple Antagonistic Drugs. *Biomacromolecules* **2017**, *18* (1), 113-126.
(42) Pramod, P. S.; Shah, R.; Chaphekar, S.; Balasubramanian, N.; Jayakannan, M. Polysaccharide nano-vesicular multidrug carriers for synergistic killing of cancer cells. *Nanoscale* **2014**, *6* (20), 11841-11855, 10.1039/C4NR03514C.
(43) Pramod, P. S.; Deshpande, N. U.; Jayakannan, M. Real-Time Drug Release Analysis of Enzyme and pH Responsive Polysaccharide Nanovesicles. *J. Phys. Chem. B.* **2015**, *119* (33), 10511-10523.
(44) Zhang, N.; Chen, H.; Fan, Y.; Zhou, L.; Trépout, S.; Guo, J.; Li, M.-H. Fluorescent Polymersomes with Aggregation-Induced Emission. *ACS Nano* **2018**, *12* (4), 4025-4035.
(45) Zhang, D.; Fan, Y.; Chen, H.; Trépout, S.; Li, M.-H. CO2-Activated Reversible Transition between Polymersomes and Micelles with AIE Fluorescence. *Angew. Chem. Int. Ed.* **2019**, *58* (30), 10260-10265.
(46) Deshpande, N. U.; Virmani, M.; Jayakannan, M. An AIE-driven fluorescent polysaccharide polymersome as an enzyme-responsive FRET nanoprobe to study the real-time delivery aspects in live cells. *Polym. Chem.* **2021**, *12* (10), 1549-1561, 10.1039/D0PY01085E.
(47) Demchenko, A. V.; Pornsuriyasak, P.; De Meo, C. Acetal Protecting Groups in the Organic Laboratory: Synthesis of Methyl 4,6-O-Benzylidene-α-D-Glucopyranoside. *J. Chem. Educ.* **2006**, *83* (5), 782.
(48) Sanford, E. M.; Smith, T. L. The Preparation and Enzymatic Hydrolysis of a Library of Esters. *J. Chem. Educ.* **2008**, *85* (7), 944.
(49) Han, X.; Liu, D.-E.; Wang, T.; Lu, H.; Ma, J.; Chen, Q.; Gao, H. Aggregation-Induced-Emissive Molecule Incorporated into Polymeric Nanoparticulate as FRET Donor for Observing Doxorubicin Delivery. *ACS Appl. Mater. Interfaces.* **2015**, *7* (42), 23760-23766.

(50) Xue, X.; Jin, S.; Zhang, C.; Yang, K.; Huo, S.; Chen, F.; Zou, G.; Liang, X.-J. Probe-Inspired Nano-Prodrug with Dual-Color Fluorogenic Property Reveals Spatiotemporal Drug Release in Living Cells. *ACS Nano* **2015**, *9* (3), 2729-2739.
(51) Virmani, M.; Deshpande, N. U.; Pathan, S.; Jayakannan, M. Self-Reporting Polysaccharide Polymersome for Doxorubicin and Cisplatin Delivery to Live Cancer Cells. *ACS Polymers Au* **2022**, *2* (3), 181-193.
(52) Lasic, D. D. Kinetic and thermodynamic effect on the structure and formation of phosphatidylcholine vesicles. *Hepatology* **1991**, *13* (5), 1010-1012.
(53) Demartis, S.; Obinu, A.; Gavini, E.; Giunchedi, P.; Rassu, G. Nanotechnology-based rose Bengal: A broad-spectrum biomedical tool. *Dyes and Pigments* **2021**, *188*, 109236.
(54) Demartis, S.; Rassu, G.; Murgia, S.; Casula, L.; Giunchedi, P.; Gavini, E. Improving Dermal Delivery of Rose Bengal by Deformable Lipid Nanovesicles for Topical Treatment of Melanoma. *Mol. Pharmaceutics* **2021**, *18* (11), 4046-4057.

Chapter 3

Structural Engineering of ESIPT probe for Bioimaging: Effect of Substitution and Self-Assembly

3.1 Abstract

Proton dynamics, critical for maintaining pH homeostasis in cells, involve complex processes regulated by evolutionarily conserved proteins and ion channels. This delicate balance affects various cellular functions, including membrane transport, growth, and cytoskeleton polymerization. Cellular compartmentalization into acidic organelles like endosomes and lysosomes highlights the importance of pH gradients for intracellular activities and has implications for disease and drug delivery mechanisms. Despite its significance, visualizing these pH-dependent processes remains challenging. Fluorescent probes, especially pH-responsive ones, facilitate understanding these mechanisms by signaling pH changes through specific interactions or reactions, yielding detectable fluorescence changes. This chapter introduces a chemodosimeter designed for high Stokes shift and dual-emission, to be able to probe endosome-lysosome interactions through irreversible reactions with protons. Excited State Intramolecular Proton Transfer (ESIPT) is known for its highly shifted emission, however, ESIPT emission suffers challenges under aqueous conditions. ESIPT reaction is highly compromised in aqueous conditions as intermolecular interactions with water molecules competes with the intramolecular hydrogen nodding reactions, leading to vanishing of the ESIPT emission. This challenge puts serious limitations onto the utility of ESIPT fluorophores for biological applications. AIE turns out as a brilliant strategy to facilitate ESIPT reactions under aqueous conditions by reducing the interaction of the chromophore with the outside water, which results in reduction of competitive intermolecular interactions with the water molecules. In current case, the probe's design incorporates aggregation-induced emission (AIE) traits to enhance ESIPT in aqueous environments, overcoming above mentioned challenges. However, dispersing the probe molecule in water led to deprotonation of the phenoxide group, causing anion emission. To this end, both the effect of electronic substitution and vectorization was studied to modulate the emission properties of the D-A scaffold too get primarily keto emission via ESIPT in water. The formation of anion depends upon the pK_a of the -OH group. By changing the electronics, it is rather possible to change the pK_a of the molecule which can affect the anion formation in water. Further, vectorization was employed to reduce the interaction of the fluorophore with outside water. These structural optimizations successfully led design of PEG-PDP-Imine molecule that only showed ESIPT emission in water and concomitantly suppressed the formation of anion and corresponding emission emanating from anion species.

3.2 Introduction

Proton extruding and importing processes orchestrated via evolutionary conserved proteins and ion channels maintain a dynamic yet delicate and finely tuned balance of pH homeostasis at cytosolic and inter-organelle level[1, 2]. Maintenance of intracellular pH is a very stringent process because of its implications in many tightly regulated cellular processes such as movement of cargo across the membrane[3], in growth and proliferation[2] and polymerization of cytoskeleton etc[4]. Needless to say, cellular compartmentalization probably evolved to provide a more hospitable and workable atmosphere to allow for a smooth conduct of many proteins and enzymes whose functions are dictated by protonation and deprotonation events to maintain their active and functional state. Cellular compartmentalization of pH yielded many acidic organelles such as endosomes, and lysosomes. The pH gradient serves as an essential force for the conduct of activities by endocytic organelles. The maintenance of the pH gradient is not just crucial in the functioning of the endosomes and lysosomes, but any fluctuations from the regular is implied under many rare diseases and pathologies. Apart from carrying out intracellular function, pH of these organelles is exploited by many drug delivery systems[5] and prodrugs to deliver active drugs[6, 7] at various intracellular targets. These organelles are known to sequester the weakly basic cytostatic drug molecules which has been discussed in the next chapter. However, a comprehensive understanding of drug sequestration abilities by endosomes and lysosomes is largely hindered due to limited ways to visualize such processes. It is therefore important to construct fluorescent probes that are able to simultaneously and discretely visualize both endosomes and lysosomes so as to be able to monitor their interactions under live cell conditions. Fluorescent probes come handy to help understand such complex processes with much ease. pH responsive fluorescent probes generally work on the principle of host-guest interactions or a specific chemical reaction to bring out a detectable change in the fluorescent intensity or shift in the fluorescence maxima of the probe[8, 9]. Generally speaking, the fluorescent probes are of two types. If the binding between the host or guest is reversible, it is called as chemosensor or sensor. However, if the binding produces irreversible chemical reaction, then these fluorescent probes are called as chemodosimeters. This chapter focus on the strategic development of chemodosimeter for discretely and simultaneously labelling of endosomes and lysosomes and to be able to study their dynamic interactions which is in depth discussed in chapter-4. Most of pH responsive probes developed for imaging endocytic organelle are rather based on enhancement in the fluorescent intensities. Such intensiometric

fluorescent probes mostly suffer from the problem of self-absorption due to their low stokes shift value and obtained intensities can be result of artifacts, as there is no internal calibration. Ratiometric probes on the other hand due to their dual excitation or emission wavelength offers distinct advantages over intensiometric probes. The ratiometric fluorescence response is dependent upon the relative change in the intensity of two or more emission bands of the probe before and after the analyte has been recognized. The concentration of the protons or the acidity increase from endosomes to endo-lysosomes to lysosomes. A fluorescent chemodosimeter that can sense this proton gradient and is able to generate the different fluorescent signal based upon the proton gradient will then be able to simultaneously and discretely label both endosomes and lysosomes Schiff bases are known to be pH sensitive nature because of their pH sensitive imine bond that cleaves into aldehyde and amine under acidic pH conditions, producing amine and aldehyde respectively. The imine bonds are generally stable under the pH conditions of the endosomes and they cleave under the pH conditions of the lysosomes. Therefore, a pH responsive fluorophore with an imine bond when intact shows a different fluorescent signal in endosomes. This further upon hydrolysis into an amine or aldehyde under acidic conditions of lysosomes shows a distinct fluorescent signal emanating from either aldehyde or amine or both as shown in *Figure* 3.1.

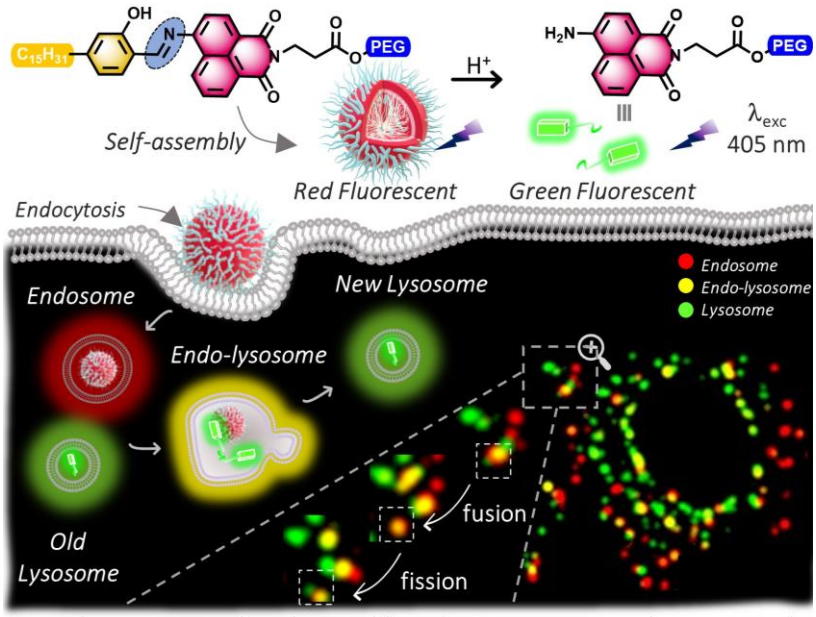

***Figure* 3.1:** *A pH-responsive probe is developed to label both endosomes and lysosomes in live cells in the current chapter. The intact imine-based probe exhibits red emission in endosomes. Upon recognition of protons (H+), the imine bond undergoes irreversible hydrolysis, producing an amine that shifts to green emission in lysosomes.*

However, π-conjugated Schiff bases are generally non-emissive as per several reported mechanisms[10-12]. The generally observed low quantum yields are due to the presence of dynamic bond rotations around the -C-C- and the -C-N- bonds that effectively consumes the excited state energy and dissipates the excited state energy through these mentioned non-radiative channels[10-12].

Ingenious strategies have recently emerged to induce fluorescence in imines. These include incorporating ESIPT[8, 13], ICT (Intramolecular Charge Transfer) properties[14], manipulating their self-assembly via non-covalent interactions[15-18], or transforming them into aggregate emitters[19]. Molecules that incorporate an appropriately placed hydrogen donor (–OH and NH_2) and hydrogen acceptor (-C=N– and -C=O) within the same scaffold tends to undergo a proton transfer in the excited state, which is referred to as Excited State intramolecular Proton Transfer[8]. ESIPT based fluorescent probes are known for their dual emission bands called as keto and enol respectively. The emission band with less stokes shift is often attributed to the enol form and the emission band with a high stokes shift is attributed to the keto emission band. The relative proportions and intensities of these two bands depends upon the proticity and polarity of the solvents. The ratio of intensities of the enol to the keto band is the function of the polarity of the solvent. The proton transfer reaction is highly sensitive to the local environment and the solvent system. Although mostly developed ESIPT dyes are emissive in good organic solvents due to favorable proton transfer upon excitation, such systems are often found to be non-emissive in water[20]. The competitive intermolecular hydrogen bonding interactions with surrounding water molecules competes with the intermolecular proton transfer following excitation[20]. This impedes the utility of these probes for bio-imaging applications which generally deals with water environment.

However, introduction of AIE with ESIPT can help alleviate the above-mentioned problem[21]. Many ESIPT probes when dispersed in water are known to form nano aggregates or aggregates in general that hinders their interaction with the outside water molecules. The hydrophobic environment of the aggregates promotes the intramolecular hydrogen bonding interactions that are required for ESPIT over the competitive intermolecular interactions with the outside solvent molecules of water. This causes an enhancement in the keto emission and leads to so-called aggregation induced emission making such systems AIE+ESIPT active[22-25].

More specifically, ESIPT+AIE type Schiff base fluorescent probes have recently garnered attention for applications in material science involving sensing[26] and cellular detection of esterase enzyme[27] and other biological applications.

Although, AIE+ESIPT dyes show enhancement in keto emission due to formation of aggregates, these systems are sometimes prone to deprotonation in protic solvents in the ground state[28-30]. It has been seen in many cases that the ESIPT dyes in water are prone to the formation of anion species due to the deprotonation of the -OH group as shown in *Figure* 3.2.

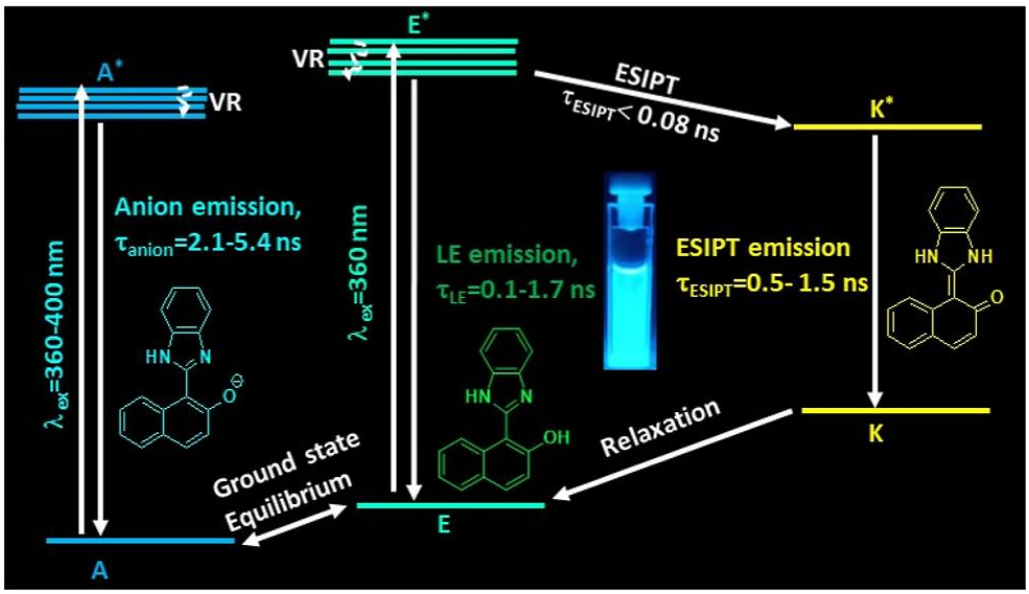

Figure* 3.2:** *Representative case for a naphthol based ESIPT active showing equilibrium between the neutral enol form and the anionic form. The excitation of the enol species leads to the normal;* ***N* *or enol emission;* ***E**** *or the tautomer emission* ***T**** *or the keto emission;* ***K**** *resulting from the keto state being formed in the excited state. Adapted from J. Phys. Chem. A* **2024**, *128*, 3495–3505.

For instance, it is well documented in literature that the deprotonation of the 3 hydroxy chomones (3-HC dyes and a few classes of flavanols forms anionic species in the ground state. The formation of the anionic species in the ground state leads to another emission band apart from the regular dual emission comprising of the enol and the keto form. The photophysics of the anionic species formed in water is completely different from enol species, which includes absorption at higher wavelength which corresponds to the anionic species then the neutral enol form. Further the emission of the anionic form is generally seen to be half way between the enol and the keto form. On the case of 3 hydroxy flavones, for instance the enol form is seen to emit N* or normal or enol emission at 406 nm, anion form; A* emits at 491 nm and tautomeric emission; T* or the keto emission is observed at 526 nm. For such classes of dyes, the dual

emission is seen to become the triple emission arising from the N*, A*, and T* form respectively instead of dual emission from just the N* and T* form.

Likewise for the case of Schiff base molecules, exhibiting AIE+ESIPT molecules, a similar equilibrium is seen to be functional in the protic solvents. For the salicylaldehyde class of dyes, the formation of anion is observed depending on the pK_a of the -OH group in the salicylaldehyde type Schiff base molecule. Although such dyes are prone to the formation of aggregates in aqueous medium due to its extremely hydrophobic core, it has been seen in many instance that these dyes are also prone to the formation of anion species in water as shown in *Figure* 3.3.

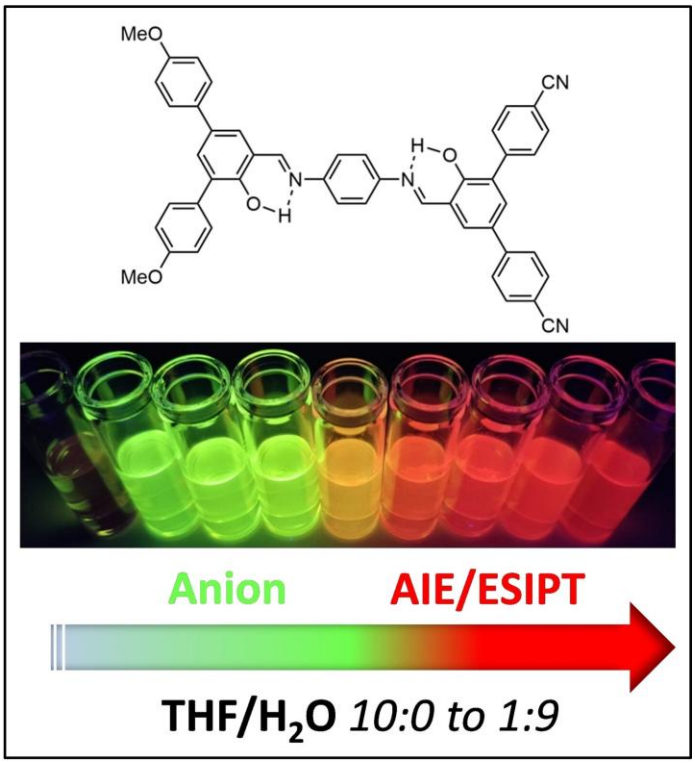

***Figure* 3.3:** *Representative case for salicylaldehyde Schiff based dye showing the anion emission in THF water composition which then switches to ESIPT emission at higher proportions of water in THF Water system due to formation of nano-aggregates at higher proportions of water leading to AIE induced ESIPT emission. Adapted from Chem. Eur. J.* **2023**, *29,* e202203766.

The aggregates and anion form coexist in the ground state. The aggregates due to their hydrophobic environment favors ESIPT, resulting in N*and T* emission. The deprotonation of the -OH group in the salicylaldehyde Schiff bases lead to the formation of anion which shows emission; A* that is usually centered between then N* and T* emitting species. Under such circumstances, both the anion and neutral enol form is present in the ground state depending upon the pH of the surrounding medium. The heterogeneous ground state comprising of anion and neural enol form

leads to excitation wavelength dependent emission Ex-De. This Ex-De property makes the fluorophore undesirable for the biological imaging. However, while exploring the literature it becomes evident to us that the emission properties of the ESIPT dyes can be modulated either by changing the electronic substitution or by changing its self-assembly properties in water. The pKa of the -OH group in the fluorophore determines its equilibrium in water leading to the dissociation of the weak acid, making the neutral enol and the anion form stay in equilibrium with each other at a given pH. Substituent effect like introducing an electron withdrawing and electron donating group can greatly affect the acidic of the phenolic group and can lead to the change in the equilibria between the enol and anion in the ground state when such dyes are dispersed in water.

Further, vectorization of ESIPT dyes has been employed as an effective strategy to modulate their interactions with the outside solvent molecules which can then effectively control the ratio of the keto and enol emission. The encapsulation of the ESIPT fluorophores in nanoparticles cavity has been utilized as an effective strategy to control the ratio of keto and enol emission[31].

Interestingly few papers recently reported on enhancing the hydrophilicity of the ESIPT fluorophores to improve on its vectorization in water or aqueous environments. This involved encapsulation of the ESIPT fluorophore inside the amphiphilic polymeric nano-carriers or included functionalization of the hydrophobic ESIPT core with neutral hydrophilic segments such as oligoethylene units. The introduction of oligoethylene group was seen to enhance the dual emission stemming from the keto and enol form in water. Introduction of charged functionalities such as carboxylic acids, sulphonic acids or the ammonium groups were further seen to not just enhance the solubility of the ESIPT chromophore in water but was also seen to enhance the proportion of enol and keto emission in PBS system. Further the authors of the paper went ahead and experimented with introducing zwitterionic handles. Under different substitutions of the zwitterionic group, different emissive states stemming from keto, enol and anionic emission were seen to be present in water and other organic solvents. In certain cases, anionic form was seen to be the more contributing species and, in some cases, the keto form primarily dominated in water system.

Inspired by the burgeoning literature, we thought of employing a fluorescent amine molecule, 4 amino naphthalimide which upon reacting with salicylaldehyde formed **SA-Imine** as shown in *Figure 3.1.* Luckily for us the perfect spatial orientation of the -OH group to the -C=H- of the imine bond facilitated ESIPT reaction and led to keto emission centered at 600 nm and

negligible enol emission due to the formation of nano-aggregates in water. This AIE+ESIPT active molecule upon hydrolysis under acidic conditions would lead to the regeneration of the green fluorescent amine molecule as discussed in *Figure* 3.1 above. The probe to red emission in water and green emission under acidic conditions would have fulfilled our design criterion. However, this AIE+ESIPT active molecule however showed an emission centered at 520−530 nm in water. This emission was confirmed to be arising from the deprotonation of the enol in water (vide infra). Owing to the presence of two photoexcitation channels (corresponding to anion and ESIPT), the **SA-Imine** showe excitation wavelength dependent emission (Ex-De). This caused triple emission arising from E*, K*, and A* form instead of otherwise expected dual emission arising from E* and K* form. The idea was to exclusively get ESIPT emission in water, which upon hydrolysis under acidic conditions will give second emission band resulting from the amine that is regenerated. As surveyed from the literature discussed above, to get exclusive ESIPT emission in water, both the substituent effect and vectorization on **SA-Imine** was conducted (*Vide Infra*).

In the results discussed ahead, it was realized that ESIPT reaction and the concomitant photophysical properties are sensitive to the substituent effect. The change in the electronic structure due electron withdrawing and electron donating groups leads to the shift in the absorbance and the emission maximum. In case of the electron donating group, the absorbance maxima showed a red shift. It was seen that due to the presence of electron donating group, intramolecular charge transfers enhanced and led to inhibition of ESIPT reaction and induced a red shift in the emission spectra. Intramolecular charge transfer reaction competes with the excited state intramolecular proton transfer reaction and leads to disappearance of the ESIPT emission in presence of electron donating group.

After exploring the substitution effect, the effect of vectorization on **SA-Imine** was then explored. As discussed earlier, the introduction of neutral hydrophilic groups such as polyethylene glycol or PEG was studied. It was seen that the introduction of PEG chain on **SA-Imine** made the derivative water soluble and emission due to formation of anion was mostly observed in water. It was hypothesized that may be by decreasing the length of the PEG chain, would provide the right balance of amphiphilicity that would then result in the retrieval of ESIPT emission in the system. However, decreasing the length of PEG-chain caused the system to rapidly precipitate in water and was not used for further analysis. Introduction of $-C_{15}H_{31}$ chain in the system balanced the

amphiphilicity and formed tiny micelles in water that led to the disappearance of the anion emission and primarily the ESIPT emission dominated in the system.

Altogether, self-assembly is an excellent strategy to suspend ground state heterogeneity that favored the enol formation over the anions in the ground state and resulted in exclusive keto emission due to ESIPT in water.

3.3 Materials and Methods

3.3.1 *Materials*

All the chemicals were purchased from local vendors (*Rankem*, *Sigma Aldrich*, *Alfa Aesar*, *ThermoFisher*, *TCI chemicals*) and were used without further purification. 4-Bromo-1,8-naphthalic anhydride, β-Alanine ethyl ester hydrochloride, DMAP (4-(Dimethylamino)pyridine), Pd/C-10% (Palladium on activated charcoal), EDC (1-ethyl-3-(3-dimethylaminopropyl)carbodiimide hydrochloride), Benzaldehyde, 2-hydroxybenzaldehyde, 3-Pentadecylphenol, Formaldehyde, Et_3N (Triethylamine), NaN_3 (Sodium Azide), $MgCl_2$ (Magnesium chloride), Polyethylene glycol (Mn= 750, Mn= 350).

3.3.2 *Instruments*

Product formation was confirmed by recoding ^1H NMR (at 400 MHz) and ^{13}C (at 100 MHz) NMR on Bruker Ascend TM 400 and JEOL ECS-400 spectrometer respectively. Deuterated solvents $CDCl_3$ (having residual chloroform) and DMSO-d^6 (having residual DMSO) were used with TMS as internal standard. The chemical shift (δ) and coupling constant (J) values were given in ppm and Hz respectively. An ESI 6540 UHD Q-TOF in positive ion mode was used to record high resolution mass spectrometry (HRMS) data. MALDI-TOF spectrum of PEG-PDP-Imine and PEG-**SA-Imine** and other PEG derivatives were recorded on 4800 plus MALDI-TOF analyser. Bruker Apex Duo diffractometer was employed to collect reflections using M_oK_α radiation (λ= 0.71073Å) at 100K. Intrinsic phasing method was used to solve the crystal structure and refinement was done using full matrix least squares on F_2. Crystallographic data is summarized in Table S2. If not stated otherwise, all hydrogen atoms were anisotropically refined. The crystals were weakly detracting at higher angles and data was truncated to $2\theta = 50^o$. Hydrogen atoms were constrained in geometric positions to their parent atoms. The diffused solvent molecules in **SA-Imine** was not modelled

properly and hence they were removed by EXTI command for better refinement data. One of the FCF reflection differed more than 10X σW and as resultant it was removed from final least square refinements. Size of nanoaggregates and micellar nanoparticles were characterized using a Dynamic Light scattering Instrument with 633 nm red laser at 90^o angle on a Malvern Nano ZS-90 instrument. Soft structures of nanoparticles were scanned by drop casting samples dispersed in water and 1% DMSO in water on silicon wafers and were scanned using a Zeiss Field Emission scanning Microscopy (FESEM) instrument. Freshly cleaved Mica sheets were used for drop-casting samples for AFM. AFM images for the samples were recorded on Keysight 5500 AFM instrument by Agilent technologies using a TAP-190AL-G50 probe from Budget sensors (nominal spring constant of 48 N/m and resonance frequency of 190) under tapping mode. Steady state photophysical characterizations (absorbance) were carried out on Shimadzu 2600 UV- visible absorption spectrophotometer and steady state Fluorescence measurements were conducted using a Horiba Jobin Yvon, Fluoromax-4 instrument. Fluorescence decays for Lifetime measurements were carried out on a time correlated single-photon counting (TCSPC) spectrometer by Horiba Jobin Yvon IBH, UK. A 375 nm diode laser was used to excite the samples. The fluorescence signals were collected at a magic angle using a MCP-PMT detector (Hamamatsu, Japan). The data was fitted using a IBH DAS 6 analysis software. The goodness of the fit was estimated using a χ^2 values and by visual inspection of the residuals. The χ^2 of less than or equal to 1.2 were an estimate of a good fit. More exponentials were introduced with caution only if the decrease in χ^2 value was significant (if the ratio decreased by a factor of 2 from the previous exponential).

3.3.3 *Methods*

3.3.3.1 *Quantum yield and lifetime measurement*

Quantum yield measurements were recorded on Horiba Fluoromax- 4 instrument using Coumarin-153 as reference sample. The quantum yield of probes was measured using the following equation 1.

$$\boldsymbol{\phi_S} = \phi_R \, X \, \frac{A_S}{A_R} \, X \, \frac{(Abs)_R}{(Abs)_S} \, X \, \frac{{\eta_S}^2}{{\eta_R}^2} \qquad \ldots\ldots \text{Equation- 1}$$

Where ϕ_s stands for quantum yield of the unknown sample, ϕ_R stands for quantum yield of the reference, $(Abs)_S$ stands for the absorbance of the unknown sample, $(Abs)_R$ stands for the

absorbance of the reference, A_s stands for area under the curve for the PL peak of unknown sample, A_R stands for area under the curve for reference sample, η_S is the refractive index of the solvent in which the unknown sample is dissolved, and $\eta_R$is the refractive index of the solvent in which the reference is dissolved. The average lifetime was calculated using the equation- 2.

$$< t > = \frac{\sum a_i t_i^2}{\sum a_i t_i} \quad \ldots\ldots\ldots \text{Equation- 2}$$

Where t_i represents the i[th] time component of a decay and a_i represents the relative amplitude of the i[th] time component.

3.3.3.2 *Nanoparticle preparation and characterization*

PEG-PDP-Imine nanoparticles were prepared via film rehydration, followed by passing the sample through extruder employing nano porous membrane of 0.1µm size cut-off. For this 0.5 mg sample was weighed in a 5 mL round bottom flask. Next, 0.25 mL of HPLC grade chloroform was added to completely dissolve the compound. Next, chloroform was slowly distilled off using a rotary evaporator. Next, the formed film was subjected under high vacuum conditions for 2 hours which ensures complete drying of the film. Next, the film was rehydrated using 1mL of MQ water for a period of 15-20 minutes at room temperature and were passed through an extruder using 0.1µm membrane filter. The formed nanoparticles were then characterized for its size using DLS and its morphology was characterized using electron microscopy techniques like FE-SEM and AFM.

3.3.3.3 *Synthesis of ethyl 3-(6-bromo-1,3-dioxo-1H-benzo[de]isoquinolin-2(3H)-yl) propanoate (Molecule 1)*

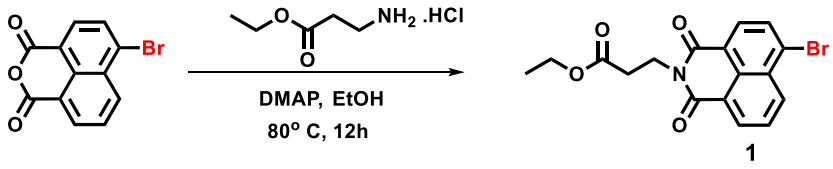

1

The synthesis was carried out following a reported procedure[32]. 200 mL ethanol was added to a mixture of 4 bromo naphthalic anhydride (10.0 g, 36.23 mmol, 1 eqv), β- alanine ethyl ester hydrochloride salt (7.76 g, 50.722 mmol, 1.4eqv) and DMAP (5.74g, 47.1 mmol, 1.3 eqv) in a single neck 500mL round bottom flask equipped with a reflux condenser. The mixture turned to a

dark brown clear homogeneous solution during reflux at 80°C. After 12 hours, the reaction was stopped and allowed to cool to room temperature. Next, the clear solution was rota evaporated to remove ethanol. The isolated brown coloured crude product was then subjected to column purification. The compound eluted in 30% PE/EA (Pet Ether/ Ethyl acetate) as an amorphous white coloured solid. **Yield**: 88%.

^{1}H NMR (400 MHz, DMSO-d_6) δ(ppm): 8.54 (m, 2H); 8.30 (d, 7.83Hz, 1H); 8.21 (d, 7.83Hz, 1H); 7.98 (dd, 7.58 Hz, 1H); 4.27 (t, 7.34 Hz, 2H); 4.04 (q, 7.09 Hz, 2H); 2.66 (t, 7.58 Hz, 2H); 1.13 (t, 7.09 Hz, 3H).

^{13}C NMR (100MHz, DMSO-d_6) δ(ppm): 170.58, 162.46, 132.40, 131.08, 130.68, 128.50, 127.88, 122.29, 121.51, 59.93, 35.55, 31.85, 13.75

HRMS- ESI (+) calculated for $C_{17}H_{14}BrNO_4$: 376.0178 ([M+H] +); found: 376.0175

3.3.3.4 *Synthesis of ethyl 3-(6-azido-1,3-dioxo-1H-benzo[de]isoquinolin-2(3H)-yl) propanoate (Molecule 2)*

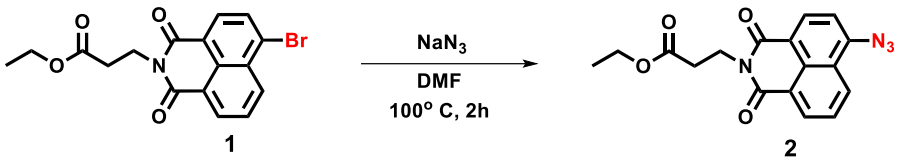

The synthesis was carried out following a reported procedure[33]. To a single neck 250mL round bottom flask containing compound 1 (10.0 g, 26.66 mmol, 1eqv), 60mL of HPLC grade DMF was added. The mixture was allowed to heat up to 100°C, followed by the addition of NaN_3 (5.19g, 79.99 mmol, 3 eqv) dissolved in 1mL water. The reaction mixture turned more turbid as the time progressed. The TLC was checked every half hour to monitor the progress of the reaction. After 2 hours, the reaction was stopped the DMF was distilled from the reaction mixture. Next, the crude mixture was precipitated slowly in water to remove excess NaN_3. The obtained solid was then vacuum filtered and this process was repeated twice. The solid was suspended in 50mL of methanol and vacuum filtered to obtain a greyish white product. The product was dried in the vacuum oven over night at 60 °C. **Yield**: 78%

^{1}H NMR (400 MHz, DMSO d_6) δ(ppm): 8.43 (d, 7.34 Hz, 1H); 8.35 (d, 8.07 Hz, 1H); 8.30 (d, 8.31 Hz, 1H); 7.79 (dd, 8.31 Hz, 1H); 7.64 (d, 7.83 Hz, 1H); 4.23 (t, 7.83 Hz, 2H); 4.06 (q, 7.09 Hz, 2H); 2.64 (t, 7.58 Hz, 2H); 1.13 (t, 7.09 Hz, 3H).

^{13}C NMR (100MHz, DMSO-d_6) δ(ppm): 172.65, 171.06, 163.33, 162.86, 143.17, 131.84, 131.76, 127.53, 122.27, 118.25, 116.19, 60.33, 35.90, 32.41, 14.16

HRMS- ESI (+) calculated for $C_{17}H_{14}N_4O_4$: 339.1078 ([M+H] +); found: 339.1075

3.3.3.5 *Synthesis of ethyl 3-(6-amino-1,3-dioxo-1H-benzo[de]isoquinolin-2(3H)-yl) propanoate (Molecule 3)*

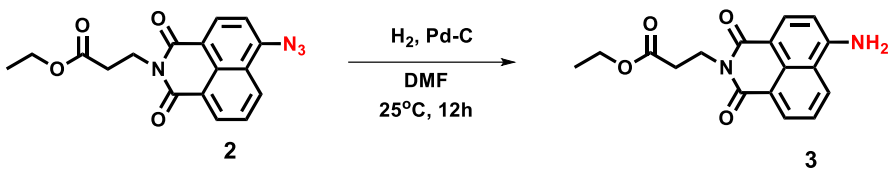

5.0 g of compound 2 was taken in a 2 neck RB. To this, 30mL of DMF was added. The resulting mixture was purged with dry nitrogen for a period of 1 hour. Next, Pd/C (~0.5 g) was quickly added to the flask and vacuum was applied to remove the atmosphere. A hydrogen filled large bladder was then applied to the reaction. The reaction mixture started to turn green immediately. After 12 hours, the hydrogen setup was removed and reaction mixture was passed through a celite column and the compound was eluted. Next, DMF was distilled off and the obtained crude solid was passed again through a celite column to get a bright fluorescent green solution of compound in DCM. The organic layer was rota evaporated to get a yellow-orange solid in **Yield**: 83%.

^{1}H NMR (400 MHz, DMSO d_6) δ(ppm): 8.52 (d, 8.56 Hz, 1H); 8.42 (d, 7.34 Hz, 1H); 8.19 (d, 8.31 Hz, 1H); 7.64 (dd, 7.58 Hz, 1H); 7.46 (s, 2H); 6.85 (d, 8.31 Hz, 1H); 4.25 (t, 7.34 Hz, 2H); 4.04 (q, 7.09 Hz, 2H); 1.11 (t, 7.34 Hz, 2H)

^{13}C NMR (100MHz, DMSO-d_6) δ(ppm): 170.53, 163.25, 152.37, 133.55, 130.57, 128.96, 123.50, 121.21, 118.91, 107.73, 59.62, 34.91, 32.08, 13.51

HRMS- ESI (+) calculated for $C_{17}H_{16}N_2O_4$: 313.1178 ([M+H] +); found: 313.1182

3.3.3.6 *Synthesis of 2-hydroxy-4-pentadecylbenzaldehyde (Molecule 4)*

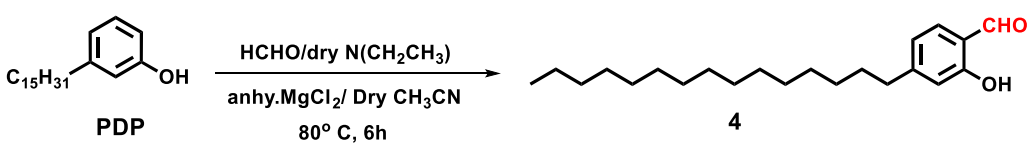

This was synthesized using a reported protocol[34]. Paraformaldehyde (6.9 g, 230 mmol, 7 eqv) dissolved in dry acetonitrile was added to a mixture of Pentadecylphenol (10.0 g, 32.86 mmol, 1 eqv), $MgCl_2$ (4.68, 49.8 mmol, 1.5 eqv), Et_3N (13.28g, 131.32 mmol, 4 eqv) in dry acetonitrile in a 2 neck RB via a cannula under nitrogen atmosphere at room temperature. After the completion of addition, the reaction mixture was then refluxed at 85°C. The solvent was distilled off, yielding a brown solid mass. A 1 M HCl solution (200 mL) was added and compound was extracted using DCM (100mL). The DCM layer was dried over Na_2SO_4 and rota evaporated to obtain the crude solid product. Next, column separation was done to isolate the product. The white waxy product eluted only in hexane. **Yield**: 68%.

^{1}H NMR (400 MHz, $CDCl_3$) δ(ppm): 11.05 (s, 1H); 9.84 (s,1H); 7.46 (d, 7.83 Hz, 1H); 6.85 (d, 8.07 Hz, 1H); 6.81(s, 1H); 2.62 (t, 7.58, 2H); 1.63 (m, 2H); 1.26 (m, 24H); 0.89 (m, 3H).

^{13}C NMR (100MHz, $CDCl_3$) δ(ppm): 195.85, 161.81, 153.88, 133.61, 120.53, 117.09, 118.87, 36.46, 31.94, 30.67, 29.7-29.55, 29.54, 29.45, 29.38, 29.25, 22.71, 14.14

HRMS- ESI (+) calculated for $C_{22}H_{36}O_2$: 333.2793 ([M+H] +); found: 333.2797

3.3.3.7 *Synthesis of ethyl (E)-3-(6-(benzylideneamino)-1,3-dioxo-1H-benzo[de]isoquinolin-2(3H)-yl) propanoate (BZA- Imine)*

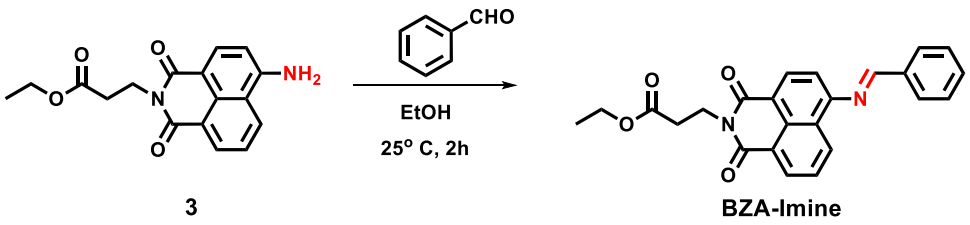

To a 10 mL round bottom flask containing compound 3 (0.5 g, 1.6 mmol, 1 eqv) dissolved in 1mL ethanol, added benzaldehyde (0.5 g, 4.8 mmol, 3 eqv). The homogeneous solution was allowed to stir at room temperature. After 20 minutes from the start of reaction, solid compound started to precipitate. TLC was checked every 0.5 hours to monitor the progress of the reaction. The reaction was stopped after 2 hours and the reaction mixture was diluted with 10mL ethanol and carefully transferred to a 50mL plastic falcon. The assembly was centrifuged at 8500g (8000 rpm, 5 minutes) in a centrifuge machine. A solid yellow colour pellet settled at the bottom of the plastic falcon. The supernatant was carefully removed without disturbing the pellet. The pellet was resuspended in 10mL (2X) of ethanol and centrifuged to remove the supernatant. The obtained pellet was

removed and transferred to a round bottom flask and dried under vacuum to obtain a crystalline light yellow coloured compound. **Yield**: 70%.

^{1}H NMR (400 MHz, DMSO- d^{6}) δ(ppm): 8.83 (s, 1H); 8.69 (d, 8.67 Hz, 1H); 8.57 (m, 2H); 8.14 (d, 6.6 Hz, 2H); 7.89 (t, 7.58 Hz, 1H); 7.63 (m, 3H); 7.55 (d, 7.82 Hz, 1H); 4.31 (t, 7.09 Hz, 2H); 4.06 (q, 7.09 Hz, 2H); 2.68 (t, 7.34 Hz, 2H); 2.68 (t, 7.34 Hz, 2H); 1.13 (t, 7.09 Hz, 3H)

^{13}C NMR (100MHz, $CDCl_3$) δ(ppm): 171.37, 163.81, 132.68, 135.54, 132.64, 131.74, 129.46, 129.04, 126.45, 122.26, 119.53, 114.13, 60.64, 36.11, 32.81, 14.13

HRMS- ESI (+) calculated for $C_{24}H_{20}N2O_4$: 401.1501 ([M+H] +); found: 401.1503

3.3.3.8 *Synthesis of ethyl (E)-3-(6-((2-hydroxybenzylidene) amino)-1,3-dioxo-1H-benzo[de]isoquinolin-2(3H)-yl) propanoate (SA- Imine)*

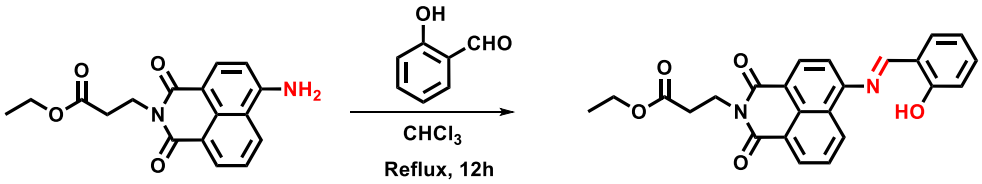

To a 10 mL round bottom flask equipped with a reflux condenser, compound 3 (0.5 g, 1.6 mmol, 1 eqv) dissolved in 0.5mL of chloroform, followed by addition of salicylaldehyde (0.59 g, 4.8 mmol, 3 eqv). The clear solution was stirred under refluxing conditions until the TLC showed complete product conversion. The reaction was stopped after 12 hours. The reaction was allowed to cool and additional 10mL of ethanol was added. A yellow crystalline product precipitated out of the crude reaction mixture. The reaction mixture was carefully transferred to a 50mL falcon and centrifuged (8000 rpm, 5 mins). Next the supernatant was carefully removed without disturbing the pellet. The pellet was resuspended in 10mL of fresh ethanol (2X) and centrifuged, followed by careful removal of the supernatant. The compound was dried under vacuum. **Yield**: 75%.

^{1}H NMR (400 MHz, DMSO- d_6) δ(ppm): 12.01 (s, 1H); 9.07 (s, 1H); 8.52 (m, 3H); 7.90 (m, 2H); 7.64 (d, 7.82 Hz, 1H); 7.51 (dd, 9.05 Hz, 1H); 7.06 (m, 2H); 4.30 (t, 7.34 Hz, 2H); 4.06 (q, 7.09 Hz, 2H); 2.67 (t, 7.58 Hz, 2H); 1.13 (t, 7.34 Hz, 3H).

^{13}C NMR (100MHz, $CDCl_3$) δ(ppm): 171.10, 165.69, 163.80, 163.38, 161.18, 151.52, 134.53, 132.91, 132.13, 131.73, 129.76, 128.68, 126.98, 126.30, 122.28, 120.30, 119.53, 118.83, 117.36, 115.18, 60.47, 35.97, 32.55, 13.92

HRMS- ESI (+) calculated for $C_{24}H_{20}N_2O_5$: 417.1450 ([M+H] +); found: 417.1447

3.3.3.9 *Synthesis of ethyl(E)-3-(6-((2-hydroxy-4-pentadecylbenzylidene) amino)-1,3-dioxo-1H-benzo[de]isoquinolin-2(3H)-yl) propanoate (PDP-Imine)*

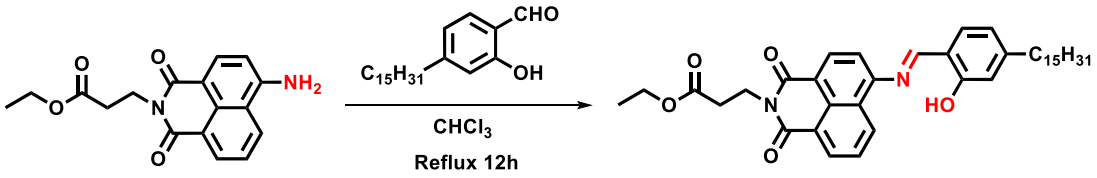

3 PDP-Imine

To a 10 mL round bottom flask equipped with reflux condenser, compound 3 (0.5 g, 1.6 mmol, 1eqv) dissolved in 0.5 mL chloroform. To this compound 4 (1.6 g, 4.8 mmol, 3 eqv) was added and reaction was refluxed for 12 hours. The reaction was stopped and the ethanol was evaporated. The compound was purified via column chromatography in PE/EA system. The pure compound eluted out as waxy yellow coloured solid in 30% PE/EA system. **Yield**: 65%.

^{1}H NMR (400 MHz, $CDCl_3$) δ(ppm): 12.67 (s, 1H0; 8.73 (s, 1H0; 8.66 (m, 3H); 7.80 (dd, 8.31 Hz, 1H); 7.40 (m, 2H); 6.95 (s, 1H); 6.88 (d, 7.83 Hz, 1H); 4.53 (t, 7.34 Hz, 2H); 4.18 (t, 7.09 Hz, 2H); 2.79 (t, 7.34 Hz, 2H); 2.67 (t, 7.58 Hz, 2H); 1.68 (m, 2H); 1.27 (m, 26H); 0.89 (m, 3H).

^{13}C NMR (100MHz, $CDCl_3$) δ(ppm): 171.12, 165.27, 163.87, 163.44, 161.23, 151.82, 151.19, 132.77, 132.21, 131.71, 129.87, 128.72, 126.88, 126.39, 122.27, 120.22, 120.05, 116.95, 116.82, 115.10, 70.33, 60.46, 36.14, 35.96, 32.57, 31.70, 30.66, 29.48- 29.05, 22.48, 13.91

HRMS- ESI (+) calculated for $C_{39}H_{50}N_2O_5$: 626.3719 ([M+H] +); found: 626.3715

3.3.3.10 *Synthesis of 3-(6-bromo-1,3-dioxo-1H-benzo[de]isoquinolin-2(3H)-yl) propanoic acid (Molecule 5)*

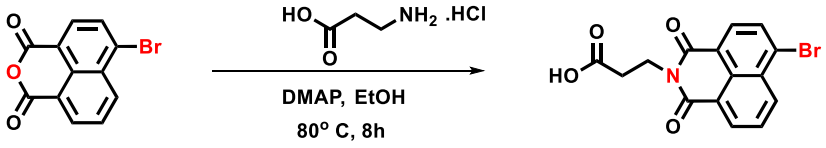

5

200mL ethanol was added to a 500 mL round bottom flask charged with 4 bromo naphthalic anhydride (10.0 g, 36.2 mmol, 1 eqv), β- alanine hydrochloride salt (5.0 g, 39.8 mmol, 1.1 eqv) and DMAP (0.45g, 3.62 mmol, 0.1 eqv). The reaction was refluxed at 80°C for 8 hours during which the reaction mixture turned turbid. The progress of reaction was monitored by TLC analysis. The reaction mixture was allowed to cool and then was subjected for Buckner filtration to obtain a brown solid and a dark brown coloured filtrate. The solid was then suspended in water and was sonicated for 5 minutes to get a uniform mixture and was Buckner filtered (2X) to get an off-white coloured solid. The solid obtained was precipitated in methanol (2X) and vacuum filtered to get an off white coloured solid product. The compound was dried overnight in the vacuum oven. **Yield**: 75%.

^{1}H NMR (400 MHz, DMSO- d^{6}) δ (ppm): 8.58 (m, 2H); 8.34 (d, 7.82 Hz, 1H); 8.24 (d, 7.82 Hz, 1H); 8.03 (dd, 7.34 Hz, 8.56 Hz, 1H); 4.28 (t, 7.83 Hz, 2H); 2.63 (t, 7.83 Hz, 2H).

^{13}C NMR (100MHz, DMSO- d^{6}) δ(ppm): 172.44, 162.77, 132.64, 131.56, 131.35, 128.80, 128.29, 122.75, 121.97, 35.86, 32.11

HRMS- ESI (+) calculated for $C_{15}H_{10}BrNO_4$: 346.9793 ([M+H] +); found: 346.9789

3.3.3.11 *Synthesis of 2-methoxyethyl 3-(6-bromo-1,3-dioxo-1H-benzo[de]isoquinolin-2(3H)-yl) propanoate (Molecule 6)*

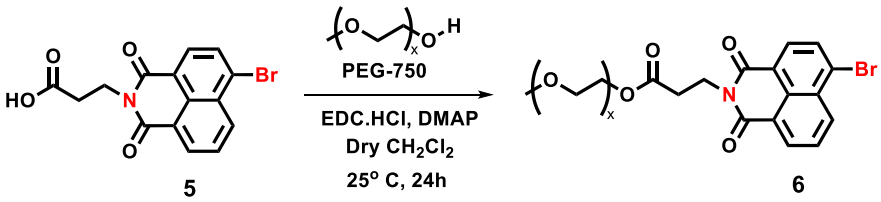

Compound 4 (2.95 g, 8.4 mmol, 1.5 eq), PEG monomethyl ether- 750 (*Note*: azeotropic distillation done with toluene before placing the reaction to remove water) (4.2g, 5.6mmol, 1eq), EDC.HCl (2.15g, 11.2 mmol, 2eq), DMAP (0.14 g, 1.12mmol, 0.2 eq) were taken in a 2 neck RB and subjected under high vacuum for 1 hour. An oven dried cannula was used to transfer freshly dried (dried 1h before) DCM through the septum into a 2 neck RB. The reaction was then continued under a nitrogen atmosphere for 24 hours. The reaction mixture turned clear dark brown solution in the initial 2 hours of the reaction. TLC was checked after 24 hours which showed good

conversion. A $NaHCO_3$ (saturated solution) workup was done to remove unreacted EDC.HCl from the reaction mixture. (*Note:* Care should be taken performing this step. A saturated solution of $NaHCO_3$ ensures that PEG coupled naphthalimide product stays in the DCM layer.) The DCM layer was dried over Na_2SO_4 and rotary evaporation was done to get a thick viscous oil. Column purification was done to isolate the product. Pure compound eluted in 1- 2% MeOH in DCM. **Yield**: 55%.

^{1}H NMR (400 MHz, $CDCl_3$) δ(ppm): 8.68 (d, 7.34 Hz, 1H); 8.61 (d, 8.56 Hz, 1H); 8.44 (d, 7.83 Hz, 1H); 8.07 (d, 8.05 Hz, 1H); 7.87 (dd, 7.34 Hz, 1H); 4.50 (t, 7.34 Hz, 2H); 4.25 (t, 6.11 Hz, 2H); 3.7- 3.6 (m, 60H); 3.56 (m, 2H); 3.38 (s, 3H); 2.82 (t, 2H).

^{13}C NMR (100MHz, $CDCl_3$) δ(ppm): 170.93, 163.15, 163.12, 133.18, 131.91, 131.88, 130.87, 130.39, 130.19, 128.75, 127.86, 122.60, 121.73, 71.64, 70.31- 70.22, 68.72, 63.58, 58.76, 35.94, 32.28

3.3.3.12 *Synthesis of 2-methoxyethyl 3-(6-azido-1,3-dioxo-1H-benzo[de]isoquinolin-2(3H)-yl) propanoate (Molecule 7)*

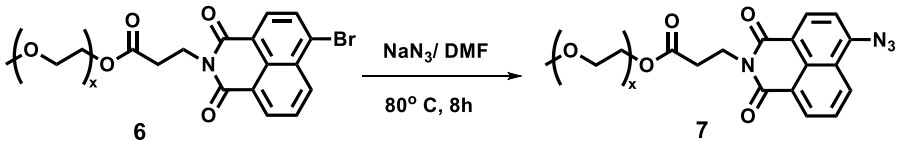

6 7

Compound 5 (3.5g, 3.18 mmol, 1 eqv) was dissolved in 5mL of HPLC grade DMF. NaN_3 (1.03 g, 15.9 mmol, 5 eqv) was added to the above solution and reaction was continued for 8 hours at 80°C. The progress of reaction was monitored every 2 hours via TLC. After 8h, the reaction was stopped and allowed to come to room temperature. NaN_3 was filtered to obtain a brown coloured filtrate. Next, DMF was distilled off to obtain a brown viscous product. Next, it was purified using column chromatography. The pure product eluted in 1% MeOH in DCM as a yellow viscous liquid. **Yield**: 70%.

^{1}H NMR (400 MHz, $CDCl_3$) δ(ppm): 8.64 (d, 8.63 Hz, 1H); 8.59 (d, 8.07 Hz, 1H); 8.46 (d, 8.56 Hz, 1H); 7.75 (dd, 7.34 Hz, 1H); 7.49 (d, 7.83 Hz, 1H); 4.49 (t, 7.34 Hz, 2H); 4.25 (t, 4.89 Hz, 2H); 3.7- 3.6 (m, 60H,); 3.5 (m, 2H); 3.38 (s, 3H); 2.81 (t, 7.58 Hz, 2H).

^{13}C NMR (100MHz, $CDCl_3$) δ(ppm): 171.62, 164.49, 163.78, 150.31, 134.06, 131.52, 129.98, 127.75, 124.63, 122.70, 119.99, 110.87, 109.31, 71.89, 70.55- 70.29, 68.96, 63.75, 59.01, 35.89, 32.92, 25.58

3.3.3.13 *Synthesis of 2-methoxyethyl 3-(6-amino-1,3-dioxo-1H-benzo[de]isoquinolin-2(3H)-yl) propanoate (Molecule 8)*

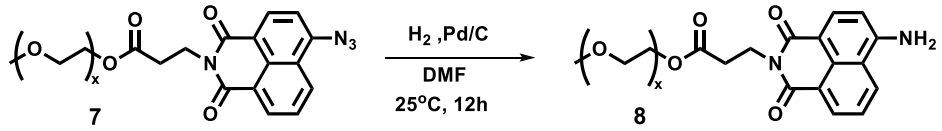

2.0 g of compound 6 was dissolved in 5mL of HPLC grade DMF. The clear yellow solution was purged with Nitrogen for 1 hour. Next, Pd/ C (~0.2 g) was quickly added and a 2-way gas adapter equipped with a hydrogen balloon was placed. Vacuum followed by hydrogen was applied and the reaction was continued under for hydrogen atmosphere for 12 hours at 25°C. Next, the compound was filtered off a celite column and the obtained solution was subjected for rotary evaporation. The obtained thick dark yellow liquid was purified using column chromatography. The pure compound eluted in 3 – 4% MeOH in DCM. **Yield**: 85%.

^{1}H NMR (400 MHz, $CDCl_3$) δ(ppm): 8.56 (d, 8.31 Hz, 1H): 8.36 (d, 8.07 Hz, 1H); 8.24 (d, 8.31 Hz, 1H); 7.62 (dd, 7.34 Hz, 1H): 6.87 (d, 8.07 Hz, 1H); 4.47 (t, 7.09 Hz, 2H); 4.22 (t, 5.14 Hz, 2H); 3.65- 3.5 (m, 62 H); 3.37 (s, 3H); 2.77 (t, 7.34 Hz, 2H).

^{13}C NMR (100MHz, $CDCl_3$) δ(ppm): 171.28, 163.80, 163.35, 143.64, 132.35, 131.86, 129.19, 128.96, 126.88, 124.37, 122.40, 188.66, 114.69, 71.89, 70.57- 70.48, 68.99, 63.81, 59.01, 36.10, 32.60

3.3.3.14 *Synthesis of 2-methoxyethyl (E)-3-(6-((2-hydroxybenzylidene) amino)-1,3-dioxo-1H-benzo[de]isoquinolin-2(3H)-yl) propanoate (PEG-SA-Imine)*

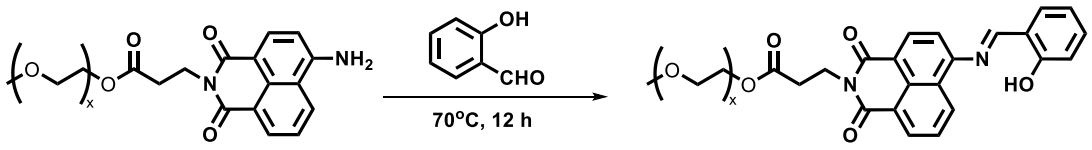

Compound 8 (250mg,) and salicylaldehyde (1mL) were taken a 5mL round bottom flask and were proceeded to react under solvent free conditions at 70°C under nitrogen atmosphere. The reaction was stopped after 12 hours as TLC showed complete conversion. The oily liquid was loaded onto a silica gel column (packed in dry hexane). Salicylaldehyde eluted in hexane. The solvent was changed from dry hexane to dry DCM to elute the product. Product eluted as a thick oil in 2- 3% MeOH in DCM. **Yield**: 70%.

^{1}H NMR (600 MHz, $CDCl_3$) δ(ppm): 12.67 (s, 1H): 8.78 (s, 1H); 8.65 (m, 2H); 8.60 (d, 9.54 Hz, 1H); 7.83 (dd, 8.31 Hz, 1H); 7.53 (m, 2H); 7.43 (d, 7.82Hz, 1H); 7.14 (d, 7.83 Hz, 1H); 7.04 (t, 7.34 Hz, 1H); 4.54 (t, 7.09 Hz, 2H); 4.27 (t, 4.89 Hz, 2H); 3.7- 3.6 (m, 60 H); 3.56 (m, 2H); 3.38 (s, 3H); 2.82 (m, 2H).

^{13}C NMR (100MHz, $CDCl_3$) δ(ppm): 171.61, 166.23, 164.31, 163.88, 161.69, 152.07, 135.06, 133.45, 132.67, 132.26, 130.29, 129.03, 127.51, 126.84, 122.82, 120.82, 120.05, 119.37, 117.86, 115.73, 72.22, 70.89- 70.80, 69.32, 64.13, 59.32, 36.45, 32.95

MALDI TOF (MATRIX: Dithranol): A distribution was obtained corresponding to $[M+Li]^+$ as shown in ***Figure*** S12.

3.3.3.15 *Synthesis of 2-methoxyethyl (E)-3-(6-((2-hydroxy-4-pentadecylbenzylidene) amino)-1,3-dioxo-1H-benzo[de]isoquinolin-2(3H)-yl) propanoate (PEG-PDP-Imine)*

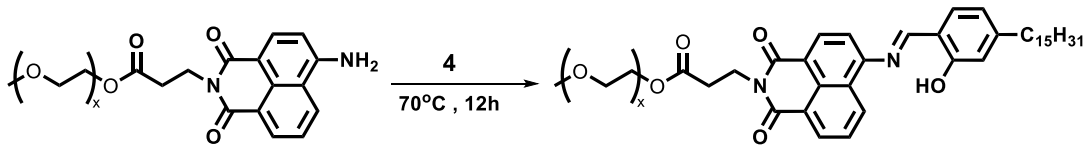

8 PEG-PDP-Imine

Compound 7 (250 mg, 0.18 mmol, 1 eqv; MW= 1340 g/mol as per MALDI-TOF data) and compound 8 (0.31 g, 0.92 mmol, 5 eqv) were taken in a 5mL round bottom flask. The mixture was heated at 70°C under melt conditions. The reaction was stopped after 12 h. Next, the reaction mixture was loaded onto a silica gel column packed in dry hexane. Unreacted PDP aldehyde was eluted in hexane. The solvent was switched from dry hexane to dry DCM to elute the product. PEG- PDP-Imine eluted in 1- 2 % MeOH in DCM as a waxy solid. The fractions collected were rota evaporated and vacuum dried. The solid compound was transferred to Eppendorf and stored under -20°C. **Yield**: 68%.

^{1}H NMR (400 MHz, DMSO- d^{6}) δ(ppm): 12.67 (s, 1H); 8.73 (s, 1H); 8.67- 8.63 (m, 2H); 8.61 (d, 8.44 Hz, 1H); 7.81 (t, 8.25 Hz, 1H); 7.40 (dd, 7.89 Hz, 1H); 6.95 (s, 1H); 6.87 (d, 7.89 Hz, 1H); 4.52 (t, 7.52 Hz, 2H); 4.27 (t, 4.77 Hz, 2H); 3.7- 3.6 (m, 60H); 3.38 (s, 3H); 2.82 (t, 7.34 Hz, 2H); 2.67 (t, 7.70 Hz, 2H); 1.67 (m, 2H); 1.37- 1.26 (m, 26H); 0.88 (m, 3H).

^{13}C NMR (100MHz, $CDCl_3$) δ(ppm): 171.33, 165.51, 164.06, 163.63, 161.43, 152.05, 151.39, 132.99, 132.44, 131.93, 130.10, 128.93, 127.10, 126.61, 122.46, 120.42, 120.22, 117.14, 117.03, 115.33, 71.89, 70.55- 70.47, 69.01, 67.95, 63.81, 59.01, 36.35, 36.12, 32.64, 31.90, 30.86, 29.67- 29.26, 25.58, 22.67, 14.11

MALDI TOF (MATRIX: Dithranol): A distribution was obtained corresponding to $[M+Na]^{+}$ can be seen in ***Figure*** S13.

3.4 Results and Discussions

3.4.1 *Synthesis of Fluorescent Salicylaldimine Compounds*

The fusion of early/late endosome (pH 6.5- 5.5) to lysosome (pH 4.5- 5.5) leads to an abrupt decrease in the pH. The design of a fluorophore exhibiting different emissive behavior in response to variation in pH is hence desirable. Schiff base linkage comprising of -C=N bond is pH sensitive and finds relevance in biology, concerning the interesting photophysics of rhodopsin's and family of fluorescent proteins. For instance, the modulation of green emission of GFP (Green Fluorescent Protein) to red emission of RFP (Red Fluorescent Protein) is a result of extension of π conjugation in the GFP chromophore bought by incorporation of -C=N linkage into its backbone.

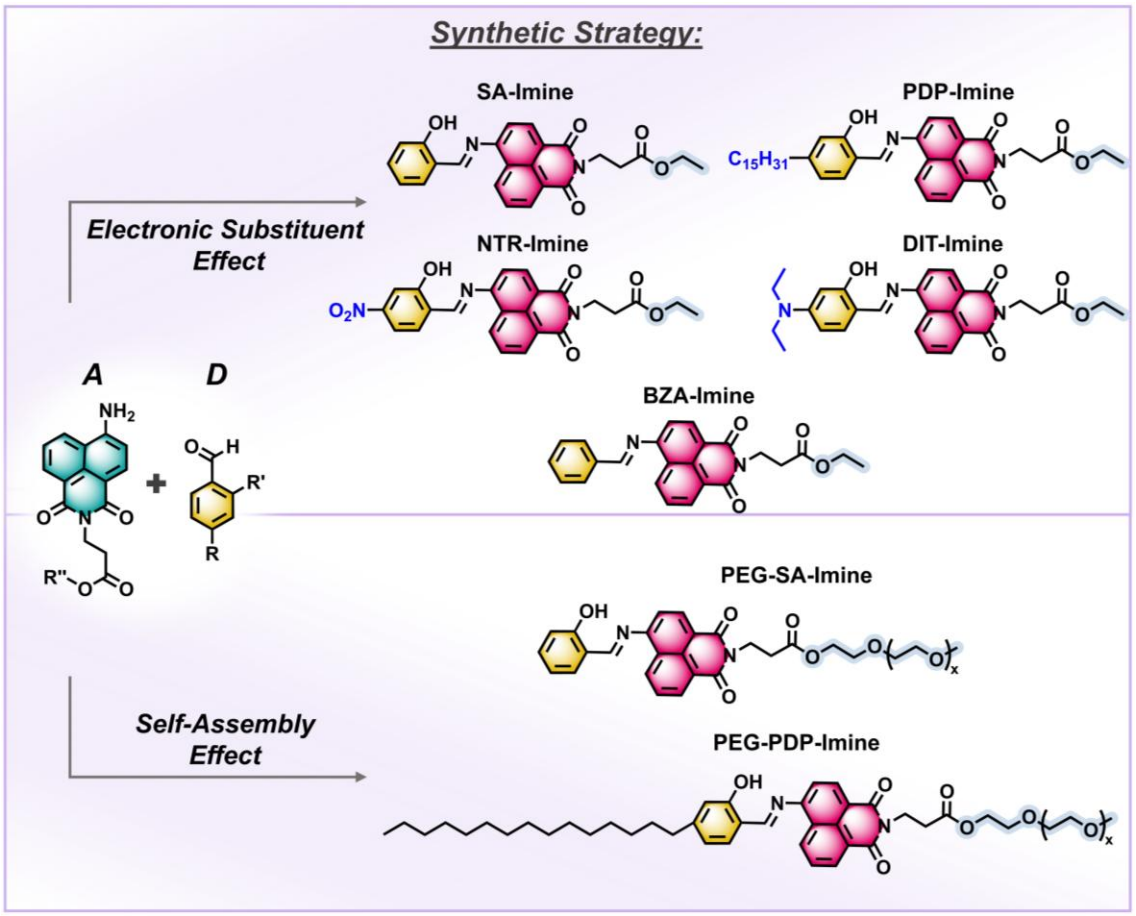

Figure* 3.4:** *Design strategy exploiting the effect of substitution and self-assembly in tuning the photophysical properties of parent fluorophore* ***SA-Imine*.*

Taking inspirations from nature for the design of pH responsive fluorophore, we selected a green fluorescence emitting 4-amino-naphthalimide (acceptor) molecule which was subsequently converted to a red emitting **SA-Imine** molecule by covalently linking it to salicylaldehyde (donor) molecule via a -C=N linkage *Figure* 3.4 and *Figure* 3.5a.

Apart from being pH sensitive, -C=N- linkage was chosen to link the donor and acceptor to spatially align the -OH towards the electronegative -N- atom of -C=N- bond to facilitate proton transfer reaction in the excited state, leading to red shifted emission. As discussed in the introduction, Schiff base ESIPT systems are prone to formation of anion in water and shows triple emission behavior corresponding to K*, E*, A* in contrast to normally expected dual emission corresponding to K* and E*. Likewise, the **SA-Imine** system also displayed triple emission due to formation of anion in water as shown in *Figure* 3.2. As will be discussed in greater details in the next sections, **SA-Imine** showed, intense red K* emission centered at 595 nm due to ESIPT and also showed green emission centered at 520-530 nm due to formation of anion in water.

The presence of dual emission channels corresponding to ESIPT and anion led to an unwarranted Excitation wavelength dependent emission or Ex-De property (*vide infra*). To have exclusive red emission via ESIPT and to get rid of green emission emanating from the anion species formed in water, following synthetic strategies were adopted (i) the effect of substitution and (ii) effect of self-assembly as shown in *Figure* 3.4. The electronic effect of substituents is intuitive for it is known that the photophysics of a molecule can be modulated by the presence of electron withdrawing and electron donating groups. Electron donating group such as $-N(Et)_2$, electron withdrawing substituent such as $-NO_2$ and alkyl tail was attached to **SA-Imine** and the resulting imine molecules **DET-Imine**, **NTR-Imine** and **PDP-Imine** were studied for their photophysical properties. The second method i.e. the effect of self-assembly was employed. As discussed previously in the introduction, vectorization of organic dyes by introducing water soluble oligoethylene tails and zwitterionic tails onto hydrophobic organic dyes, a reasonable ESIPT emission was seen in water. Depending upon the structure modification in dyes, different excited sate species were observed raging from normal and tautomeric excited state species and in some cases the competitive anionic species was also seen in water. Motivated by this, in the current investigation the -PEG tail was introduced onto the backbone of the hydrophobic parent fluorophore **SA-Imine** resulting in **PEG-SA-Imine**. Later, the amphiphilicity in the molecule was established by anchoring a $-C_{15}H_{31}$ chain, leading to the formation of **PEG-PPD-Imine** as shown

in *Figure* 3.4. To test the first strategy, the small molecules were then synthesized and characterized by routine analytical techniques (*Figure*s A1-A8, NMR). The synthesis was carried out according to the scheme shown in *Figure* 3.5 and the detail synthetic procedure is discussed in experimental section. The NMR of parent chromophore, **SA-Imine** is discussed as a representative.

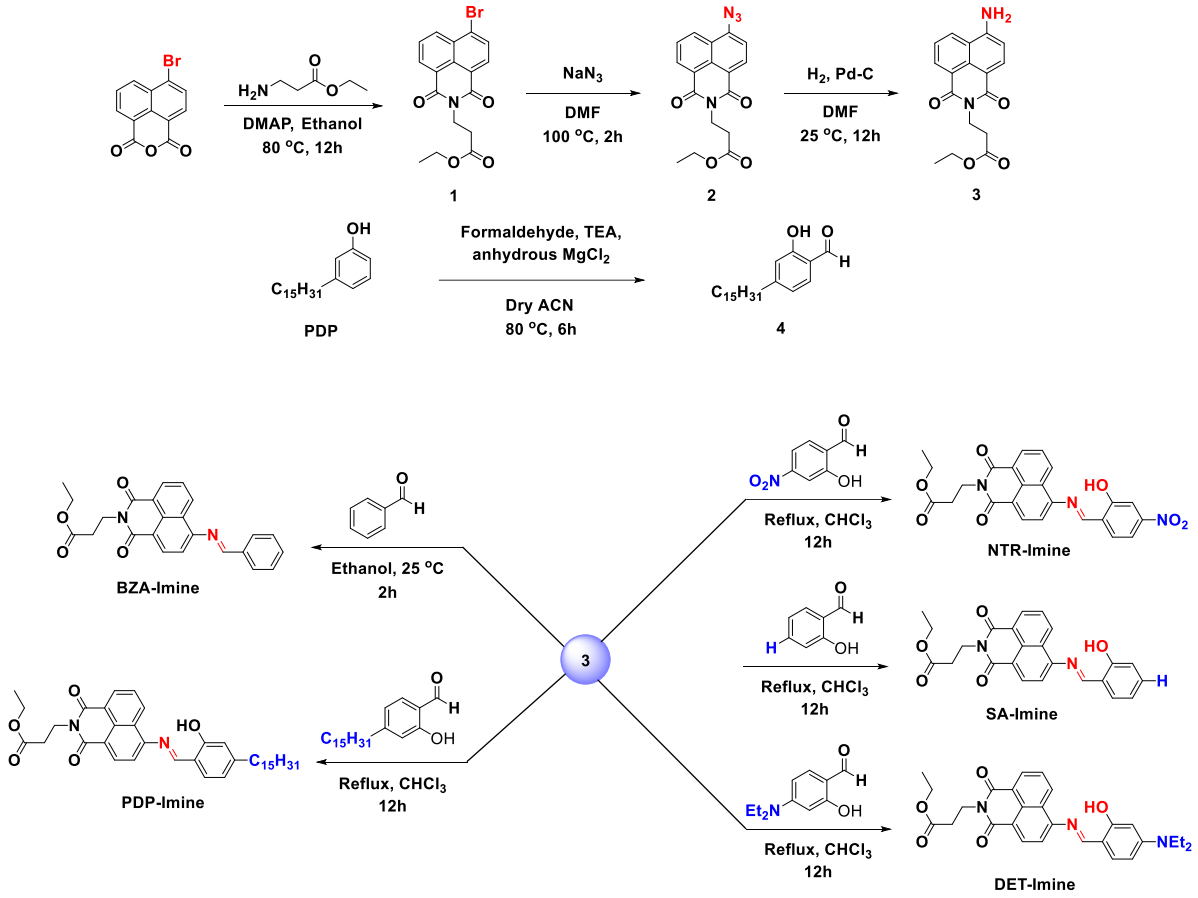

***Figure* 3.5:** *Synthetic scheme showing the synthesis of small molecule Schiff base to explore the effect f electronic substitution on photophysical properties.*

The NMR spectrum acquired in $CDCl_3$, shows a highly de-shielded singlet proton which resonates at 12 ppm corresponding to (Ar**OH**) and another singlet proton appearing at 9 ppm which corresponds to imine proton (C**H**=N). The extremely downfield shifted -OH proton is suggestive of an increase in acidity of this proton owning to the presence of strong intramolecular hydrogen bonding interactions. Also, the singlet -OH proton sheds light on ground state tautomeric equilibria of the compound which essentially favors the enol- imine tautomer over the keto-amine tautomer.

The single crystal data recorded for **SA-Imine** further furnished necessary evidence for the existence of the enol form in the ground state, which is discussed in more details in the subsequent section.

3.4.2 *Single Crystal for SA-Imine*

Further, single crystal obtained for ***SA-Imine*** (in ethanol) provided necessary evidence and advocated for apt geometrical requirements to promote ESIPT emission (see Table B.1- B.4 for crystallographic parameters)[35].

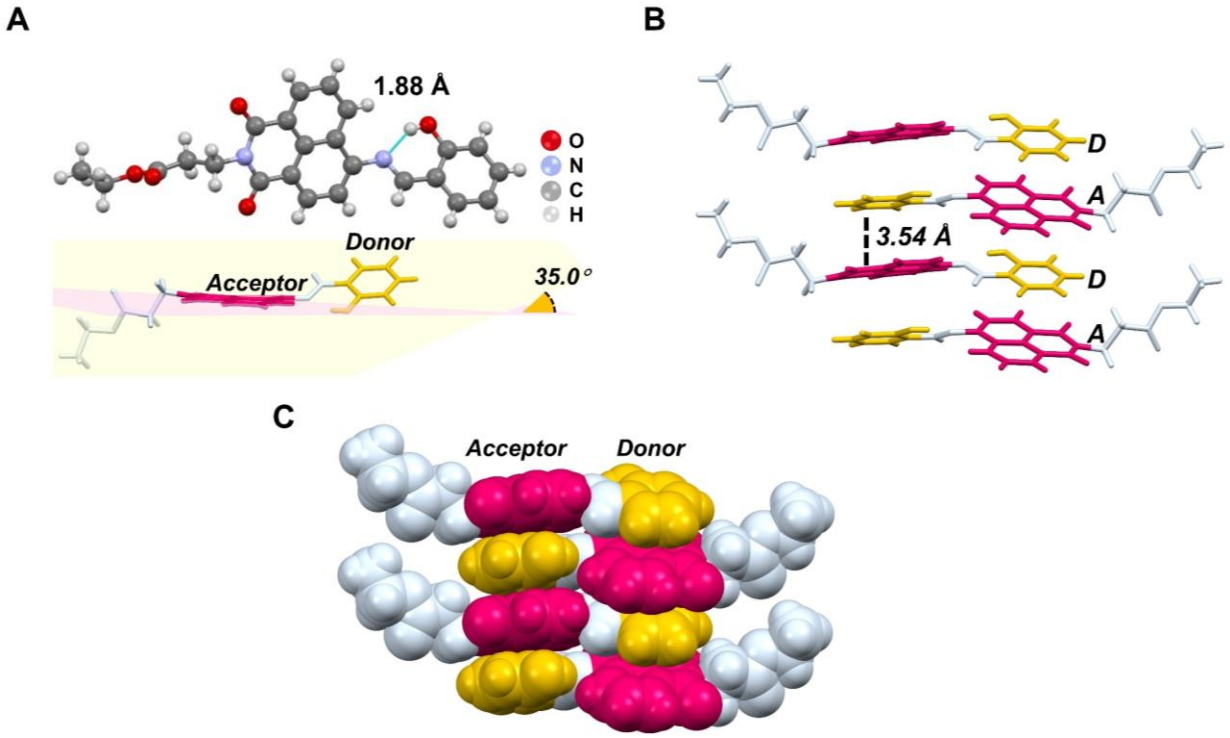

Figure* 3.6:** Single crystal of ***SA-Imine. ***A:*** *Single crystal data for* ***SA-Imine*** *crystalized in ethanol represented in ball and sticks model showing intramolecular Hydrogen bonding distance between nitrogen of –C=N– and –OH group as 1.88Å and a twist of 35.0^o between donor (salicylaldehyde) and acceptor (naphthalimide) in single molecule of* ***SA-Imine***. ***B:*** *Anti-parallel stacking arrangement between two* ***SA-Imine*** *molecules with interplanar distance of 3.54 Å.* ***C:*** *Single crystal data in Calotte model showing tight intermolecular π-π aromatic interactions between donor and acceptor.*

Single crystal is very crucial to understand the structure and structure guided photophysical phenomenon. The structural requirements for ESIPT reaction are rather stringent and crystal data provides necessary evidence for the presence of appropriate geometry to facilitate the proton

transfer reactions in the excited state. Fortunately, **SA-Imine** crystalized as light-yellow crystals in ethanolic solution. **SA-Imine** crystalized in the monoclinic system. The crystal structure also revealed the presence of intramolecular hydrogen bonding of 1.88 Å between O-H----N (*Figure* 3.6a). This distance between the acidic center and the basic center is favorable for the intramolecular hydrogen bonding interactions, which leads to proton transfer reaction in the excited state. A small twist angle of 35.0^{o} was seen between the donor- acceptor plane (*Figure* 3.5b), suggesting the molecule is almost planar, which is supportive of intramolecular hydrogen bonding interactions. Two adjacent molecules of **SA-Imine** are positioned anti-parallel to each other having interplanar distance of 3.54 Å (*Figure* 3.5c). The strong π-π interactions between donor and acceptor moieties of closely placed neighboring molecules becomes evident from the space filling model (*Figure* 3.5c). This arrangement was would then facilitate the formation of nanoaggregates in solution state. The crystal clearly advocated for the presence of enol form in the ground state and appropriate geometrical requirements that would then facilitate ESIPT reaction. The single crystal data for **SA-Imine** looked promising and persuaded us to investigate the photophysical behavior which is subsequently discussed in next sections.

3.4.3 *Photophysical Characterization of SA-Imine*

We next commenced our photophysical studies by systematically recording the absorbance and emission profiles of parent molecule ***SA-Imine***. As shown in the representation diagram, the molecule exists as enol in the ground from which upon excitation leads to E*. The E* form can decay in a radiative manner giving the enol emission or can phot tautomerize to the excited keto, K* form. The K* forms then decay to give the corresponding keto emission and subsequently returns to the ground state keto form which eventually tautomerizes back to the enol form. This simple phenomenon is complicated by the presence of another ground state species which is generated due to deprotonation of the -OH group. The resulting anion is emissive in nature as shown in the *Figure* 3.7a. The ground state absorbance spectra of ***SA-Imine*** studied in 1% DMSO in water (*Figure* 3.2b, DMSO: Water- 1:99), DMSO (*Figure* 3.2b) and other organic solvents (*Figure* 3.2d) exhibits a broad peak centered at 375- 390 nm. The absorbance maxima shift in a hypochromic manner in water as compared to DSMO. This blue shift in the absorbance spectra

upon moving from good solvent to bad solvent and broadening in the spectra are in general indicative of formation of aggregates in the ground state[36].

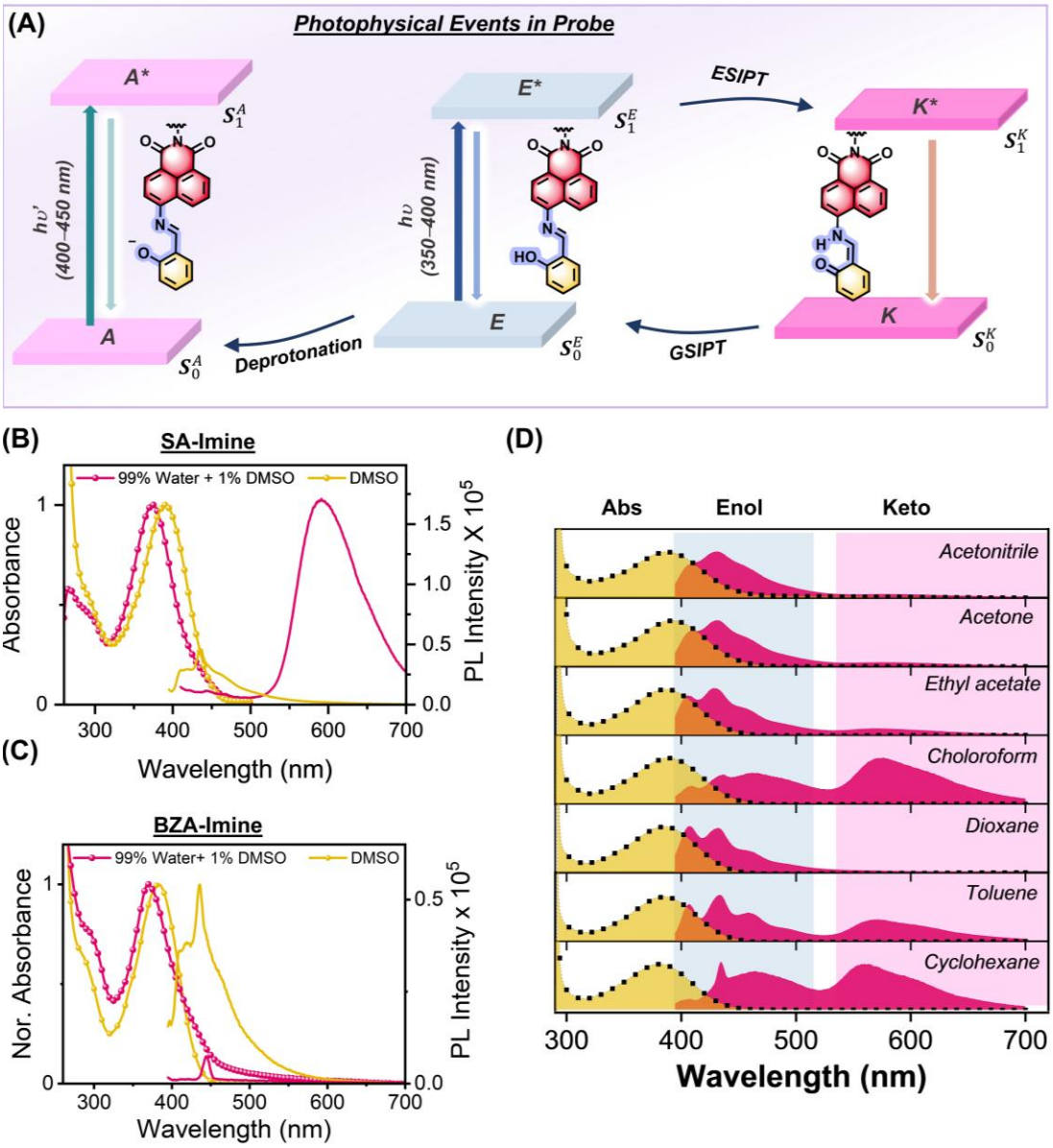

Figure* 3.7:** ***A: *Schematic showing the keto enol tautomerization in the excited state and presence of anion in ground state in aqueous conditions.* ***Absorbance*** *(Left axis) and fluorescence (Right axis) of* ***C: SA-Imine*** *and* ***D: BZA-Imine*** *in DMSO and 1% DMSO in Water.* ***D:*** *Solvent dependent absorbance (yellow) and fluorescence profile (magenta) of* ***SA-Imine*** *and categorizing them as enol (blue), and keto (pink) emission.*

A simple Schiff base system comprising of a donor and acceptor resembles substituted stilbene or azobenzene, provided that the conjugation is not interrupted at the nitrogen atom of the -C=N- bond, owing to the loss of planarity[37]. Likewise, the broad absorbance spectrum of **SA-Imine** is reminiscent of coplanarity which facilitates uninterrupted delocalization of electrons from donor to acceptor ring along the molecular skeleton[38]. An otherwise loss in coplanarity of donor and acceptor moieties in **SA-Imine** would make overall spectrum look more or less like a superposition of weakly interacting donor and acceptor moieties of the conjugated system. The broad absorption, typically is an intramolecular charge transfer (ICT) band originating from the mixing of π-π*and n-π* states[37, 38]. The high molar absorptivity further reaffirmed the possibility of mixing of π-π*and n-π* states. Next, the photoluminescence (PL) of ***SA-Imine*** was recorded in 1% DMSO in water and other solvents as shown in *Figure* 3.7b and *Figure* 3.7d. Upon photoexcitation at 380 nm (λ_{abs}), ***SA-Imine*** showed an intense red emission peak at 595 nm along with a less intense but structured emission band spanning from 410- 500 nm. This extremely red shifted centered at 595 nm emission with large stokes shift was assigned as keto form and the less stokes shifted and structured emission was assigned as enol emission for **SA-Imine**.

Interestingly, in DMSO, this structured emission from 420 nm- 500 nm became prominent and the red shifted emission at 595 nm vanished. ESIPT is sensitive to the polarity and protacity of the surrounding medium. Generally, the polar solvents are known to participate in hydrogen bonding interactions with the solvent molecules. These interactions compete with the intramolecular hydrogen bonding interactions that are required for ESIPT emission. Therefore, ESIPT emission is seen to be a absent in polar solvents. Water being a polar solvent, however is sometimes seen to facilitate ESIPT in many small molecules such as in current case. The small molecules due to their hydrophobic structure forms nano-aggregates in water. These nano-aggregates provide hydrophobic environment and at the same time suspend interactions with the outside water molecules which therefore stabilized ESIPT reaction and intense keto emission is seen in such cases. This property is typically called as aggregation induced emission which is known to enhance ESIPT emission. Schiff bases although less emissive in solution state show enhanced emission in water due to this AIE/ESIPT property which has been reported for many unrelated Schiff base systems. Likewise, **SA-Imine** showed an enhance ESIPT emission in water which can be attributed to the AIE emission. Further, the control molecule **BZA-Imine**, lacking the -OH group showed no red shifted emission in either DMSO, water as shown in *Figure* 3.7c or any other organic solvent

studied (*Figure* 3.8). The absence of -OH group in **BZA-Imine** led to the disappearance of the red emission, which proves that the red emission in **SA-Imine** stems from ESIPT.

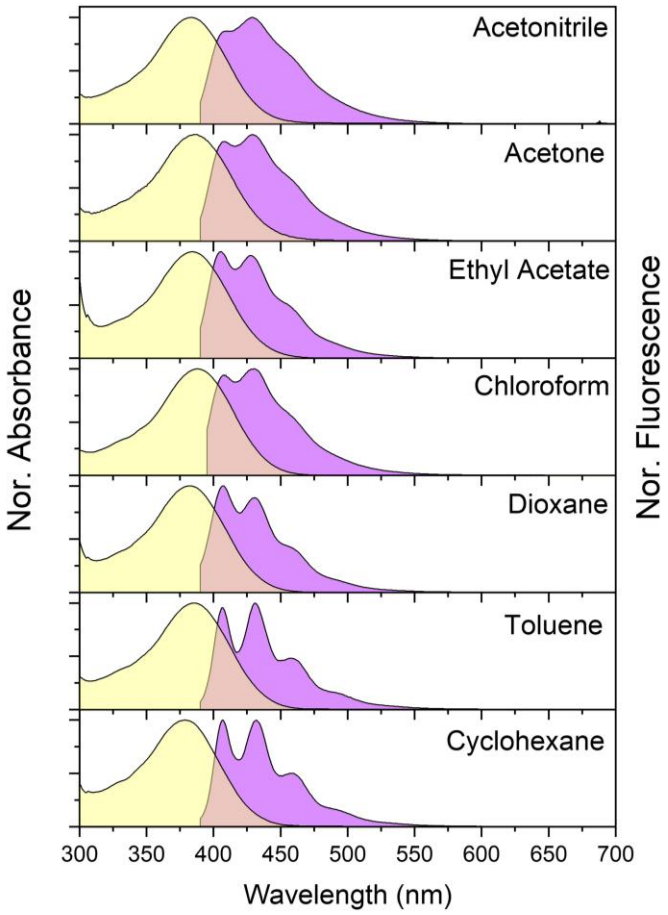

***Figure* 3.8:** Fluorescence and absorbance spectra recorded for **BZA-Imine** in various solvents.

However, the emission spectrum of **SA-Imine** recorded in solvents of various polarity showed variation in the intensities of keto and enol emission. ESIPT emission is known to be sensitive to the polarity if the solvents. The ratio of the keto to enol emission was seen to be decreasing as the solvent polarity increased[39]. This is because, the enol forms a more stable intermolecular hydrogen bonding interactions with the outside polar solvent molecules and leads to the prevalence of enol emission more in the system. Whereas in non-polar solvents such as toluene, cyclohexane where intermolecular hydrogen bonding interactions are rather absent and that facilitates the intramolecular hydrogen bonding interactions required for ESIPT, results in keto emission over enol emission.

P1/Solvent	Fluorescence spectra	I_{E^*}/I_{K^*}
Cyclohexane	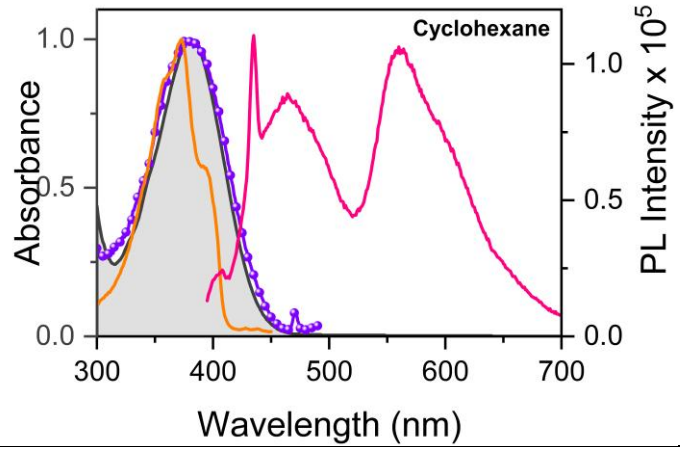	**0.83**
Toluene	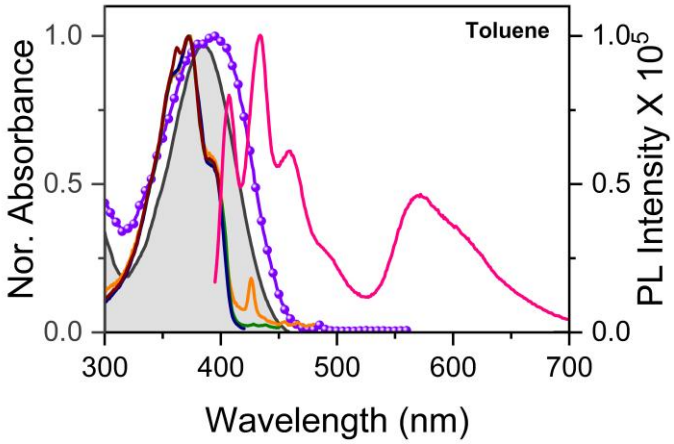	**2.17**
Ethyl Acetate	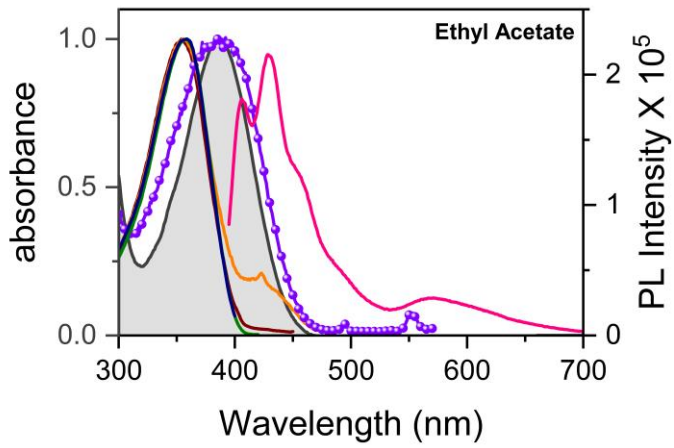	**7.33**

Chloroform	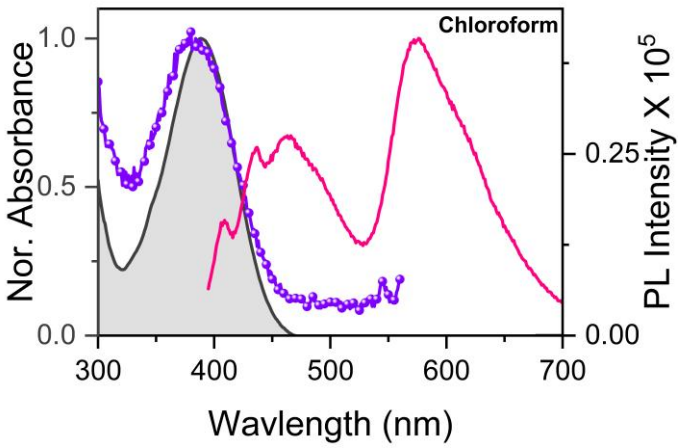	**0.67**
Acetone	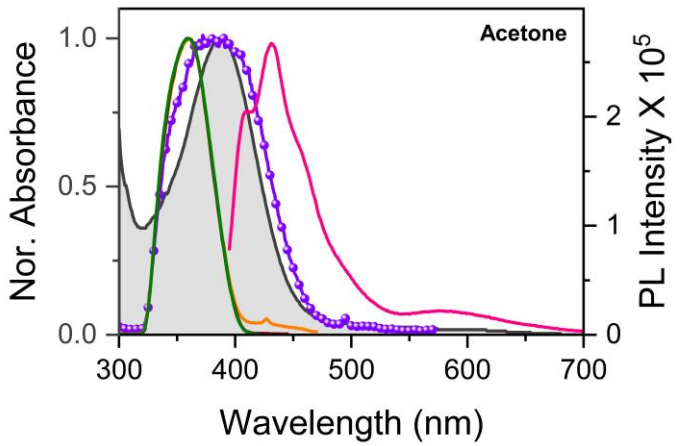	**12.09**
Acetonitrile	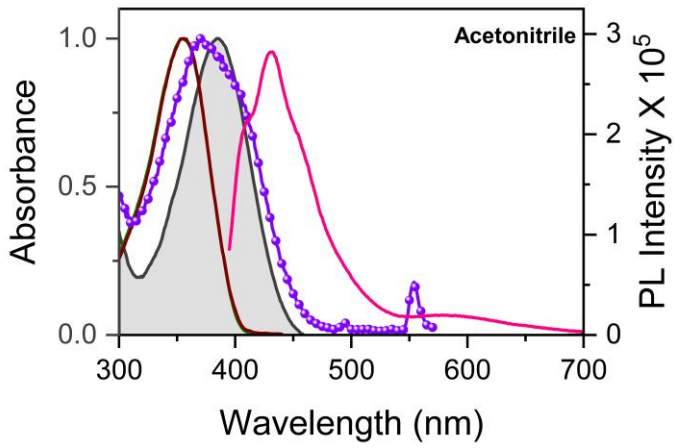	**14.7**

Dioxane	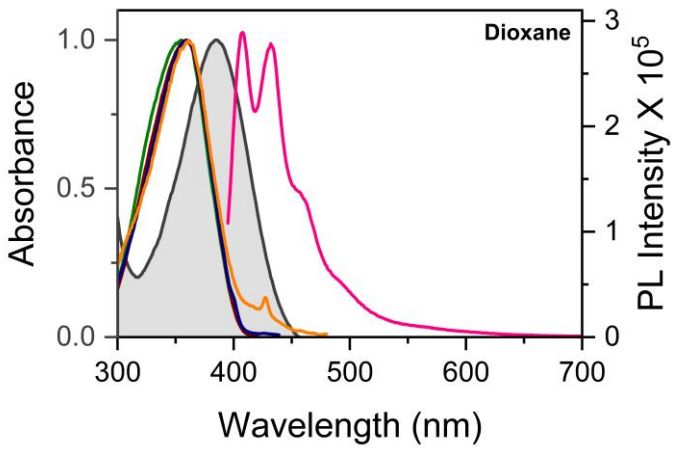	---

Table 3.1: *Solvent dependent absorbance, excitation and emission spectra and variation of ratio with the polarity of the solvent.*

Further, the excitation spectra for the enol emission and keto emission matched with its absorbance spectra showing the same ground state species responsible for the emission in the excited state (*Figure* 3.9). This is typically expected for the ESIPT compounds. However, the excitation spectra for the enol emission rather appeared more structured in comparison to the excitation spectra for the ESIPT emission (*Figure* 3.9). The excitation spectra of the enol emission showed more similarity with the excitation spectra for the emission recorded for salicylaldehyde alone in water (*Figure* 3.9). This could be due to the fact that the enol emission primarily comes from the salicylaldehyde part of the donor-acceptor system. Such a trend for salicylaldehyde Schiff bases has been seen in other unrelated systems.

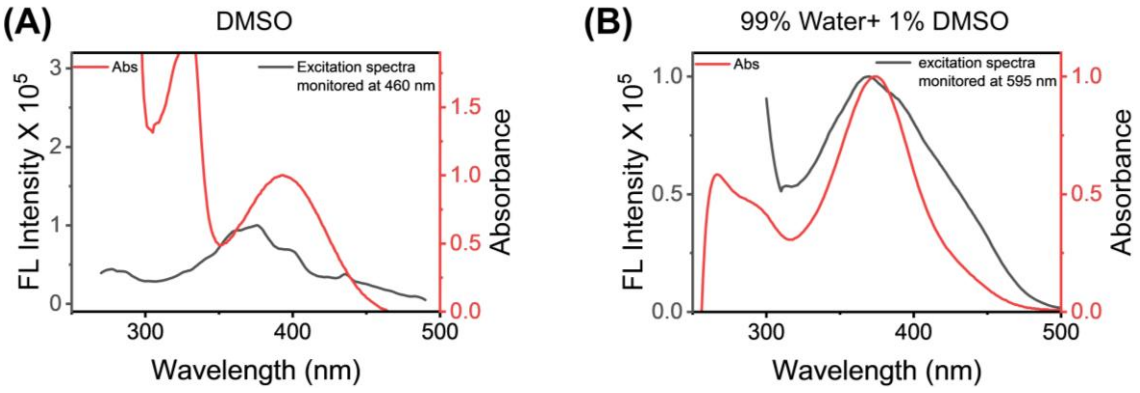

***Figure* 3.9:** *Figure showing the absorbance, excitation spectra of* **SA-Imine** *in* **A:** *DMSO and* **B:** *99% Water + 1% DMSO*

A small hump in the excitation spectra recorded for ESPIT emission in water is seen which is not matching with the absorbance spectra. The mismatch in the excitation spectra simply reflects a heterogeneity in the ground state. This could be possibly arising due to anion generated as a result of deprotonation in water. Interestingly the emission spectra recorded for **SA-Imine** in water shows a small hump at around 520- 530 nm in water. This could be the emission coming from the anion being generated in water. However, no such emission was seen in DMSO or other organic solvents. To prod into the nature of this species, experiments were taken to first populate it in the ground state. At ambient conditions, the organic solvents have tendency to absorb 5 to 10 percent of moisture. Hence, we chose to record the emissions in dry solvents to be able to understand the effect of addition of water in such systems. The emission spectra of **SA-Imine** in dry acetonitrile showed a structured enol emission centered at 420- 500 nm region and a very less intense keto emission at 580 nm (*Figure* 3.10a). As the fraction of water increased in acetonitrile up to 4 percent, the emission corresponding to the anionic form appeared at 510 nm. Likewise, a similar trend was observed in DMSO-Water system (*Figure* 3.10a). In DMSO, structured enol emission was seen and as the fraction of water increased, emission at 525 nm emerged and remained the prominent emission peak until 40 percent water composition (*Figure* 3.10b). Beyond this composition, the intensity of this peak started to drop with concomitant enhancement of keto emission at 595 nm. Interestingly, at 40 percent, the presence of aggregation in the system was clearly evident as the particle size continued to grow with increasing proportions of water as can be seen in the DLS data in *Figure* 3.10c. The emission at 520- 530 nm dominated when there were no aggregates present in the system suggesting that the emission doesn't come from aggregates formed in the systems. In fact, as the amount of water increased 99 percent, the emission at 520-530 nm almost vanished. This simply means that the emission at 525 nm comes from the anionic form. The absorbance spectra recorded at various composition of DSMO and water for **SA-Imine** further supported this argument. The absorbance of spectra of **SA-Imine** was recorded in various compositions of DMSO and water. The absorbance band initially centered at 390 nm showed a hump with increasing proportions of water. There was broadening of the spectra in the region from 400- 450 nm with substantial tailing. The tailing is due to Mie scattering which is due the formation of aggregates in the system. The broadening at 400- 450 became prominent at 70 percent composition as a hump appeared in this range as shown in *Figure* 3.10d. This hump was assigned

as the anionic form generated as result of deprotonation of the **SA-Imine** molecule. The formation of anion is dependent upon the pK_a of the system as shown in Figure 3.11a.

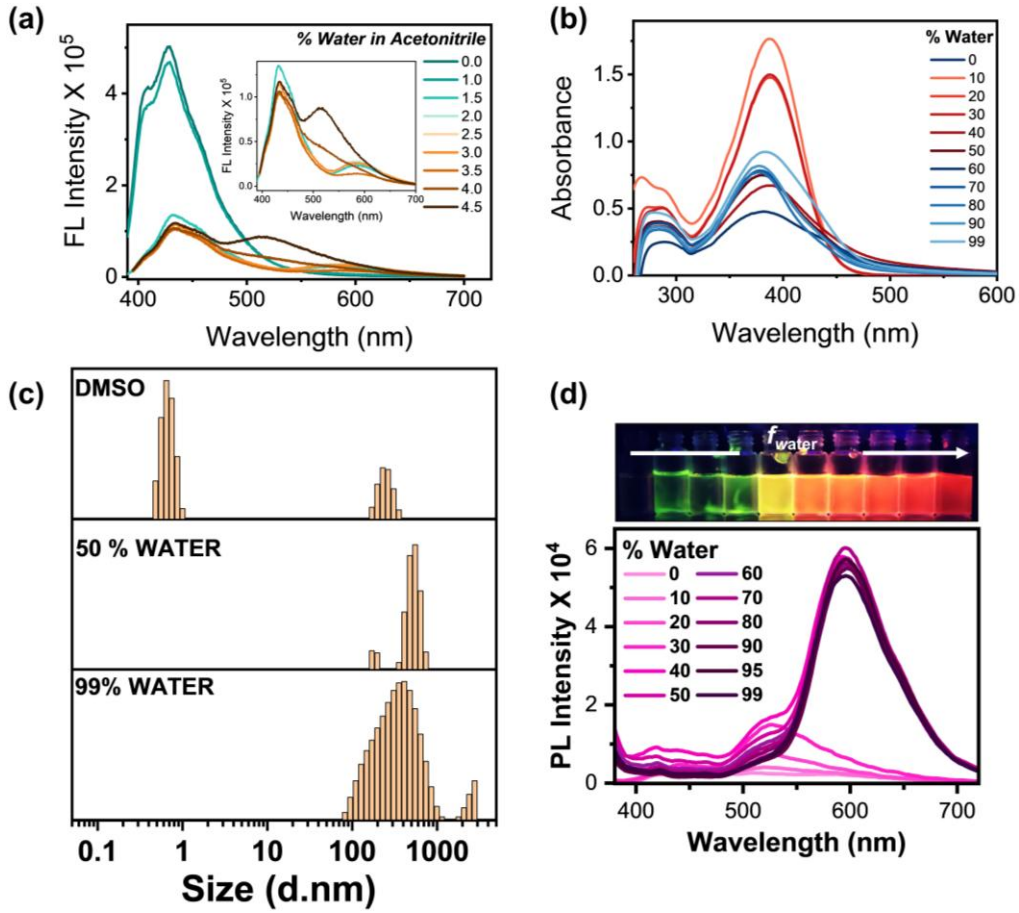

Figure* 3.10.** ***A: *Fluorescence spectra recorded for* ***SA-Imine*** *in Acetonitrile-Water system.* ***B:*** *Absorbance spectra recorded for* ***SA-Imine*** *in DMSO-Water system.* ***C:*** *DLS recorded for* ***SA-Imine*** *in various compositions of DMSO and water.* ***D:*** *Fluorescence spectra recorded for* ***SA-Imine*** *in DMSO-Water system.*

At neutral conditions, i.e. in water, the formation of anion is rather less because the -OH unit acts as a weak acid due to its high pK_a value which is greater than the pH of the neutral water. In water, the **SA-Imine** will lose its proton to the surrounding water molecules to a lesser extent. However, as the pH of the surrounding environment increases more than the pK_a of the **SA-Imine**, the proton will be readily lost to the surroundings. This will lead to the population of the anion more in the system at basic pH, whereas the reverse is true for the acidic conditions where the pH of surroundings less than the pK_a of the **SA-Imine** system will prevent the loss of the proton and thus less anion species will be produced under slightly acidic conditions.

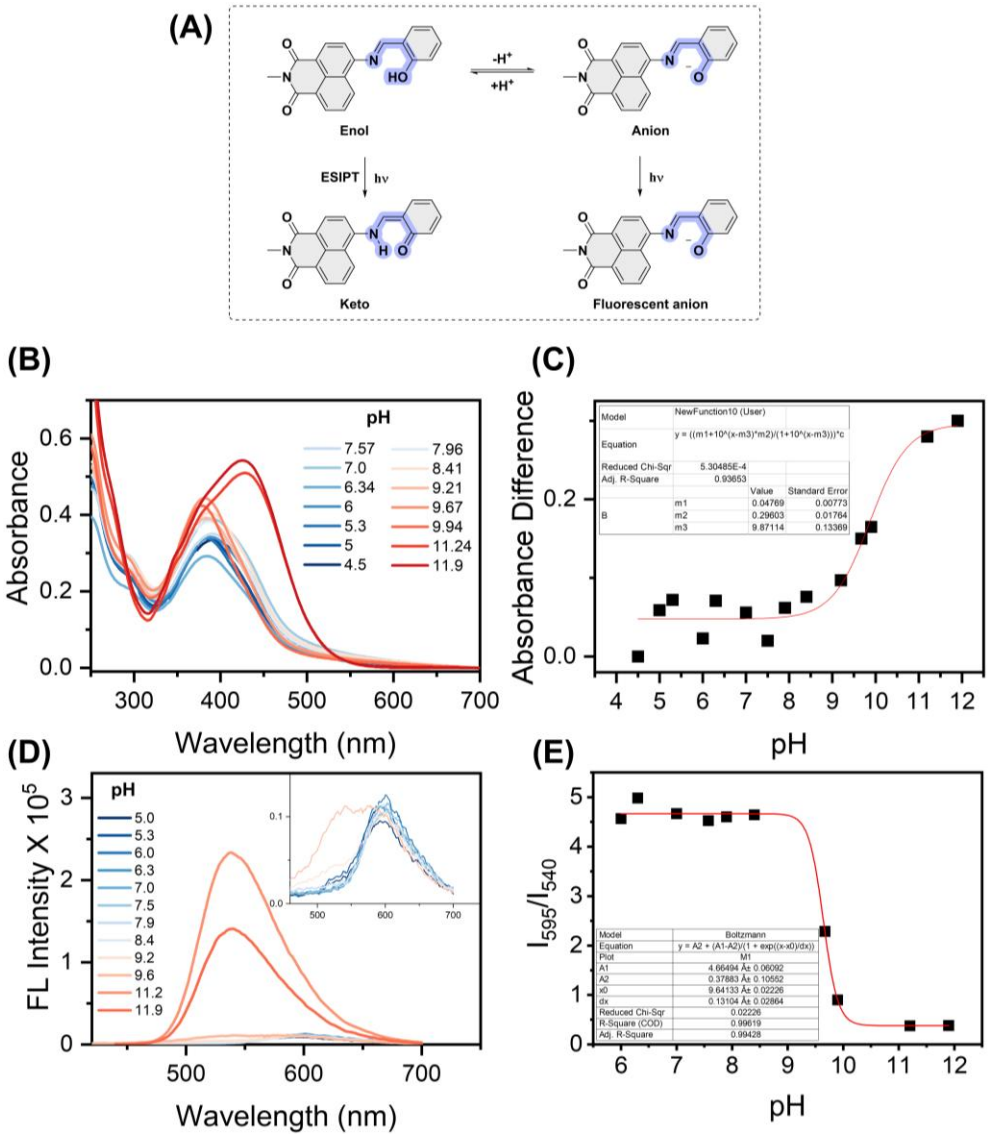

Figure* 3.11:** ***A: *Schematic showing the presence pof the anion nd enol form in water.* ***B:*** *Absorbance and fluorescence of* ***SA-Imine*** *dispersed in various buffers and* ***C:*** *Plot of the absorbance maxima difference with pH.* ***D:*** *pH dependent fluorescence profile of* ***SA-Imine.*** ***E:*** *Plot of ratio of intensity at 595/540 nm against pH for calculation of the* pK_a *of the system.*

A point to be noted here, under extreme acidic conditions, the imine will be simply hydrolyzed. Hence, we choose to work in a pH range between 6-12 where the imine bond remains stable. **SA-Imine** was dispersed in different buffers to understand the extent of its deprotonation.

To understand the deprotonation in water, the absorbance of **SA-Imine** was recorded under different pH conditions for pH 6 to pH 11.8. As expected there a clear hump centered at 425 nm appeared under basic conditions which matched with the hump present at pH 7.56 as shown in

Figure 3.11b. This suggests that at neutral pH, **SA-Imine** is slightly deprotonated to form phenoxide anion. The absorbance data recorded at various conditions for **SA-Imine** was then used to calculate the pK_a of **SA-Imine**, which came out as 9.8 as shown in Figure 3.11 c. This simply means that even at neutral pH conditions in water, some amount of the **SA-Imine** will be deprotonated. Similarly, the fluorescence behavior of **SA-Imine** under various pH conditions was then recorded. At extreme basic conditions which are physiologically irrelevant, the green emission emanating from the anionic form greatly enhanced in the system. No keto emission was seen present at extremely basic conditions. This is intuitive because the proton involved in ESIPT is essentially sequestered by the surrounding basic environment. This impedes the ESIPT process and subsequent vanishing of the keto emission centered at 595 nm under basic water conditions as shown in Figure 3.11d. Using the fluorescence data, the pK_a of **SA-Imine** was calculated which came out as 9.6 and was close to the 9.8 as calculated by the absorbance data as shown in figure 3.11c, e. Using Henderson–Hasselbalch's equation, the percentage of the anionic species present at equilibria can be calculated under neutral water conditions.

$$\mathrm{pH} = \mathrm{p}K_a + \log\frac{A^-}{HA}$$

Using this equation, the percentage of the anionic form generated under neutral water conditions i.e. pH 7.4, was calculated as < 1%. A point to be noted here is that not just pH but the extent of aggregation controls the proportions of anion and enol in the ground state. In an aggregated state, the enol form but be preserved in the aggregate environment and would contacts with the outside environment. To explore this hypothesis, various compositions of DMSO and water buffered at various compositions were tested and the associated observations and results are discussed in details in next few paragraphs. In the first system, the composition was varied from DMSO with water buffered at pH 7.4. Clearly, as the anion emission dominated up to 40 percent water composition. Following this, with the increase in water, the keto emission dominated in the system. The keto emission was centered at 593 nm in buffered water system as opposed to 595 nm in Mili-q water. It seems plausible at compositions that doesn't support aggregation, anions were freely formed and substantial anion emission was seen. However, at compositions that favored the formation of aggregates, keto emission dominated in system. This supports the hypothesis that the aggregates preserve the enol form and also prevent its interaction from the outside environment, which thereby reduces the formation of anion in the system. As shown in the schematic, in water,

the aggregates are formed that preserve the enol form and a little anion is generated. Therefore, SA-Imie upon forming aggregates in water primarily show keto emission.

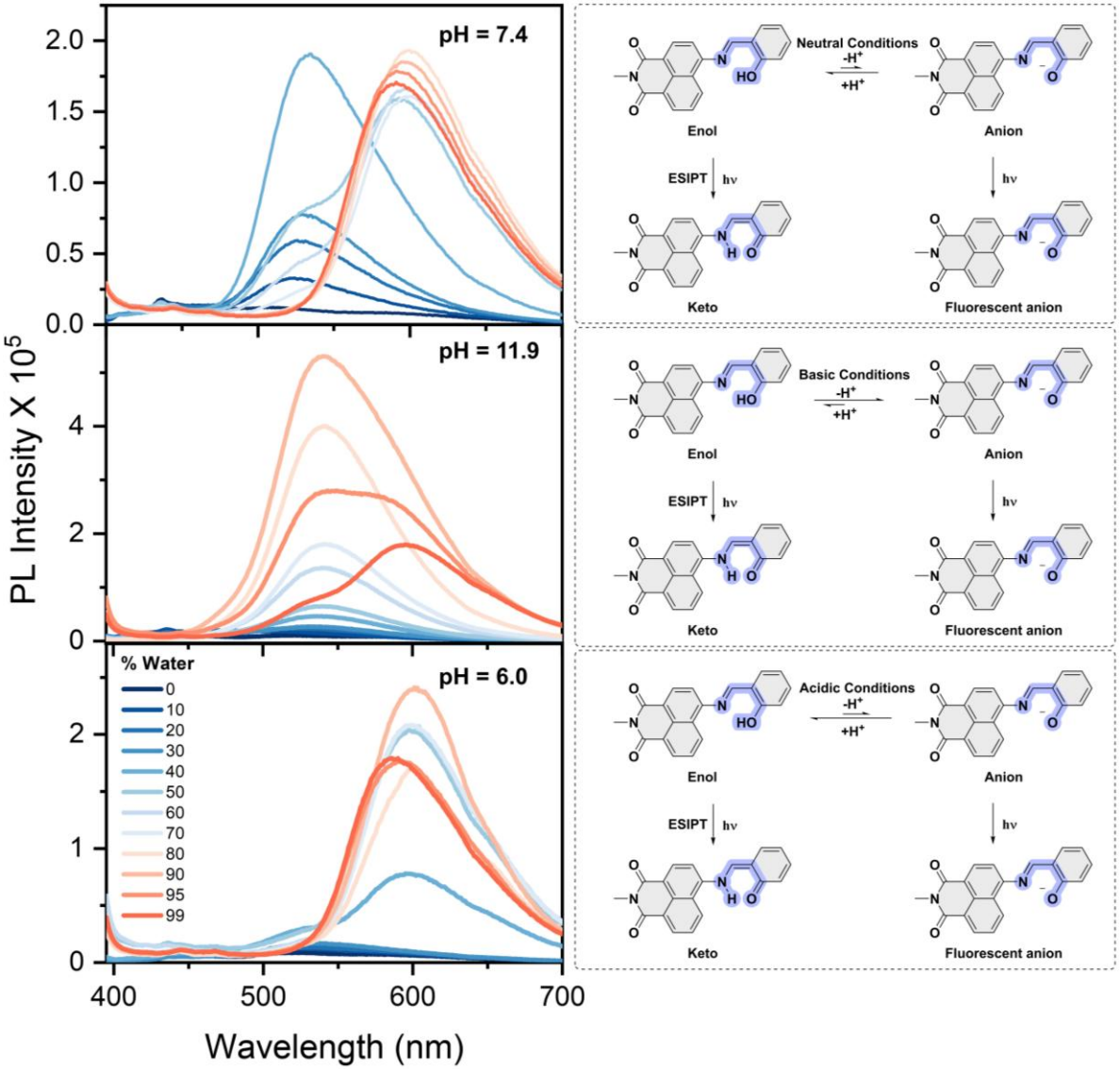

Figure* 3.12:** Fluorescence spectra recorded for **SA-Imine** in various compositions of DMSO and water buffered at ***A: pH 7.4, ***B:*** pH 11.9, and ***C:*** pH 6.0.

A small amount of anion generated shows considerable green emission in water probably due to its high quantum yield. If this hypothesis is true then an opposite trend should be seen under basic conditions because the basic conditions will favor the generation of the anion more over neutral conditions. Therefore, another composition was tried wherein composition of DMSO was varied with water buffered at pH 11.9. No keto emission was seen until 95 percent composition of water

in DMSO. This is attributed to the fact that the -OH proton is lost to the basic environment which therefore completely arrests the ESIPT phenomenon and no keto emission is seen. However, at higher water compositions, the nano-aggregates are formed that preserves some enol form that shows the keto emission along with the anion emission at 95 percent water composition and above. It is only intuitive that under acidic conditions, the proton loss of the -OH group is retarded as compared to neutral and basic conditions. As expected, as the composition of DMSO was varied with water buffered at pH 6.0, primarily keto emission was seen. The anion emission was reduced at 10- 40 percent composition and was almost suppressed at higher water fractions. It was seen that anionic emission was substantially suppressed in this composition system. It is rather expected because at acidic water conditions, the deprotonation is substantially reduced, reducing the population of anionic species formed at the equilibrium, which concomitantly leads to a decrease in the anionic emission. A clear comparison between the relative proportion so keto and anion emission can be seen at all three compositions as shown in *Figure* 3.12. It is very rational to believe that the proportion of and keto emission in water depends on both pH of the environment and extent of aggregation in a particular environment.

Further, the extent of formation of anion is dependent on the presence of water as solvent. For any weak acid, water acts as a medium to furnish the protons and the conjugate weak base in the system. However, in the absence of dissociating media, the weak acid will such as SA-imine will exist in its enol form. Hence, the anion emission should be completely absent in the crystalline state or the solid state. This seems plausible to assume that the anion emission therefore should be completely absent in the solid state of the compound. Further, as evident form the crystal structure the -OH proton remains intact in the ground state which will makes it rational to believe that the solid state should primarily show the red emission due to keto form generated upon ESIPT. To explore the above hypothesis, we next recorded the solid-state fluorescence for SA-Imine as shown in Figure 3.13a-b. It was clearly seen that SA-Imine showed red emission which matched with the red emission showed by SA-Imine in water. Due to alike emission properties of SA-Imine in water and solid state, it is plausible to believe that maximum aggregation is achieved for SA-Imine when it forms nano-aggregates in water. The pictures of the solid casted on the glass plate shows red emission under the hand-held UV lamp as can be seen in the images in Figure 3.13 b. To prove that the ESIPT emission indeed stems for the proton transfer reaction in the excited state, the solid-state spectra of BZA-Imine was further recorded which clearly was non-fluorescent in the solid

state as shown in Figure 3.13 c-d. Hence, it was proved without any doubt that red emission stems from AIE+ESIPT and not just AIE. If it was only due to AIE, then BZA-Imine would also have shown some fluorescence in the solid state.

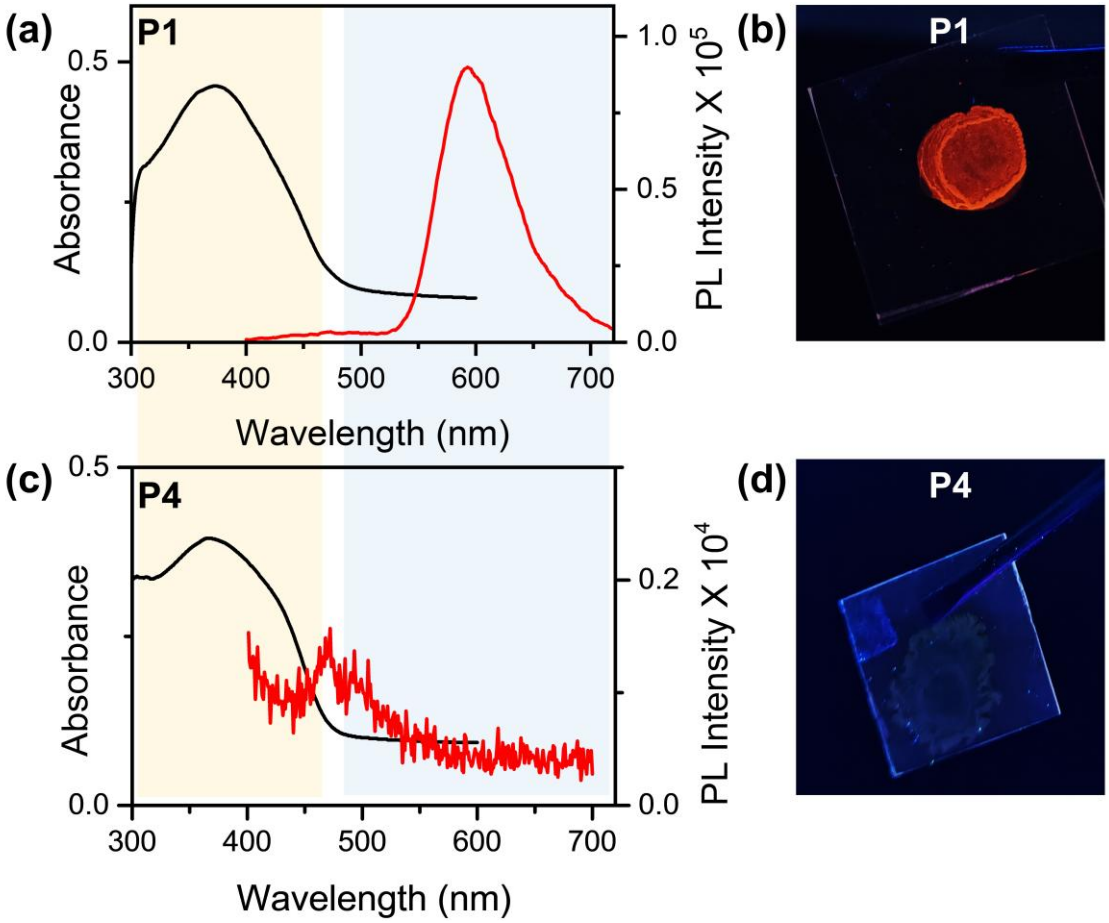

Figure* 3.13:** Solid state fluorescence spectra recorded for ***A:* SA-Imine and *B:* BZA-Imine. *C, D: *photograph under hand held UV-lamp.*

3.4.4 *Excitation Wavelength Dependent Emission (Ex-De) in SA-Imine*

The presence of two species leads to heterogeneity in the ground state, which then drastically effects the excited state properties as discussed in the previous few sections. In water, the excited state landscape is painted by both anion in green emission color and keto form in red emission color. Composition of solvent modulated the proportions of anion and keto emission, which manifested from heterogeneous ground state composed of anion and enol form.

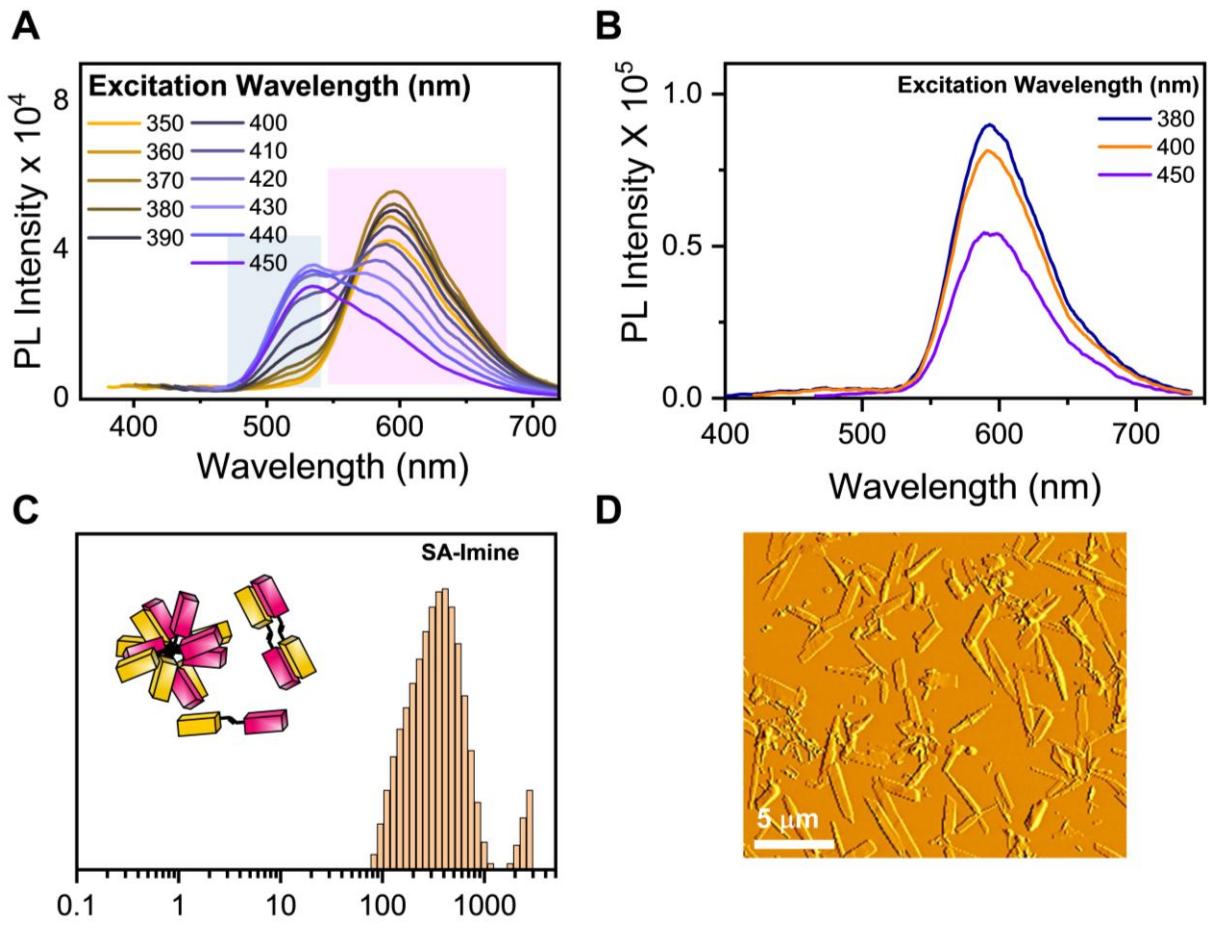

***Figure* 3.14:** *Ex-De property of **SA-Imine**. **A:** Serial Excitation-emission spectra of **SA-Imine** recorded in 1% DMSO in water and **B:** in slid state. **C:** Nano-aggregates like self-assembly of **SA-Imine** in water as confirmed by DLS and **D:** AFM.*

At this point, it is convenient to believe that there are two internal conversion (IC) channel operational in SA- Imine molecule corresponding to anion and ESIPT which is typical of Ex-De materials[40, 41]. It is obvious that the two species will emit strongly at their respective emission wavelengths but will also show considerable emission at the intermediate excitation wavelengths where both the species will be co-excited and will show dual emission signal corresponding to both the keto and the anion forms in water. We, therefore, performed a serial excitation (350- 450 nm) study to record the emission profile of ***SA-Imine*** in water, which clearly showed Ex-De property as shown in Figure 3.14a. Excitation at 350-370 nm in water resulted in ESIPT emission accompanied by a subtle anion emission. Anion emission comparable to ESIPT emission was seen at intermediate excitation wavelengths (390- 420 nm), whereas anion emission dominated at higher

excitation wavelengths (*Figure* 3.14a). A heterogeneous ground state comprising of anion and enol forms in water, gives rise to both anion and ESIPT emission, leading to Ex-De (*Figure* 3.14a). The presence of non-uniform nano-aggregates formed in 1% DMSO in water was confirmed by AFM and DLS profiles (*Figure* 3.14c, d).

Interestingly, the excitation wavelength dependent emission spectra recorded for SA-Imine in solid state showed red emission irrespective of the excitation wavelength as shown in Figure 3.14b. This is clearly opposite to what was seen for SA-Imine when dispersed in water, where the emission due to both the keto form and the anion were seen. This clearly tells that SA-Imine in its aggregated or solid form shows red keto emission due to ESIPT. However, the heterogeneity stems in its aqueous dispersions, where apart from forming nano-aggregates it forms anions. The formation of aggregates and anions leads to Ex-De.

The detailed photophysics conducted for SA-Imine can be summarized as follows:

1. **In organic solvents:** In the most stripped-down version, the emission of **SA-Imine** in organic solvents comes form the enol and the keto forms whose population depends on the polarity and protacity of the solvent. Generally, the keto emission is seen to more prominent in solvents of low polarity that lack the tendency of intermolecular hydrogen bonding interactions with **SA-Imine**. Typically, in non-polar solvents like cyclohexane, toluene, chloroform, ethyl acetate a prominent keto emission is seen along with the enol emission. However, in polar solvents with a tendency of intermolecular hydrogen bonding interactions with SA-Imine, the keto emission is absent or is present with less intensity.
2. **In water and buffers:** The -OH group ortho to -C=N- linkage is slightly acidic and therefore SA-Imine acts as a weak base in water. The pK_a of SA-Imine was calculated as 9.6$\pm$0.2. This leads to slight deprotonation at neutral water conditions leading to generation of anionic species in the ground state that leads to anionic emission centered at 520- 530 nm. This emission is seen to be enhanced under basic conditions with concomitant decrease in the ESIPT emission. As expected, the formation of anionic form is reduced which leads to a reduction in the anionic emission under slightly acidic conditions.
3. **Ex-De in water:** The ground state of SA-Imine in water possesses heterogeneity stemming from the equilibria existing between the enol and the anion forms. This ground state heterogeneity is manifested to a greater extent in the excited state as evident from an equi-

intense keto and anionic emission, when excited at their respective excitation wavelengths and intermediate excitation wavelengths. Specifically, when excited at 405 nm, which is generally excitation laser employed for confocal microscopic imaging, an equal intensity keto and anion emission was seen under neutral water conditions.

However, for biological studies, employing 405 nm laser, such dual emission will pose a problem as the green emission stemming from the anion is close by to the emission of the amine molecule generated upon hydrolysis of the imine bond. This will simply lead to misinterpretation or artifacts in the data. An exclusive red emission for endosome labeling and green emission only upon hydrolysis in lysosomes was desired. A heterogeneous ground state leads to Ex-De properties, which could be modulated by changing the electronics of the molecule by the introduction of various electronic substituents and by promoting self-assembly that will shield the interaction of the enol form with the outside water. We first attempted to modulate emission properties of **SA-Imine** by introducing electronic substituents as discussed ahead. In other words, the effects of electronics and self-assembly on pK_a of SA-Imine was studied. By changing the pK_a of the parent chromophore, the extent of formation of anion at equilibria in the ground state can be greatly controlled.

3.4.5 *Effect of Electronic Substituents on photophysics of SA-Imine*

Having established an unexpected Ex-De property in **SA-Imine**, we thought of ways to structurally engineer the chromophore to get exclusively get ESIPT emission. A simple literature survey made us realize the effect of electronic substitution can help modulate the emission properties of the chromophore. In simple words, the pK_a of any weak acid and weak base can be tuned through the substituent effect[42, 43]. We carried out our investigation with electron withdrawing; **-NO_2** group and electron donating; **-$N(Et)_2$** and **-$C_{15}H_{31}$** alkyl chain group. The molecules were synthesized as shown in synthetic scheme in *Figure* 3.1 and characterized by 1H NMR and were subjected to a routine photophysical analysis. The absorbance and emission properties of the synthesized three molecules were checked in solvents of varying polarity at a concentration of 1μM in the solvents tested (*Figure* 3.15). Compound with electron withdrawing NO_2 group; NTR-Imine and electron donating -$C_{15}H_{31}$ group; PDP-Imine showed identical absorbance profiles (*Figure* 3.15a, b). However, the absorbance spectra of compound with electron donating -$N(Et)_2$ group, DET-Imine led to red shift in the absorbance spectra (*Figure* 3.15c).

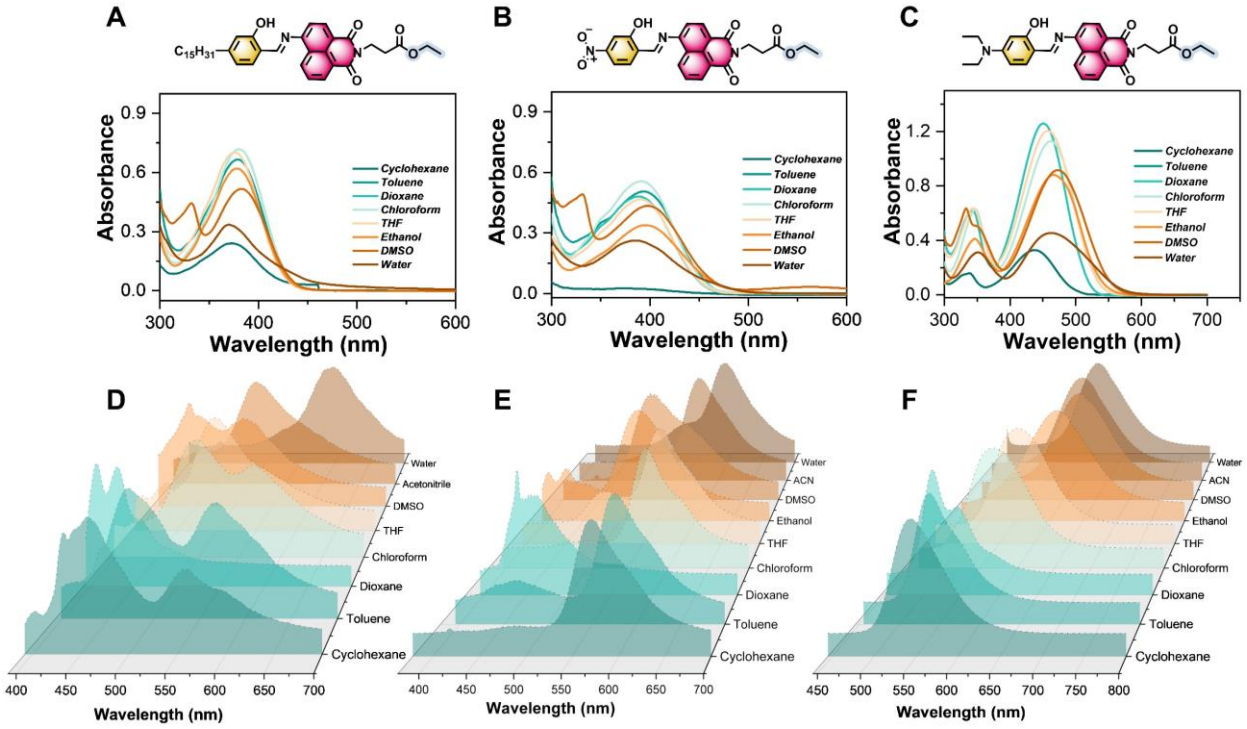

Figure* 3.15:** *Photophysical characterization of substituted derivatives. Absorbance and emission profiles of* ***A: *PDP-Imine,* ***B:*** *NTR-Imine, and* ***C:*** *DET-Imine in various solvents.*

This clearly is suggestive of the charge transfer nature of the state, which enhances as the push pull nature in the molecule increases. However, electron donating group **-**$C_{15}H_{31}$ had little to no effect on the emission properties (*Figure* 3.15d). It mimicked the emission properties of the parent molecule. However, a point worth noticing is the extreme hydrophobic nature of this molecule which causes precipitation as the sample ages with time. Lower concentrations of 0.2 μM was used to record the spectra and to avoid the process of precipitation. However, the presence of electron withdrawing group; -NO_2 seemed to effect both the intensity and position of ESIPT emission band (*Figure* 3.15e). There was a blue shift observed in ESIPT emission along with anion emission of considerable intensity was seen in water, which was very subtle in the parent molecule. Overall, the presence of anion emission was snot suppressed with the -NO_2 substitution. The presence of electron donating, **-N(Et)$_2$** had unexpected outcome. The absorbance maxima were clearly fond to be red shifted as compared to the parent molecule. The broad intramolecular charge transfer (ICT) band originating from the mixing of π-π*and n-π* states was red shifted in comparison to the parent molecule. However, the charge transfer was manifested in the excited

state much more strongly than the ground state (*Figure* 3.15f). There was a bathochromic in the emission maxima along with the reduction in the fluorescence intensity which is the characteristic feature of an ICT dye (***Figure*** 3.15f).

The presence of dimethylamine group disturbed ESIPT reaction and favored ICT intermolecular charge transfer more over the Proton transfer reaction. Hence, this led to complete disappearance of ESIPT emission in the system. It was realized that proton transfer reactions are extremely delicate to the environment and are rather result of serendipity. Modulations in terms of electronics can altogether disturb the delicate balance of electronics and molecular orientation which bought ESIPT reaction in the first place in SA-Imine. Thinking of alternative mechanisms to modulate Ex-De emission properties of **SA-Imine** without comprising on the ESIPT emission, we thought of employing self-assembly, with an effort of minimally perturbing this delicate balance of electronics and molecular orientation. The effect of self-assembly is discussed in next section.

3.4.6 *Effect of Self- Assembly on pKa of SA-Imine*

Molecular cooperativity is the hallmark of self-assembled systems in which the self-assembled system behaves differently from the isolated building components[44]. Thinking of ways, one could enforce cooperativity in the system by tuning the hydrophobic-hydrophilic balance[45, 46]. Self-assembly enhances ground state homogeneity by forming coherently ordered structures leading to modulation in emission properties[46-48] . Further, it is known that the pK_a of dyes can be altered greatly by nano-confinement such as micelles and vesicles[49, 50]. The properties of the solubilizes can be altered to greater extent upon solubilization in the pseudo phases of the micellar self-assembly. So is the case with the weak acids where the pK_a of the acid-base indicator in the presence of the micellar assembly can be expected to be different from that in water. This difference could be due to the combination of both the medium and the electrostatic effect[49]. The medium effect comprises of the shift in the pK_a due to change in polarity of the medium, dielectric constant of the medium. Many weak acids and bases have been studied for their acid base equilibria in presence and absence of various surfactants. Surfactants such as CTAB, Triton X, CTABr, Bri 35 have been investigated thoroughly and difference in the pK_a of the indicator in presence and absence of the surfactant has been observed. Particularly, for Triton X for that being a neutral surfactant, has been seen to affect the pK_a of the phenol containing indicators in a drastic manner.

The Δ pK_a (pK_a in presence of the surfactant- pK_a in the aqueous solution) is seen to be varied between 0.4 to 1.7 for most of the naphthol molecules studied in the paper[49].

Ensuing this, a hydrophilic PEG-chain (Mn= 750 g/mol) was incorporated in the molecular design to balance the hydrophobicity of ***SA-Imine***, resulting in ***PEG-SA-Imine*** (See *Figure* 3.4, 3.16). The amphiphilic molecules were characterized via analytical techniques as shown in appendix A9-A13.

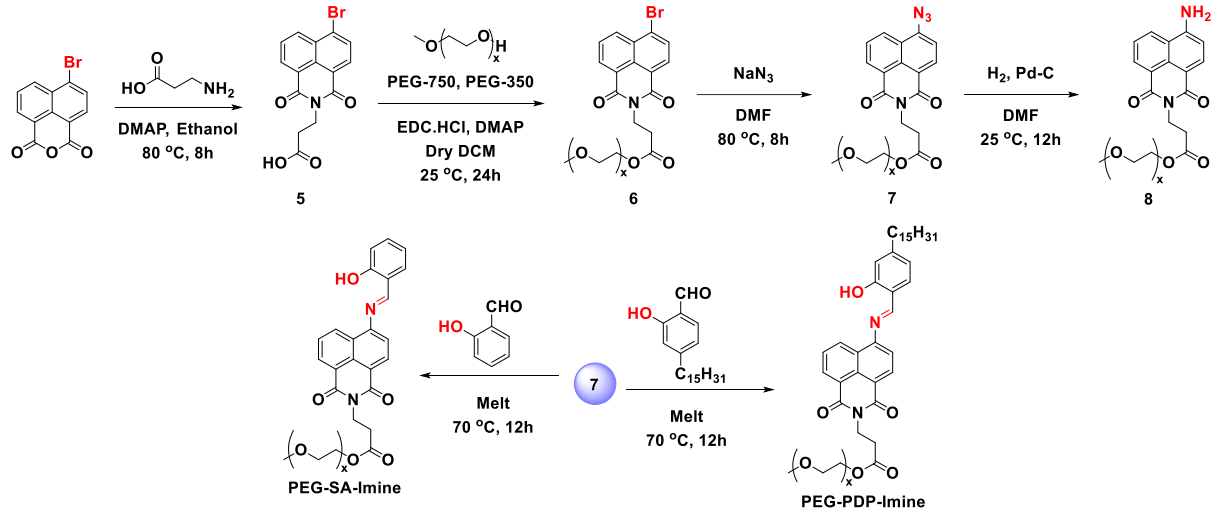

Figure* 3.16:** *Synthetic scheme for the amphiphilic derivatives of* ***SA-Imine*.*

For this, 4-Bromo naphthalimide was coupled with PEG chain via imide linkage yielding molecule 5 which upon subsequent chemical reactions was converted into molecule PEG-ylated naphthalimide amine; **PEG-Naph**. It retained its fluorescent chemical properties even after chemical conjugation with the PEG chain. The photophysical properties of PEG-Naph was characterized in various solvents and water and its self-assembly property was also studied as shown in *Figure* 3.17. The PEG-Naph molecule showed high molar extinction coefficient and quantum yield as calculated for DMSO and water.

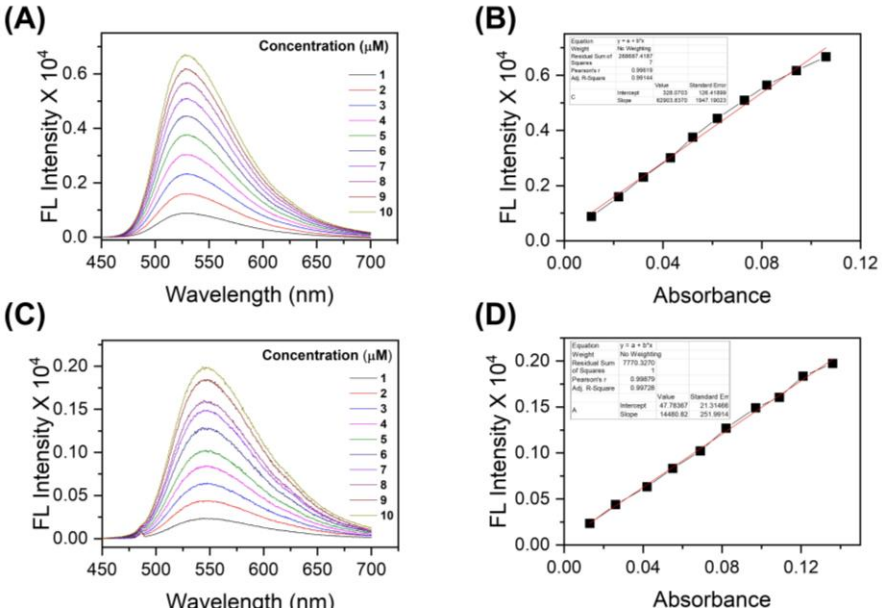

Figure* 3.17:** *Quantum yield calculation for PEG-Naph in* ***A: *DMSO and* ***B:*** *Water.*

PEG-Naph showed emission in the range of 510 in toluene to 540 nm in water as shown in *Figure* 3.18a. The emission showed a decent red shift with increase in the solvent polarity from toluene to water as shown in *Figure* 3.18a. The solid state of the PEG-Naph showed green emission which matched with its solution state properties as shown in *Figure* f-g.

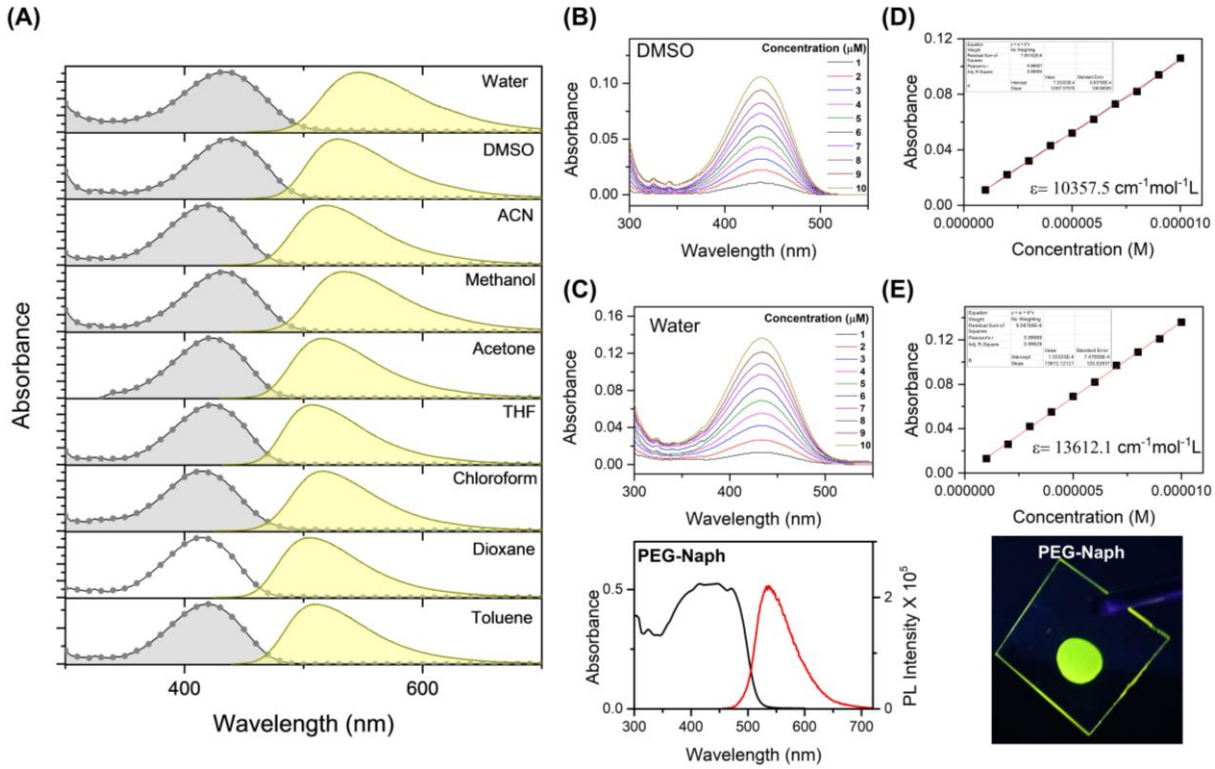

Figure 3.18: ***A:*** *Fluorescence spectra of PEG-Naph recorded in various solvents.* ***B:*** *Molar extinction coefficient calculation for PEG-Naph in* ***C:*** *DMSO and* ***D:*** *Water.* ***E:*** *Solid state absorbance and fluorescence spectra for PEG-NAPH and* ***F:*** *photograph under hand held UV lamp.*

The synthesized PEG-Naph was then condensed with salicylaldehyde, resulting in the formation of ***PEG-SA-Imine***. To our dismay, ***PEG-SA-Imine*** exhibited enol emission centered 420- 490 nm and an anionic emission centered at 540 nm, with complete disappearance of ESIPT properties (*Figure* 3.19a).

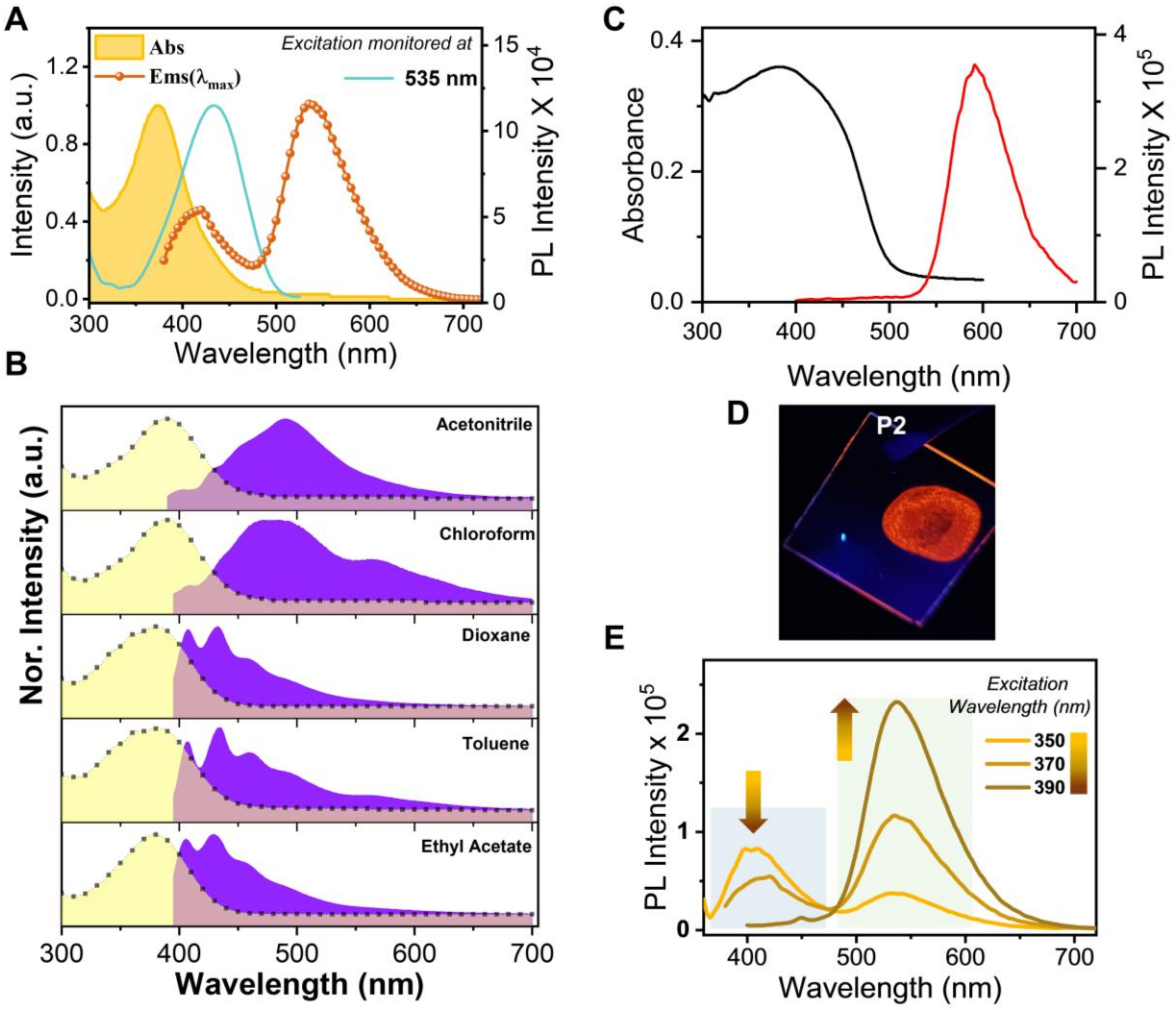

Figure* 3.19:** *Photophysical properties of* ***PEG-SA-Imine*. **A:** Fluorescence spectra for SA-Imine in water. **B:** Solvent dependent absorbance and emission profile of* ***PEG-SA-Imine. C:*** *The solid-state absorbance and emission of* ***PEG-SA-Imine. D:*** *Solid state photograph under hand held UV lamp.* ***E:*** *Excitation wavelength dependent emission of* ***PEG-SA-Imine*** *in water switching primarily enol to exciplex emission with increase in excitation wavelength.*

This happened because the system ended up being highly soluble in water. The enhanced solubility increased the intermolecular hydrogen bonding interactions with water which led to increase in the enol emission and the disappearance of the keto emission. The enol emission was comparatively higher for PEG-SA-Imine as compared to SA-Imine in water. This is because the lack of ESIPT reaction in the excited state which lead to enhancement in the enol emission instead. The enhancement in the intermolecular interactions with water molecules not just led to disappearance of the ESIPT emission but also favored the formation of anion in water. The anion formed in water

showed green emission as see in the case of SA-Imine discussed in the previous sections. No sizes were detected via DLS experiment, supporting the fact that the PEG-SA-Imine molecule was not amphiphilic enough to promote the formation of micellar self-assemblies which would afford environment that would further prevent the formation of the anion in water. SA-Imine shows no ESIPT emission due to lack of aggregation in the water medium and is freely soluble that promotes the formation of anion that shows green emission. If this hypothesis is true, then PEG-SA-Imine is anticipated to show red emission via ESIPT in the solvents of low polarity which do not promote solvent assisted intermolecular hydrogen bonding interactions. Further, the fluorescence properties of SA-Imine studied in solvents of various polarity and proticity confirmed the existence of ESIPT as shown in Figure 3.19 b. In the solvents of low polarity such as toluene, chloroform, PEG-SA-Imine showed emission emanating from both the enol and the keto form. The presence of keto emission in solvents of low polarity and solid state establishes the fact that the introduction of PEG chains apart from altering the solubility of chromophore in water, didn't change the tendency of the chromophore to undergo ESIPT reaction. Further, as the water promotes the formation of anions in water, this process should be arrested in solid state as mentioned previously for the case of SA-Imine. To this end, the solid-state fluorescence properties of PEG-SA-Imine was recorded. As expected, the solid-state properties of PEG-SA-Imine were analogous to that of SA-Imine as shown in *Figure* 3.19c-d. The solid casted on the glass plate showed intense red emission. This confirms our hypothesis that the high solubility of PEG-SA-Imine impedes its aggregation in water and thereby promotes the formation of anion and leads to green emission emanating from the anion.

Due to presence of both the enol and the anion species in water, the PEG-SA-Imine showed dual emission in water. It showed Ex-De properties as it was serially excited from 350 to 390 nm, where emission altered from enol to anion at higher wavelength (*Figure* 3.19e). To balance the amphiphilicity in PEG-SA-Imine, attempts were made to decrease the PEG chain length. Working with lower chain; Mn= 350, formed visible precipitates in water, hence, was not used further (data not shown).

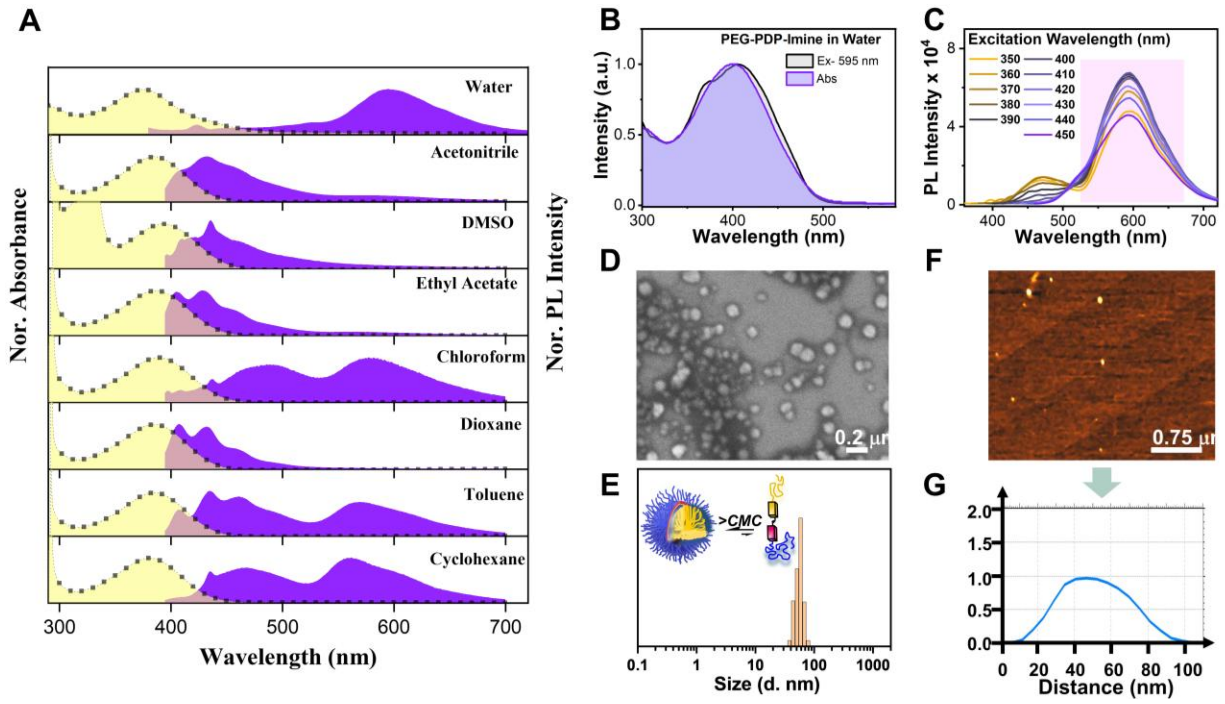

Figure* 3.20:** *Photophysical properties of PEG-PDP-Imine.* ***A: *Solvent dependent absorbance and emission profile of PEG-**SA-Imine.** **B:*** *The excitation spectra monitored for 595 nm emission in water.* ***C:*** *Excitation wavelength dependent emission of PEG-PDP-Imine in water showing ESIPT emission primarily with increase in excitation wavelength.* ***D:*** *FE-SEM,* ***E:*** *DLS,* ***F:*** *AFM and* ***G:*** *AFM height profile confirming the micellar nature of PEG-PDP-Imine in water.*

To get an exclusive ESIPT emission over anion whilst maintaining the amphiphilicity was a sweet spot, hard to attain! To strike the right balance of amphiphilicity, salicylaldehyde unit was then replaced with an alkyl chain bearing analogue; PDP-aldehyde (*Figure* 3.4). Introduction of alkyl chain substitution from the donor side was a cautious choice to balance the amphiphilicity. We first synthesized a control molecule ***PDP-Imine***, long tail analogue of ***SA-Imine*** (*Figure* 3.4). It had identical photophysical properties as that of ***SA-Imine*** as shown in *Figure* 3.15d. Next, the imine formation of PDP-aldehyde with PEG-Naph amine (*Figure* 3.14) afforded ***PEG-PDP-Imine*** and product formation was confirmed analytically (*Figure* A13- A19). PEG-PDP-Imine showed dual emission just like its analogues SA-Imine and PEG-SA-Imine in solvents of different polarity. It showed ESIPT emission in non-polar solvents such as Toluene cyclohexane and chloroform. To our relief, it self-assembled in water to form micelles (henceforth called ***nano-emitter***) and showed intense ESIPT emission free of anion emission in water (*Figure* 3.20). Self-assembly often causes

a red shift in the absorbance; it absorbs at 400 nm in water which is 15 nm redshifted compared to other organic solvents (Figure 3.20).[48] This enhancement is due to self-assembly which then also causes increase in quantum yield (~2.2%) of the ESIPT emission of ***nano-emitter***[51]. The excitation spectra recorded for the 595 nm emission showed a high overlap with its absorbance spectra, with negligible component from the anion (Figure 3.20).

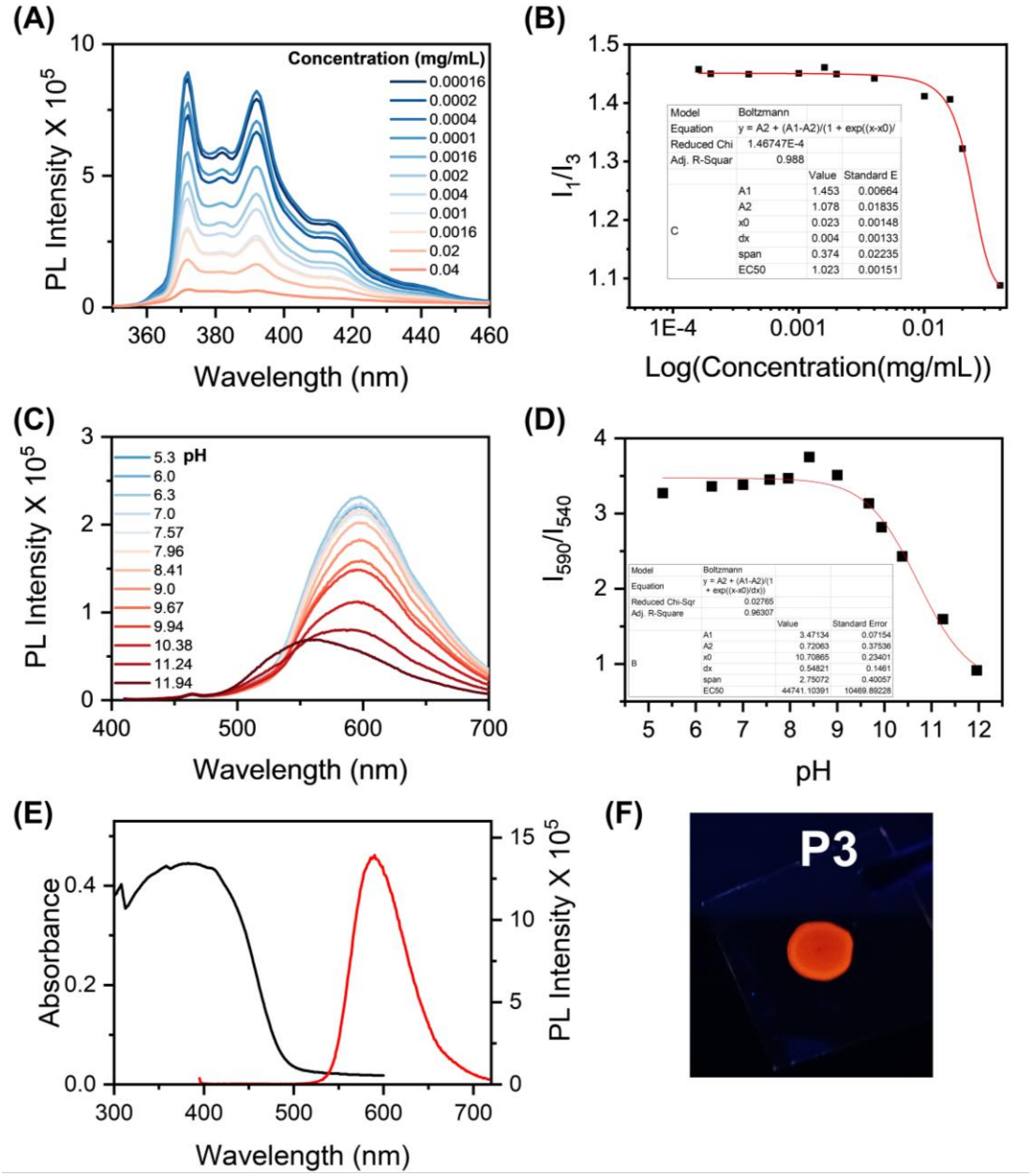

Figure* 3.21:** *Photophysical properties of PEG-PDP-Imine.* ***A: *Pyrene probe experiment for calculating CMC of the probe in water and* ***B:*** *variation of its I_1/I_3 ratio with concentration.* ***C:*** *Variation of the fluorescent profile with pH of the solution.* ***D:*** *Plot of its I_{590}/I_{540} ratio with pH of the solution.* ***E:*** *Solid state absorbance and fluorescent profile of PEG-PDP-Imine and* ***F:*** *its photograph under hand held UV lamp.*

Micellar self-assembly directed the chromophore unit to form tight hydrophobic core which was stabilized in water by protruding PEG chains (Figure 3.20). The self-assembly pushed the hydrophobic core inside the micellar self-assembly. The tiny micellar nano-architecture was confirmed by DLS that showed 10- 15 nm sized particles by number average DLS (Figure 3.20). This corroborated with AFM, FESEM data and TEM data (Figure 3.20). AFM height profile clearly showed 50- 60 nm particles (Figure 3.20). CMC experiment conducted sing pyrene as probe confirmed the formation of self-assembled structures as evident form the decreasing I_1/I_3 value of the pyrene probe when it encountered the hydrophobic environment of the forming self-assembly as sown in Figure 3.21a-b. Pyrene is a fluorophore whose vibration levels are sensitive to the environment of the fluorophore it is into. Its I_1/I_3 is close to 1.8 when it senses water environment but as a self-assembly due to the surfactant is formed and that the pyrene molecule goes inside the self-assembly, it senses a more hydrophobic environment which leads to the reduction in the value. The CMC is then calculated form the plot of I_1/I_3 vs. the concentration of the amphiphile. The CMC for PEG-PDP-Imine came out as 0.02 mg/mL in water. The self-assembly shielded the chromophore units from coming in contact with water and that prevented the formation of anion. This was also evident form the increased pK_a of the PEG-PDP-Imine system as shown in Figure 3.21c-d. It is a well-established fact in literature that the pK_a of the chromophores are known to increase as they are encapsulated inside the micellar or higher ordered self-assemblies. The micellar aggregates effectively shielded the chromophore form outside environment, thereby preventing its interaction with water which further prevented he formation of the anion species and suspended ground state heterogeneity responsible for Ex-De as shown in Figure 3.20. The micellar assembly necessarily provided a suitable environment that exclusively promoted ESIPT. The nano-emitter showed no Ex-De property and primarily showed ESIPT emission even at higher wavelength, making it suitable for bioimaging applications employing 405 nm lasers. The emission seen in self-assembled state in water matches with the solid-state fluorescence spectra recorded for PEG-PDP-Imine as shown in Figure 3.21e-f, which essentially tells that maximum packing closest to solid state has been achieved in the self-assembled state in water. ***Nano-emitter*** showed an optically pure emission at 595 nm solely arriving from ESIPT,

when excited using 405 nm laser, successfully fulfilling the foremost criterion of design parameters. Next, the synthesized probes were checked for imaging applications in cells.

3.4.7 *Behaviour of Probes in Bioimaging*

After the structure was engineered to achieve the desired photophysical properties, the compounds were tested in cells to determine if there was any coherence between the photophysics observed in vitro and those observed in the cells.

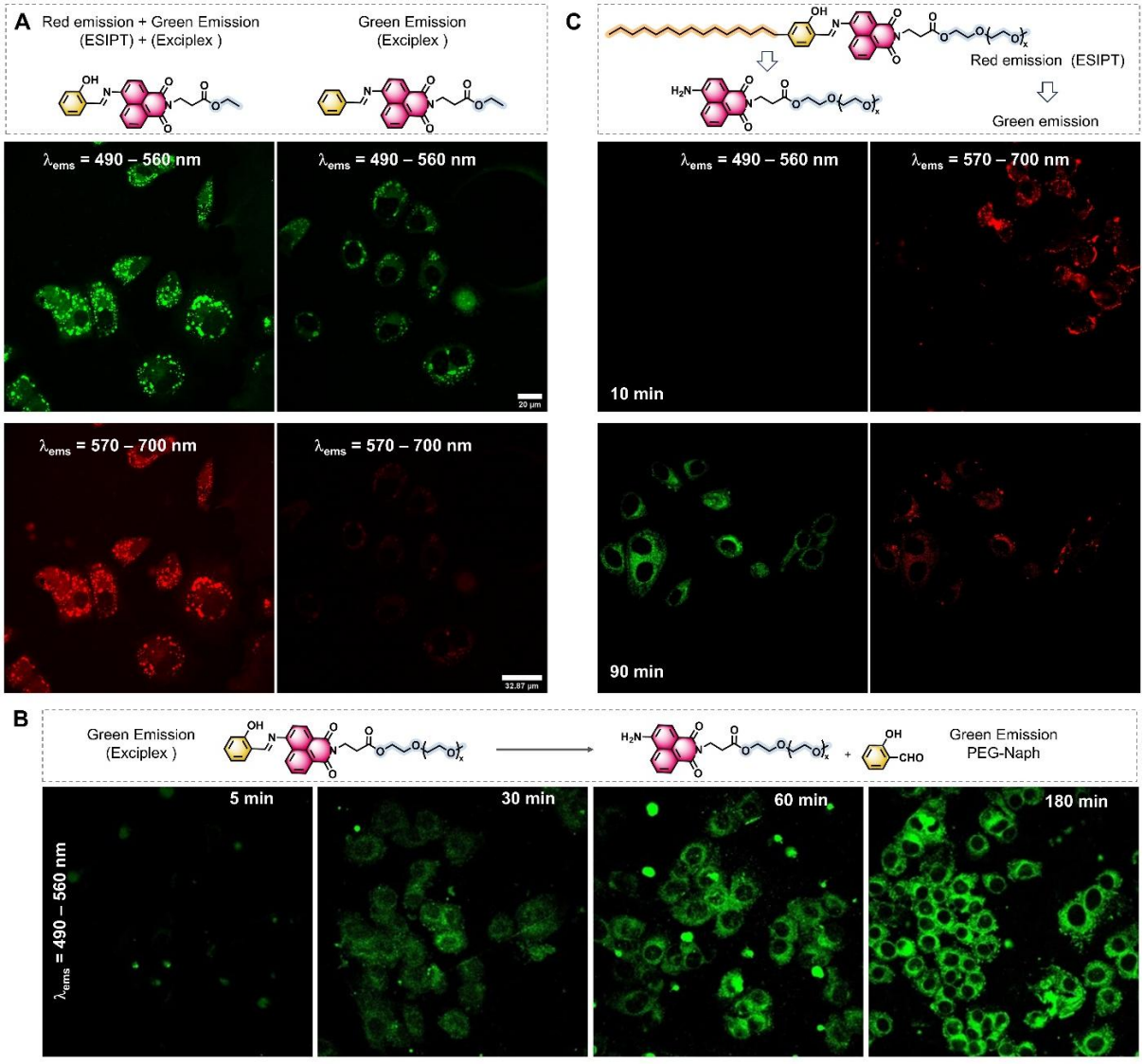

Figure* 3.22:** *Cellular imaging with synthesized probes.* ***A: *Cellular imaging was done using* ***SA-Imine*** *and with control molecule BZA-Imine and emission was collected in two channels; red (λ_{ems}= 600- 720 nm) and green (λ_{ems}= 490- 550 nm) channel respectively.* ***B:*** *Time dependent imaging was carried out for PEG-****SA-Imine****.* ***C:*** *Time dependent imaging was carried out for PEG-PDP-Imine and emission was collected in red and green channels. Excitation laser used in all cases: 405 nm.*

The following compounds namely; **SA-Imine**, BZA-Imine, **PEG-SA-Imine**, PEG-PDP-Imine and DET-Imine were tested for bio imaging applications. Due to high hydrophobicity induced precipitating nature of PDP-Imine and slightly toxicity of NTR-Imine, these two compounds were not analyzed in biological imaging. For bioimaging, 405 nm confocal laser was used. As anticipated, **SA-Imine** indeed showed two emission signals in the cells for it showed good intensity signals in both the green (λ_{ems}= 490- 550 nm) and red channels (λ_{ems}= 600- 720 nm) created (Figure 3.22a). To confirm, if the intensity in the red channel was due to ESIPT and not due to any spectral spill over from green channel, we imaged BZA-Imine inside the cells. BZA-Imine due to lack of ESIPT emission, showed only green emission as discussed earlier. A likewise results were observed in the cells (Figure 3.22a). No emission in the red channel was seen for BZA-Imine, which help us conveniently believe that the emission in the red channel was indeed the ESIPT emission coming from **SA-Imine** (Figure 3.22a). The green emission could have originated from the hydrolysis of the probes under acidic conditions.

Next, a time dependent experiment was done where the hydrolysis of the probe in a time dependent manner will sure show an enhancement in the intensity in the green channel like an intensiometric probe. **SA-Imine** due to its anion mediated green emitting nature could be easily confused for the green emission coming from the hydrolysis of the probe as it was highlighted earlier. There was appreciable green emission seen coming from the anion form even at neutral conditions. This emission could be easily be confuse for emission coming due to hydrolysis of probe under acidic conditions. Further, SA-Imine due to its tendency to form micron sized aggregates in water, showed precipitation onto the cell surface, making the imaging experiments really challenging to reproduce. After having confirmed this hypothesis to image cells, we further discontinued any studies with **SA-Imine**. We instead checked for intensiometric properties with ***PEG-SA-Imine*** which was seemingly a better choice over **SA-Imine** to study for intensiometric response of fluorophore in the cells. ***PEG-SA-Imine*** shows only green anion emission like BZA-Imine. However, due to its solubilizing PEG group, ***PEG-SA-Imine*** dissolved perfectly in culture media and offer distinct advantage over BZA-Imine. An intensiometric probe shows an

enhancement in the fluorescence intensity upon participating in a chemical reaction or binding with analyte. In this case, ***PEG-SA-Imine*** upon incubation in cells showed a residual green emission at 5 minutes, which continued to increase visibly in a time dependent manner as shown in Figure 3.22b We continued our systematic investigation with PEG-PDP-Imine next in the series to justify our rationale for structural engineering to design an ESIPT probe that gave stable ESIPT emission in water. PEG-PDP-Imine was self-assembled in water using extrusion employing 0.05μm filter. The self-assembled nanoparticles were the diluted with media and was pulsed for 5 minutes and then chased for 10 and 90 minutes respectively before being fixed for cellular imaging Figure 3.22c. As shown earlier, PEG-PDP-Imine showed primarily red emission due to ESIPT. Indeed, the cells glowed red when imaged using 405 nm laser at 10 minutes. To our delight, after 90 minutes, green emission could be seen coming from the cells when shined with a 405 nm laser. This could have happened due to the traversing of nano-emitter from endosomes to more acidic lysosomes. Delighted with this, we carried out extensive set of experiments to monitor the interactions between endosomes and lysosomes in real time. We subsequently found that such interactions are instrumental in sequestering of drug molecules as introduced in chapter-1. The detailed investigation and results are summed in the chapter-4.

DET-Imine showed a highly stokes shifted emission which was highly dependent on the polarity of the medium. Such a dye with ICT characteristics and highly stokes shifted emission finds extensive applications in the field of lipid droplets. Lipid droplets are unique cellular organelles in with a hydrophobic lipid ester core, which is surrounded by a phospholipid monolayer. These organelles are involved in storage of fatty acids and are also suspected store houses of various enzymes. These lipid droplets also serve as a platform for the degradation of various hydrophobic proteins. Due to its involvement in storage of fatty acids, it is implied in fatty liver diseases and many other pathologies. There are commercially available to stain lipid droplets like Nile Red etc. to stain these suspicious organelles. However, these probes suffer from low stokes shift and hence the problem of self-absorption while imaging. DET-Imine has a similar di-ethyl unit as that in Nile red and such a unit is known to target lipid droplets. We checked for the ability of DET-Imine for staining lipid droplets. To our surprise, the probe quickly stains lipid droplets of the cells in no time. We live imaged cells following incubation of probe for 5 minutes. DET-Imine seems to stain round and large cellular organelles with high contrast in DIC. These round organelles with high contrast in DIC are suspected lipid droplets. Lipid droplets due to their oily core has a better

refractive index and hence these organelles appear high contrasting compared to other subcellular structure in DIC imaging. These organelles were exclusively stained with DET-Imine as shown in Figure 3.23a, b.

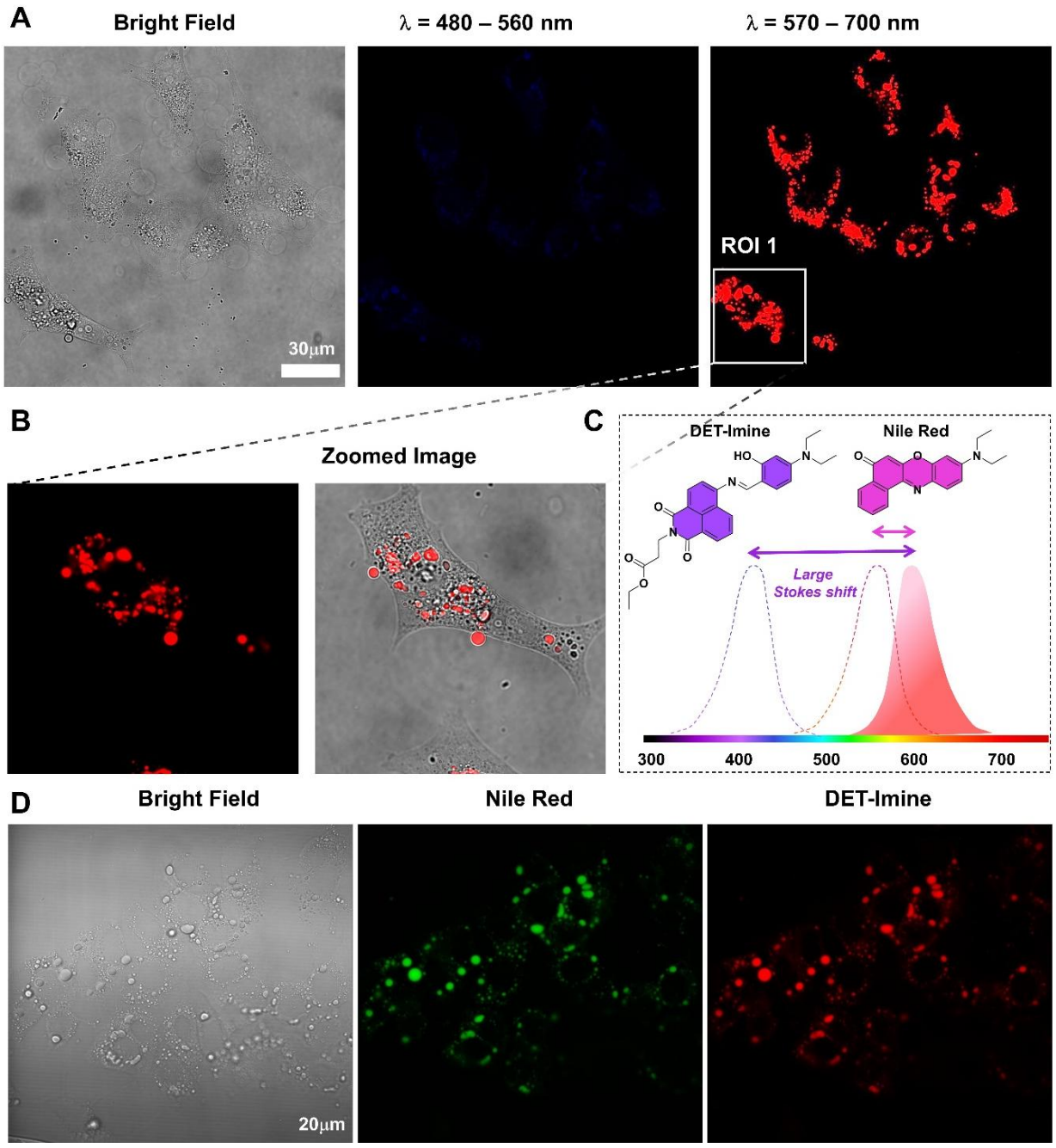

Figure* 3.23:** *Lipid droplet staining with synthesized probe.* ***A: *Confocal images of the cells incubated with DET-Imine that exclusively marks lipid droplets of the cells.* ***B:*** *The zoomed image for a given ROI shows distinct structure of lipid Droplet with a core illuminated with red fluorescence emanating from*

DET-Imine. ***C:*** *Cartoon sketch of excitation and emission spectra shown for Nile red and DET-Imine.* ***D:*** *Co-staining of lipid droplets with Nile red and DET-Imine.*

To really confirm the identity of these suspected lipid droplets, we co-stained cells with DET-Imine and Nile-red Figure 3.23c. Nile-red is excitable using 564 nm laser and emits in the red region, whereas DET-Imine is excitable using a 405 nm laser and emits in the red channel as shown in Figure 3.23c. The sample was co-excited using both the lasers and DET-Imine was given a pseudo color of red for the intensity collected in red channel. Likewise, Nile-Red for the intensity collected in the red channel upon excitation using 564 nm laser was given a pseudo color green. Both green and red emission happen to come from the same sub cellular structures Figure 3.23d. Hence, DET-Imine was able to annotate lipid droplets of the cells with greater ease. However, these results are rather preliminary and are currently under investigation and project details of which are summarized in future directions section of this thesis.

3.5 Conclusion

The study aimed to structure engineer a pH responsive ESIPT probe that give stable ESIPT emission in water and which upon pH mediated hydrolysis gives another fluorescence color. This was done with an aim to use this probe for monitoring interactions between endocytic organelle which have an inherent pH gradient. However, the design of ESIPT probes for bioimaging applications in water is rather challenging. This is due to competitive intermolecular interactions in the water which competes with the intramolecular proton transfer reaction, thus rendering most ESIPT dyes not suitable for bioimaging applications. We addressed this challenge by employing two intuitive approaches. 4 amino naphthalimide dye with green fluorescence was stitched to salicylaldehyde via imine linkage. However, the synthesized parent dye, **SA-Imine** showed dual emission stemming from ESIPT and anion. This dual emission resulted in Ex-De. Two approaches were employed to modulate the emission properties of the parent molecule, **SA-Imine**. The first approach studied the effect of electronic substitution with electron withdrawing and electron donating group, which seem to disturb the ESIPT emission. A decrease in intensity and blue shit in the emission maxima corresponding to ESIPT was seen in the case of electron withdrawing, nitro group. However, a complete vanishing and instead appearance of ICT emission was seen in presence of electron donating substituent; Diethyl amine. It was evident that ESIPT is a delicate combination of electronics and molecular geometries. Employing self-assembly was realized as a

simple yet elegant strategy to modulate emission Behaviour of **SA-Imine** without disturbing its delicate electronics and geometry crucial for ESIPT. A combination of hydrophobic and hydrophilic balance in **SA-Imine** resulted in PEG-PDP-Imine that showed exclusive ESIPT emission upon self-assembly into small miscelles in water. Next, the proof of concept of structurally optimized probes was checked in cell lines. PEG-PDP-Imine showed red emission emanating from cells and green emission emanated from cellular organelles in a time dependent manner. Further, we also checked for the utility of DET-Imine for imaging lipid droplets inside the cells. DET-Imine indeed stains lipid droplets of the cells with great ease. However, the results are rather preliminary and will be addressed in the future. Overall, a methodological, intuitive yet simple approach was employed to structurally optimize a pH sensitive ESIPT dye with stable ESIPT emission in water. The utility of PEG-PDP-Imine for monitoring endosome and lysosome interaction are extensively discussed in next chapter.

3.6 Bibliography

(1) Casey, J. R.; Grinstein, S.; Orlowski, J. Sensors and regulators of intracellular pH. *Nat. Rev. Mol. Cell Biol.* **2010**, *11* (1), 50-61.
(2) Waddell, W. J.; Bates, R. G. Intracellular pH. *Physiol. Rev.* **1969**, *49* (2), 285-329.
(3) Doyen, D.; Poët, M.; Jarretou, G.; Pisani, D. F.; Tauc, M.; Cougnon, M.; Argentina, M.; Bouret, Y.; Counillon, L. Intracellular pH Control by Membrane Transport in Mammalian Cells. Insights Into the Selective Advantages of Functional Redundancy. *Front. mol. biosci.* **2022**, *9*, Review.
(4) Brian, T. E.; John, M.; John, C. pH Regulation of the F-actin Binding Properties of Dictyostelium Elongation Factor 1α(∗). *J. Biol. Chem.* **1995**, *270* (25), 15222-15230.
(5) Gao, W.; Chan, J. M.; Farokhzad, O. C. pH-Responsive Nanoparticles for Drug Delivery. *Mol. Pharmaceutics* **2010**, *7* (6), 1913-1920.
(6) Dong, X.; Brahma, R. K.; Fang, C.; Yao, S. Q. Stimulus-responsive self-assembled prodrugs in cancer therapy. *Chem. Sci.* **2022**, *13* (15), 4239-4269, 10.1039/D2SC01003H.
(7) Taresco, V.; Alexander, C.; Singh, N.; Pearce, A. K. Stimuli-Responsive Prodrug Chemistries for Drug Delivery. *Adv. Ther.* **2018**, *1* (4), 1800030.
(8) Sedgwick, A. C.; Wu, L.; Han, H.-H.; Bull, S. D.; He, X.-P.; James, T. D.; Sessler, J. L.; Tang, B. Z.; Tian, H.; Yoon, J. Excited-state intramolecular proton-transfer (ESIPT) based fluorescence sensors and imaging agents. *Chem. Soc. Rev.* **2018**, *47* (23), 8842-8880, 10.1039/C8CS00185E.
(9) Munan, S.; Yadav, R.; Pareek, N.; Samanta, A. Ratiometric fluorescent probes for pH mapping in cellular organelles. *Analyst* **2023**, *148* (18), 4242-4262, 10.1039/D3AN00960B.
(10) Greenhill, J. V. Enaminones. *Chem. Soc. Rev.* **1977**, *6* (3), 277-294, 10.1039/CS9770600277.
(11) Bourgeaux, M.; Skene, W. G. A Highly Conjugated p- and n-Type Polythiophenoazomethine: Synthesis, Spectroscopic, and Electrochemical Investigation. *Macromolecules* **2007**, *40* (6), 1792-1795.
(12) Tsuchiya, M.; Sakamoto, R.; Shimada, M.; Yamanoi, Y.; Hattori, Y.; Sugimoto, K.; Nishibori, E.; Nishihara, H. β-IminoBODIPY oligomers: facilely accessible π-conjugated luminescent BODIPY arrays. *Chemical Communications* **2017**, *53* (54), 7509-7512, 10.1039/C7CC03279J.
(13) Sedgwick, A. C.; Dou, W.-T.; Jiao, J.-B.; Wu, L.; Williams, G. T.; Jenkins, A. T. A.; Bull, S. D.; Sessler, J. L.; He, X.-P.; James, T. D. An ESIPT Probe for the Ratiometric Imaging of Peroxynitrite Facilitated by Binding to Aβ-Aggregates. *J. Am. Chem. Soc.* **2018**, *140* (43), 14267-14271.
(14) He, L.; Dong, B.; Liu, Y.; Lin, W. Fluorescent chemosensors manipulated by dual/triple interplaying sensing mechanisms. *Chem. Soc. Rev.* **2016**, *45* (23), 6449-6461, 10.1039/C6CS00413J.
(15) Rao, K. V.; George, S. J. Synthesis and Controllable Self-Assembly of a Novel Coronene Bisimide Amphiphile. *Organic Letters* **2010**, *12* (11), 2656-2659.
(16) González-Rodríguez, D.; Schenning, A. P. H. J. Hydrogen-bonded Supramolecular π-Functional Materials. *Chem. Mater.* **2011**, *23* (3), 310-325.
(17) Molla, M. R.; Ghosh, S. Aqueous self-assembly of chromophore-conjugated amphiphiles. *Physical Chemistry Chemical Physics* **2014**, *16* (48), 26672-26683, 10.1039/C4CP03791J.
(18) Görl, D.; Zhang, X.; Würthner, F. Molecular Assemblies of Perylene Bisimide Dyes in Water. *Angew. Chem. Int. Ed.* **2012**, *51* (26), 6328-6348.

(19) Chen, X.; Zhang, S.; Jiang, Y.; He, G.; Zhang, M.; Wang, J.; Deng, Z.; Wang, H.; Lam, J. W. Y.; Hu, L.; et al. Turning Non-Emissive Schiff Bases Into Aggregate Emitters. *Angew. Chem. Int. Ed.* **2024**, *63* (19), e202402175.
(20) Jayabharathi, J.; Thanikachalam, V.; Jayamoorthy, K.; Srinivasan, N. Synthesis, spectral studies and solvatochromism of some novel benzimidazole derivatives – ESIPT process. *Spectrochimica Acta Part A: Molecular and Biomolecular Spectroscopy* **2013**, *105*, 223-228.
(21) Mei, J.; Leung, N. L. C.; Kwok, R. T. K.; Lam, J. W. Y.; Tang, B. Z. Aggregation-Induced Emission: Together We Shine, United We Soar! *Chem. Rev.* **2015**, *115* (21), 11718-11940.
(22) Tang, W.; Xiang, Y.; Tong, A. Salicylaldehyde Azines as Fluorophores of Aggregation-Induced Emission Enhancement Characteristics. *The Journal of Organic Chemistry* **2009**, *74* (5), 2163-2166.
(23) Cao, X.; Zeng, X.; Mu, L.; Chen, Y.; Wang, R.-x.; Zhang, Y.-q.; Zhang, J.-x.; Wei, G. Characterization of the aggregation-induced enhanced emission, sensing, and logic gate behavior of 2-(1-hydroxy-2-naphthyl)methylene hydrazone. *Sensors and Actuators B: Chemical* **2013**, *177*, 493-499.
(24) Xiao, H.; Chen, K.; Cui, D.; Jiang, N.; Yin, G.; Wang, J.; Wang, R. Two novel aggregation-induced emission active coumarin-based Schiff bases and their applications in cell imaging. *New Journal of Chemistry* **2014**, *38* (6), 2386-2393, 10.1039/C3NJ01557B.
(25) Wei, R.; Song, P.; Tong, A. Reversible Thermochromism of Aggregation-Induced Emission-Active Benzophenone Azine Based on Polymorph-Dependent Excited-State Intramolecular Proton Transfer Fluorescence. *The Journal of Physical Chemistry C* **2013**, *117* (7), 3467-3474.
(26) Devasia, J.; Aishwarya, B. N.; Joy, F.; Nizam, A. ESIPT-AIE Active Schiff Base Fluorescent Organic Nanoparticles Based on 2-(2-(4-(4-bromo Phenyl) Thiazol-2-yl)Vinyl)Phenol (BTVP) Utilized as a Multi-Functional Fluorescent Probe. *Advanced Optical Materials* **2023**, *11* (23), 2300966.
(27) Peng, L.; Xu, S.; Zheng, X.; Cheng, X.; Zhang, R.; Liu, J.; Liu, B.; Tong, A. Rational Design of a Red-Emissive Fluorophore with AIE and ESIPT Characteristics and Its Application in Light-Up Sensing of Esterase. *Analytical Chemistry* **2017**, *89* (5), 3162-3168.
(28) Kwon, J. E.; Park, S. Y. Advanced Organic Optoelectronic Materials: Harnessing Excited-State Intramolecular Proton Transfer (ESIPT) Process. *Advanced Materials* **2011**, *23* (32), 3615-3642.
(29) Bhattacharyya, A.; Das, A.; Guchhait, N. Investigating the Photophysical Aspects of a Naphthalene-Based Excited-State Proton Transfer Dye 1-(1H-Benzo[d]imidazol-2-yl)naphthalen-2-ol: pH-Dependent Modulation of Photodynamics. *The Journal of Physical Chemistry A* **2024**, *128* (18), 3495-3505.
(30) Stoerkler, T.; Retailleau, P.; Jacquemin, D.; Ulrich, G.; Massue, J. Heteroaryl-Substituted Bis-Anils: Aggregation-Induced Emission (AIE) Derivatives with Tunable ESIPT Emission Color and pH Sensitivity. *Chem. Eur. J.* **2023**, *29* (14), e202203766.
(31) Munch, M.; Ulrich, G.; Massue, J. Synthesis and Optical Properties of Excited-State Intramolecular Proton Transfer (ESIPT) Emitters with Sulfobetaine Fragments. *Organic & Biomolecular Chemistry* **2022**, *20* (22), 4640-4649, 10.1039/D2OB00691J.
(32) Lee, M. H.; Park, N.; Yi, C.; Han, J. H.; Hong, J. H.; Kim, K. P.; Kang, D. H.; Sessler, J. L.; Kang, C.; Kim, J. S. Mitochondria-Immobilized pH-Sensitive Off–On Fluorescent Probe. *Journal of the American Chemical Society* **2014**, *136* (40), 14136-14142.

(33) Choi, S.-A.; Park, C. S.; Kwon, O. S.; Giong, H.-K.; Lee, J.-S.; Ha, T. H.; Lee, C.-S. Structural effects of naphthalimide-based fluorescent sensor for hydrogen sulfide and imaging in live zebrafish. *Scientific Reports* **2016**, *6* (1), 26203.
(34) Amarnath, N.; Appavoo, D.; Lochab, B. Eco-Friendly Halogen-Free Flame Retardant Cardanol Polyphosphazene Polybenzoxazine Networks. *ACS SustainableChem.Eng.* **2018**, *6* (1), 389-402.
(35) Haldar, R.; Rao, K. V.; George, S. J.; Maji, T. K. Exciplex Formation and Energy Transfer in a Self-Assembled Metal–Organic Hybrid System. *Chem. Eur. J.* **2012**, *18* (19), 5848-5852.
(36) Kapuria, N.; Sharma, V.; Kumar, P.; Koner, A. L. Exploration of dynamic self-assembly mediated nanoparticle formation using perylenemonoimide–pyrene conjugate: a tool towards single-component white-light emission. *J. Mater. Chem. C* **2018**, *6* (42), 11328-11335, 10.1039/C8TC03730B.
(37) El-Bayoumi, M. A.; El-Aasser, M.; Abdel-Halim, F. Electronic spectra and structures of Schiff's bases. I. Benzanils. *J. Am. Chem. Soc.* **1971**, *93* (3), 586-590.
(38) Kandappa, S. K.; Valloli, L. K.; Ahuja, S.; Parthiban, J.; Sivaguru, J. Taming the excited state reactivity of imines – from non-radiative decay to aza Paternò–Büchi reaction. *Chem. Soc. Rev.* **2021**, *50* (3), 1617-1641, 10.1039/D0CS00717J.
(39) Klymchenko, A. S.; Shvadchak, V. V.; Yushchenko, D. A.; Jain, N.; Mély, Y. Excited-State Intramolecular Proton Transfer Distinguishes Microenvironments in Single- And Double-Stranded DNA. *J. Phys. Chem. B.* **2008**, *112* (38), 12050-12055.
(40) Zhang, Y.; Yang, H.; Ma, H.; Bian, G.; Zang, Q.; Sun, J.; Zhang, C.; An, Z.; Wong, W.-Y. Excitation Wavelength Dependent Fluorescence of an ESIPT Triazole Derivative for Amine Sensing and Anti-Counterfeiting Applications. *Angew. Chem. Int. Ed.* **2019**, *58* (26), 8773-8778.
(41) Man, Z.; Lv, Z.; Xu, Z.; Liu, M.; He, J.; Liao, Q.; Yao, J.; Peng, Q.; Fu, H. Excitation-Wavelength-Dependent Organic Long-Persistent Luminescence Originating from Excited-State Long-Range Proton Transfer. *J. Am. Chem. Soc.* **2022**, *144* (28), 12652-12660.
(42) Stratton, S. G.; Taumoefolau, G. H.; Purnell, G. E.; Rasooly, M.; Czaplyski, W. L.; Harbron, E. J. Tuning the pKa of Fluorescent Rhodamine pH Probes through Substituent Effects. *Chem. Eur. J.* **2017**, *23* (56), 14064-14072.
(43) Mazi, W.; Adhikari, R.; Zhang, Y.; Xia, S.; Fang, M.; Luck, R. L.; Tajiri, M.; Tiwari, A.; Tanasova, M.; Liu, H. Fluorescent probes with high pKa values based on traditional, near-infrared rhodamine, and hemicyanine fluorophores for sensitive detection of lysosomal pH variations. *Methods* **2019**, *168*, 40-50.
(44) Li, Y.; Wang, Y.; Huang, G.; Gao, J. Cooperativity Principles in Self-Assembled Nanomedicine. *Chem. Rev.* **2018**, *118* (11), 5359-5391.
(45) De Greef, T. F. A.; Smulders, M. M. J.; Wolffs, M.; Schenning, A. P. H. J.; Sijbesma, R. P.; Meijer, E. W. Supramolecular Polymerization. *Chem. Rev.* **2009**, *109* (11), 5687-5754.
(46) Fukaya, N.; Ogi, S.; Sotome, H.; Fujimoto, K. J.; Yanai, T.; Bäumer, N.; Fernández, G.; Miyasaka, H.; Yamaguchi, S. Impact of Hydrophobic/Hydrophilic Balance on Aggregation Pathways, Morphologies, and Excited-State Dynamics of Amphiphilic Diketopyrrolopyrrole Dyes in Aqueous Media. *J. Am. Chem. Soc.* **2022**, *144* (49), 22479-22492.
(47) Han, K.-H.; Lee, E.; Kim, J. S.; Cho, B.-K. An Extraordinary Cylinder-to-Cylinder Transition in the Aqueous Assemblies of Fluorescently Labeled Rod−Coil Amphiphiles. *J. Am. Chem. Soc.* **2008**, *130* (42), 13858-13859.

(48) Wang, Q.; Zhang, Q.; Zhang, Q.-W.; Li, X.; Zhao, C.-X.; Xu, T.-Y.; Qu, D.-H.; Tian, H. Color-tunable single-fluorophore supramolecular system with assembly-encoded emission. *Nat. Commun* **2020**, *11* (1), 158.
(49) El Seoud, O. A. Effects of organized surfactant assemblies on acid-base equilibria. *Advances in Colloid and Interface Science* **1989**, *30*, 1-30.
(50) McHedlov-Petrossyan, N. O.; Vodolazkaya, N. A.; Doroshenko, A. O. Ionic Equilibria of Fluorophores in Organized Solutions: The Influence of Micellar Microenvironment on Protolytic and Photophysical Properties of Rhodamine B. *Journal of Fluorescence* **2003**, *13* (3), 235-248.
(51) Zhou, Z.; Hauke, C. E.; Song, B.; Li, X.; Stang, P. J.; Cook, T. R. Understanding the Effects of Coordination and Self-Assembly on an Emissive Phenothiazine. *J. Am. Chem. Soc.* **2019**, *141* (8), 3717-3722.

Chapter 4

ESIPT-Active Nano-emitter Mediated Real-Time Tracking of Endosome-Lysosome Dynamics for Elucidating Drug Sequestration in Live Cells.

4.1 Abstract

Vesicle trafficking is a fundamental process in cellular biology, involving fusion and fission events between membranous organelles like lysosomes and late endosomes. Lysosomes, once considered mere waste disposal units, are now recognized for their diverse roles in autophagy regulation and exocytosis. Disruptions in lysosome biogenesis, whether increased in cancer or impaired in rare diseases, profoundly affect cellular function. Understanding these dynamics is crucial for drug delivery systems utilizing endocytic pathways. However, current labeling techniques often suffer from limitations like spectral cross-talk or inefficacy in abnormal organelle states. Emerging monochromatic, dual-emission single-molecule probes offer promising solutions. Here, we present a pH-responsive probe utilizing ESIPT reaction, capable of distinctly labeling endosomes and lysosomes under monochromatic excitation. This probe enables real-time tracking of fusion-fission events between organelles, shedding light on drug sequestration mechanisms within lysosomes. Leveraging monochromatic excitation enhances imaging speed and reduces phototoxicity, providing a versatile tool for studying intracellular dynamics and drug sequestration mechanisms. Our findings support the hypothesis that fusion-fission interactions between acidic vesicles contribute to the persistence of sequestered drugs within cells, offering valuable insights for therapeutic interventions.

4.2 Introduction

Vesicle trafficking involving fusion and fission between membranous organelles is at the heart of cellular biology, as it is inextricably involved in myriad functions ranging from constitutive secretion to housekeeping tasks like endocytosis[1]. Enzyme-loaded lysosomes interact and exchange contents with cargo-loaded late endosomes via transient or complete fusion, forming endo-lysosomes that facilitate catabolic degradation[2]. Beyond their colloquial role as passive waste disposal systems, lysosomes now garner recognition for their multifaceted involvement in autophagy regulation, and mediation of exocytosis etc[3]. These processes necessitate the fusion of lysosomes with other organelles resulting in the rapid consumption and depletion of lysosomal pools. Nonetheless, lysosomes spatiotemporally reshape their pools by enhancing their biogenesis to elicit cellular adaptation and maintain homeostasis. Biogenesis occurs through two mechanisms: transcription of lysosome genes or the reformation of lysosomes via fission of parent lysosomes or endo-lysosomes[3].

Impaired biogenesis, stemming from aberrations in either fusion or fission, is implicated in many rare diseases[4-7], while enhanced lysosome biogenesis is a hallmark of many cancers[8]. During malignant transformation, cancer cells hijack and expand their lysosomal system, i.e., (increase in the number, size, and activity of lysosomes) to their advantage for supporting catabolic requirements[8]. Expanded lysosome compartments assist cancer cells by sequestering drugs and preventing them from reaching their intracellular targets, thereby contributing to multi-drug resistance (MDR)[9, 10]. The subcellular biological barriers discussed in Chapter 1, such as lysosome-mediated drug sequestration, exacerbate off-target and non-specific drug deposition which concomitantly impedes drug efficacy. Moreover, understanding lysosome fusion with endosomes and subsequent fission is crucial for nanomedicine, which utilizes the cell's endocytic machinery for delivering genes and therapeutics[11]. It is becoming evident that heterogeneity at the single-cell level leads to limited therapeutic responses in clinical trials, prompting scientists to proactively question the pharmacological mechanisms of drug action at the single-cell level[12]. Understanding the dynamic interactions between endosomes and lysosomes, as well as identifying defects in their interaction, can provide valuable insights for disease prognosis and help guide therapeutic interventions[13]. A probe with the ability to simultaneously and distinctly label both endosomes and lysosomes could greatly enhance the monitoring of their dynamic interactions. The acidity of

endocytic vesicles increases progressively from early endosomes (pH= 6.5) to late endosomes (pH= 5.5) and eventually to lysosomes (pH= 4.5). Significant efforts have been dedicated to annotate these organelles by fluorescently mapping their acidity. Matile et al. employed mechanosensitive flipper probes conjugated with cell-penetrating peptides with pKa ~10.6 to unidirectionally penetrate the pH gradient along the endocytic pathway[14, 15].

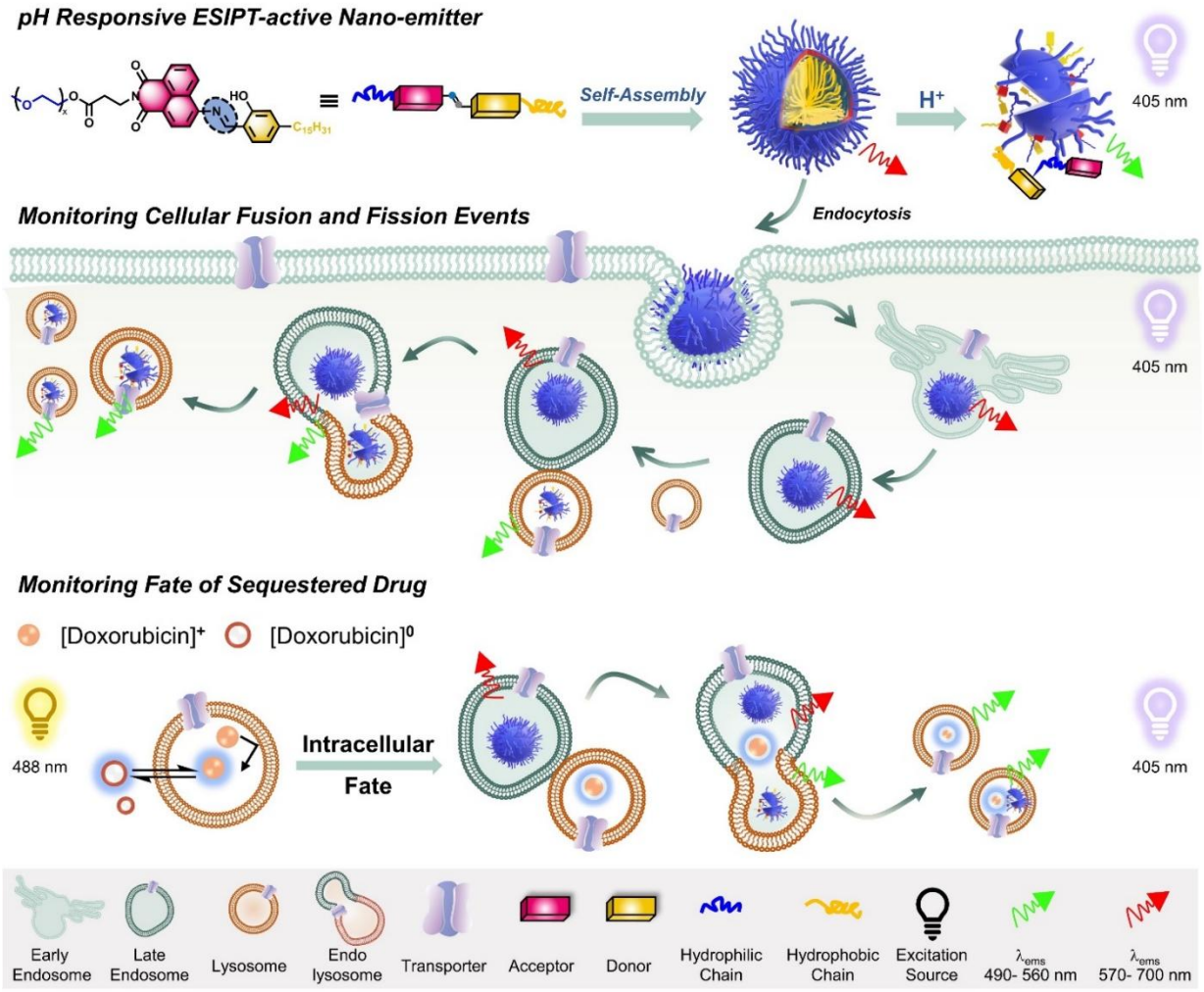

Figure* 4.1:** *Design of a pH responsive donor-acceptor fluorophore;* ***nano-emitter*. Self-assembly mediated the photophysical properties of* ***nano-emitter*** *to show ESIPT emission. Schematic showing the use of* ***nano-emitter*** *in tracing fusion and fission events between endosomes and lysosomes.* ***Nano-emitter*** *was further employed to monitor the fate of sequestered drug, Doxorubicin.*

Utilizing Fluorescence Lifetime Imaging Microscopy (FLIM), these mechanosensitive flipper probes were demonstrated to effectively annotate endocytic vesicles, notably endosomes, which are typically challenging to label. Recently, there has been a shift in focus towards designing probes capable of annotating endocytic organelles regardless of targeting features, particularly in cases of abnormal organelle status where many pH probes lose their efficacy. An example of such an approach involves anchoring an intensiometric pH probe to the plasma membrane, providing an opportunity to monitor vesicle dynamics as it inwardly invaginates, forming endocytic vesicles with the anchored pH probe still anchored to its inner leaflet[16]. The intensiometric probe showed an enhancement in fluorescence intensity as it moved from the environment of low acidity in early endosomes to high acidity in lysosomes. Although several attempts have been made to label the endocytic organelles, probes proficient to monitor their dynamic interactions remains scarce. Contemporary technology employs double labeling using a two-fluorophore system to monitor these dynamic interactions as they engage in content exchange of two fluorescent dyes. For instance, double staining with traditional green fluorophore, Dextran-FITC (λ_{exc}= 488 nm, λ_{ems}= 500- 540 nm) and red fluorophore, Dextran-Rhodamine (λ_{exc}= 561, λ_{ems}= 580- 700 nm) is used to stain endosomes and lysosomes respectively[17]. However, such a system utilizing two sources of excitation often causes spectral cross-talk or excitation cross-talk due to overlap between their excitation wavelengths[18]. While to a lesser extent, rhodamine can be co-excited when exciting fluorescein using a 488 nm laser. Further, emissions corresponding to fluorescein may be detected in photomultiplier or widefield channels typically reserved for rhodamine. Additionally, such systems are difficult to multiplex with other fluorescent drugs and dyes which have overlapping excitation and emission profiles. Recently, monochromatic wavelength excitable and dual emitting single-molecule fluorescent probes have gained significant attention. They were employed in imaging of heterogeneous interactions between mitochondria- autolysosomes[19] and homogeneous interactions between lysosomes[20]. This technique gained popularity due to their streamlined detection and instrumentation requirements for bio-imaging applications[19, 21]. Motivated by this, we aimed to address the scarcity of single-molecule fluorescent probes to study dynamic interactions between endosomes and lysosomes. The fusion of late endosomes to lysosomes leads to an abrupt decrease in the pH. Also, studies indicate the presence of a differential H+ gradient across the membrane microdomains of endo-lysosome, wherein the reduction in the pH promotes lysosome fission[7]. The design of a pH responsive single-molecule fluorescent probe capable of

simultaneously and distinctly label both lysosomes and endosomes with two fluorescent colors upon monochromatic excitation as it unidirectionally traverses the endocytic pathway featured an ESIPT active salicylaldimine core. ESIPT fluorophores for their high stokes shift, potential for ratiometric sensing, finds diverse applications in studying biological phenomenon[22, 23]. The design of single-molecule fluorophore comprised of a hydrophilic PEG-functionalized 4-amino-naphthalimide (A), ***PEG-Naph*** connected via imine-linkage to a hydrophobic long tail containing salicylaldehyde (D) forming a salicylaldimine core. The ESIPT active salicylaldimine core with balanced amphiphilicity fostered cooperativity and guided its self-assembly into micellar ***nano-emitter***. It exclusively showed red fluorescence upon 405 nm excitation (first color) via ESIPT as it remained intact under endosome's (pH= 5.5-6.5) environment. Further, its stimuli responsive hydrolysis inside lysosomes (pH ~ 4.5) regenerated the acceptor core, ***PEG-Naph***, which exhibited green fluorescence (second color) under the same excitation. Hence, monochromatic wavelength co- Closely absorbing ***nano-emitter*** and ***PEG-Naph*** are co-excited using monochromatic wavelength but shows well separated red and green fluorescence respectively, thereby reducing excitation crosstalk[24]. Employing monochromatic excitation wavelength, can further enhance the maximum available imaging speed while reducing laser-induced phototoxicity and photoimaging[24]. Furthermore, monochromatic co-excitation provides an opportunity to multiplex such fluorophore with other fluorescent drugs and dyes. This two-color labelling of endosomes and lysosomes facilitated the dynamic tracking of their transient and complete fusions in real-time. The transient and complete fusion resulted in yellow fluorescent (due to overlap of red and green fluorescent signals) endo-lysosomes. Lysosome reformation via endo-lysosome fission was also captured, as newly formed tiny nascent lysosomes with green fluorescence were easily differentiated from large yellow parent endo-lysosomes. We leveraged ***nano-emitter***'s dual staining ability by multiplexing it with fluorescent anti-cancer drug doxorubicin to unravel the uncertainties surrounding the fate of sequestered drug molecules by lysosomes. A mainstream hypothesis suggests that the sequestered drug molecules remain "persistently trapped" in lysosomes or are "expelled" from cells via lysosomal exocytosis[10, 25]. However, the visual evidence of how the drug remains persistently trapped in lysosomes is scarce. We hypothesized fusion-fission type interactions between endosomes and lysosomes to be instrumental in the "persistent entrapment" of the drugs. The present findings demonstrated in MCF 7 cells support this

hypothesis. To the best of our knowledge, the role of fusion-fission interactions among acidic vesicles in facilitating the persistence of sequestered drugs within the cells is yet to be documented.

4.3 Materials and Methods

4.3.1 *Materials*

All the chemicals were purchased from local vendors (*Rankem*, *Sigma Aldrich*, *Alfa Aesar*, *ThermoFisher*, *TCI chemicals*) and were used without further purification. Salts for making buffers were purchased from sigma Aldrich. H_3PO_4 (Phosphoric acid), H_3BO_3 (Boric acid), CH_3COOH (Acetic acid), NaOH (Sodium hydroxide), KCl (Potassium chloride), Na_2HPO_4 (Disodium Phosphate), KH_2PO_4 (Monopotassium Phosphate). Cell culture reagents were purchased from ThermoFisher. Fetal Bovine serum (FBS, *Product Code*: 10270106), Dulbecco's Modified Eagle's Medium (DMEM, *Product Code*: 11995040), Penicillin-Streptomycin (*Catalogue No.*: 15070063), Trypsin EDTA solution, paraformaldehyde (PFA). Tissue culture grade Hanks balanced salt solution; Live Cell imaging solution were purchased from ThermoFisher. Fluorescent dyes for staining cellular organelles: SYTO™ Deep Red Nucleic Acid Stain (Catalogue number: S34900); Lysotracker Tracker Red DND-99 (Catalogue Number: L7528); Lysotracker Green DND-26 (L7526); Anionic Dextran-Fluorescein, 10,000 MW (Catalogue number: D1821) DAPI (4′,6-diamidino-2-phenylindole), MTT (3-(4,5-Dimethylthiazol-2-yl)-2,5-Diphenyltetrazolium Bromide) reagent were purchased from ThermoFisher. Plasmids for transient transfections were from Addgene; for GFP-rab5 plasmid no. #134858 (pLVX-EF1a-EGFP-RAB5A-IRES-Puromycin), for GFP-rab7A plasmid no.#133027 (pLVX-EF1a-EGFP-RAB7A-IRES-Puromycin), and for lamp1 plasmid no. # 134868 (pLVX-EF1a-LAMP-1-mGFP-IRES-Puromycin) were used. Transient transfections were achieved using lipofectamine-2000 (cat. No.-11668030) from Invitrogen. Dextran-FITC (cat no.- D22910) was purchased from ThermoFisher. Coverslips and glass slides were cleaned, ethanol rinsed, flame dried, and UV-treated prior to fixed cell imaging. 35 mm Nunc™ Glass Bottom Dishes (Catalogue number: 150680) were used for live cell imaging.

4.3.2 *Instruments*

Live cell imaging was carried on top of a pre-heated (@37^{o}C) stage top setup of Leica SP8 confocal microscope under 5% CO_2 atmosphere. Confocal Imaging was in general carried with a 63X or

100X oil immersion objective lens with imaging laser set of 405 and 488 nm. Image processing was done using image J (fiji software). Laser power was attenuated to 0.5 % of the normal value to avoid phototoxicity and photobleaching due to long term imaging. A Varioskan™ LUX multimode microplate reader from ThermoFisher was used for photometric reading at 560 nm (λ_{max} for MTT reagent) wavelength for a 96 well plate for MTT analysis.

4.3.3 *Methods*

4.3.3.1 *Nano-emitter preparation for Biological Experiments.*

PEG-PDP-Imine nanoparticles were prepared via film rehydration, followed by passing the sample through extruder employing nano porous membrane of 0.1μm size cut-off. For this 0.5 mg sample was weighed in a 5 mL round bottom flask. Next, 0.25 mL of HPLC grade chloroform was added to completely dissolve the compound. Next, chloroform was slowly distilled off using a rotary evaporator. Next, the formed film was subjected under high vacuum conditions for 2 hours which ensures complete drying of the film. Next, the film was rehydrated using 1mL of autoclaved MQ water for a period of 15-20 minutes at room temperature and were passed through an extruder using 0.1μm membrane filter. Next, the solution was spined at 1000 to spin down any particulate aggregates. 20 μL of the supernatant was aliquoted in 2 mL centrifuge tubes and was gently diluted with prewarmed 1mL media at 37 °C before adding it to the imaging plates containing cells. For MTT experiments, volumes (3, 6, 9, 12, 15 and 18μL) were aliquoted in 2 mL centrifuge tubes and media was added to make up the volume till 300 μL before adding it to the 96-well plate. *Note:* This ***nano-emitter*** preparation was done fresh before the imaging experiments, which yielded consistent results.

4.3.3.2 *Cell Culture maintenance*

MCF 7 cell cultures were maintained in DMEM containing 5% FBS and 1% penicillin-streptomycin (5000 U/mL) (Cat no. 15070063) under standard conditions comprising of 5% CO_2 atmosphere with 95% humidity and maintained at 37^0C in incubator. The experiments commenced after maintaining the cells at sufficient confluency (not more than 70%) for not more than a period of 72 hours which was followed by trypsinization and centrifugation. The obtained cell pellet was used for further experiments or for maintaining the cell cultures. Before initiating the experiments,

the cell lines were checked for mycoplasma contamination or any fungal infection. The cell passage was maintained at < 15 for the experiments conducted. Cultures were examined rigorously for any changes in cellular morphology or colour changes in media.

4.3.3.3 *Cell Viability assay*

The cytotoxicity of ***nano-emitter*** was examined using a well-established and standard protocol for measuring cellular viability using a MTT reagent. For this, cells were cultured in a 96- well petri dish under standard conditions to assimilate and grow for 18 hours. Next, the media was aspirated and replenished with media containing ***nano-emitter*** at various concentrations and was incubated for a period of 24 hours independently. After, the respective time points, the media was aspirated and cells were incubated with MTT containing (0.5mg/mL) medium (100µL) for another 4 hours inside the incubator. After this the medium was carefully aspirated without disturbing the formed formazan crystals and 100uL of HPLC grade DMSO was added. The plate covered with aluminium foil was transferred atop a thermos shaker setup to allow the formazan crystals to dissolve completely in DMSO for a total of 30 minutes. Cell viability as a function of absorbance at 570 nm was measured using a Varioskan™ LUX multimode microplate reader. The data was plotted as bar graph.

4.3.3.4 *Time dependent activity for probe*

For this, a 6 petri dishes equipped with coverslips was UV treated for a period of 1 hour. After this, 10000 cells/ cm^2 were seeded onto the glass bottom surface of a Nunc glass bottom dish and were left to assimilate for 36h hours in the incubator. Next, the media was aspirated and each petri dish containing cells were incubated with 20µg/ 0.5 mL of ***nano-emitter*** in DMEM for a period of 1 hour. After, 1 hour, media was removed from all petri dishes and was subsequently incubated with fresh media for 0.5, 2, 6, 8 hours and were imaged under confocal microscope equipped with stage top CO2 incubator. PEG-PDP-Imine was excited using 405 nm laser and emission was collected in both red (600- 720 nm) and green channel (490- 550 nm). Fiji was used for process the fluorescent micrographs. Fluorescence intensity quantification was done for n= 10 cells in one experiment. Experiment was repeated two times (N= 2) with similar results.

4.3.3.5 *Uptake Inhibition*

MCF 7 cells were grown under standard conditions for 36 hours in circular glass bottom dishes, 40.4 mm. In control experiment, the cells were incubated with compound containing DMEM for 30 minutes and chased in fresh media for another 30 minutes, followed by confocal imaging. Independently, the cells grown in dishes were treated with inhibitor solution of either NaN_3 (10mM), Dynasore (80 μM) or Chlorpromazine (50 μM) for 30 minutes. Next, the cells were incubated with fresh DMEM containing ***nano-emitter*** along with the same inhibitor concentration for another 30 minutes. This was followed by wash and chased in medium containing same concentration of inhibitors for another 30 minutes, followed by imaging. Images were captured in single focal plane on a stage top incubator maintained at conditions of 5% CO_2, 90% humidity maintained at 37 °C. The fluorescent micrographs were processed using image j software. The quantification of fluorescence intensities in the perinuclear and pericellular region was determined using a simple method reported elsewhere. The region surrounding the nucleus is described as the perinuclear region. Measurement is made by sketching oval or circular ROI starting from center of nucleus to r+ 0.5r for circular nucleus or to R+ 0.5R, r+0.5r for oval looking nucleus; where r and R and the long and short radius of irregular shaped nucleus. Both r and R can be measured using analyze> measure option in image j. Next, pericellular region is determined as region from the end of perinuclear region to the border of the cell. After recognizing the ROI's, using merged images (green+ red channel) corrected fluorescence intensity was calculated for perinuclear region; $ID_{\text{perinuclear region}}$ Next, the corrected fluorescence intensity for whole cell; $ID_{\text{total cell}}$ is calculated by constructing a ROI around the entire cell using free hand section tool in Image j. Pericellular intensity; $ID_{\text{pericellular region.}}$ was calculated by following equation: $ID_{\text{pericellular region}} = ID_{\text{total cell}} - ID_{\text{perinuclear region.}}$ The intensities are recorded for different cells and intensities are stratified as MNP'S: Membrane associated nanoparticle (for pericellular intensity); INP's: Internalized Nanoparticles (for perinuclear intensity) and Total Cellular uptake (for total cell intensity). Error bars correspond to mean +/- S.D.; n=7.

4.3.3.6 *Colocalization assay*

To understand the cellular localization of ***nano-emitter***, colocalization experiment with commercially available organelle markers were carried out. For this, Nunc glass bottom dishes were used. The entire assembly was UV-treated for 1 hour before commencement of the

experiment. Next, 10,000 cells/cm^2 were seeded onto a glass coverslip for a period of 36 hours. Next, each well containing cells were incubated with DMEM containing ***nano-emitter*** (20μg/mL) for 1 hour, followed which the media containing compound was aspirated. The cells were washed with pre warmed 2mL HBBS solution (3X) to remove uninternalized/ excess probe and chased for 2 hours. Next, individual wells were subsequently incubated with media containing commercially available Mito tracker (25 nM), Lysotracker (25nM), and Er-tracker (50nM) each for a period of 0.5 hours, washed and chased in fresh media for another 0.5 h before subjecting to confocal microscopy. Following laser configuration was used for imaging: Mito-tracker, Lyso-tracker, and ER-tracker were excited using 488 nm laser and emission was collected in Green Channel (490-550 nm). PEG-PDP-Imine was excited using 405 nm laser and emission was collected in both red (570- 720 nm) and green channel (490- 550 nm).

4.3.3.7 *Transient transfection studies*

Transient transfections employing following plasmids #134858, #133027, and #134868 were used to GFP label Rab5 proteins of early endosomes, Rab7a protein of late endosomes and lamp1 protein of lysosomes in the cells. For a typical transfection, cells were allowed to grow under ambient conditions for 36 hours at no more than 50% confluency. Next two solutions were made; solution-A: briefly .65ug plasmid was dissolved in 100 μL of serum free media and solution-B: 25μL of lipofectamine was dissolved in 100 μL of serum free media. Next, solution a and b were mixed gently and allowed to rest for 30 minutes inside the hood. Next, the cells were rinsed with serum free media twice and 800 μL serum free media was added to the cells. Next, the premix was then added in drop wise manner to the cells. The cells were then shifted to the incubator and continued for 18 hours. After 18 hours, the transfection media was removed and was replaced with complete media and cells were allowed to grow for another 36 hours. Next the cells were briefly observed under regular fluorescent microscope to confirm the transfections by visualizing them under GFP filter. Rab5-GFP labelled cells were then treated with ***nano-emitter*** for 1 hour and chased in fresh media for 30 minutes and then imaged with Leica sp8 confocal instrument. Similarly, Rab7a-GFP labelled cells were then treated with ***nano-emitter*** for 1 hour and then chased for 2 hours and then checked under confocal microscope. Likewise, the Lamp1-GFP labelled cells were treated with ***nano-emitter*** for 1 hour and then chased in fresh media for a total

of 6 hours and then imaged using confocal microscope. The acquired images were then processed using Fiji software.

4.3.3.8 *Live Cell imaging of Lysosome-endosome interactions*

Nunc glass bottom petri dishes were used for live cell imaging. 5000 cells/cm2 were seeded onto the glass bottom surface of the Petri dishes following which the cells were allowed to assimilate to their natural growth conditions. Next, the media was removed and was replaced with fresh media contaminating ***nano-emitter*** probe for a period of 1 hour. Thereafter, the media was removed and was gently washed with HBBS solution (3X) to remove uninternalized probe. The cells were then incubated with live cell imaging media and was directly taken for microscopy imaging. Live cell imaging was then carried out on a Leica Sp8 confocal instrument with a 63 X 1.4 or 100 X 1.4 numerical aperture oil DIC Plan Apochromatic Lens. A 405 nm laser at 1% of laser power was used throughout for imaging. The emission was collected in two distinct channels: Green channel (490-550 nm) and red Channel (600- 720 nm). The pixel dwell time was set to 800 ns with an average of 4-line scan and the pinhole was et to 1 airy unit. The images were acquired every 61.61 seconds for a period of 30 minutes on a stage top CO_2 incubator. The acquired images were then examined and deconvolution was carried out using fiji. The frames were stitched and movie was created in fiji.

4.3.3.9 *Tracking the Fate of Sequestered Doxorubicin*

The cells were grown under standard conditions for a total of 36 hours. Next, it was pulsed with ***nano-emitter*** for a total of 1 hour and then washed using (2x HBBS 2mL) solution. Next, the cells were pulsed with doxorubicin at concentration of 100 nm for 2 hour and chased in fresh media for 0.5 hours, followed which the cells were imaged live. The images were acquired every 79 seconds and was imaged for 1500 seconds or 25 minutes. The cells were shown with two lasers, 405nm for ***nano-emitter*** and 488 nm for doxorubicin. The emission for ***nano-emitter*** was collected in ***nano-emitter*** and PEG-Naph channel. The emission for doxorubicin was collected from 490- 550 nm. The time series collected was then analysed in image j.

4.4 Results and Discussions

4.4.1 *Photophysics of nano-emitter*

The ***nano-emitter*** exclusively showed ESIPT emission in water, a property that was optimized in the previous chapter. The ***nano-emitter*** showed stable ESIPT emission at different dilutions as evident from the fluorescence recorded at various concentrations. The ESIPT intensity decreased with decrease in the concentration, but no emission corresponding to anion was seen. The self-assembly is critical to concentrations.

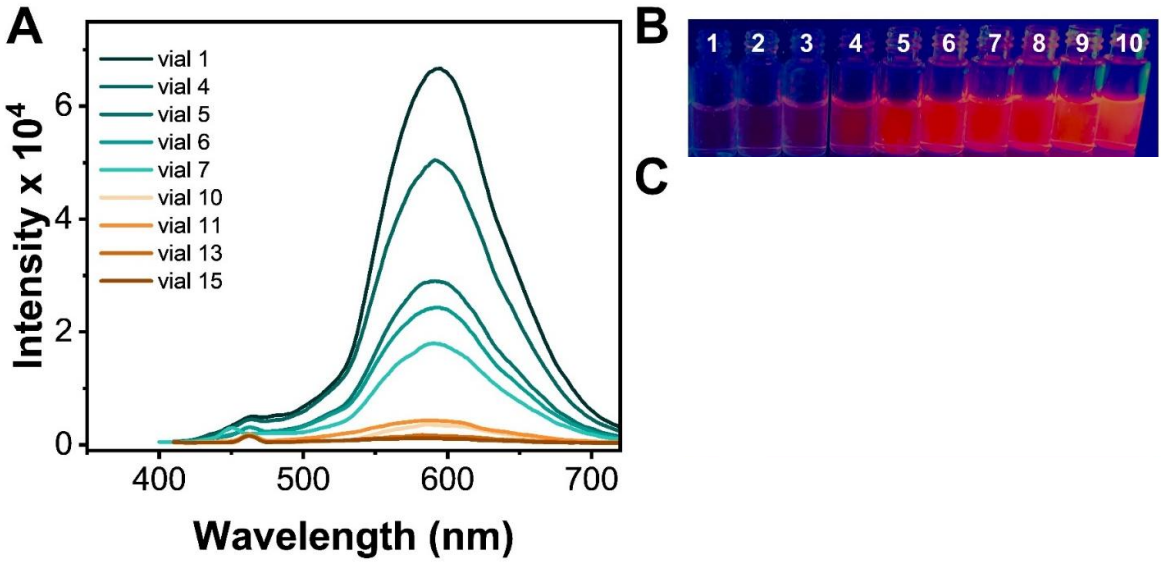

Figure* 4.2:** *Concentration dependance of ESIPT of* ***nano-emitter *in water.* ***A:*** *Fluorescence intensity profile of* ***nano-emitter*** *in water at various concentrations;* λ_{exc}*= 405 nm.* ***B:*** *Photographs of vials showing* ***nano-emitter*** *at various concentrations in water when excited using long wavelength (365 nm) of hand-held UV lamp.*

It is expected that at low concentration, the self-assembly breaks to form isolated PEG-PDP-Imine molecules which might lead to anion emission. However, at such low concentration, no emission corresponding to anion was seen. This may be due to the extremely low concertation of the chromophore to show any detectable anion emission. Hence, a gradual reduction in ESIPT emission was seen with decrease in concentration as seen in fluorescence intensity profile and vial images in ***Figure*** 4.2a, 4.2b. At concentration lower than this, the self-assembly breaks and the emission intensity decreases. Next, the response of ***nano-emitter*** to various pH conditions was checked in vials. It was anticipated that the ***nano-emitter*** shows red ESIPT emission under

cytosolic and endosome's pH conditions when excited under 405 nm laser as shown in ***Figure*** 4.3a, 4.3b.

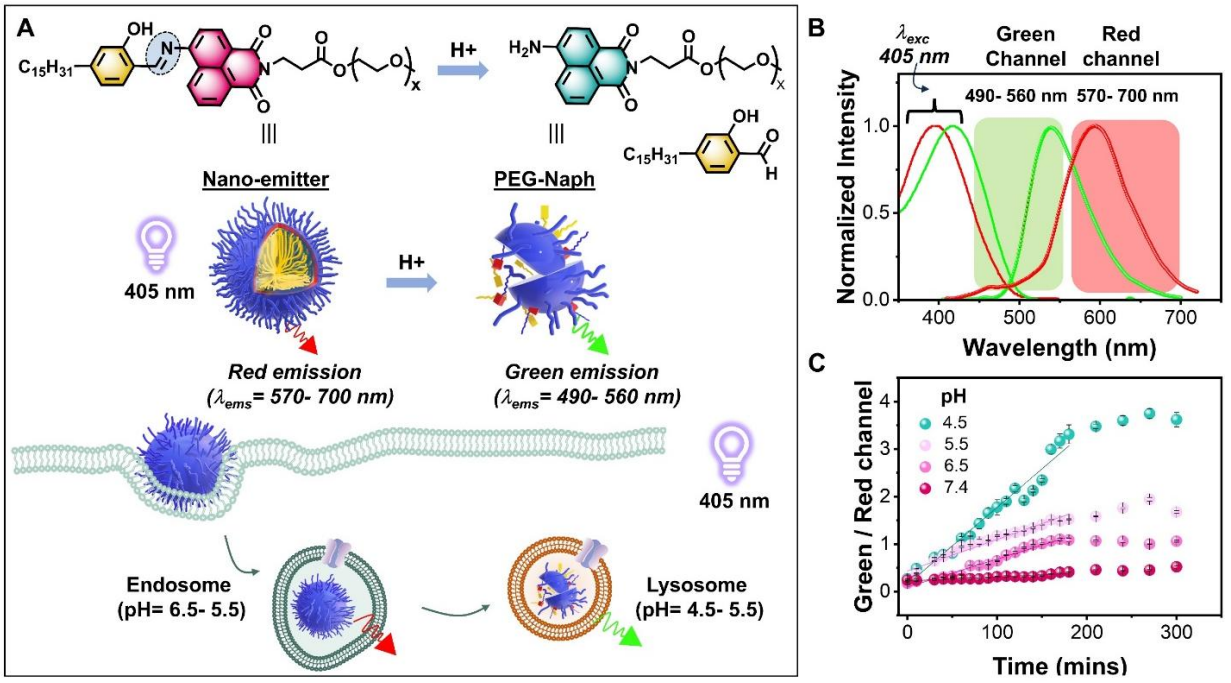

Figure* 4.3:** pH responsive fluorescent response of ***nano-emitter. ***A:*** *Schematic of* ***nano-emitter*** *showing red emission and its pH responsive hydrolyzed form* ***PEG-Naph****, showing green emission under single 405 nm excitation. Endosomes(E) containing* ***nano-emitter*** *glows red and lysosomes(L) containing hydrolyzed* ***PEG-Naph*** *glow green, under single 405 nm confocal excitation.* ***B:*** *Absorbance and emission spectra of* ***nano-emitter*** *and PEG-Naph in water. Both* ***nano-emitter*** *and PEG-Naph due to similar absorbance can be co-excited using a 405 nm confocal laser and emits differently.* ***Nano-emitter*** *emits in the red range, 570- 700 nm and PEG-Naph emits in the green range, 490- 560 nm.* ***C:*** *The response of* ***nano-emitter*** *at various pH conditions when plotted for the ratio of green to red fluorescence intensity against time.*

Further upon entering lysosomes, it was expected to hydrolyze and then show green emission coming from regenerated PEG-Naph when excited using 405 nm laser as shown in ***Figure*** 4.3a. The hydrolyzed form of ***nano-emitter*** i.e. PEG-Naph showed green emission when excited using 405 nm laser as shown in ***Figure*** 4.3b. Due to similar absorbance of ***nano-emitter*** and PEG-Naph, they can be co-excited in the system using 405 nm confocal laser. To understand the pH responsiveness of ***nano-emitter***, it was subjected to different pH conditions of cytosol (7.4), early endosomes (6.5), late endosomes (5.5) and lysosomes (4.5) and the change in fluorescence intensity was monitored with time. It showed fast hydrolysis when pH is lowered to 4.5, as evident from the rapidly increasing slope of Green: red channel (***Figure*** 4.3c). The ESIPT emission

persisted for a longer time at cytosol and endosome's pH conditions due to slow hydrolysis of ***nano-emitter*** in a time dependent manner. The ***nano-emitter*** hence showed red emission at endosomal pH condition and showed green emission at lysosome's pH condition when excited using 405 nm laser. After having established pH responsiveness of ***nano-emitter*** in vitro, we next explored this ability to monitor fusion and fission events between endocytic organelles in cells. Finally, we leveraged its potential to understand the fate of sequestered drug molecules by lysosomes.

4.4.2 *Bio-imaging applications*

We commenced our studies by first checking ***nano-emitter***'s compatibility with living cells. It was well tolerated by cells as evident from MTT data as shown in ***Figure*** 4.4. The ***nano-emitter*** was well tolerated by cells at the concentrations tested and hence could be usefully used for live imaging applications.

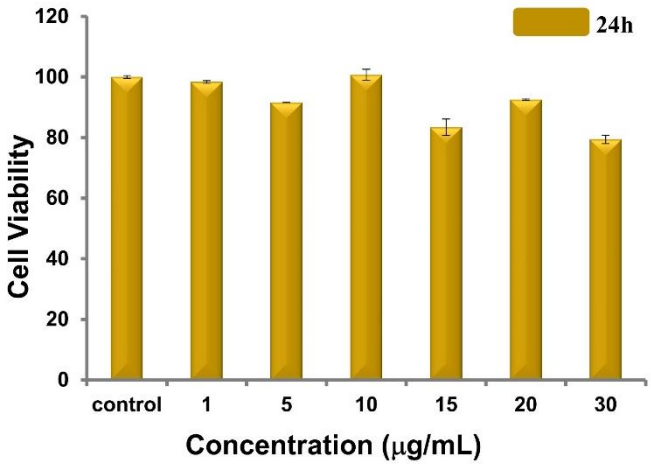

Figure* 4.4:** *Cell viability assay for* ***nano-emitter*. MTT assay for* ***nano-emitter*** *check at various concentrations in MCF 7 cells.*

A pulse-chase assay was next conducted to evaluate the fluorescent behavior and organelle staining capacity of the ***nano-emitter*** in MCF 7 cell line. The ***nano-emitter*** was expected to display red fluorescence in organelles with pH > 5.5 and green fluorescence in organelles with pH < 5.5, resulting from its hydrolysis to ***PEG-Naph***, when monochromatically co-excited with a 405 nm laser (see ***Figure*** 4.5a).

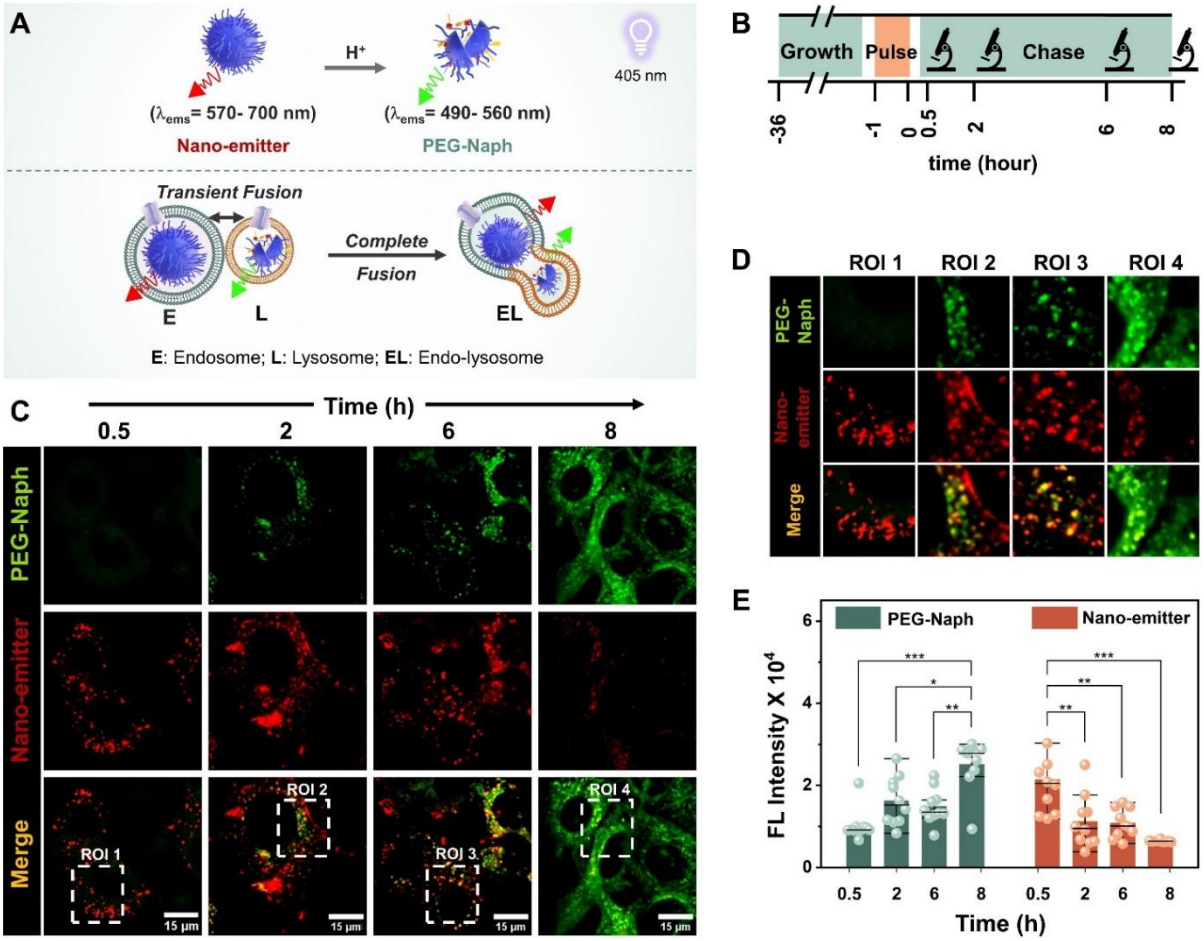

Figure* 4.5:** *Pulse-chase assay employing* ***nano-emitter *in MCF 7 cells.* ***A:*** *Schematic of* ***nano-emitter*** *showing red emission and its pH responsive hydrolyzed form* ***PEG-Naph****, showing green emission under single 405 nm excitation. Endosomes(E) containing* ***nano-emitter*** *glows red and lysosomes(L) containing hydrolyzed* ***PEG-Naph*** *glow green, when imaged under single 405 nm confocal excitation. Their complete fusion results in the formation of endo-lysosomes (EL) that shows yellow fluorescence (due to overlay of green & red fluorescent signals).* ***B:*** *Schematic showing Pulse-chase assay employing* ***nano-emitter*** *in MCF 7 cell lines which were grown for 36 h, followed by incubating with 20 ug/mL* ***nano-emitter*** *for 1 hour (pulse), and chased in* ***nano-emitter*** *free media for 4 time points followed by imaging.* ***C:*** *Fluorescent micrographs of cells chased for different time points under a 405 nm laser and emission collected in green channel; 490- 550 nm (annotated as* ***PEG-Naph*** *in green color) and red channel; 600- 720 nm (annotated as* ***nano-emitter*** *in red color).* ***D:*** *Zoomed in (15 X 15 µm) images for selected ROI to show the green and red-emitting vesicle cohorts.* ***E:*** *Quantification of change in fluorescence intensities in red and green channel with time. Error bars correspond to Mean ± S.D., n=10. All difference between means with p< 0.05 are indicated (within the same category). *, p< 0.05; **, p< 0.01; ***, p< 0.001; paired comparison plot on origin.*

In a systematic investigation, cells were cultured and allowed to grow for 36 hours (see ***Figure*** 4.5b). The cells were then exposed to the ***nano-emitter*** for 1 hour (pulsing) before being chased in fresh media without the ***nano-emitter*** for various time intervals. Subsequent imaging was

performed employing a 405 nm laser (see ***Figure*** 4.5b). After 0.5 hours, ***nano-emitter*** was chased into a single cohort of vesicular bodies of heterogeneous size and shape (*possibly early endosomes*) that fluoresced red (see ***Figure*** 4.5c, see zoomed ROI-1 in ***Figure*** 4.5d). After a chase of 2 hours, the red fluorescence was detected coming from round and regularly shaped vesicular bodies (*possibly late endosomes*) near the juxtanuclear area. Also, a small cohort of green-emitting vesicle population (probably lysosomes) in the juxtanuclear region became apparent (***Figure*** 4.5c, see zoomed ROI-2, ROI-3 in ***Figure*** 4.5d). The hydrolysis of the ***nano-emitter*** to ***PEG-Naph*** under acidic pH conditions of lysosomes could have resulted in green emission (***Figure*** 4.5a). Notably, distinct yellow signals were too observed, as can be seen in ROI-2 and ROI-3, resulting either from transient contacts between green and red vesicles or due to the complete collapse of green and red vesicles, forming endo-lysosomes (***Figure*** 4.5a). As the ***nano-emitter*** traversed the intracellular space with time, the green emitting cohort of vesicular bodies increased and crowded the juxtanuclear region, eventually becoming the predominant population after a chase of 6 to 8 hours (see ***Figure*** 4.5c, see zoomed ROI 3, 4 in ***Figure*** 4.5d).

The data was quantified based on fluorescence intensity readouts in green (490-560 nm, *annotated as* ***PEG-Naph***) and red (600-720 nm, *annotated as* ***nano-emitter***) channels (see ***Figure*** 4.5e). The visual inspection of the images correlated with the quantification data, showing an evident increase in the green fluorescence intensity in ***PEG-Naph*** channel and a corresponding decrease in red fluorescence intensity in ***nano-emitter*** channel over time. The ***nano-emitter*** displayed pH responsive dual emission properties in cells as it distinguished two cohorts of vesicle populations with red and green fluorescence under 405 nm laser illumination. However, it is crucial to ascertain whether the red and green vesicles labeled by the ***nano-emitter*** correspond to endosomes and lysosomes, respectively, in order to provide accurate insights into their fusion and fission events.

To ascertain the identity of green and red fluorescent vesicles, we first analysed the ***nano-emitter***'s mode of entry into the cells in the presence of various inhibitors.[26]. The ***nano-emitter***'s mode of entry is decisive in facilitating its access to and staining of endocytic vesicles. Given the ***nano-emitter's*** shape, size, and ability to illuminate vesicular organelles, its entry into cells via endocytosis was deemed highly plausible. Under regular conditions (control), few to negligible nanoparticles were found on cell membrane, referred to as MNP (membrane associated nanoparticles). Instead, substantial amount of ***nano-emitter*** was internalized by the cells, referred

to as INP internalized nanoparticles) as evident from red and green emitting vesicles (*case i*, ***Figure*** 4.6a).

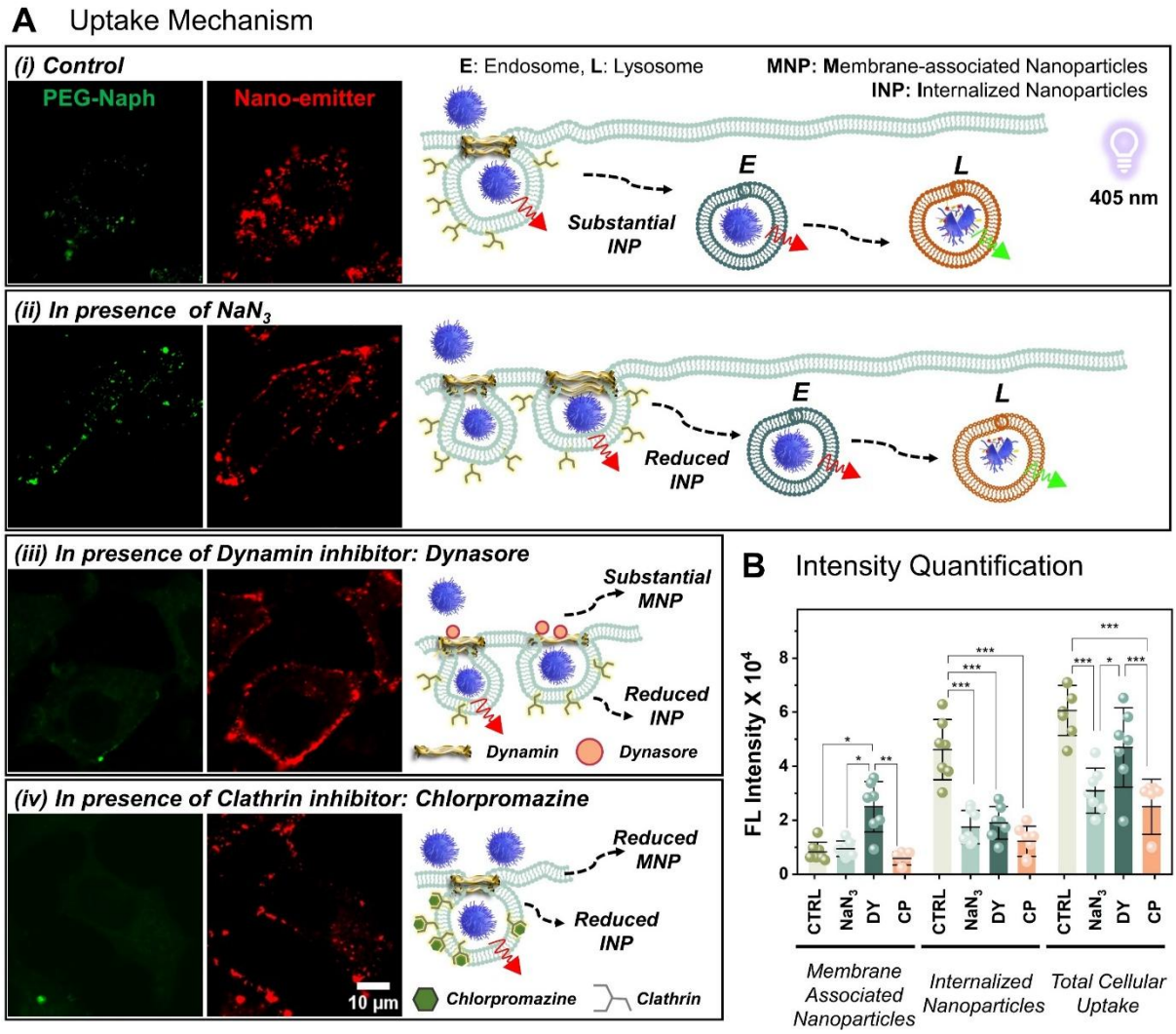

Figure* 4.6:** *Investigation of uptake mechanism of* ***nano-emitter *in MCF 7 cells.* ***A:*** *Fluorescent micrographs of a single-cell illustrating* ***nano-emitter*** *uptake under normal conditions: control* ***(i)*** *and following treatment with specific inhibitors, namely NaN_3* ***(ii)***, *Dynasore* ***(iii)***, *and Chlorpromazine* ***(iv)***. ***B:*** *Quantitative assessment of* ***nano-emitter*** *uptake in the presence and absence of inhibitors, gauged by fluorescence signal intensities in merged channel (red + green). The data is stratified to compare the effect of inhibitors on localization of nanoparticle on the membrane (MNP's); internalized within cells (INP's) and total cellular uptake. Error bars correspond to Mean ± S.D., n=7. All difference between means with $p < 0.05$ are indicated (within the same category). *, $p< 0.05$; **, $p< 0.01$; ***, $p< 0.001$; paired comparison plot on origin.*

The presence of endocytosis inhibitor NaN_3 led to an apparent increase in MNPs as evident from an increased red signal that illuminated the cell periphery and a decrease in INPs, suggesting an

ATP-dependent uptake (*case ii,* ***Figure*** 4.6a). The involvement of dynamin in endocytosis was studied by treating the cells with a known dynamin inhibitor, Dynasore. Dynamin is a protein that regulates the pinching and release of the cargo loaded endocytic vesicles from the plasma membrane by forming a helix around the neck of endocytic vesicles. A compromised dynamin function diminishes the release of ***nano-emitter*** loaded endocytic vesicles into the intracellular space. They instead remain attached to the plasma membrane as evident from increased red emission signal form cell periphery (*case iii,* ***Figure*** 4.6a). Quantitative analysis revealed a substantial reduction in total cellular uptake in the presence of inhibitors compared to the control (***Figure*** 5b). Quantification showed significant enhancement in MNP's and a concomitant decrease in INP's, following Dynasore treatment as opposed to control and other treatment groups (***Figure*** 4.6b). This indicates dynamin strong involvement in ***nano-emitter's*** uptake. Next involvement of Clathrin in ***nano-emitter*** uptake was analysed. Clathrin is a triskelion molecular scaffold that assembles to form cage like lattice around the incoming cargo at the plasma membrane to facilitate its vesicular transport. Chlorpromazine is known to inhibit Clathrin-coated pits around incoming cargo at the plasma membrane. As evident from diminished red emission around the cell periphery, treatment with chlorpromazine results in reduced membrane localization of the ***nano-emitter***. Further the internalization of the ***nano-emitter*** into the cells was diminished, as indicated by the absence of both red and green emission signals emanating from within the cells (*case iv,* ***Figure*** 4.6a). Also, quantification reveals a substantial reduction in both MNP and INP, underscoring the significant role of Clathrin (***Figure*** 4.6b). These findings suggest Clathrin-coated pit-mediated endocytosis (CME), which relies on both Clathrin and dynamin, as the likely mechanism. This makes staining of both endosomes and lysosomes highly likely.

Next, we conducted experiments to annotate two vesicle cohorts precisely. We did a colocalization study with commercially available Mito-tracker (for mitochondria), ER-tracker (for endoplasmic reticulum), and Lyso-tracker (for late endosomes and lysosomes), as these organelles are involved in endocytic trafficking pathway (see ***Figure*** 4.7a). After sufficiently populating red and green fluorescent vesicles by pulsing the cells with the ***nano-emitter*** for 1 hour and chasing for an additional 2 hours, we incubated the cells with media containing different tracker dyes (***Figure*** 4.7b).

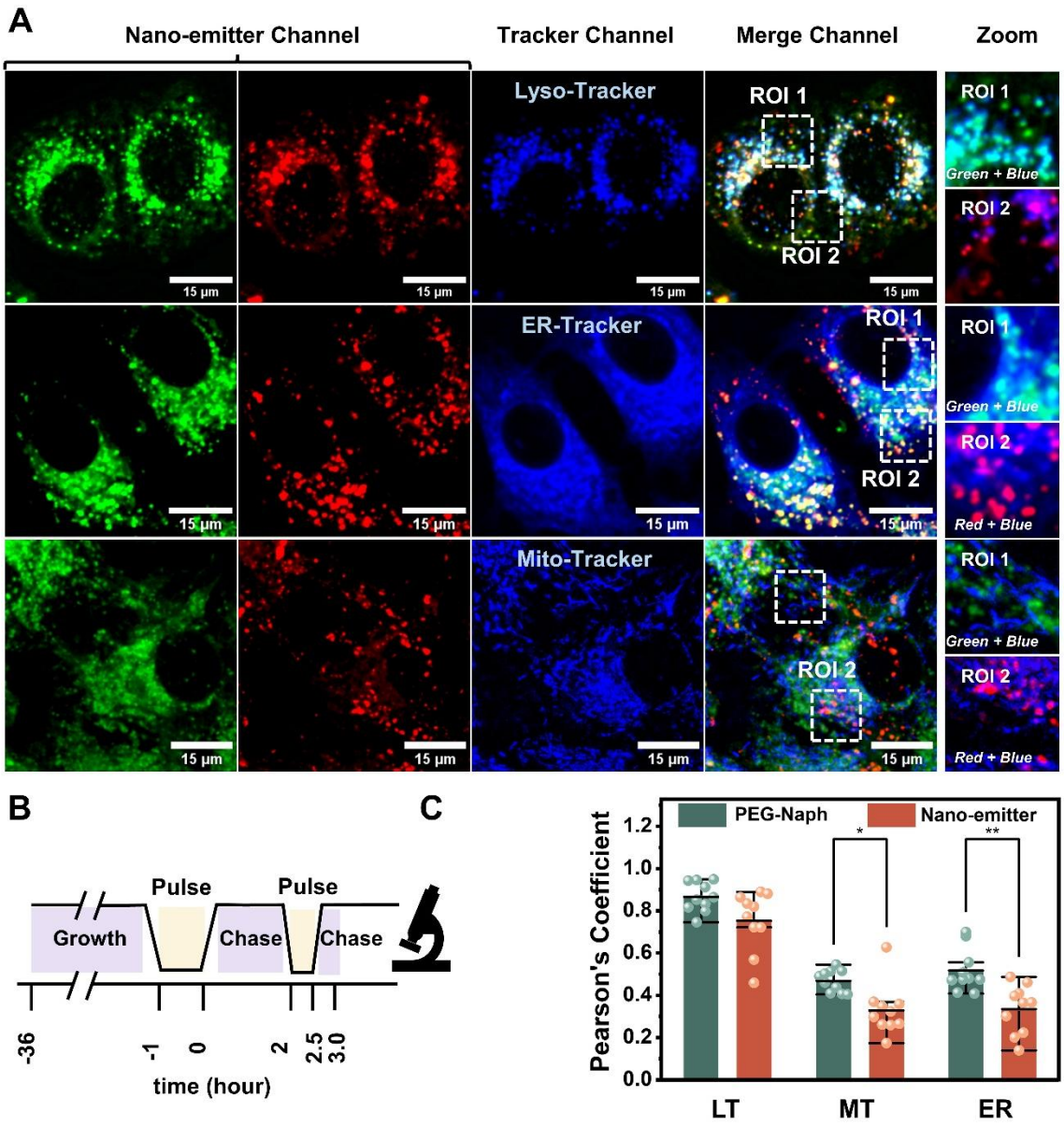

***Figure* 4.7:** *Understanding fluorescent color-based organelle annotation by **nano-emitter**. **A:** Colocalization of **nano-emitter** with different organelle trackers (given pseudo color- blue; Exc-488 nm, Ems- 490- 560 nm for all organelle trackers). **B:** Experimental design showing the addition steps and duration of **nano-emitter** and organelle trackers. **C:** Pearsons colocalization coefficient for all organelle trackers with **nano-emitter** channel. Error bars correspond to Mean ± S.D., n=10. All difference between means with p< 0.05 are indicated (within the same category). *, p< 0.05; **, p< 0.01; ***, p< 0.001; paired comparison plot on origin.*

Live imaging was performed, and Pearson correlation coefficient (ρ) was used to quantify the degree of colocalization between the green and red vesicles labeled by the ***nano-emitter*** and the commercial organelle trackers (assigned pseudo-color-blue for all trackers). Correlation

coefficients of magnitude 0.7-1 are significant and are typical of a high colocalization, whereas magnitudes 0.5 and lower suggest low colocalization and hold no significance. Based on this criterion, Mito-tracker ($\boldsymbol{\rho}_{green}$= 0.46, $\boldsymbol{\rho}_{red}$= 0.32) and ER tracker ($\boldsymbol{\rho}_{green}$= 0.51, $\boldsymbol{\rho}_{red}$= 0.34) showed a low correlation with green and red fluorescent vesicles; hence, these vesicles were not of mitochondrial or ER origin (***Figure*** 4.7a, 4.7c). These vesicles showed a high degree of colocalization with the lysotracker; only the green vesicles colocalized with blue labeled Lyso-tracker ($\boldsymbol{\rho}_{green}$= 0.86) more than the red vesicles ($\boldsymbol{\rho}_{red}$= 0.79) (see ***Figure*** 4.7a and zoomed ROI's). A point worth noting is that even though the ***nano-emitter*** divided the endocytic vesicles into green and red cohorts, the lysotracker dye stained them equitably, annotating them as lysosomes. Lyso-tracker is an acidotropic probe that indistinctly labels endosomes and lysosomes[27]. Green and red emitting vesicles could possibly be lysosomes and endosomes respectively.

Therefore, to accurately annotate the green and red vesicles, we transiently transfected cells to GFP (green fluorescent protein tag) label Rab 5, Rab 7, and Lamp1 proteins of early endosomes, late endosomes and lysosomes respectively (see ***Figure*** 4.8). In three independent experiments, GFP labeled early endosomes, late endosomes, and lysosomes showed blue fluorescence (pseudo color, λ_{exc}= 488 nm, λ_{ems}= 490- 560 nm) as shown in ***Figure*** 5c. After a successful transfection confirmed by confocal microscopy, the Rab5- GFP labeled cells were imaged live following a pulse/chase (30/30 minutes) with ***nano-emitter.*** Red fluorescent probe-laden vesicles were observed lining up the plasma membrane, while some progressed in the endocytic journey and colocalized with GFP-tagged blue fluorescent early endosomes (first row in ***Figure*** 5c, see zoomed ROI-1). Similarly, Rab 7-GFP labeled cells were then pulsed with ***nano-emitter*** for 30 minutes and chased the cells in fresh media for 2 hours (pulse/chase: 30/120 minutes). The colocalization study revealed that the red fluorescent vesicles exhibited colocalization with blue fluorescent late endosomes. Notably, the ***nano-emitter*** illuminated the dark and hollow lumen of the blue fluorescent late endosome vesicles (second row in ***Figure*** 4.8, see zoomed ROI-2). Likewise, Lamp 1-GFP labeled cells were pulsed with ***nano-emitter*** for 30 minutes and chased in fresh media for 6 hours (pulse/chase: 30/360 minutes), following which the cells were imaged live. The green fluorescence emerged from lumen of GFP-Lamp 1 positive lysosomes (third row in ***Figure*** 4.8, see zoomed ROI-3). This finding indicates that the ***nano-emitter*** localized and hydrolyzed to ***PEG-Naph*** within the lumen of the GFP-illuminated membrane of lysosomes. Hence, upon monochromatic co-excitation with 405 nm laser, the ***nano-emitter*** distinctly mark endosomes

(both early and late) with red and lysosomes with green fluorescence. Now confident in staining properties of ***nano-emitter*** to mark endosomes and lysosomes, we utilized it to conduct live imaging experiments and monitor their fusion and fission events.

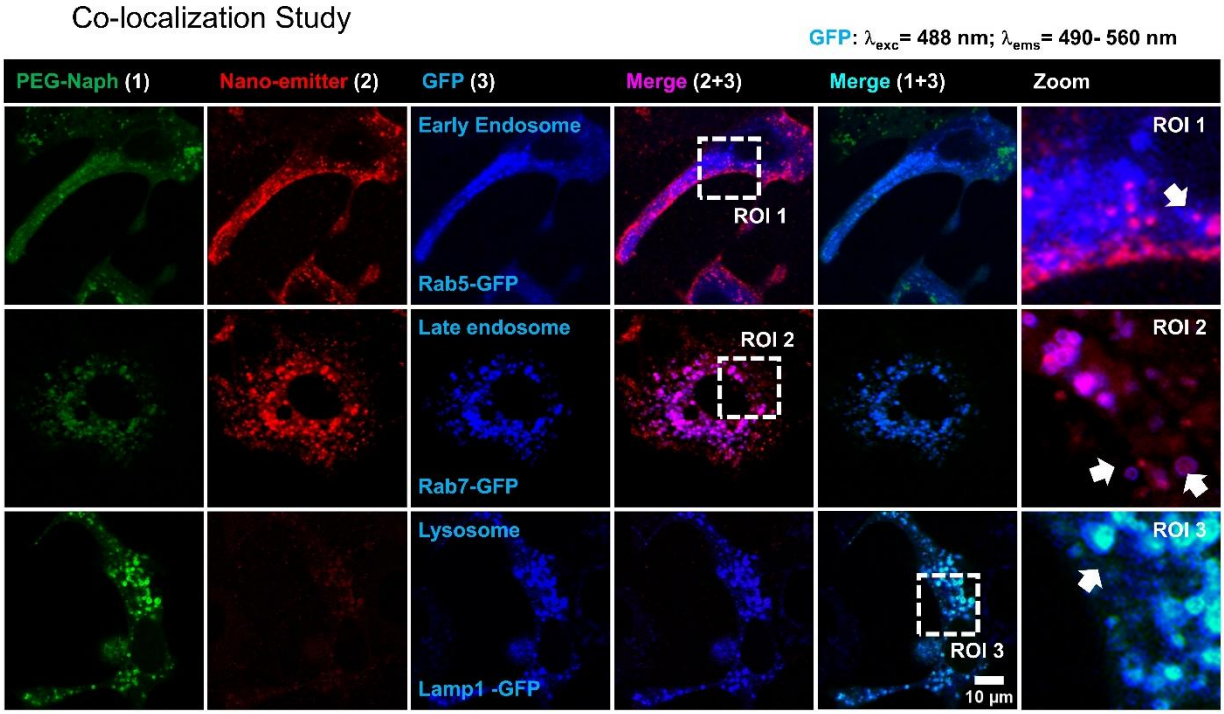

Figure* 4.8:** *Genetic transfections to differentiate between endocytic organelle. A colocalization study to investigate the localization of* ***nano-emitter *in endocytic vesicles. Transient transfection was used to GFP label Rab5 proteins of early endosomes, Rab7a protein of late endosomes and LAMP 1 protein of lysosomes in the cells. Three imaging channels were created.* ***Nano-emitter*** *was excited using 405 nm laser and two channels; PEG-Naph channel: 490- 550 nm and* ***Nano-emitter*** *channel: 600- 720 nm were created for collecting its emission of* ***nano-emitter*** *depending on the organelle it was localized into as shown in row 1 and 2. GFP was excited using a 488 nm laser and emission corresponding to GFP chromophore was collected in GFP channel: 490- 550 nm as shown in row 3. Colocalization between* ***nano-emitter*** *and GFP was realized via merging these two channels as shown in row 4. Similarly, colocalization between GFP and PEG-Naph was realized via merging these two channels as shown in row 5. Zoom imgaes of selected ROI was shown in row 6.*

Vesicular fusion and fission events result in exchange of contents (such as small molecules, drugs and macromolecules etc.) between endocytic organelles, promoting essential catabolism for maintaining cellular homeostasis. Fusions between endosomes and lysosomes typically occurs through two main methods. First, through *kiss-and-run*, that involves the transient fusion or interaction of endosomes with lysosomes, facilitating the exchange of contents between them and leads to formation of hybrid organelles (see ***Figure*** 4.9a).

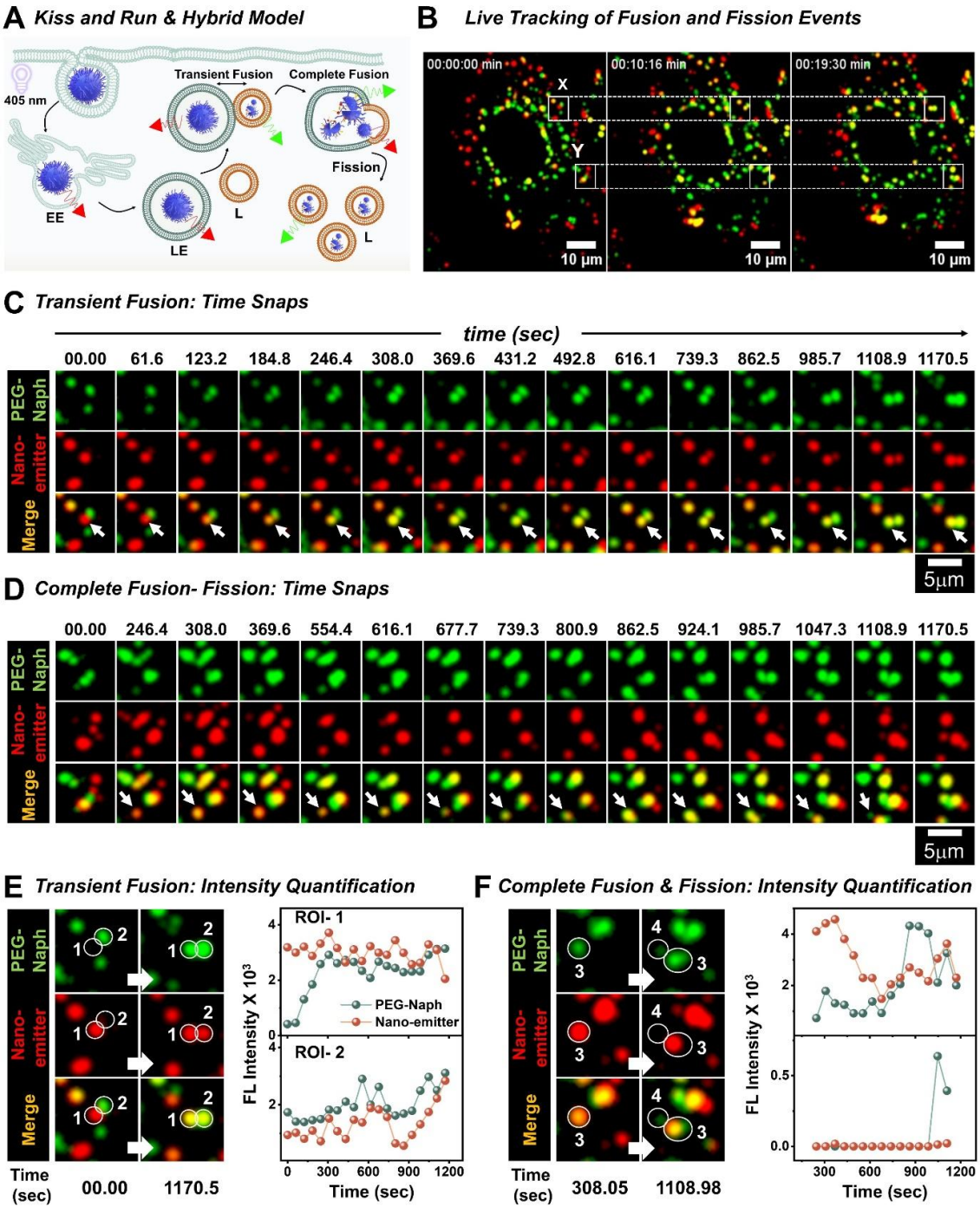

Figure* 4.9:** *Live cell imaging employing* ***nano-emitter *to monitor endosome- lysosome fusion and fission events in MCF 7 cells.* ***A:*** *Schematic showing Kiss and Run mediated transient fusions and hybrid organelle mediated complete fusions to exchange contents between endocytic vesicles. Lysosomes are reformed following fission of hybrid organelles.* ***B:*** *Selected time snaps of a single cell showing transient fusion (marked in square ROI- X) and complete fusion (marked in square ROI-Y).* ***C:*** *Zoomed-in time snapshots of ROI-X showing transient fusion between endosome and lysosome marked by white arrow.* ***D:*** *Zoomed-in time snapshots of ROI-Y showing complete fusions and reformation of lysosome from*

hybrid organelle as followed by white arrow. Scale bar: 5μm. Snaps were recorded every 61.1 seconds over a duration of 1170.5 seconds or 19.5 minutes. ***E:*** *The exchange of content via transient fusion is quantified by changes in fluorescence intensity in both the* ***nano-emitter*** *channel and the* ***PEG-Naph*** *channel for ROI-1 and ROI-2, which are marked for endosomes and lysosomes, respectively.* ***F:*** *The reformation of lysosomes from hybrid organelles is quantitatively confirmed by recording changes in the fluorescence intensity values with time for both the* ***PEG-Naph*** *and* ***nano-emitter*** *channels of ROI-3 and ROI-4, which are marked for endo-lysosomes and budding nascent lysosomes respectively.*

Second, via *fusion-fission* that leads to complete fusion of endosomes and lysosomes, forming a hybrid organelle (see ***Figure*** 4.9a). Transient fusions are sometimes, but not necessarily always, preceded by complete fusion events, emphasizing that they are not mutually exclusive. Both transient and complete fusions following content exchange forms hybrid organelles called, endo-lysosomes which have properties intermediate between late endosome and lysosome. Fusion consumes lysosomes, depleting cellular lysosome pools. New lysosomes called nascent lysosomes are regenerated through the fission of hybrid organelles (such as endo-lysosomes or autolysosomes), in a process called lysosome reformation. The nascent lysosomes then bud off, containing luminal content from the parent endo-lysosome (see ***Figure*** 4.9a). A single cell was selected for illustration, showing both transient (square frame- X, ***Figure*** 4.9b) and complete fusions (square frame-Y, ***Figure*** 4.9b). Cells were pulsed with ***nano-emitter*** for 1 hour and was chased in fresh media for 2 hours and was then imaged live under 405 nm laser illumination. Images were snapped every 61.1 seconds and selected snaps are shown from 0- 1170.5 seconds to follow transient fusion (***Figure*** 4.9c) and complete fusion-fission (***Figure*** 4.9d) events with time. Transient interaction between juxtaposed red fluorescent endosome and green fluorescent lysosome was monitored (follow white arrow in ***Figure*** 4.9e, Movie S1). The red endosome received a sudden influx of green fluorescence at around 123 seconds, and continued to increase sharply till 308 secs and turned yellow with time (see ***PEG-Naph*** and merged channel). Similarly, the green lysosome also received contents from interacting endosome turning yellow with time. Endosome was marked as ROI-1 and lysosome as ROI-2 to quantify the change in fluorescence intensities in the ***PEG-Naph*** and ***Nano-emitter*** channel with time (see marked ROI in ***Figure*** 4.9e). A substantial increase in fluorescence intensity in ***PEG-Naph*** channel and a decrease in ***nano-emitter*** channel of ROI-1 is seen (refer to the graph in ***Figure*** 4.9e). Concomitantly, intensity in both ***nano-emitter*** and ***PEG-Naph*** channel of ROI-2 increased with time (t_1= 0 to t_2= 1170.5 seconds). This intensity changes are due to the bi-directional flow of contents from endosome to

lysosome and vice-versa[28]. The transient fusions amongst them leads to formation of yellow fluorescent (due to overlap of both red and green emission signals) endo-lysosomes.

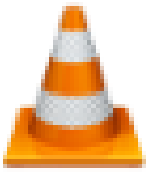

Movie-1.avi

Movie S1: *This movie illustrates the live monitoring of fusion of endosome (with red color) with lysosome in a kiss and run manner. This movie also features complete fusion between many endosomes and lysosomes coming together and fusing to form one body from which lysosome is regenerated.* ***To play****: double click and open the file with media player*.

In an isolated event, few yellow fluorescent endo-lysosomes appeared at around 246.5 seconds (follow white arrow in ***Figure*** 4.9e, Movie S1). The endo-lysosome marked with white arrow remained intact for a while until 862.5 seconds, following which budding like process started. It lasted till 1047.3 seconds, before green fluorescent nascent lysosome buds off from yellow parent endo-lysosome at 1108.9 seconds, leading to the reformation of lysosome. The endo-lysosome was designated as ROI-3, while ROI-4 was assigned to the position where the budded lysosome appeared over time (see marked ROI in ***Figure*** 4.9f). The fluorescence intensity increased in the ***PEG-Naph*** channel and decreased in the ***nano-emitter*** channel of ROI-3, indicating pH-mediated hydrolysis of the ***nano-emitter*** in the acidic lumen of endo-lysosomes with time (t_1= 0 to t_2= 1108.95 seconds). The fluorescence intensity increased only in the ***PEG-Naph*** channel, with no change detected in the ***nano-emitter*** channel of ROI-4 over time (refer to the graph in ***Figure*** 4.9f).

4.4.3 *Drug Sequestration by endocytic vesicles*

This quantification aligns with visual inspection, where the nascent lysosome is observed to depart with hydrolyzed ***PEG-Naph***, resulting in green fluorescence. Nascent lysosomes, with their green fluorescent luminal contents, exhibit properties more characteristic of mature lysosomes. Employing a single 405 nm excitation source, ***nano-emitter*** captured live images of endosomes and lysosomes, along with their interactions, in distinct fluorescent signals of red, green, and yellow as it ferried down the endocytic pathway. Additionally, ***nano-emitter*** facilitated

visualization of lysosome reformation from endo-lysosome in two colors as a green nascent lysosome budded off from the yellow fluorescent parent lysosome.

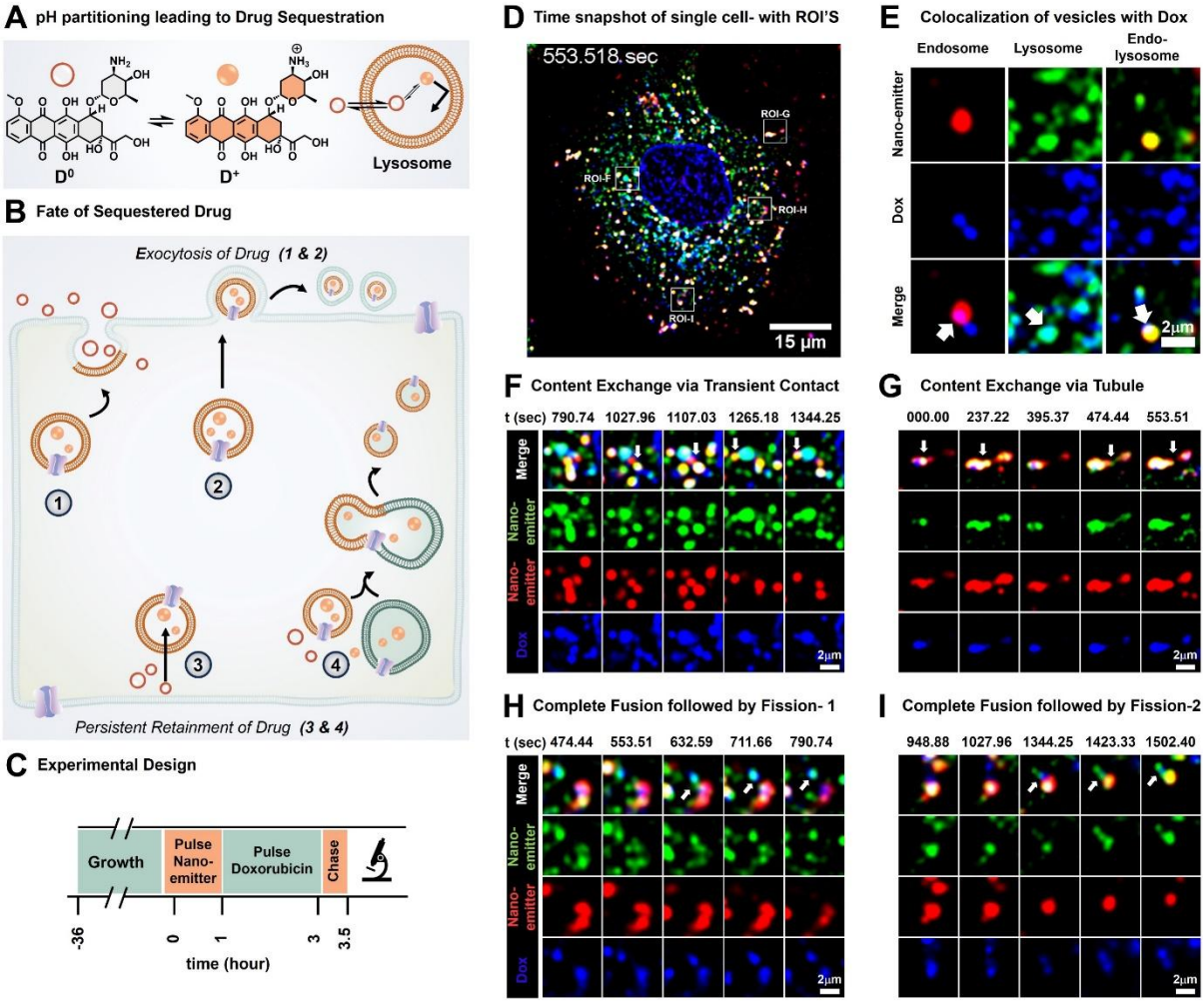

***Figure* 4.10:** *Employing **nano-emitter** to investigate the fate of drugs sequestered within lysosomes. **A:** pH partitioning of weak base Doxorubicin; D^0 which upon protonation forms D^+, leading to its sequestration inside the lysosomes. **B:** Illustration describing the fate of sequestered drug: (i) Drug Exocytosis as shown in 1 and 2 and (ii) persistent entrapment of drug as shown by 3 and 4. **C:** Experimental design to investigate the fate of sequestered drug. The cells were grown for 36 hours under standard conditions and are first treated with **nano-emitter** for 1 hour, followed by wash and then subsequently treated with Doxorubicin for 2 hours, chased for 1 hour and then imaged live. **D:** A time snapshot (553.51 seconds) of a single cell, marked with* ROIs, illustrates events related to drug sequestration by endocytic vesicles. ***E:** Images displaying the colocalization of **nano-emitter**-stained red endosomes, green lysosomes, and yellow endo-lysosomes with blue fluorescent doxorubicin. **F:** Zoomed-in time snapshots of ROI-F depict transient fusion-mediated exchange of doxorubicin among endocytic vesicles. **G:** Zoomed-in time snapshots of ROI-G depict doxorubicin exchange mediated via tubule*

formation. ***H, I:*** *Zoomed-in time snapshots of ROI-H & ROI-I depict the fission of drug-sequestered endo-lysosomes, dispersing the drug among newly generated nascent lysosomes.*

Subsequently, the ***nano-emitter*** was multiplexed with the fluorescent anticancer drug Doxorubicin to observe the drug's fate after sequestration by lysosomes in MCF 7 cells, which are drug sensitive. Lysosome acts as "drug-safe" house, where weakly basic cytostatic drugs are sequestered in acidic organelles due to pH partitioning. For instance, doxorubicin is a weak basic drug (pka= 8.2), which is membrane-permeable when in its neutral form ($\mathbf{D^0}$). However, upon entering the lysosome, it undergoes protonation ($\mathbf{D^+}$), resulting in reduced membrane permeability and consequently remains trapped inside them (see ***Figure*** 4.10a). However, the fate of drug molecules post drug sequestration remains elusive. They either are "expelled" from cells (see ***Figure*** 4.10b, mechanism-1,2) or are "persistently retained" in lysosomes of cells (***Figure*** 4.10b, mechanism-3). A lysosome carrying drug molecule fuses with plasma membrane to expel or release drug into the extracellular space (mechanism-1). Evidence in favour of lysosomal exocytosis comes from excessive lysosomal contents such as cathepsin- D and V-ATPase in the extracellular space. However, following drug exocytosis, previously trapped cytostatic drugs become abundant in the extracellular space to be again taken up by cells.

In lieu of this, recently, a novel mechanism was discovered in brain epithelial capillary cells as another way to expel drugs (mechanism-2). These cells dispose of drugs by releasing lysosome-derived vesicles as whole bodies into the extracellular space, which are then phagocytized by neutrophils. This process represents an effective means of processing cytostatic cargo, involving brain endothelial cells and is currently under study for other cell types. Apart from being expelled from the cells, the drug is suspected to be persistently retained within the lysosomes (mechanism-3). However, this pathway is not clearly elucidated. Here, we propose and elaborate on the persistent retention of drug molecules within acidic vesicles, spanning lysosomes, endosomes, and endo-lysosomes (mechanism-4), extending beyond the previously recognized mechanism limited to lysosomes (mechanism-3). First, the time-dependent partitioning of drug molecules within acidic organelles and the nucleus was investigated. Cells was pulsed with a subtoxic concentration of doxorubicin (100 nM) at various time points. At approximately 4 hours, a drug partition equilibrium was achieved as the blue fluorescence signal of doxorubicin (pseudo color, λ_{exc}= 488

nm, λ_{ems}= 490- 560 nm) in both acidic vesicles and the nucleus became constant. The blue fluorescence inside acidic vesicles persisted even at 12 hours (data not shown). Therefore, post-sequestration events were monitored 2 hours after drug treatment, before the establishment of drug partition equilibrium.

In a typical experimental setup, MCF 7 cells were pulsed with a ***nano-emitter*** for 1 hour and then washed. Subsequently, they were pulsed with doxorubicin for 2 hours, after which fresh medium was added, and was subjected to live imaging after 30 minutes of chase in fresh media (***Figure*** 4.10c). A single-cell image was chosen to represent the series of events (highlighted in white square ROI-F, G, H, I in ***Figure*** 4.10d) that led us to propose mechanism 4. Doxorubicin was observed present in endosomes, endo-lysosomes and lysosomes. The blue fluorescent signal of doxorubicin (pseudo-color) colocalized with green fluorescent lysosomes, resulting in a cyan appearance. In contrast, it resulted in white appearance when observed alongside yellow fluorescent endo-lysosomes, and in magenta appearance with red endosomes (***Figure*** 4.10e). Several events as marked by ROI-F, G, H, I will be discussed to then propose a mechanism. As marked in ROI-F and ROI-G, transient contact mediated content exchange led to dispersal of doxorubicin amongst vesicular bodies (***Figure*** 4.10f). A series of events occurring between 790.74- and 1027.96-seconds results in a red endosome making transient contacts with a drug-containing lysosome (cyan) and an endo-lysosome (white) from both sides (merge panel, ***Figure*** 4.10f). At 1107.03 seconds, doxorubicin moves from the lysosome towards the endosome, causing it to turn magenta (see merge and Dox panel). Subsequently, at 1265.18 seconds, another endo-lysosome is observed transiently fusing with the cyan lysosome, and at 1344.25 seconds, it transfers doxorubicin into the endo-lysosome (see Dox panel, ***Figure*** 4.10f). In a rare event, transient contact mediated content transfer via tubule formation was captured (ROI-G and ***Figure*** 4.10g). An endo-lysosome with doxorubicin interacted with a neighbouring endosome, leading to the transfer of some doxorubicin at 237.22 seconds (see Dox panel). Interestingly, at around 474.44 seconds, a tubule was seen connecting both bodies and visibly transferred doxorubicin before breaking contact at 553.51 seconds (see Dox panel). Not just transient, but complete interactions followed by fission mediated the dispersal of drug to newly formed lysosomes. The process of complete fusion gives rise to an endo-lysosome containing doxorubicin, maintaining its integrity until 474.44 seconds (ROI-H, see merge panel of ***Figure*** 4.10h). Subsequently, at 553.51 seconds,

green nascent lysosomes emerged as buds from the endo-lysosome, with blue doxorubicin becoming apparent in the developing bud by 632.59 seconds (see merge panel and Dox panel). At 711.66 seconds, the lysosome successfully buds off from the parent endo-lysosome, effectively sharing its doxorubicin content. In another event, a series of fissions were observed consecutively (ROI-I, see ***Figure*** 4.10i). While some led to the dispersal of doxorubicin, others did not. An endo-lysosome remains intact until 948.88 seconds, featuring a small blue bud that eventually buds off and drifts apart at 1027.96 seconds. A few seconds later, around 1344.25 seconds, two green lysosomes appear to bud, with one containing doxorubicin.

Out of the 11 single-cell experiments recorded (N= 2), fusion-fission mediated doxorubicin transfer was highly conserved, with content transfer via tubule formation being rare. The interplay among these acidic organelles, mediated by fusion-fission, was instrumental in exchanging and distributing the sequestered cytostatic content. These observations led us to propose an alternative mechanism, depicted as Mechanism-4 in ***Figure*** 4.10b, involving endosomes and lysosomes that initially sequester drugs effectively due to pH partitioning. Subsequently, they exchange doxorubicin among themselves via transient fusions. Complete fusions result in the formation of drug-carrying endo-lysosomes, which then undergo budding to distribute doxorubicin into newly formed lysosomes. This division of the cytostatic payload might also contribute to reducing organelle damage. Fusion and fission enhance the efficiency of drug sequestration and assist acidic vesicles in persistently retaining the drug. Mex-De enabled ***nano-emitter*** was easily multiplexed with doxorubicin with no excitation caused bleed through as excitation sources are far separated. Employing ***nano-emitter***, we acknowledged the role of fusions and fissions in helping cells to persistently trap drugs, a finding that is yet to be documented. Further studies are underway to employ ***nano-emitter*** in investigating the fate of sequestered drugs in resistant cell lines. This will pave way for the development of therapeutic strategies to mitigate resistance caused by drug sequestration.

4.5 Conclusions

Vesicular fusion and fission events result in exchange of contents (such as small molecules, drugs and macromolecules etc.) between endocytic organelles, promoting essential catabolism for maintaining cellular homeostasis. Fusions between endosomes and lysosomes typically occurs

through two main methods. First, through *kiss-and-run*, that involves the transient fusion or interaction of endosomes with lysosomes, facilitating the exchange of contents between them and leads to formation of hybrid organelles. Secondly, via fusion-fission in which endosomes and lysosomes form hybrid organelles, from which lysosomes are regenerated via fission. Employing nano-emitter transient fusion between red fluorescent endosomes and green fluorescent lysosome were easily monitored using a single excitation wavelength. Further, complete fusion could be easily seen as the yellow endo-lysosomes were clearly distinguished from endosomes and lysosomes. Further, the process of fission was easily monitored from Endo lysosomes.

Further, we leveraged ***nano-emitter*** in understanding of fate of sequestered drugs by lysosomes in MCF 7 cells. We acknowledged a new mechanism, employing role of fusions and fissions between endocytic vesicles to persistently trap drugs, a finding that is yet to be documented. This study clearly helps understand the role of endosomes and lysosomes in sequestering drug molecules, which can lead to decreased therapeutic efficacy and can help rationalize heterogeneity in patient response to therapeutics at cellular level.

4.6 Bibliography

(1) White, J. M. Membrane Fusion. *Science* **1992**, *258* (5084), 917-924.
(2) Luzio, J. P.; Pryor, P. R.; Bright, N. A. Lysosomes: fusion and function. *Nat. Rev. Mol. Cell Biol.* **2007**, *8* (8), 622-632.
(3) Mutvei, A. P.; Nagiec, M. J.; Blenis, J. Balancing lysosome abundance in health and disease. *Nat. Cell Biol.* **2023**, *25* (9), 1254-1264.
(4) Lloyd-Evans, E.; Morgan, A. J.; He, X.; Smith, D. A.; Elliot-Smith, E.; Sillence, D. J.; Churchill, G. C.; Schuchman, E. H.; Galione, A.; Platt, F. M. Niemann-Pick disease type C1 is a sphingosine storage disease that causes deregulation of lysosomal calcium. *Nat Med* **2008**, *14* (11), 1247-1255.
(5) Treusch, S.; Knuth, S.; Slaugenhaupt, S. A.; Goldin, E.; Grant, B. D.; Fares, H. Caenorhabditis elegans functional orthologue of human protein h-mucolipin-1 is required for lysosome biogenesis. *Proc Natl Acad Sci USA* **2004**, *101* (13), 4483-4488.
(6) Durchfort, N.; Verhoef, S.; Vaughn, M. B.; Shrestha, R.; Adam, D.; Kaplan, J.; Ward, D. M. The Enlarged Lysosomes in beigej Cells Result From Decreased Lysosome Fission and Not Increased Lysosome Fusion. *Traffic* **2012**, *13* (1), 108-119.
(7) Golam, T. S. a. R. J. B. Lysosome Fission: Planning for an Exit. *Trends in Cell Biology* **2019**, *29* (8), 635-646.
(8) Machado, E. R.; Annunziata, I.; van de Vlekkert, D.; Grosveld, G. C.; d'Azzo, A. Lysosomes and Cancer Progression: A Malignant Liaison. *Frontiers in Cell and Developmental Biology* **2021**, *9*, Review.
(9) Zhao, B.; Dierichs, L.; Gu, J.-N.; Trajkovic-Arsic, M.; Axel Hilger, R.; Savvatakis, K.; Vega-Rubin-de-Celis, S.; Liffers, S.-T.; Peña-Llopis, S.; Behrens, D.; et al. TFEB-mediated lysosomal biogenesis and lysosomal drug sequestration confer resistance to MEK inhibition in pancreatic cancer. *Cell Death Discov.* **2020**, *6* (1), 12.
(10) Zhitomirsky, B.; Assaraf, Y. G. Lysosomal accumulation of anticancer drugs triggers lysosomal exocytosis. *Oncotarget; Vol 8, No 28* **2017**.
(11) Rennick, J. J.; Johnston, A. P. R.; Parton, R. G. Key principles and methods for studying the endocytosis of biological and nanoparticle therapeutics. *Nat. Nanotechnol.* **2021**, *16* (3), 266-276.
(12) Miller, M. A.; Weissleder, R. Imaging of anticancer drug action in single cells. *Nat. Rev. Cancer.* **2017**, *17* (7), 399-414.
(13) Bonam, S. R.; Wang, F.; Muller, S. Lysosomes as a therapeutic target. *Nat. Rev. Drug Discov.* **2019**, *18* (12), 923-948.
(14) Assies, L.; Mercier, V.; López-Andarias, J.; Roux, A.; Sakai, N.; Matile, S. The Dynamic Range of Acidity: Tracking Rules for the Unidirectional Penetration of Cellular Compartments. *ChemBioChem* **2022**, *23* (15), e202200192.
(15) Chen, X.-X.; Bayard, F.; Gonzalez-Sanchis, N.; Pamungkas, K. K. P.; Sakai, N.; Matile, S. Fluorescent Flippers: Small-Molecule Probes to Image Membrane Tension in Living Systems. *Angew. Chem. Int. Ed.* **2023**, *62* (20), e202217868.
(16) Qiu, K.; Seino, R.; Han, G.; Ishiyama, M.; Ueno, Y.; Tian, Z.; Sun, Y.; Diao, J. De Novo Design of A Membrane-Anchored Probe for Multidimensional Quantification of Endocytic Dynamics. *Adv. Healthc. Mater.* **2022**, *11* (8), 2102185.
(17) Bright, N. A.; Gratian, M. J.; Luzio, J. P. Endocytic Delivery to Lysosomes Mediated by Concurrent Fusion and Kissing Events in Living Cells. *Curr. Biol.* **2005**, *15* (4), 360-365.

(18) Arppe, R.; Carro-Temboury, M. R.; Hempel, C.; Vosch, T.; Sørensen, T. J. Investigating dye performance and crosstalk in fluorescence enabled bioimaging using a model system. *PLoS One* **2017**, *12* (11), e0188359.
(19) Hu, F.; Cai, X.; Manghnani, P. N.; Kenry; Wu, W.; Liu, B. Multicolor monitoring of cellular organelles by single wavelength excitation to visualize the mitophagy process. *Chem. Sci.* **2018**, *9* (10), 2756-2761, 10.1039/C7SC04585A.
(20) Jun, Y. W.; Wang, T.; Hwang, S.; Kim, D.; Ma, D.; Kim, K. H.; Kim, S.; Jung, J.; Ahn, K. H. A Ratiometric Two-Photon Fluorescent Probe for Tracking Lysosomal ATP: Direct In Cellulo Observation of Lysosomal Membrane Fusion Processes. *Angew. Chem. Int. Ed.* **2018**, *57* (32), 10142-10147.
(21) Niino, Y.; Hotta, K.; Oka, K. Simultaneous Live Cell Imaging Using Dual FRET Sensors with a Single Excitation Light. *PLoS One* **2009**, *4* (6), e6036.
(22) Sedgwick, A. C.; Dou, W.-T.; Jiao, J.-B.; Wu, L.; Williams, G. T.; Jenkins, A. T. A.; Bull, S. D.; Sessler, J. L.; He, X.-P.; James, T. D. An ESIPT Probe for the Ratiometric Imaging of Peroxynitrite Facilitated by Binding to Aβ-Aggregates. *J. Am. Chem. Soc.* **2018**, *140* (43), 14267-14271.
(23) Guo, L.; Tian, M.; Zhang, Z.; Lu, Q.; Liu, Z.; Niu, G.; Yu, X. Simultaneous Two-Color Visualization of Lipid Droplets and Endoplasmic Reticulum and Their Interplay by Single Fluorescent Probes in Lambda Mode. *J. Am. Chem. Soc.* **2021**, *143* (8), 3169-3179.
(24) Ejike, J. O.; Sadoine, M.; Shen, Y.; Ishikawa, Y.; Sunal, E.; Hänsch, S.; Hamacher, A. B.; Frommer, W. B.; Wudick, M. M.; Campbell, R. E.; et al. A Monochromatically Excitable Green–Red Dual-Fluorophore Fusion Incorporating a New Large Stokes Shift Fluorescent Protein. *Biochem.* **2024**, *63* (1), 171-180.
(25) Vyas, A.; Gomez-Casal, R.; Cruz-Rangel, S.; Villanueva, H.; Sikora, A. G.; Rajagopalan, P.; Basu, D.; Pacheco, J.; Hammond, G. R. V.; Kiselyov, K.; et al. Lysosomal inhibition sensitizes TMEM16A-expressing cancer cells to chemotherapy. *Proc Natl Acad Sci USA* **2022**, *119* (12), e2100670119.
(26) Jiang, X.; Dausend, J.; Hafner, M.; Musyanovych, A.; Röcker, C.; Landfester, K.; Mailänder, V.; Nienhaus, G. U. Specific Effects of Surface Amines on Polystyrene Nanoparticles in their Interactions with Mesenchymal Stem Cells. *Biomacromolecules* **2010**, *11* (3), 748-753.
(27) Barral, D. C.; Staiano, L.; Guimas Almeida, C.; Cutler, D. F.; Eden, E. R.; Futter, C. E.; Galione, A.; Marques, A. R. A.; Medina, D. L.; Napolitano, G.; et al. Current methods to analyze lysosome morphology, positioning, motility and function. *Traffic* **2022**, *23* (5), 238-269.
(28) Bucci, C.; Thomsen, P.; Nicoziani, P.; McCarthy, J.; van Deurs, B. Rab7: A Key to Lysosome Biogenesis. *Molecular Biology of the Cell* **2000**, *11* (2), 467-480.

Conclusions and Future Directions

Conclusions

This thesis work scrutinized the role of inter-organelle interactions such as that between endosomes and lysosomes in mediating drug delivery aspects of nanocarriers. Interestingly, such interactions are also actively involved in sequestering of drug molecules. The endocytosis of polymersomes shuttles them across endocytic organelle where in they finally land up in lysosomes. We tracked this process using FRET active polymersomes, that showed FRET signal which lasted up to 2 hours, possibly because it the polymersomes resided in endosomes before finally reaching lysosomes, where FRET signal started to decrease and self-emission corresponding to Rose Bengal started to increase. This happened due to hydrolytic capacity of lysosomes which break opens the polymersomes to releases the Rhodamine dye. The cells illuminated red until 2 hours due to FRET emission coming from possibly endosomes, when excited at 405 nm i.e. TPE excitation. However, as the time progressed, the blue emission from TPE illuminated the cytoplasmic space, which emanated from lysosomes. This points towards the unloading of cargo, rose Bengal in presence of enzyme. The enzyme responsiveness of polymersomes inside of the cells could be easily monitored by changes in the FRET readout and retrieval of self-emission of TPE. Having confidence in the polymersomes, enzyme responsiveness unloading of cargo, its efficiency was tested to translocate doxorubicin to lysosomes of the cells and ultimately to its nuclear DNA. Polymersomes stood up to our expectations. It formed a dark pair with the drug, doxorubicin and showed quenching in the fluorescence. However, as the time progressed, the polymersomes upon reaching the lysosomal site underwent disintegration and subsequently lead to disassembly of the dark pair. This led to retrieval of blue fluorescence emanating form TPE and illuminated the lysosomes blue as were seen in the single cell images. The doxorubicin successfully found its way to the nuclear DNA, where it showed intense red emission, which was previously quenched upon interacting with TPE. Clearly, its due to the interactions between endocytic organelles, that polymersomes could land up to lysosomes, which are terminal stations for cargo degradation, where enzyme mediated disassembly of polymersomes happened to release the drug molecules. Had it been not for this endocytic organelle interaction, the polymersomes might not have reached lysosomes to do the needful. This could actually be a case at clinical settings where response to therapeutic remains highly heterogeneous amongst the patients. This calls for investigation at the

single cell level and elucidate the pharmacology mechanism happening at individual patient's cell level. Recently, it's been long known the role of cellular endosomes and lysosomes in sequestering of weakly basic drug molecules such as doxorubicin. However, the fate of these sequestered drugs continues to be a mystery. This ability of lysosomes to keep hold of drug molecules leads to Multi drug resistance. The mechanistic understating of sequestration by these organelles sequesters drug molecules and continues to trap them will help find ways to intervene therapeutically and resolve the problem of drug sequestration and reduced drug efficacy. However, such mechanistic insights are rather rare. We attempted to devise a fluorescent probe that could distinctly two-color mark endosomes and lysosome, so as to make the understanding of their interaction easy to monitor under live conditions. we designed single wavelength excitable pH responsive nano emitter that showed red ESIPT emission in the endosomes and green emission in the lysosomes. Some structural engineering helped us optimize a nano-emitter structure integrated with pH sensitive imine linkage that showed red ESIPT emission. We analyzed the role of electronic substituents and the effect of self-assembly in modulating the emission properties to yield only ESIPT emission. Self-assembly is a simple yet effective strategy to modulate the emission properties of fluorophores. The ESIPT active anno-emitter upon undergoing pH dependent cleavage results in the hydrolysis of the nano-emitter to yield green emission under a dingle wavelength excitation. Subsequently this probe was employed in biology to study intraorganellar interactions. Their dynamic interactions of fusions and fusion-fission leading to formation of new lysosomes was successfully captured. Leveraging the abilities of nano-emitter, we employed to images the dynamics of endosomes and lysosomes in sequestering doxorubicin. The single wavelength excitable nano emitter could be easily multiplexed with doxorubicin, Nano-emitter is excitable using g 405 nm laser and leaves pretty much the entire visible range to be multiplexed with itself. We realized endosomes and lysosomes work in unison to sequester doxorubicin and keeps on shuttling it amongst amongst themselves or by dividing the drug payload into newly formed lysosomes. This helps the cells to persistently keep hold of drugs and always keep their equilibrium concentration low to cause any cytotoxic effects and ensure continued survival of cancer cells.

Future Directions

The nano-emitter is highly sturdy in understanding the drug sequestration abilities by the lysosomes. It is important to realize its full potentials in terms of studying cell lines which have higher or a are completely resistant to the drug molecules. The application and understanding of

drug sequestration mechanism by different cell lines will help understand different defense mechanism a cell can adopt to protect itself from a cytostatic shock. This needs careful investigation with different model cell lines of advanced cancers and possibly to animal tissue sections. The application and scope of anna emitter probe could be broadened by tagging of this fluorophore to the polymeric backbone, which upon self-assembly can load drug molecules. This system offers better insights into both the drug release and drug sequestration abilities under the lysosomal atmosphere. Such project is currently under investigation. Dextran was stitched with carboxylic acid functionalized nano-emitter and was characterizer analytically. The primary investigations showed that they retained ESIPT emission. Work is currently under progress for this project.

In an unrelated project, we can aim to study Lipophagy, a highly concerted cellular process. The Schiff dyes are highly sensitive to electronic substituents which led to the formation of DET-Imine that showed intramolecular charge transfer characteristics. DET-Imine showed excellent and very fast staining of lipid droplets inside the cells in less than 5 minutes and gave red emission inside the lipid droplets. Such dyes can be exploited further to study Lipophagy which is the indication between lipid droplets and lysosomes. It is very obvious that the dye will hydrolyze in the lysosomes which will give green emission. Such dual color targeting is very beneficial in studying organelle interaction between lipid droplets and lysosomes.

List of publications

1. Virmani, M.[#]; Deshpande, N. U[#].; Pathan, S.; Jayakannan, M. Self-Reporting Polysaccharide Polymersome for Doxorubicin and Cisplatin Delivery to Live Cancer Cells. *ACS Polymers Au* **2022**, *2* (3), 181-193. DOI: 10.1021/acspolymersau.1c00042. *(Invited article)*
2. Deshpande, N. U[#].; Virmani, M[#].; Jayakannan, M. An AIE-driven fluorescent polysaccharide olymersome as an enzyme-responsive FRET nanoprobe to study the real-time delivery aspects in live cells. *Polym. Chem.* **2021**, *12* (10), 1549-1561, 10.1039/D0PY01085E. DOI: 10.1039/D0PY01085E.
3. Roy, P.; Virmani, M.; Pillai, P. P. Blue-emitting InP quantum dots participate in an efficient resonance energy transfer process in water. Chem. Sci. **2023**, 14 (19), 5167-5176. DOI: 10.1039/D3SC00164D *(not included in this thesis)*
4. Virmani, M.; Jayakannan, M. ESIPT-Active Nano-emitter Mediated Real-Time Tracking of Endosome-Lysosome Dynamics for Elucidating Drug Sequestration in Live Cells. *(Manusript under Review)*
5. Virmani, M.; Jayakannan, Effect of electronic substitution on Structural Engineering of ESIPT probe for Bio-imaging appliactions. M. *(Manusript under preperation)*

\# *Equal Authourship*

Polymer Chemistry

ROYAL SOCIETY OF CHEMISTRY

PAPER

View Article Online
View Journal | View Issue

Cite this: *Polym. Chem.*, 2021, **12**, 1549

An AIE-driven fluorescent polysaccharide polymersome as an enzyme-responsive FRET nanoprobe to study the real-time delivery aspects in live cells†

Nilesh Umakant Deshpande,‡ Mishika Virmani‡ and Manickam Jayakannan *

We report aggregation induced emission (AIE) driven polysaccharide polymersomes as fluorescence resonance energy transfer (FRET) nanoprobes to study their intracellular enzyme-responsive delivery by real-time live-cell confocal microscopy bio-imaging techniques. An AIE active tetraphenylethylene (TPE) optical chromophore and plant-based vesicular directing hydrophobic unit were grafted on clinically relevant polysaccharide-dextran *via* enzyme-cleavable aliphatic ester chemical linkages. The TPE-tagged dextran self-assembled as 180 ± 20 nm blue-luminescent polymersomes in aqueous medium and exhibited excellent encapsulation capabilities for water soluble Rose Bengal (RB) and water insoluble Nile red (NR) fluorophores. The selective photoexcitation of the TPE chromophore enabled the FRET process between the TPE donor and RB (or NR) acceptor molecule in <50 Å Förster distance afforded by the polymersome. The FRET probe was very stable under extracellular conditions and it exclusively underwent lysosomal esterase enzymatic biodegradation at the intracellular compartments to release RB. The enzyme-trigger enabled the FRET probe to function as an extracellular turn-ON → intracellular turn-Off red-fluorescent signal (Probe-1). In this process, the AIE self-emission was also simultaneously restored on the TPE chromophore (blue-luminescent, Probe-2) followed by the isolation of donor and acceptor in the cytosol. As a result, this new design enabled the visualization of real-time enzyme-responsive delivery by monitoring the dual fluorescent signals from both the polymer host (blue) and encapsulated guest (red) in a single nano-platform. *In vitro* cytotoxicity studies established that the polymersome probe was non-toxic to cells up to 300 μg mL^{-1}. Lyso-tracker staining experiments supported the FRET probe internalization in the lysosomal compartments for enzymatic-biodegradation. Live cell confocal microscopy with selective photo-excitation was used to directly monitor the enzyme-responsive FRET action in human breast cancer MCF 7 and wild-type mouse embryonic fibroblast cell lines (WT-MEFs). It was found that the tailor-made polymersome FRET probe was efficient to deliver the loaded cargo in <3 h in live cells which predicts the usefulness of the probe in biomedical research.

Received 29th July 2020,
Accepted 17th December 2020

DOI: 10.1039/d0py01085e

rsc.li/polymers

Introduction

Fluorescent polymer nano-assemblies are dual-purpose biomaterials for delivering therapeutic drugs (or genes) while simultaneously probing their function in intracellular compartments or tumor micro-environments by bioimaging techniques.[1–3] Amphiphilic block copolymer nanoparticles,[4,5] unimolecular micelles,[6] dendrimers,[7] supramolecular nano-assemblies,[8] polymersomes (or polymer vesicles)[9,10] *etc.*, are some of the most important fluorescent macromolecular nano-assemblies that are explored in cancer therapy. Among them, polymersomes are unique self-assembled nano-scaffolds and they possess well-defined compartmentalization of the hydrophilic core and hydrophobic layer for loading both water soluble and insoluble drugs and fluorescent molecules, respectively.[11,12] These unique features of the polymersome nano-assemblies make them distinct nano-scaffolds for loading wide ranges of cargoes irrespective of their solubility parameters.[13–19] Aggregation induced emission (AIE) is a newly emerging photophysical phenomenon and it is an excel-

Department of Chemistry, Indian Institute of Science Education and Research (IISER Pune), Dr. Homi Bhabha Road, Pune 411008, Maharashtra, India. E-mail: jayakannan@iiserpune.ac.in

†Electronic supplementary information (ESI) available: ^{1}H-NMR, ^{13}C NMR, HRMS and MALDI-TOF spectra of the compounds and polymers, absorbance and emission spectral details, enzyme-responsiveness release data, FRET overlap, confocal images, and MALDI-TOF and HRMS spectra. See DOI: 10.1039/d0py01085e

‡These authors have contributed equally.

ACS POLYMERS Au

pubs.acs.org/polymeraau

Article

Self-Reporting Polysaccharide Polymersome for Doxorubicin and Cisplatin Delivery to Live Cancer Cells

Mishika Virmani, Nilesh Umakant Deshpande, Shahidkhan Pathan, and Manickam Jayakannan*

Cite This: ACS Polym. Au 2022, 2, 181−193

Read Online

ACCESS | Metrics & More | Article Recommendations | Supporting Information

ABSTRACT: We report self-reporting fluorescent polysaccharide polymersome nanoassemblies for enzyme-responsive intracellular delivery of two clinical anticancer drugs doxorubicin (DOX) and cisplatin to study the real-time drug-releasing aspects by fluorescent resonance energy transfer (FRET) bioimaging in live cancer cells. Fluorescent polymersomes were tailor-made by tagging an aggregation-induced emission (AIE) optical chromophore, tetraphenylethylene (TPE), and a plant-based vesicular directing hydrophobic unit through enzyme-biodegradable aliphatic ester chemical linkages in the polysaccharide dextran. The blue-luminescent polymersome self-assembled in water and exhibited excellent encapsulation capability for the red-luminescent anticancer drug DOX. FRET between the AIE polymersome host and DOX guest molecules resulted in a completely turn-off probe. At the intracellular level, the lysosomal enzymatic disassembly of the polymersome restored the dual fluorescent signals from DOX and TPE at the nucleus and the lysosomes, respectively. Live-cell confocal microscopy coupled with selective photoexcitation was employed to study the real-time polymersome disassembly by monitoring the turn-on fluorescent signals in human breast cancer cell lines. Alternatively, carboxylic acid-functionalized AIE polymersomes were also tailor-made for cisplatin stitching to directly monitor Pt drug delivery. The polymersome nanoassemblies exhibited excellent structural tolerance for the chemical conjugation of the Pt drugs, and the fluorescence signals were unaltered. An in vitro drug release study confirmed that the cisplatin-stitched fluorescent polymersomes were very stable under physiological conditions and underwent lysosomal enzymatic degradation to inhibit the cancer cell growth. A lysosomal colocalization experiment using confocal microscopy substantiates the enzyme-responsive degradation of these polymersomes to release both the encapsulated and conjugated drugs at the intracellular level. The present design provides a unique opportunity to deliver more than one anticancer drug from a single polymersome platform in cancer research.

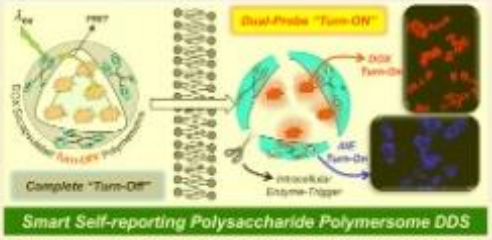

KEYWORDS: *drug delivery, fluorescent probes, polymersomes, enzyme-responsive, polysaccharides, cisplatin, doxorubicin*

INTRODUCTION

Enlarging therapeutic effects of anticancer drugs has become the holy grail of oncotherapy, thereby paving the way for the development of drug-delivery systems (DDSs) in cancer treatment.[1−4] Multitudes of delivery scaffolds ranging from liposomes,[5] microspheres,[6] dendrimers,[7] polymeric drug conjugates,[8] polymeric micelles,[9] and polymersomes[10−12] have been a subject of extensive clinical research. The rationale of loading therapeutics in delivery vehicles is to reduce systemic toxicity by shielding the drug against a plethora of plasma components during its transport via the bloodstream and later accumulating inside the target site leading to enhanced efficacy.[13] The choice of the delivery scaffold and its concomitant effects on drug efficacy is worth paying attention to improve the cancer treatment.[14] For instance, liposomal encapsulation of the chemotherapy drug doxorubicin (DOX) has shown considerable reduction in cardiotoxicity, simultaneously maintaining a high level of efficacy.[15,16] Surprisingly, liposomal formulation of cisplatin-conjugated drug (SPI-77 or stealth cisplatin) showed rather poor efficacy owing to slow release inside the tumor.[17,18] The problem of reduced efficacy due to poor uptake can be mitigated by a thoughtful choice of engineering the structural aspects of the nanoscaffold. Sugars are ubiquitous to cell membranes, and hence, polysaccharide-based scaffolds such as dextran become candidates of choice as they are easily taken up by the cells owing to like−like interactions.[8,19−21] Tagging the scaffold with a fluorophore can further help shed light on its uptake mechanism at the cellular level and also enable the tracking of the polymer nanocarriers.[22,23] Therefore, next-generation polymer nanocarriers are required to create a smart self-

Received: September 30, 2021
Revised: December 11, 2021
Accepted: December 13, 2021
Published: December 28, 2021

https://doi.org/10.1021/acspolymersau.1c00042
ACS Polym. Au 2022, 2, 181−193

Chemical Science

ROYAL SOCIETY OF CHEMISTRY

EDGE ARTICLE

View Article Online
View Journal | View Issue

Check for updates

Cite this: Chem. Sci., 2023, 14, 5167

All publication charges for this article have been paid for by the Royal Society of Chemistry

Blue-emitting InP quantum dots participate in an efficient resonance energy transfer process in water†

Pradyut Roy, Mishika Virmani and Pramod P. Pillai *

Development of stable blue-emitting materials has always been a challenging task because of the necessity of high crystal quality and good optical properties. We have developed a highly efficient blue-emitter, based on environmentally friendly indium phosphide/zinc sulphide quantum dots (InP/ZnS QDs) in water, by controlling the growth kinetics of the core as well as the shell. A rational combination of less-reactive metal-halides, phosphorus, and sulphur precursors is the key for achieving the uniform growth of the InP core and ZnS shell. The InP/ZnS QDs showed long-term stable photoluminescence (PL) in the pure-blue region (~462 nm), with an absolute PL quantum yield of ~50% and a colour purity of ~80% in water. Cytotoxicity studies revealed that the cells can withstand up to ~2 micromolar concentration of pure-blue emitting InP/ZnS QDs (~120 μg mL^{-1}). Multicolour imaging studies show that the PL of InP/ZnS QDs was well-retained inside the cells as well, without interfering with the fluorescence signal of commercially available biomarkers. Moreover, the ability of InP based pure-blue emitters to participate in an efficient Förster resonance energy transfer (FRET) process is demonstrated. Installing a favorable electrostatic interaction turned out to be crucial in achieving an efficient FRET process (E ~75%) from blue-emitting InP/ZnS QDs to rhodamine B dye (Rh B) in water. The quenching dynamics fits well with the Perrin formalism and the distance-dependent quenching (DDQ) model, which confirms an electrostatically driven multi-layer assembly of Rh B acceptor molecules around the InP/ZnS QD donor. Furthermore, the process of FRET was successfully translated into the solid state, proving their suitability for device-level studies as well. In short, our study expands the spectrum of aqueous QDs based on InP towards the blue region for future biological and light harvesting studies.

Received 11th January 2023
Accepted 20th April 2023

DOI: 10.1039/d3sc00164d

rsc.li/chemical-science

Introduction

Luminescent materials find applications in broad areas of science and technology including full-color display devices, photovoltaics, bioimaging and targeting, sensing, and so on.[1–3] The diversity of modern science demands for the need of luminescent materials that emit in all regions of the visible and near-infrared spectra.[3–5] But, it is challenging to prepare 'pure' blue-emitting luminescent materials as they often fail to meet the stringent requirement of colour purity, high and stable quantum yield, and long-term photostability.[1,2] This has been an obstacle in realizing the full use of luminescent materials in different areas of energy and medical research. Quantum dots (QDs) can be one class of materials that could solve this challenge, as they possess unique optoelectronic properties, such as large absorption cross-section, tunable and narrow emission bandwidth, high photoluminescence quantum yield (PL QY), and enhanced photostability.[3,6–14] In this direction, indium phosphide (InP) based QDs are emerging as one of the luminescent materials of choice because of their intrinsically lower toxicity over traditional Cd- and Pb-based QDs.[15–17] However, the creation of highly luminescent blue-emitting InP QDs is not a straight-forward task in QD research because of the necessity of an ultra-small sized QD core (<2 nm).[8,18] The ultra-small QDs are prone to contain more crystal defects that could hamper their luminescent properties, and this demands for improved synthetic strategies. Moreover, the high covalent nature of InP QDs makes them more vulnerable to oxidizing environments.[19] A few protocols are available to prepare blue-emitting InP QDs in organic medium, wherein the growth kinetics of QDs is slowed down by controlling the reaction temperature, precursor reactivity, surface etching, shell growth, competitive secondary nucleation process, *etc.*[19–26] In one example, stable blue-emitting InP/ZnS/ZnS QDs (λ_{em} ~475 nm) were prepared by fine-tuning the inherent reactivity between phosphorus and indium precursors, thereby achieving a control

Department of Chemistry, Indian Institute of Science Education and Research (Pune), Dr Homi Bhabha Road, Pashan, Pune – 411008, India. E-mail: pramod.pillai@iiserpune.ac.in

† Electronic supplementary information (ESI) available: Detailed experimental methods, synthesis, and characterization of QDs, stability studies, bioimaging, uptake mechanism, proof of electrostatics and calculation of various parameters involved in the FRET study. See DOI: https://doi.org/10.1039/d3sc00164d

Appendix A: NMR's and MALDI of compounds synthesized for this thesis

A.1 (a) ^{1}H (400 MHz, DMSO-d_6) *and* (b) ^{13}C (100 MHz, DMSO-d_6) NMR of *Molecule-1*

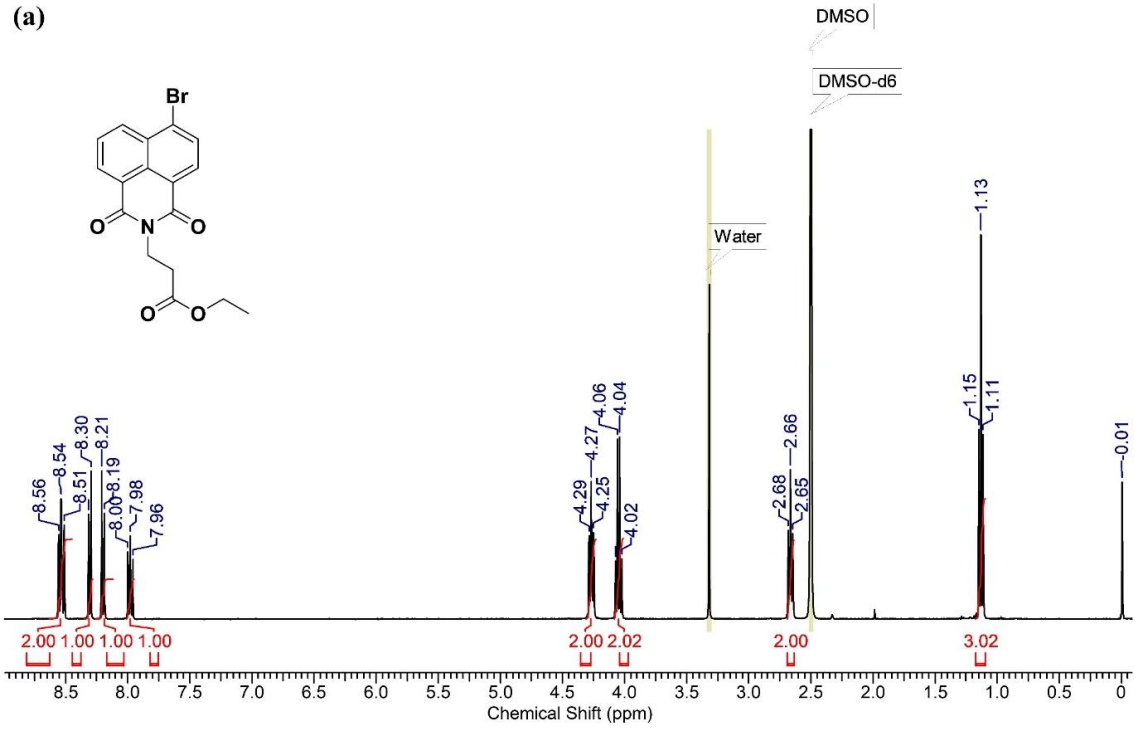

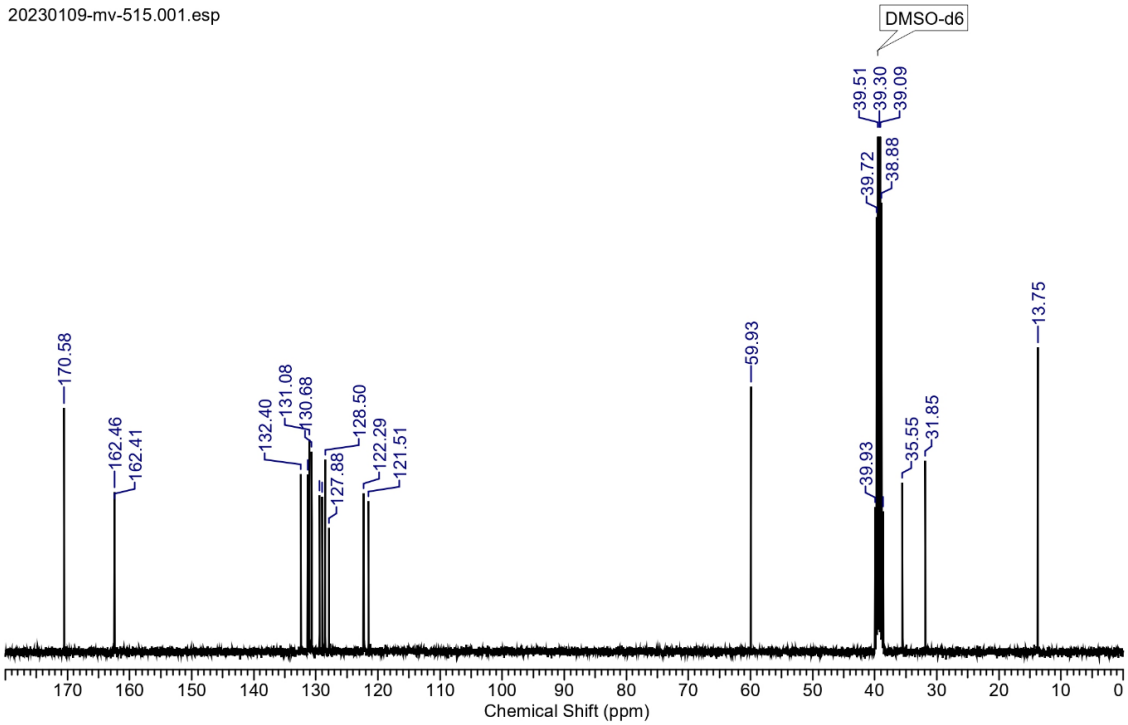

A.2 (a) ^{1}H (400 MHz, DMSO-d$_6$) *and* (b) ^{13}C (100 MHz, DMSO-d$_6$) NMR of *Molecule-2*

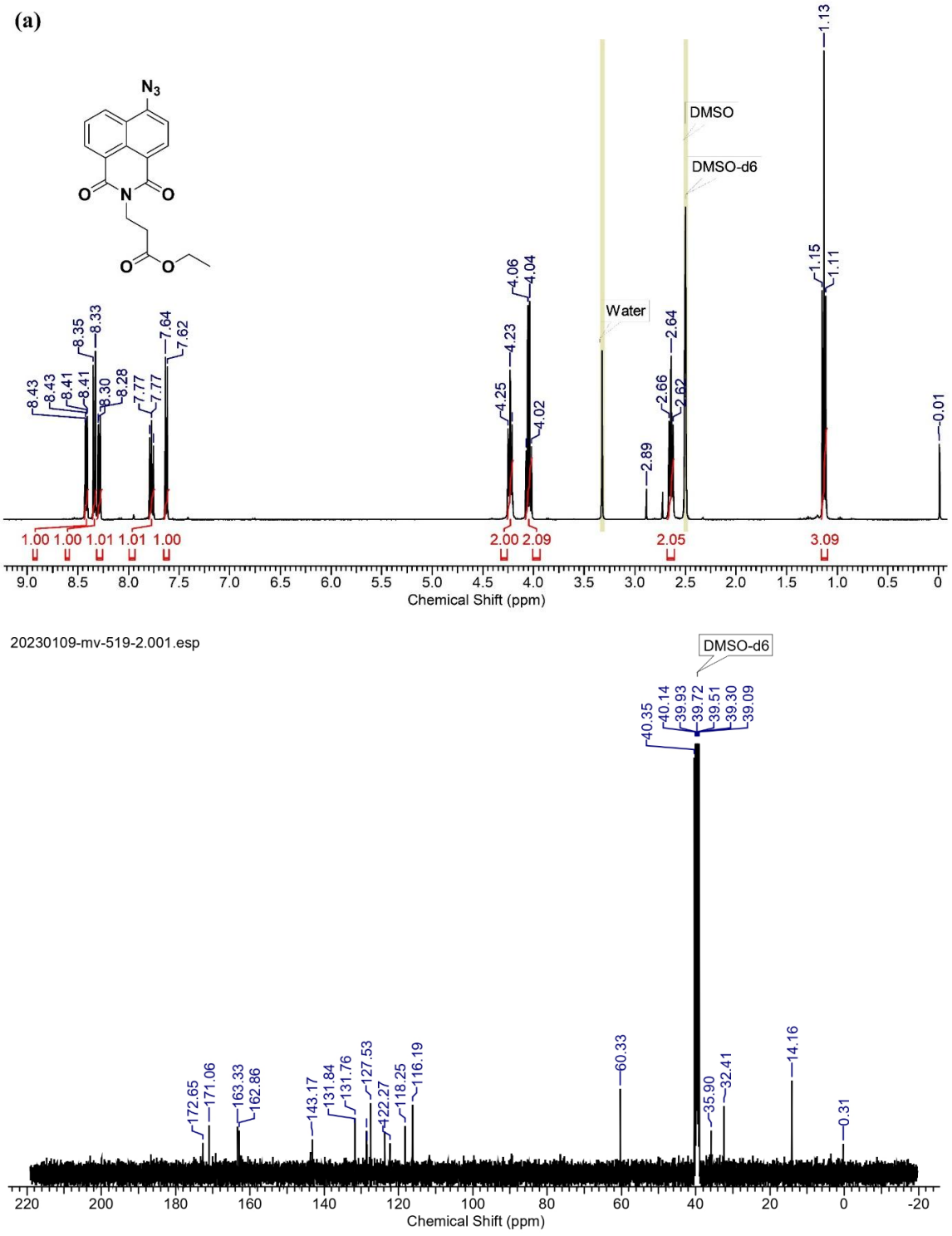

A.3 **^{1}H (400 MHz, DMSO-d$_6$) *and* (b) ^{13}C (100 MHz, DMSO-d$_6$) NMR of *Molecule-3***

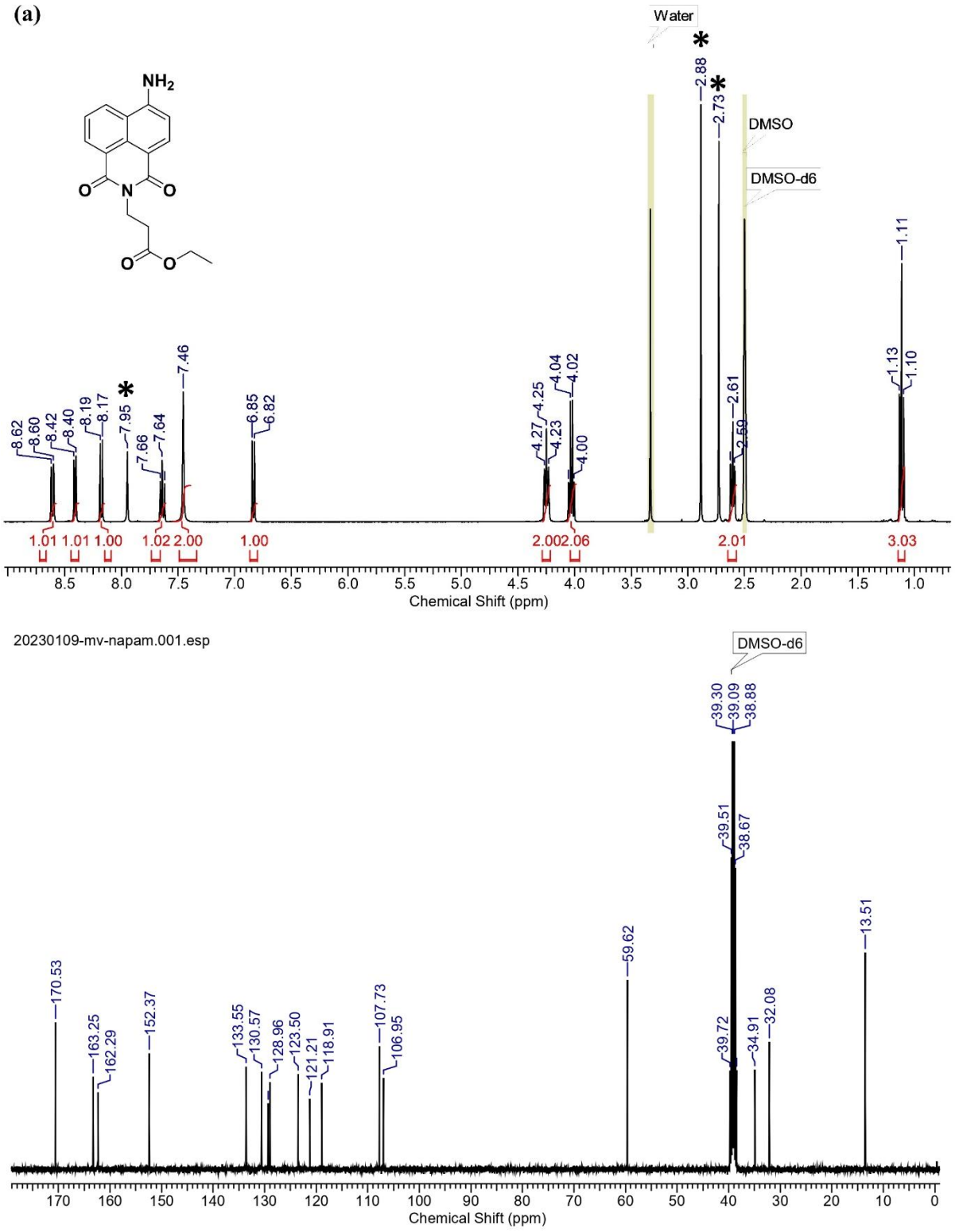

A.4 **^{1}H (400 MHz, $CDCl_3$) *and* (b) ^{13}C (100 MHz, $CDCl_3$) NMR of *Molecule-4***

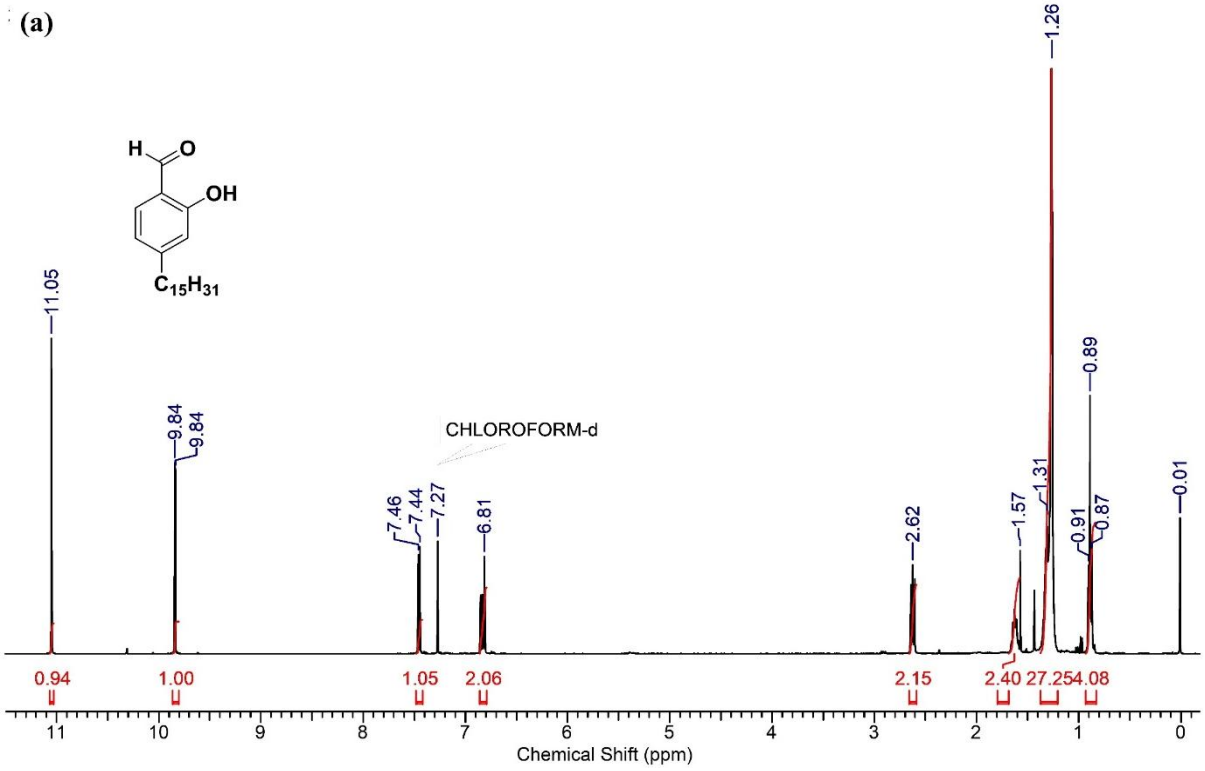

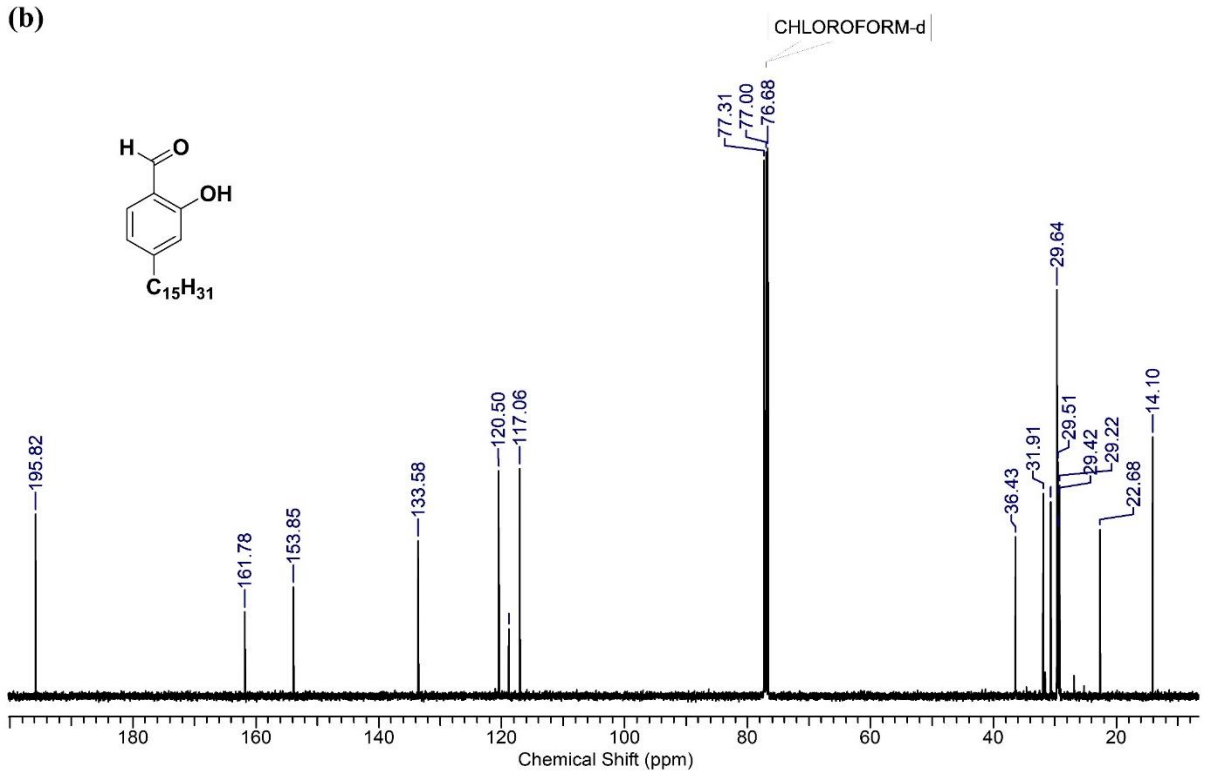

A.5 **^{1}H (400 MHz, DMSO- d_6) *and* (b) ^{13}C (100 MHz, $CDCl_3$) NMR of *SA-Imine***

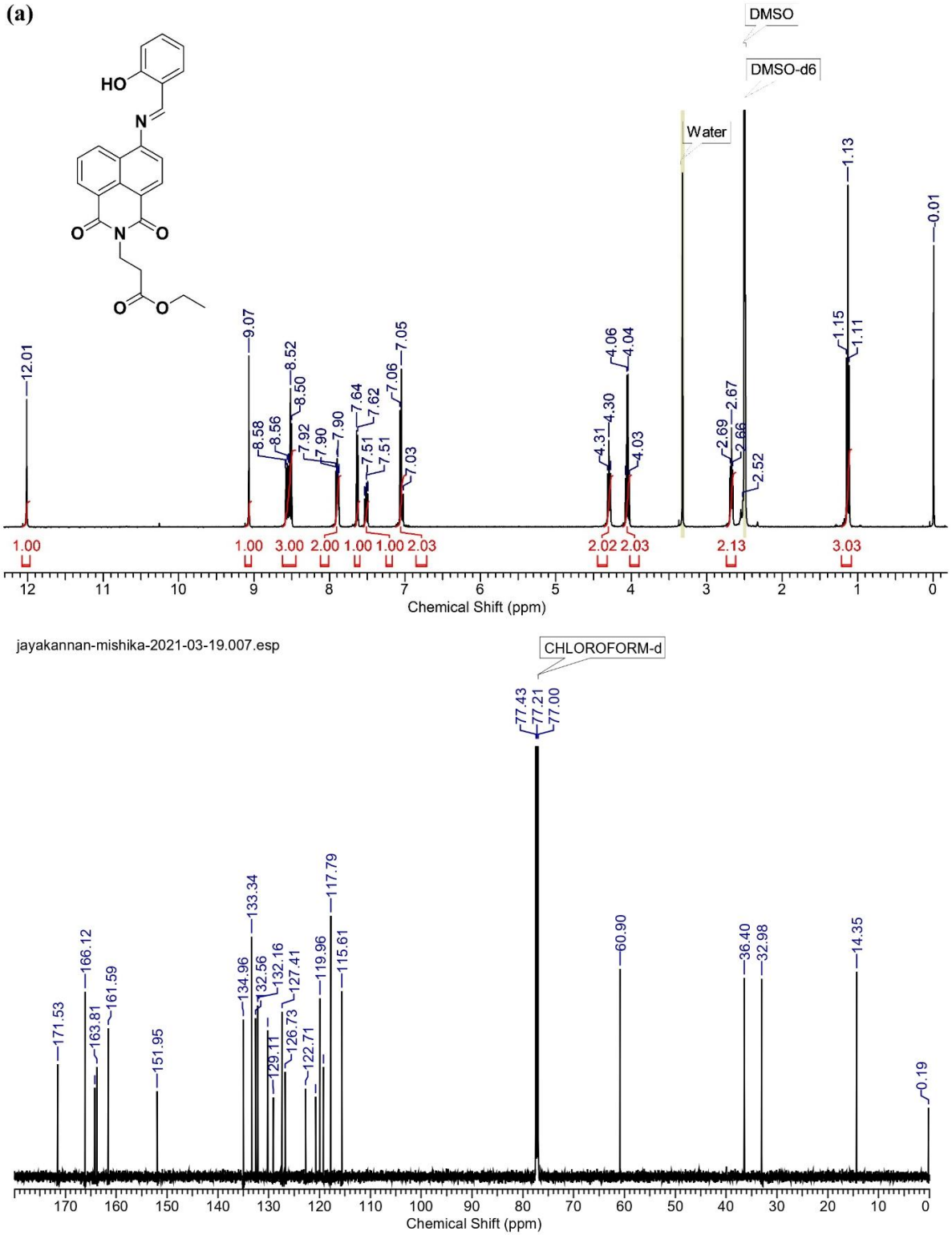

A.6 HRMS of *SA-Imine*

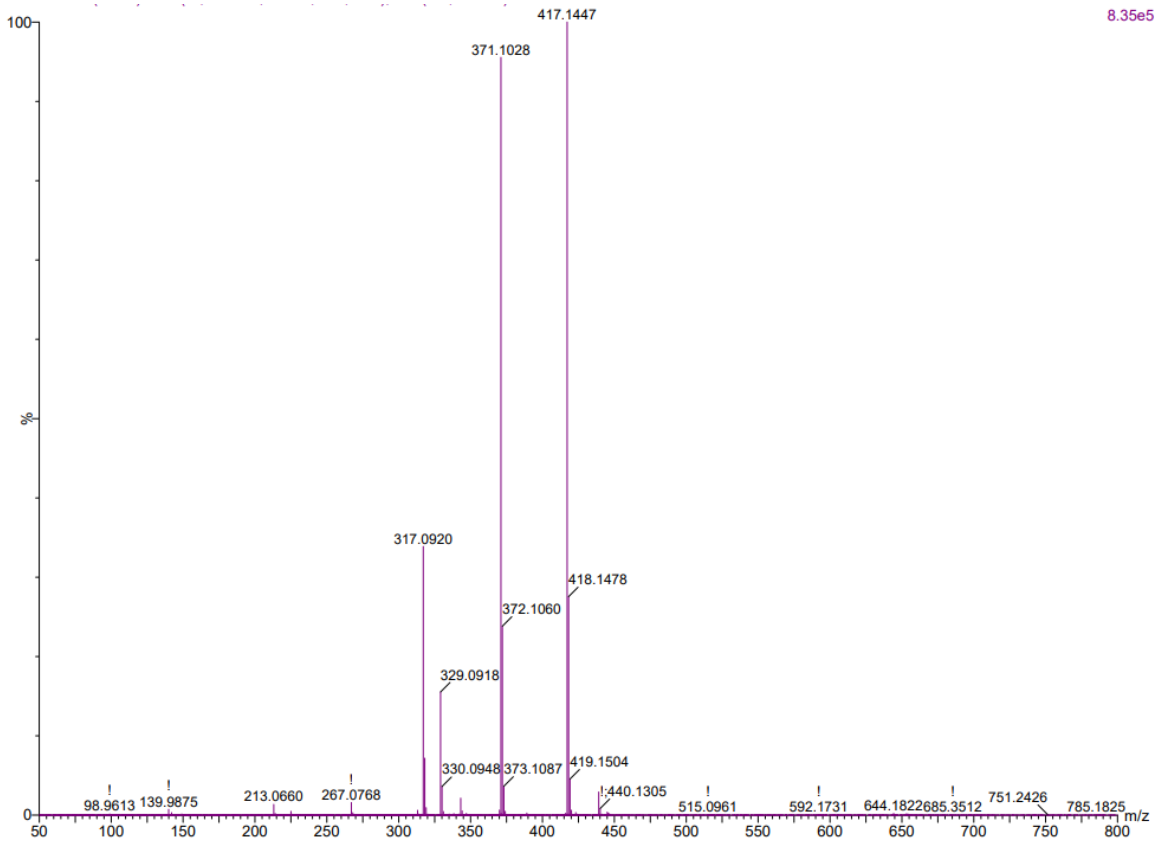

A.7 **^{1}H (400 MHz, DMSO- d_6) *and* (b) ^{13}C (100 MHz, $CDCl_3$) NMR of *BZA-Imine***

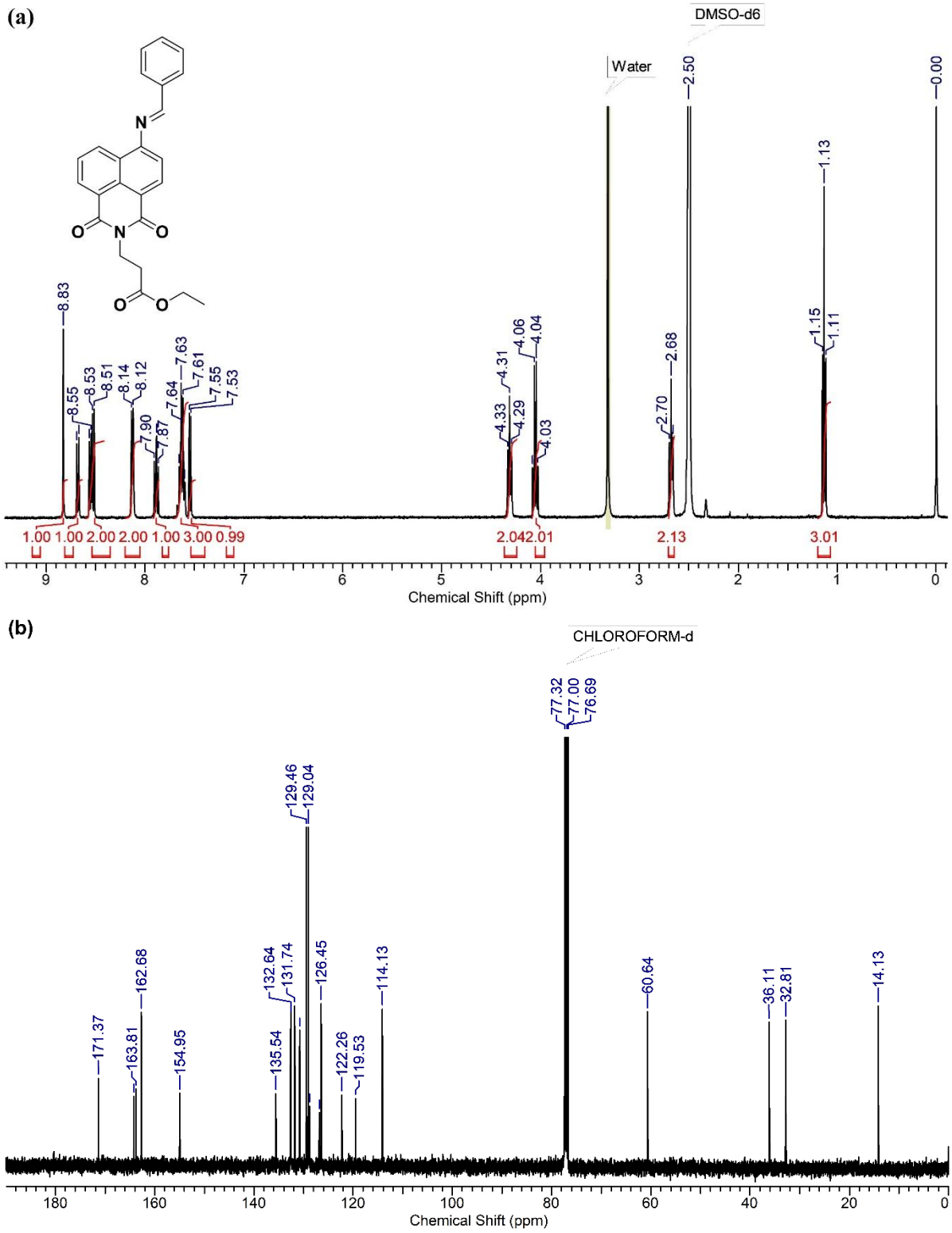

A.8 HRMS of *BZA-Imine*

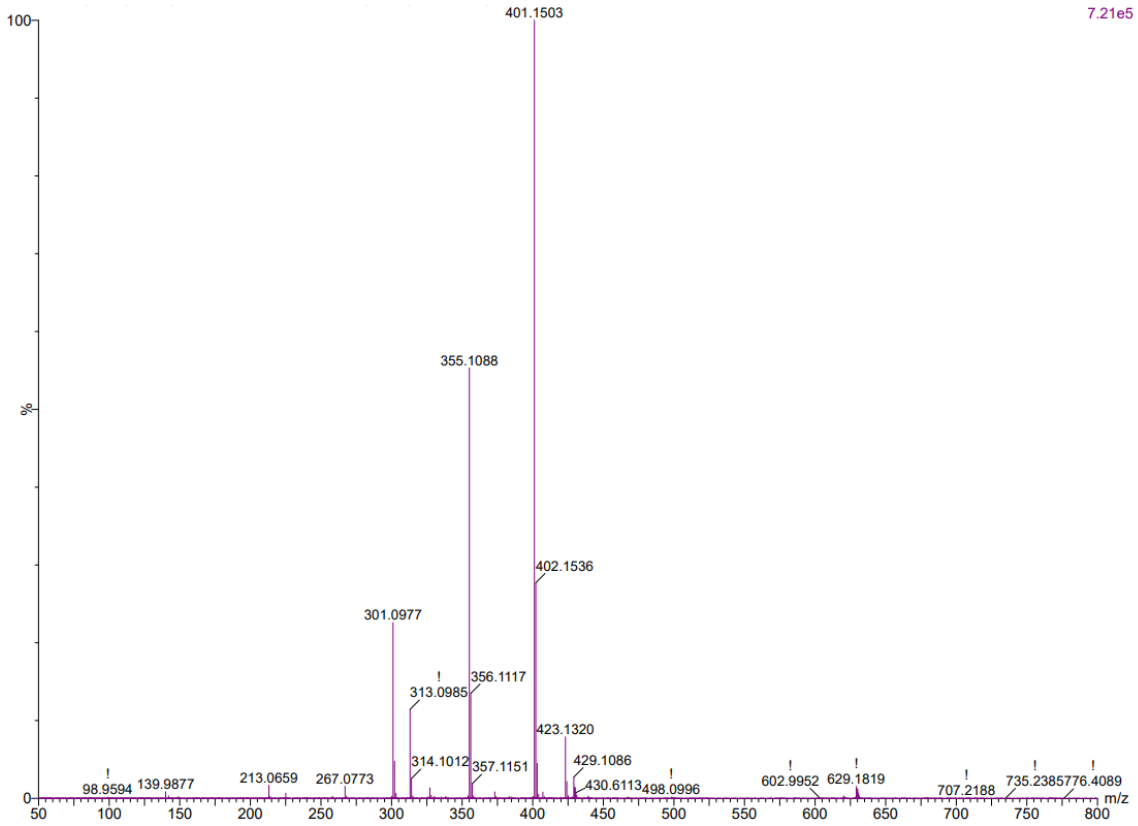

A.9 **^{1}H (400 MHz, $CDCl_3$) *and* (b) ^{13}C (100 MHz, $CDCl_3$) NMR of *PDP-Imine***

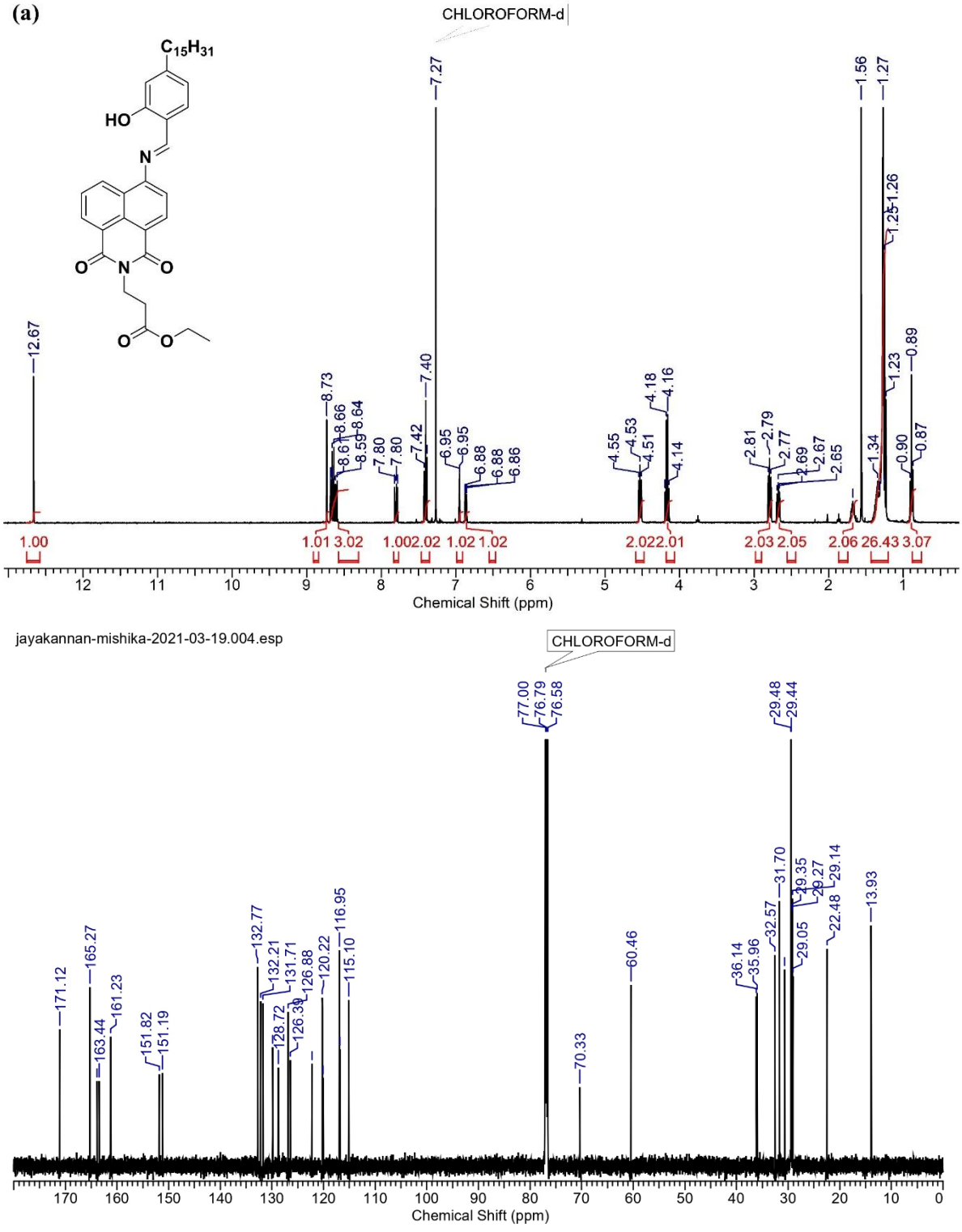

A.10 **^{1}H (400 MHz, DMSO- d_6) *and* (b) ^{13}C (100 MHz, DMSO- d_6) NMR of *Molecule-5***

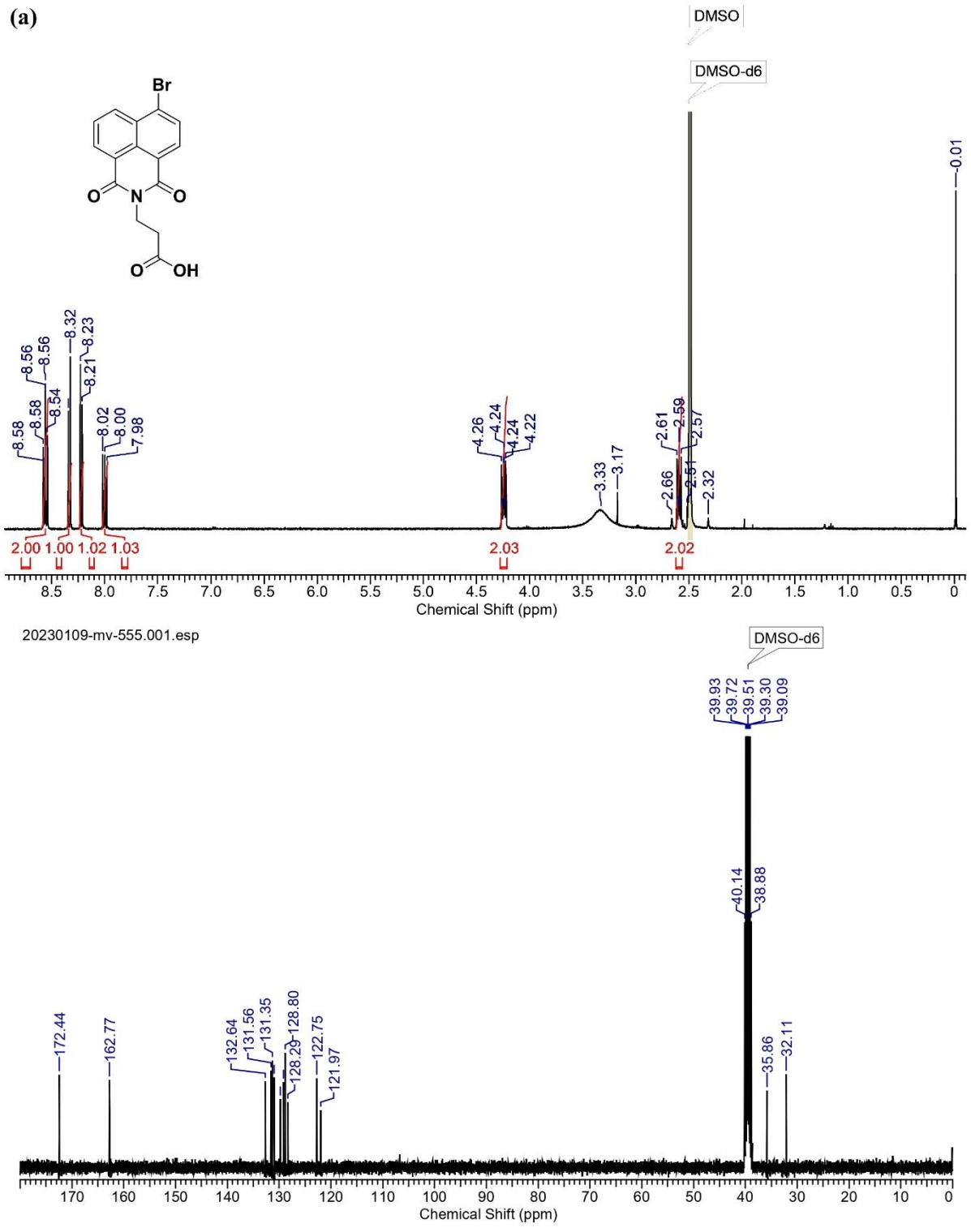

A.11 **^{1}H (400 MHz, CDCl$_3$) *and* (b) ^{13}C (100 MHz, CDCl$_3$) NMR of *Molecule-6***

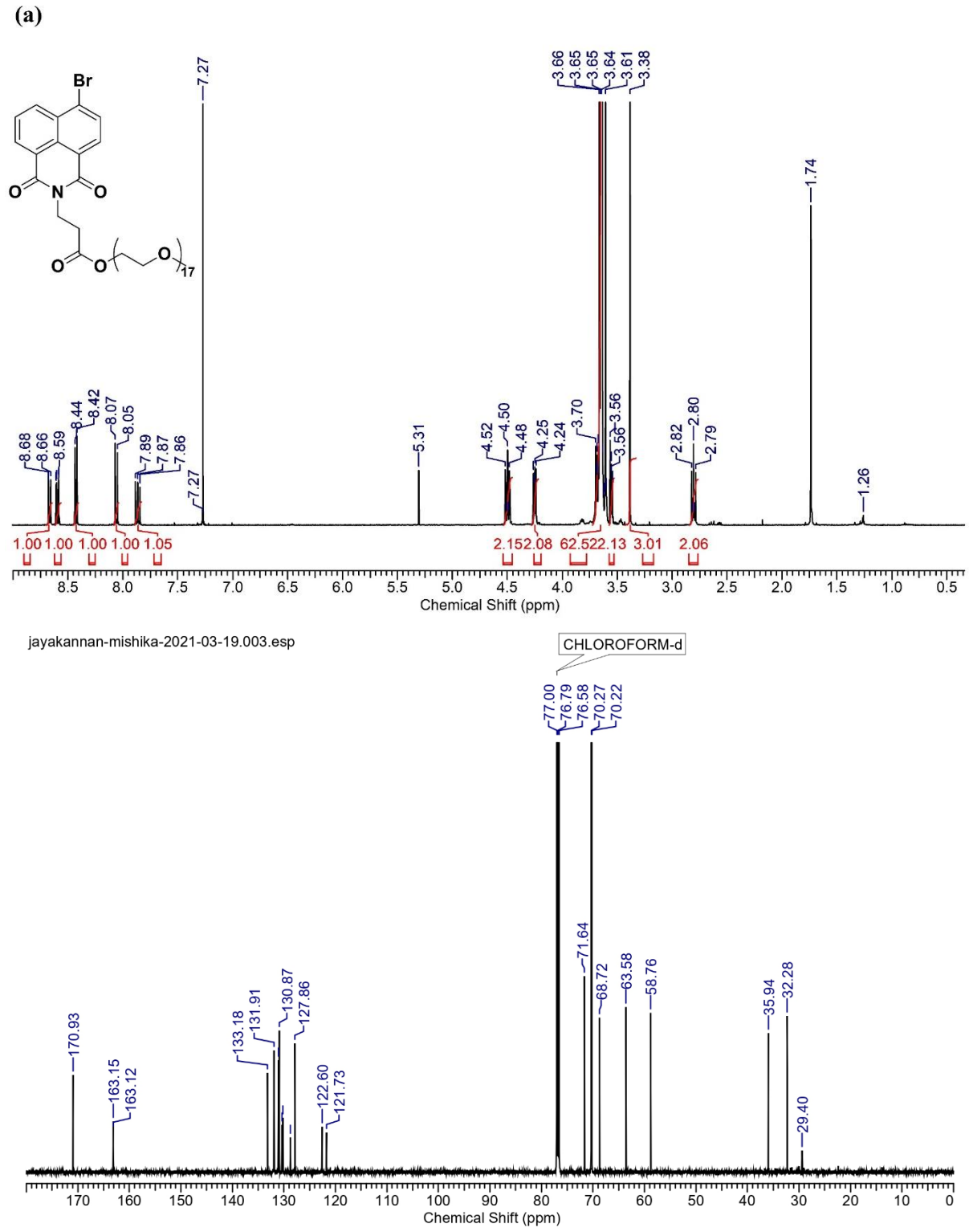

A.12 **^{1}H (400 MHz, CDCl$_3$) *and* (b) ^{13}C (100 MHz, CDCl$_3$) NMR of *Molecule-7***

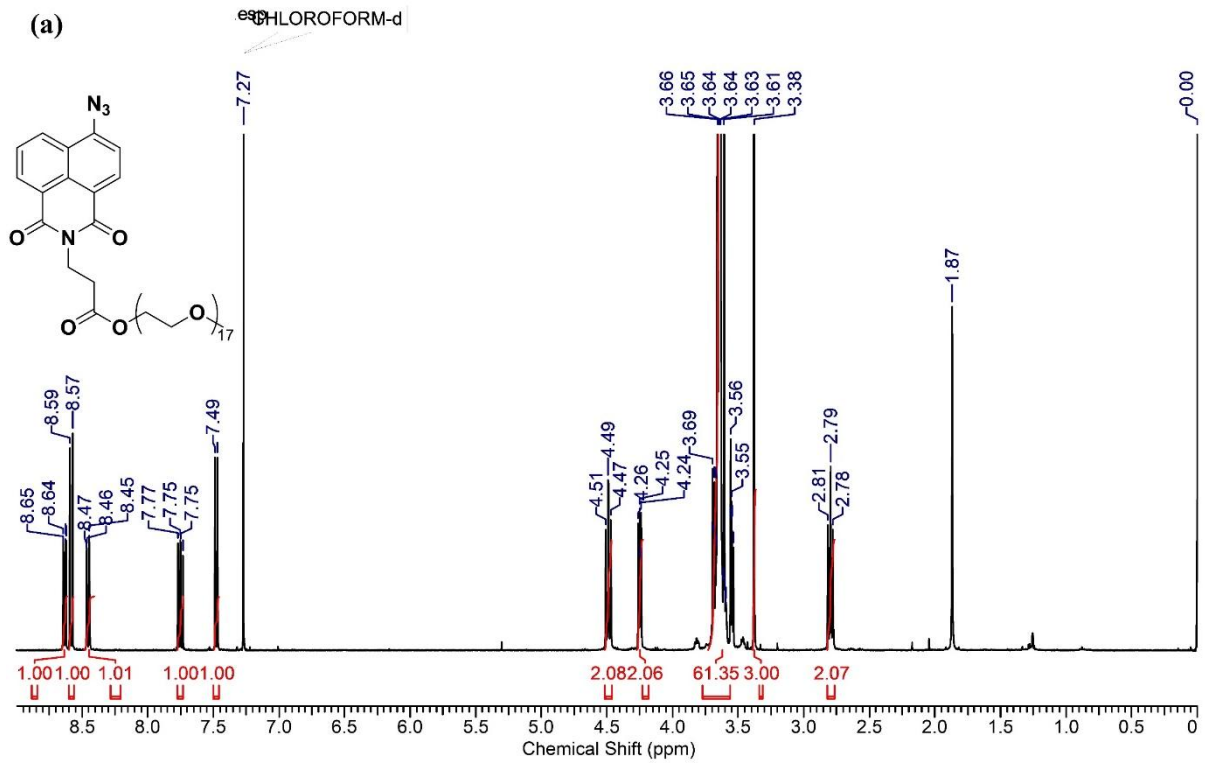

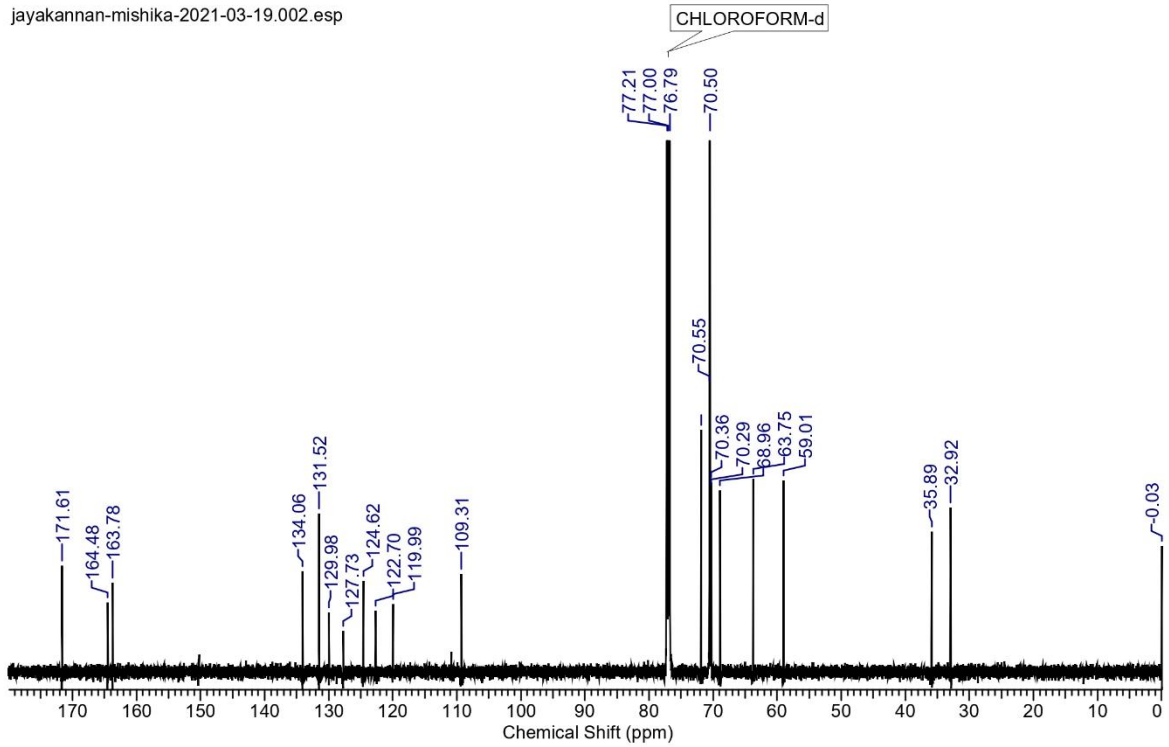

A.13 **^{1}H (400 MHz, CDCl$_3$) *and* (b) ^{13}C (100 MHz, CDCl$_3$) NMR of *Molecule-8***

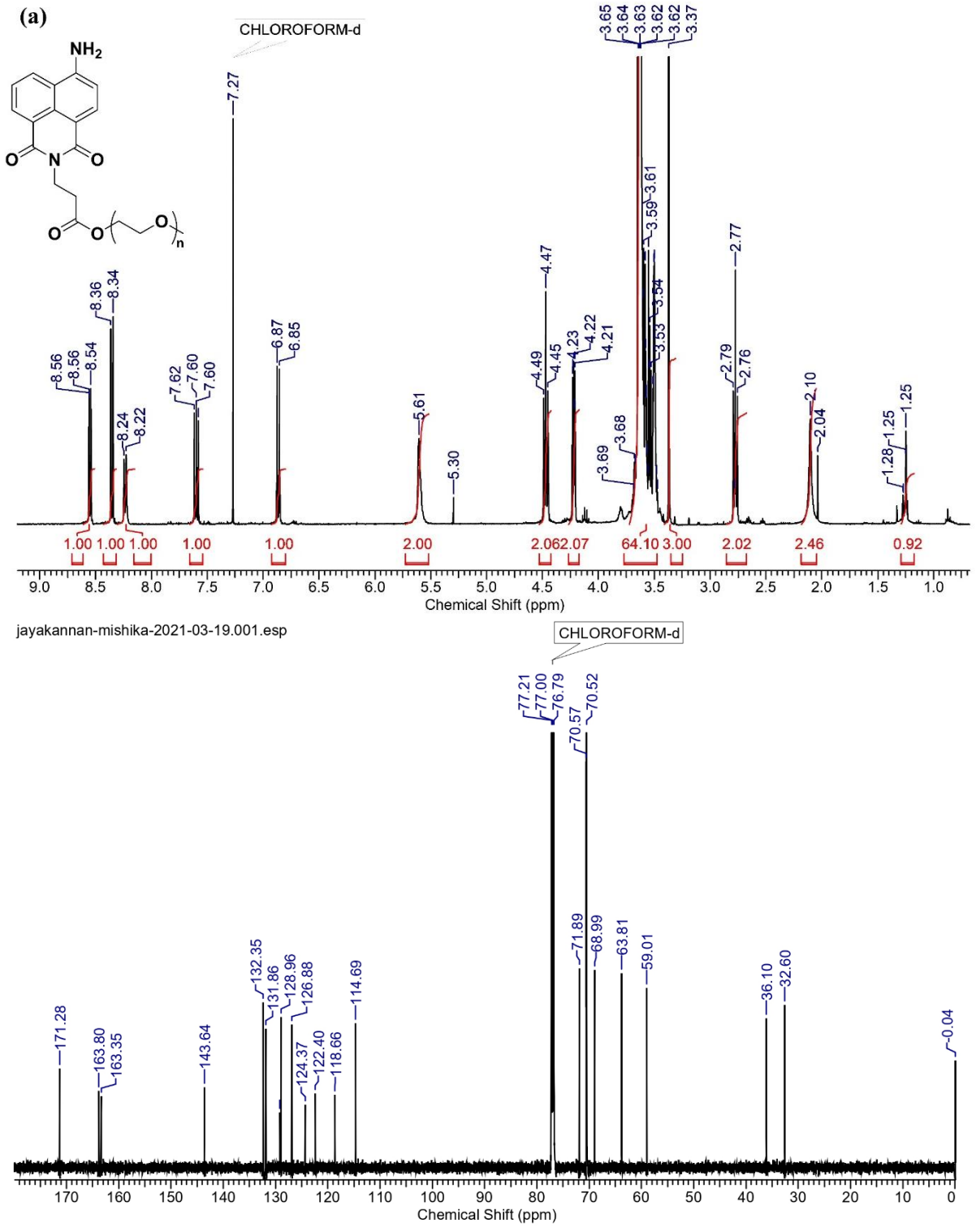

A.14 **^{1}H (400 MHz, CDCl$_3$) *and* (b) ^{13}C (100 MHz, CDCl$_3$) NMR of *PEG-SA-Imine***

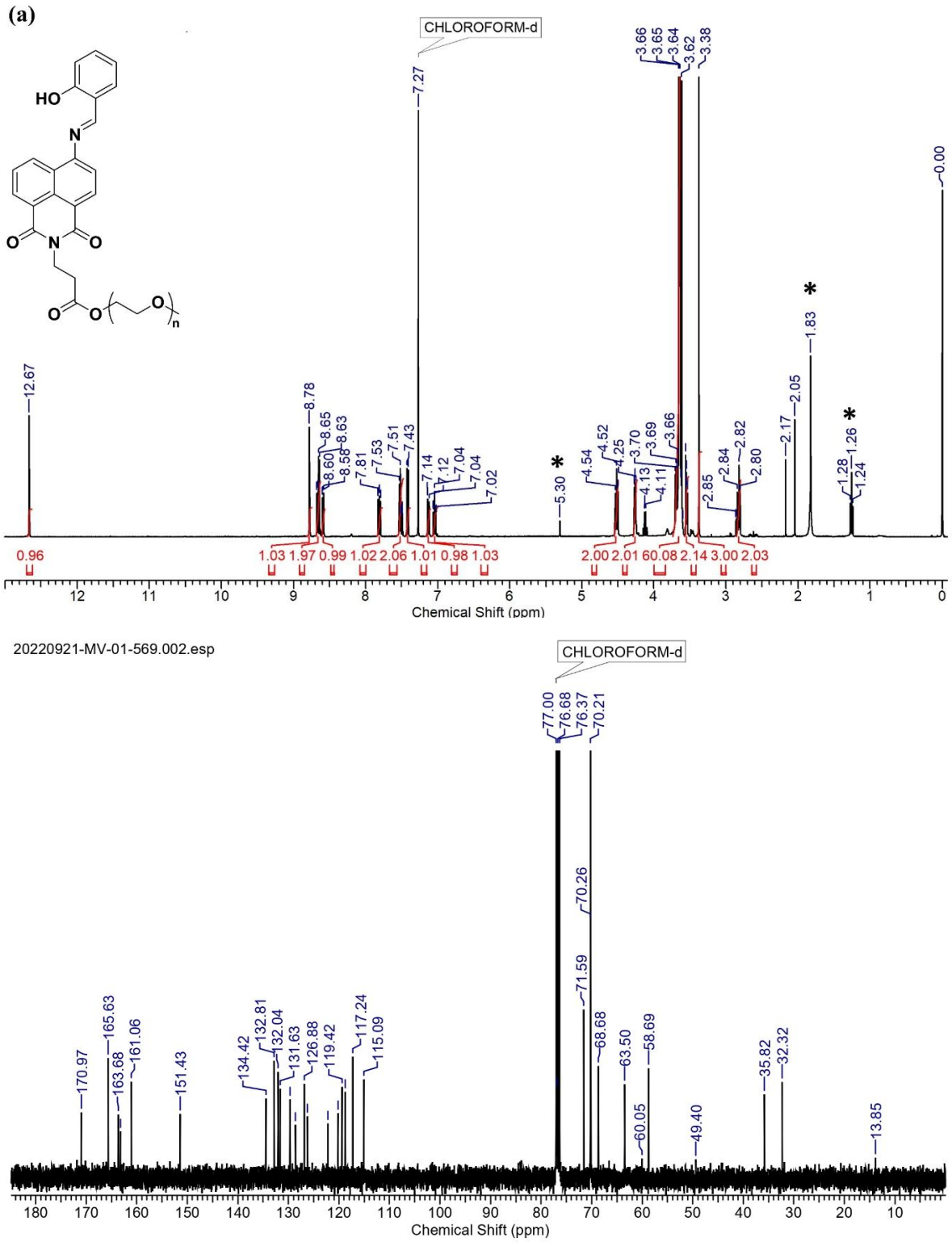

A.15 MALDI of PEG-SA-Imine

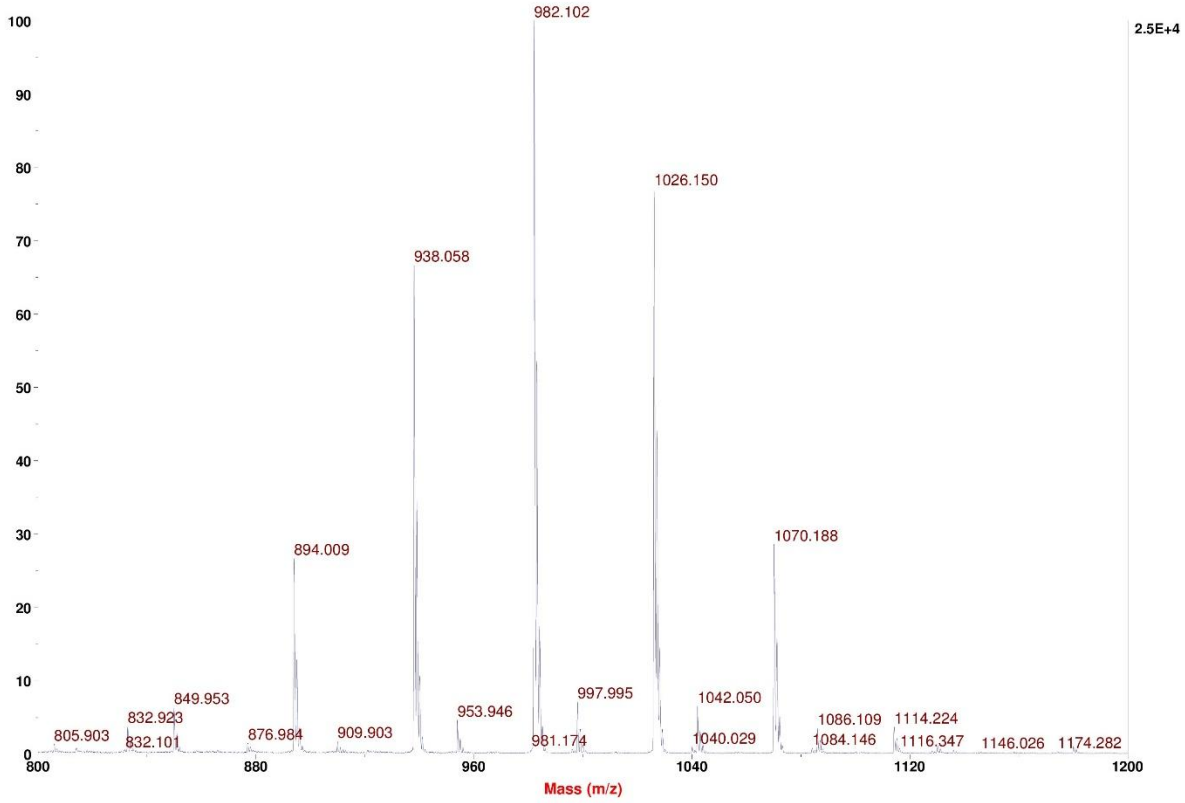

A.16 **^{1}H (400 MHz, CDCl$_3$) *and* (b) ^{13}C (100 MHz, CDCl$_3$) NMR of *PEG-PDP-Imine***

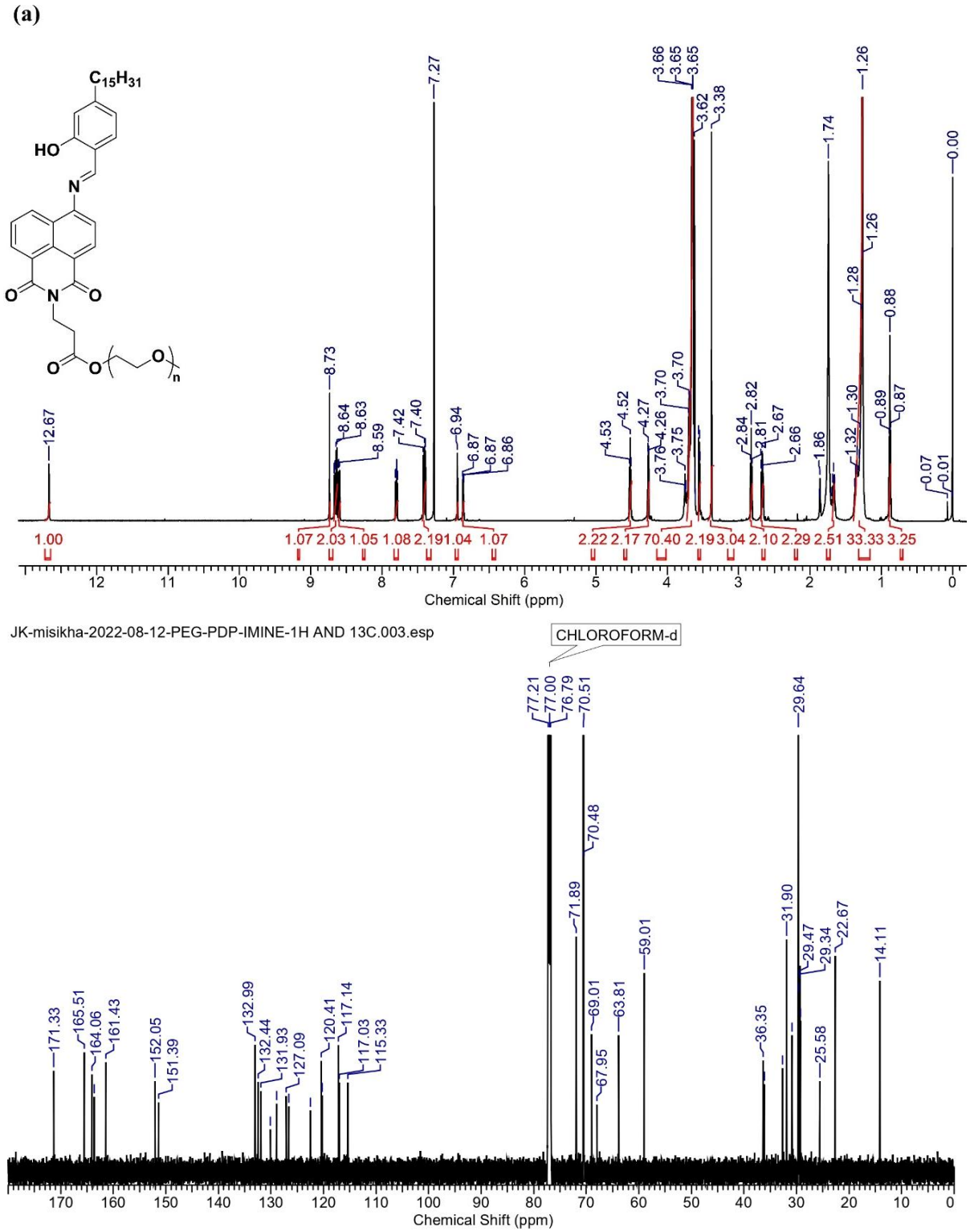

A.17 MALDI of PEG-PDP-Imine

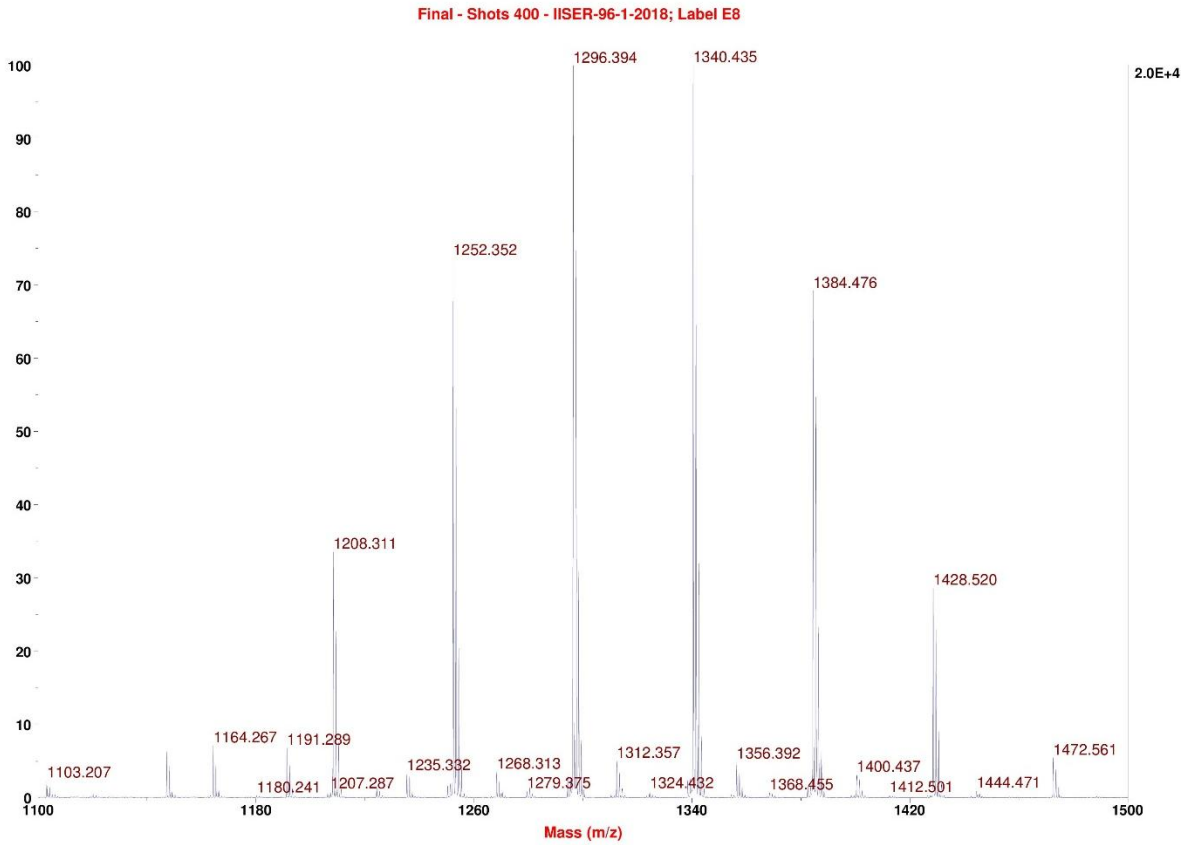

A.18 ^{1}H (400 MHz, $CDCl_3$) NMR of *TPE-COOH and PDP, TPE substituted Dextran*

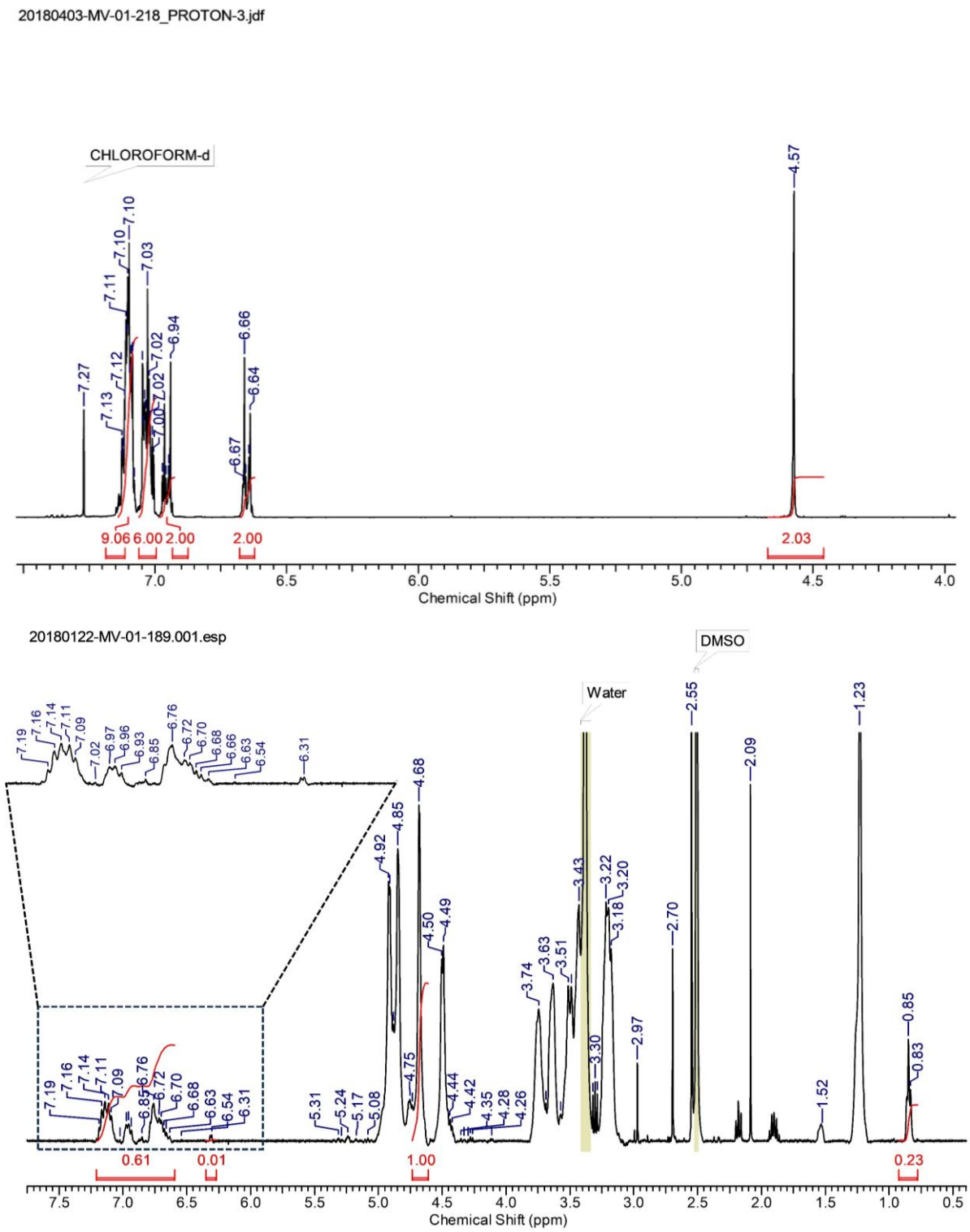

A.19 **^{1}H (400 MHz, CDCl$_3$) *and* ^{13}C (100 MHz, CDCl$_3$) NMR of *Sugar derivative-1***

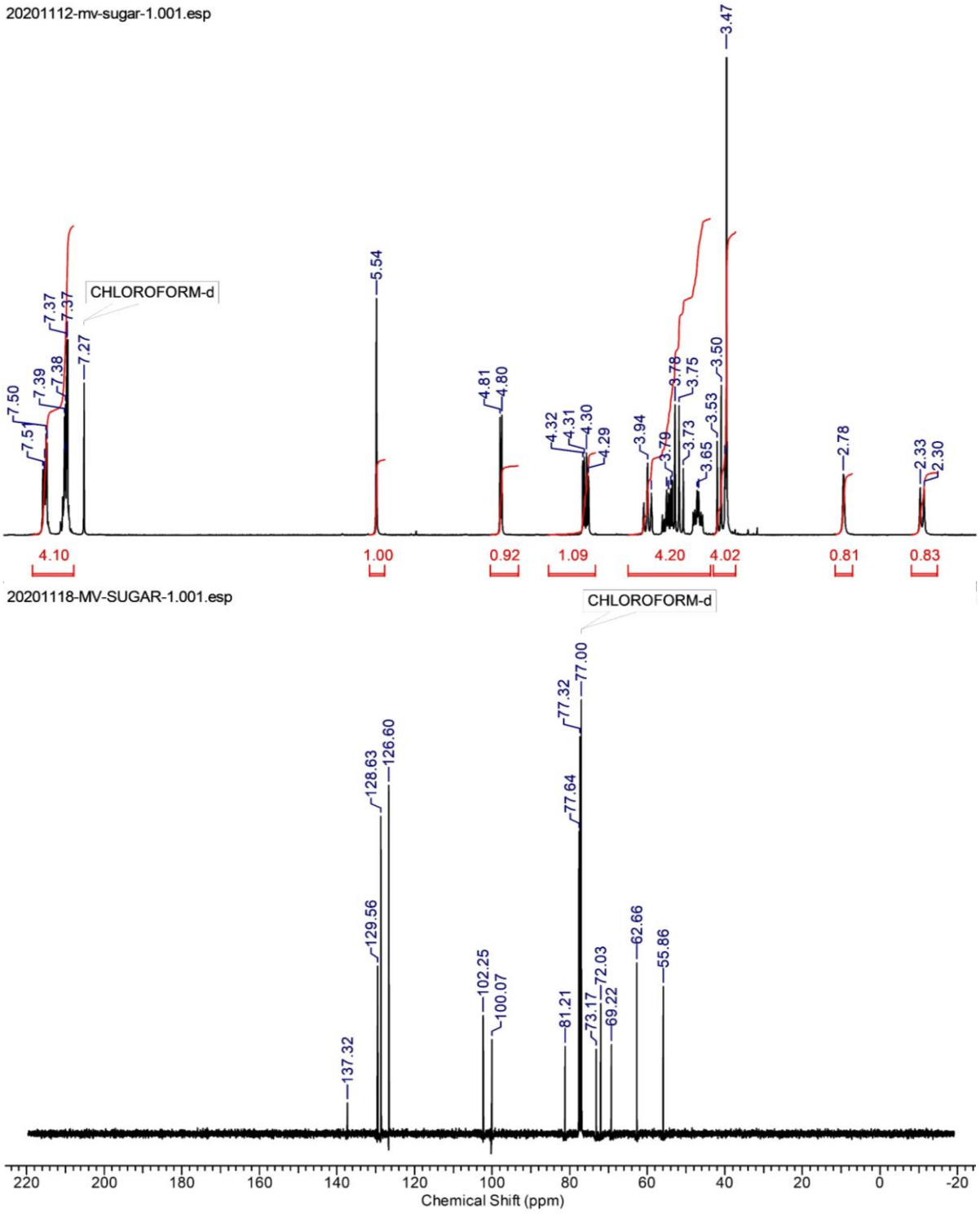

A.20 **^{1}H (400 MHz, CDCl$_3$) *and* ^{13}C (100 MHz, CDCl$_3$) NMR of *Sugar derivative-2***

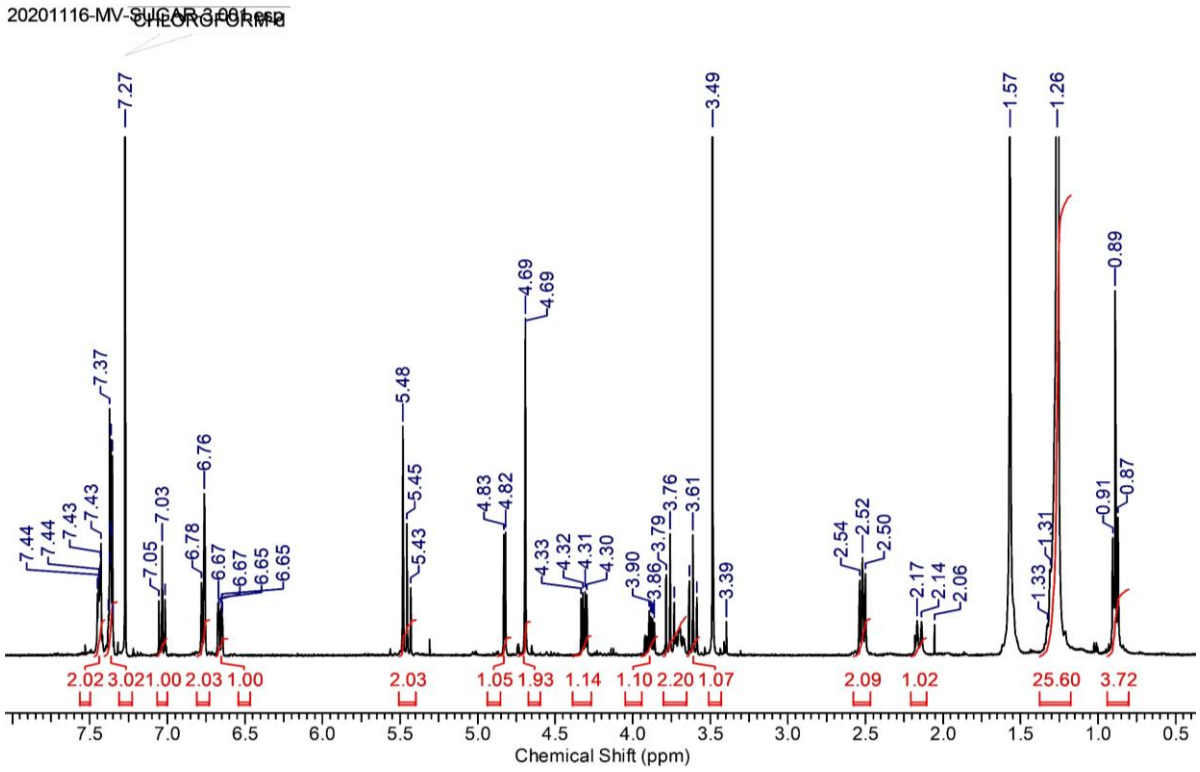

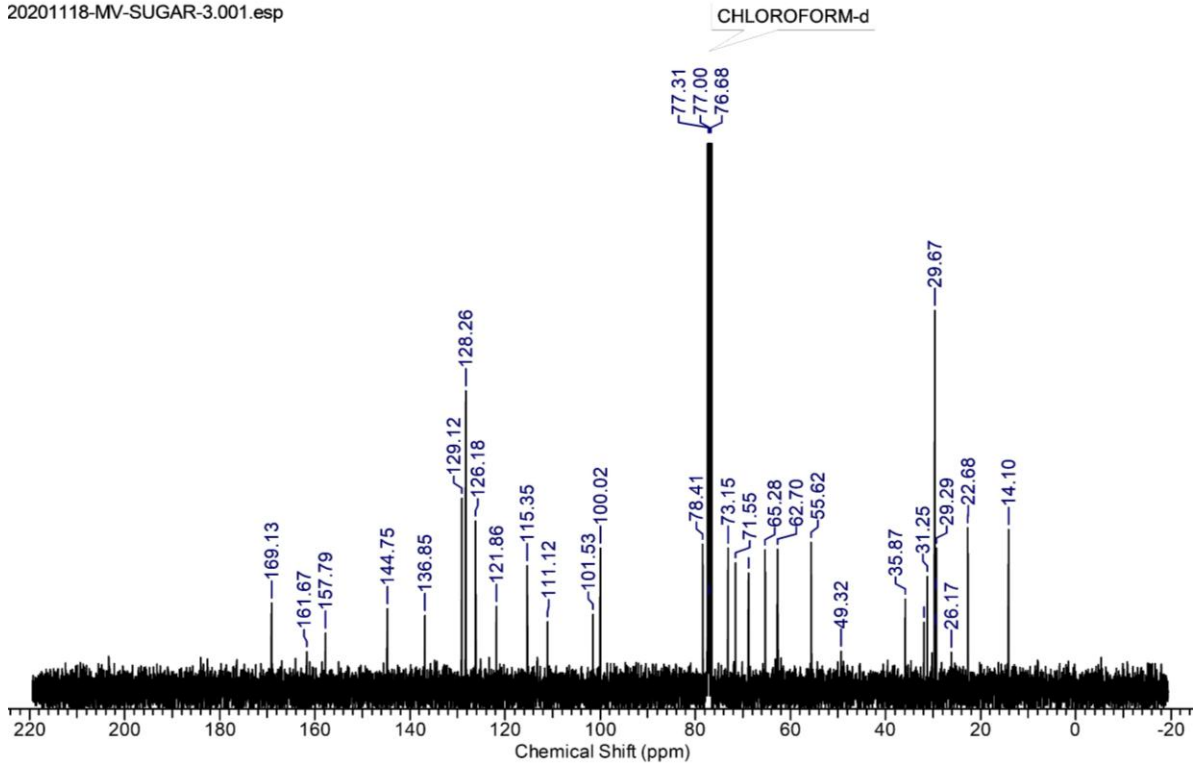

A.21 **^{1}H (400 MHz, CDCl$_3$) of *Sugar derivative-3 (disubstituted derivative) & derivative-4***

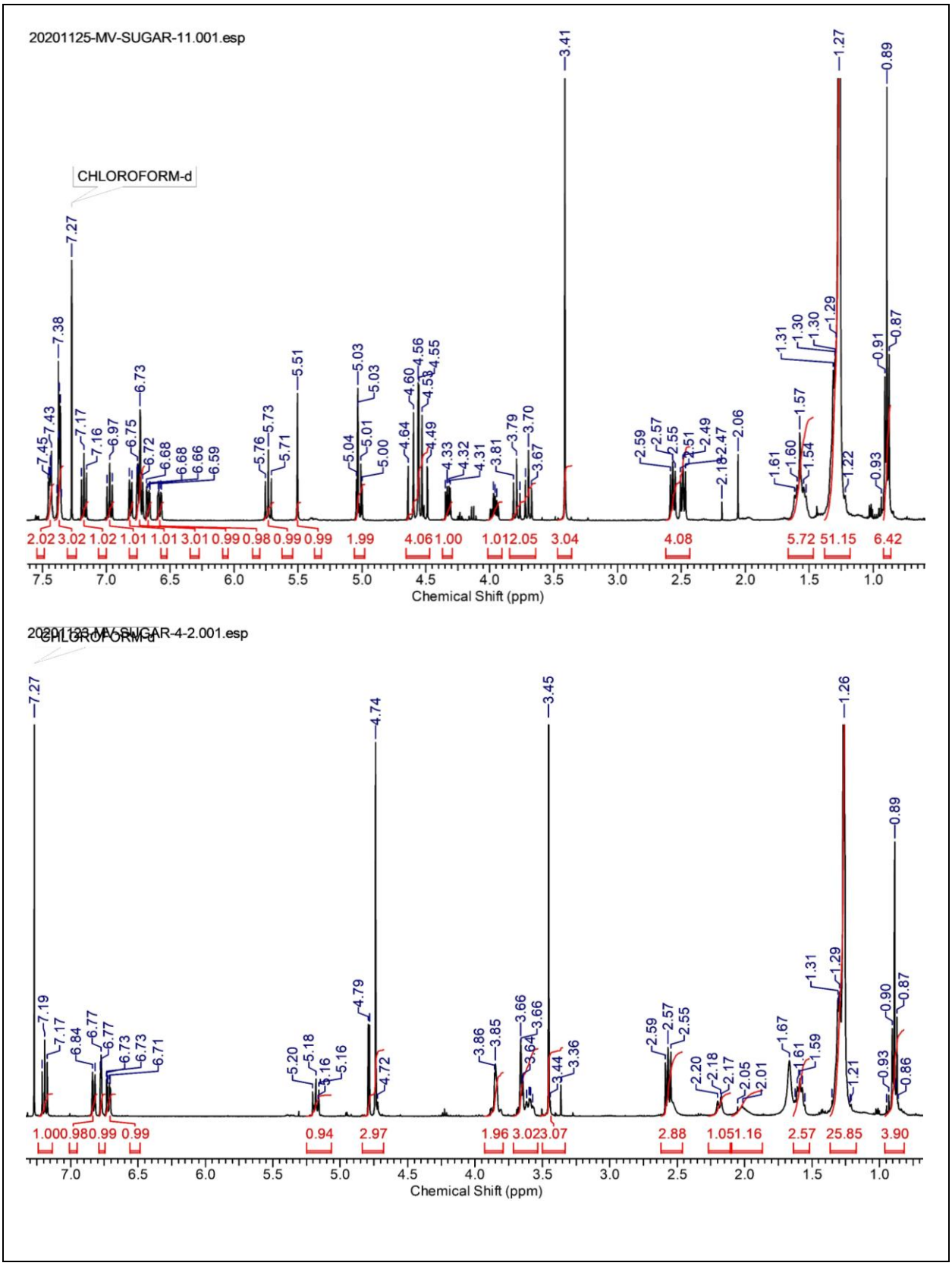

A.22 **^{1}H (400 MHz, CDCl$_3$)** ***showing enzyme degradation of sugar derivative-4***

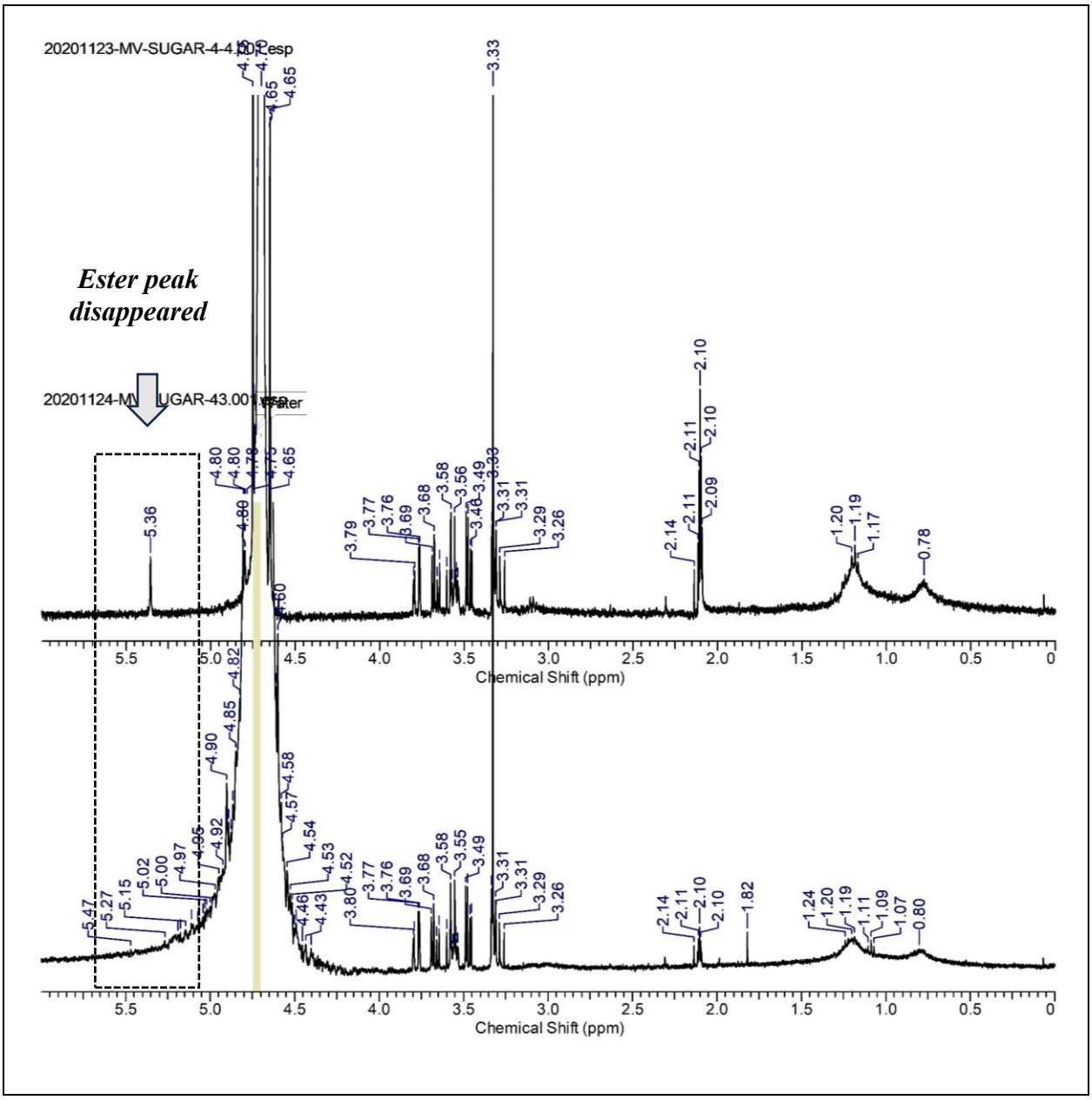

Appendix B: Table of Crystallographic data for SA-Imine synthesized in chapter 3

Table B.1: Crystallographic data for **SA-Imine**

Chemical formula	C_{24} H_{20} N_2 O_5
Formula weight	416.42
Temperature	273(2) K
Wavelength	0.71073 Å
Crystal system	Monoclinic
Space group	P 21/c
Unit cell dimensions	a = 17.87(2) Å, a= 90°. b = 7.022(8) Å, b= 104.72(3) °. c = 16.028(19) Å, g = 90°.
Volume	1945(4) $Å^3$
Z	4
Density (calculated)	1.422 Mg/m^3
Absorption coefficient	0.101 mm^{-1}
F (000)	872
Theta range for data collection	2.356 to 25.028°.
Reflections collected	19788
Independent reflections	3431 [R(int) = 0.3504]
Completeness to theta = 25.028°	99.9 %
Absorption correction	None

Refinement method	Full-matrix least-squares on F^2
Data / restraints / parameters	3431 / 12 / 283
Goodness-of-fit on F^2	0.983
Final R indices [I>2sigma(I)]	R1 = 0.0980, wR2 = 0.1757
R indices (all data)	R1 = 0.2798, wR2 = 0.2542
Extinction coefficient	0.011(2)
Largest diff. peak and hole	0.410 and -0.384 e.$Å^{-3}$

Table B.2: Atomic coordinates (x 10^4) and equivalent isotropic displacement parameters ($Å^2$x 10^3) for **SA-Imine**. U(eq) is defined as one third of the trace of the orthogonalized U^{ij} tensor.

	x	y	z	U(eq)
O(1)	9320(3)	2207(6)	4166(4)	37(2)
N(1)	7703(3)	5042(7)	5822(5)	23(2)
C(1)	10255(4)	440(9)	3665(6)	44(3)
O(2)	9198(3)	5406(7)	4114(4)	44(2)
N(2)	4875(3)	4107(7)	7617(4)	23(2)
C(2)	9771(4)	2266(10)	3535(6)	35(2)
O(3)	8703(3)	5761(6)	6961(4)	34(2)
C(3)	9069(4)	3889(11)	4418(6)	32(2)
C(4)	8641(4)	3589(8)	5085(5)	30(2)
O(4)	6747(3)	4007(6)	4679(4)	33(2)
C(5)	8197(4)	5375(8)	5232(5)	29(2)
O(5)	4515(2)	3570(7)	9082(3)	32(2)
C(6)	8018(4)	5365(9)	6706(6)	26(2)
C(7)	7486(4)	5231(9)	7260(6)	24(2)

C(8)	6693(4)	4700(8)	6911(5)	18(2)
C(9)	6428(4)	4223(9)	6026(5)	20(2)
C(10)	6953(4)	4379(9)	5452(6)	25(2)
C(11)	5679(4)	3638(9)	5693(5)	25(2)
C(12)	5153(4)	3597(9)	6213(5)	22(2)
C(13)	5378(4)	4108(9)	7069(6)	25(2)
C(14)	6180(4)	4629(9)	7465(5)	23(2)
C(15)	6469(4)	5005(8)	8330(5)	26(2)
C(16)	7242(4)	5467(8)	8660(5)	24(2)
C(17)	7738(4)	5604(9)	8123(6)	28(2)
C(18)	4167(4)	4675(9)	7299(5)	26(2)
C(19)	3600(4)	4687(9)	7796(5)	21(2)
C(20)	3787(4)	4166(9)	8668(6)	25(2)
C(21)	3236(4)	4225(8)	9136(5)	25(2)
C(22)	2477(4)	4795(8)	8741(6)	26(2)
C(23)	2276(4)	5304(9)	7878(6)	30(2)
C(24)	2831(4)	5273(9)	7414(5)	26(2)

Table B.3: Bond lengths [Å] for **SA-Imine**

O(1)-C(3)	1.361(8)
O(1)-C(2)	1.445(8)
N(1)-C(10)	1.401(8)
N(1)-C(6)	1.404(10)
N(1)-C(5)	1.467(9)
C(1)-C(2)	1.530(8)
C(1)-H(1A)	0.9600
C(1)-H(1B)	0.9600
C(1)-H(1C)	0.9600
O(2)-C(3)	1.217(8)
N(2)-C(18)	1.301(8)
N(2)-C(13)	1.408(9)

C(2)-H(2A)	0.9700
C(2)-H(2B)	0.9700
O(3)-C(6)	1.221(8)
C(3)-C(4)	1.479(10)
C(4)-C(5)	1.534(8)
C(4)-H(4A)	0.9700
C(4)-H(4B)	0.9700
O(4)-C(10)	1.227(9)
C(5)-H(5A)	0.9700
C(5)-H(5B)	0.9700
O(5)-C(20)	1.366(8)
O(5)-H(5)	0.8200
C(6)-C(7)	1.459(10)
C(7)-C(17)	1.367(10)
C(7)-C(8)	1.434(9)
C(8)-C(9)	1.417(10)
C(8)-C(14)	1.430(9)
C(9)-C(11)	1.373(9)
C(9)-C(10)	1.475(10)
C(11)-C(12)	1.406(9)
C(11)-H(11)	0.9300
C(12)-C(13)	1.374(10)
C(12)-H(12)	0.9300
C(13)-C(14)	1.459(9)
C(14)-C(15)	1.377(10)
C(15)-C(16)	1.386(9)
C(15)-H(15)	0.9300
C(16)-C(17)	1.388(9)
C(16)-H(16)	0.9300
C(17)-H(17)	0.9300
C(18)-C(19)	1.440(9)
C(18)-H(18)	0.9300
C(19)-C(20)	1.399(10)
C(19)-C(24)	1.416(9)

C(20)-C(21)	1.383(9)
C(21)-C(22)	1.401(9)
C(21)-H(21)	0.9300
C(22)-C(23)	1.385(11)
C(22)-H(22)	0.9300
C(23)-C(24)	1.384(9)
C(23)-H(23)	0.9300
C(24)-H(24)	0.9300

Table B.4: Bond angles [°] for **SA-Imine**

C(3)-O(1)-C(2)	117.9(5)
C(10)-N(1)-C(6)	125.2(7)
C(10)-N(1)-C(5)	116.6(7)
C(6)-N(1)-C(5)	118.2(6)
C(2)-C(1)-H(1A)	109.5
C(2)-C(1)-H(1B)	109.5
H(1A)-C(1)-H(1B)	109.5
C(2)-C(1)-H(1C)	109.5
H(1A)-C(1)-H(1C)	109.5
H(1B)-C(1)-H(1C)	109.5
C(18)-N(2)-C(13)	117.8(7)
O(1)-C(2)-C(1)	106.1(6)
O(1)-C(2)-H(2A)	110.5
C(1)-C(2)-H(2A)	110.5
O(1)-C(2)-H(2B)	110.5
C(1)-C(2)-H(2B)	110.5
H(2A)-C(2)-H(2B)	108.7
O(2)-C(3)-O(1)	122.0(7)
O(2)-C(3)-C(4)	126.8(7)
O(1)-C(3)-C(4)	111.2(6)

C(3)-C(4)-C(5)	112.2(6)
C(3)-C(4)-H(4A)	109.2
C(5)-C(4)-H(4A)	109.2
C(3)-C(4)-H(4B)	109.2
C(5)-C(4)-H(4B)	109.2
H(4A)-C(4)-H(4B)	107.9
N(1)-C(5)-C(4)	112.8(6)
N(1)-C(5)-H(5A)	109.0
C(4)-C(5)-H(5A)	109.0
N(1)-C(5)-H(5B)	109.0
C(4)-C(5)-H(5B)	109.0
H(5A)-C(5)-H(5B)	107.8
C(20)-O(5)-H(5)	109.5
O(3)-C(6)-N(1)	119.0(7)
O(3)-C(6)-C(7)	124.4(8)
N(1)-C(6)-C(7)	116.6(7)
C(17)-C(7)-C(8)	118.9(7)
C(17)-C(7)-C(6)	120.3(7)
C(8)-C(7)-C(6)	120.8(8)
C(9)-C(8)-C(14)	120.7(7)
C(9)-C(8)-C(7)	119.8(7)
C(14)-C(8)-C(7)	119.5(7)
C(11)-C(9)-C(8)	120.3(7)
C(11)-C(9)-C(10)	119.5(8)
C(8)-C(9)-C(10)	120.2(7)
O(4)-C(10)-N(1)	120.5(7)
O(4)-C(10)-C(9)	122.6(7)
N(1)-C(10)-C(9)	116.9(8)
C(9)-C(11)-C(12)	120.6(8)
C(9)-C(11)-H(11)	119.7
C(12)-C(11)-H(11)	119.7
C(13)-C(12)-C(11)	121.0(7)
C(13)-C(12)-H(12)	119.5
C(11)-C(12)-H(12)	119.5

C(12)-C(13)-N(2)	123.4(7)
C(12)-C(13)-C(14)	120.4(7)
N(2)-C(13)-C(14)	116.1(8)
C(15)-C(14)-C(8)	118.9(7)
C(15)-C(14)-C(13)	124.2(8)
C(8)-C(14)-C(13)	116.9(8)
C(14)-C(15)-C(16)	120.7(8)
C(14)-C(15)-H(15)	119.6
C(16)-C(15)-H(15)	119.6
C(15)-C(16)-C(17)	120.8(8)
C(15)-C(16)-H(16)	119.6
C(17)-C(16)-H(16)	119.6
C(7)-C(17)-C(16)	121.1(7)
C(7)-C(17)-H(17)	119.4
C(16)-C(17)-H(17)	119.4
N(2)-C(18)-C(19)	122.5(7)
N(2)-C(18)-H(18)	118.8
C(19)-C(18)-H(18)	118.8
C(20)-C(19)-C(24)	117.9(7)
C(20)-C(19)-C(18)	121.8(7)
C(24)-C(19)-C(18)	120.3(8)
O(5)-C(20)-C(21)	117.8(8)
O(5)-C(20)-C(19)	121.5(7)
C(21)-C(20)-C(19)	120.7(7)
C(20)-C(21)-C(22)	120.3(8)
C(20)-C(21)-H(21)	119.9
C(22)-C(21)-H(21)	119.9
C(23)-C(22)-C(21)	120.1(7)
C(23)-C(22)-H(22)	120.0
C(21)-C(22)-H(22)	120.0
C(24)-C(23)-C(22)	119.5(7)
C(24)-C(23)-H(23)	120.2
C(22)-C(23)-H(23)	120.2
C(23)-C(24)-C(19)	121.5(8)

C(23)-C(24)-H(24)	119.3
C(19)-C(24)-H(24)	119.3